

***In situ* Studies of Peptide and Protein Assemblies
at the Solid-Liquid Interface: Hierarchical Self-Assembly,
Dynamics and Functional Properties**

THÈSE N° 8369 (2018)

PRÉSENTÉE LE 2 FÉVRIER 2018

À LA FACULTÉ DES SCIENCES DE BASE
LABORATOIRE DE SCIENCE À L'ÉCHELLE NANOMÉTRIQUE
PROGRAMME DOCTORAL EN PHYSIQUE

ÉCOLE POLYTECHNIQUE FÉDÉRALE DE LAUSANNE

POUR L'OBTENTION DU GRADE DE DOCTEUR ÈS SCIENCES

PAR

Bart Willem STEL

acceptée sur proposition du jury:

Prof. R. Houdré, président du jury
Dr M. A. Lingenfelder, Prof. K. Kern, directeurs de thèse
Prof. J. de Yoreo, rapporteur
Prof. U. Steiner, rapporteur
Prof. A. Radenovic, rapporteuse



ÉCOLE POLYTECHNIQUE
FÉDÉRALE DE LAUSANNE

Suisse
2018

Acknowledgements

Looking back at the years that I have spend here at the EPFL, it were the many discussions with my colleagues that I appreciated most. During the good times, they helped me share my enthusiasm, and during the inevitable difficult times of my PhD, it were these discussions that pulled me back and motivated me to keep going. For this, thanks to all of you!

First of all, I would like to thank Dr. Magalí Lingenfelder for giving me this amazing opportunity to do my doctoral studies here at the MPI-EPFL Nanolab. It has been a great experience to be able to work on such interesting research projects, while having the freedom to find my own way and develop myself as an independent scientist. Her personal involvement, motivation, optimism and overall qualities as a scientist are inspiring.

I would like to thank Prof. Klaus Kern for having me as part of his research group at the Max Planck Institute for Solid State Research. I greatly appreciate that this allowed me to broaden my experience and to do a part of my research at the MPI in Stuttgart.

I would also like to thank Prof. Aleksandra Radenovic, Prof. James de Yoreo and Prof. Ullrich Steiner for taking the time to be members in my PhD jury committee.

Many thanks go to the scientific collaborators for their invaluable contributions to my research. Specifically, I would like to thank Dr. Ilja Gunkel for his expertise and help in preparing block copolymer thin films, Dr. Mina Hong for the calcite nucleation rate data on S-layers and Dr. Behzad Rad for his help in purifying SbpA proteins.

Of course I want to thank my colleagues, Daniel Hurtado, Dr. Gustavo Ruano, Rado Vanta, Karla Banjac and Dr. Thanh Hai Phan, for all the interesting conversations and laughs we shared. In particular, I would like to thank Dr. Fernando Cometto for his insights and discussions, which helped me a lot during the analysis and writing of this thesis.

Great experimental research critically depends on the infrastructure that supports it. The people at the department of physics here at the EPFL were invaluable in maintaining the high quality that I have gotten so used to. In particular I would like to thank Gilles Grandjean, Claude Amendola, Primo Locatelli, Chantal Roulin, Carole Pascalon and Angeles Alarcon.

Thanks, also, to my parents and sisters. They have always been supportive and gave me insights into myself and the world around me that I would not have had without them.

Last but not least, I want to thank Ilze. Her strength, her care and her love were always there for me. She weathered all my complaints, doubts and frustrations and managed to keep me on track. Without her, I could not have finished this thesis as I did. Thank you for being the most inspiring person that I know.

Lausanne, January 17, 2018

Bart Stel

Abstract

At the interface between science and engineering, there is the field of biomimicry: Innovations inspired by the observation of natural, evolutionary optimized biological structures and processes. To understand the challenges of biomimicry, the concept of “Molecular Tectonics” is particularly useful. It describes how different self-assembling processes are spatially and dynamically integrated to form successively more complex structures. This integration makes it difficult to isolate the underlying mechanisms, which are often on the scale of individual molecules. Molecular biomimicry therefore critically depends on the observation of natural systems at the molecular scale. Advances in scanning probe microscopy have enabled the study of molecular self-assembly in unprecedented detail. However, many of these advances critically depend on the use of Ultra High Vacuum (UHV) conditions. To study natural systems at the molecular scale, a transition from UHV towards solvated systems is required.

In the first part of this thesis, small synthetic peptides are used as model system for molecular self-assembly. The self-assembly of peptides at interfaces has been studied by systematically varying the chemical structure and deposition method. By using ElectroSpray Ion Beam Deposition (ES-IBD) as well as *in situ* drop casting, the self-assembly at the solid-vacuum interface (UHV conditions) and at the solid-liquid interface was directly compared. This comprehensive study on the effect of solvent, structure and deposition method on the assembly of peptides at gas-solid and solid-liquid biointerfaces has shown that the same AcFA₅K peptide can organize into various structures, from β -sheets to tubular and globular assemblies, depending on their local environment.

The study of molecular self-assembly was extended to 2D protein crystals. By using high-speed and high-resolution Atomic Force Microscopy (AFM), it was possible to resolve both spatially and dynamically the mechanisms involved in S-layer self-assembly at the solid-liquid interface, such as monomer adsorption, condensation into high-density clusters, crystallization and finally conformational changes of existing S-layer crystals.

In the second part of this thesis, the integration of different self-assembling systems is explored and their functional properties are investigated. It combines the concepts of self-assembly and molecular tectonics. Self-assembled striped PS-*b*-PEO block copolymer (BCP) thin film substrates were used to confine and align S-layer self-assembly, without affecting the internal structure. Furthermore, the nucleation rate and S-layer growth was greatly enhanced on PS-*b*-PEO substrates, compared to the pure PS or PEO constituents. The hierarchical use of different self-assembling systems can be seen as a functional approach to the concept of molecular tectonics.

The catalytic properties of S-layers regarding the formation of CaCO₃ were studied. By studying the catalytic properties of S-layers *ex vivo*, their role can be investigated independently from the internal metabolism of their parent bacteria. Synchrotron based *in situ* X-ray Absorption Spectroscopy (XAS) and AFM are combined with continuous flow conditions, demonstrating that S-layers are able to stabilize amorphous forms of CaCO₃ and catalyze the nucleation of calcite at extremely low supersaturations.

Key words: Biomimicry, Self-assembly, Molecular tectonics, Solid-liquid interface, Peptides, Block-copolymer thin films, S-layers, Atomic Force Microscopy (AFM), X-ray Absorption Spectroscopy (XAS), Electro spray-Ion Beam Deposition (ES-IBD).

Résumé

À l'interface entre la science et l'ingénierie, on trouve le domaine du biomimétisme : des innovations inspirées par l'observation de structures et processus biologiques optimisées évolutives. Pour comprendre les récursions du biomimétisme, le concept de «Tectonique moléculaire» est particulièrement utile. Il décrit comment différents processus d'auto-assemblage sont intégrés spatialement et dynamiquement pour former des structures successivement plus complexes. Cette intégration rend difficile l'isolation des mécanismes sous-jacents, souvent à l'échelle des molécules individuelles. Le biomimétisme moléculaire dépend donc de manière critique de l'observation des systèmes naturels à l'échelle moléculaire. Les progrès de la microscopie à sonde à balayage ont permis d'étudier l'auto-assemblage moléculaire dans des détails sans précédent. Cependant, beaucoup de ces progrès dépendent de manière critique de l'utilisation des conditions de vide ultra élevé (UHV). Pour étudier les systèmes naturels à l'échelle moléculaire, une transition de l'UHV vers des systèmes solvatés est nécessaire.

Dans la première partie de cette thèse, de petits peptides synthétiques sont utilisés comme système modèle pour l'auto-assemblage moléculaire. L'auto-assemblage des peptides aux interfaces a été étudié en faisant varier systématiquement la structure chimique et la méthode de dépôt. En utilisant "l'ElectroSpray Ion Beam Deposition" (ES-IBD) ainsi que "drop casting" *in situ*, l'auto-assemblage à l'interface solide-vide (conditions UHV) et à l'interface solide-liquide a été directement comparé. Cette étude sur l'effet du solvant, de la structure et de la méthode de dépôt sur l'assemblage de peptides aux bio-interfaces gaz-solide et solide-liquide a montré que le même peptide AcFA₅K peut s'organiser en diverses structures, des feuillettes bêta aux assemblages tubulaires et globulaires, en fonction de leur environnement local.

L'étude de l'auto-assemblage moléculaire a été étendue aux cristaux de protéines 2D : En utilisant la microscopie à force atomique (AFM) haute vitesse et haute résolution, il s'est avéré possible de résoudre spatialement et dynamiquement les mécanismes impliqués dans l'auto-assemblage de "S-layers" à l'interface solide-liquide tel que : l'adsorption des monomères, la condensation dans grappes de haute densité, cristallisation et enfin changements de conformation de cristaux de S-layer existants.

Dans la deuxième partie de cette thèse, l'intégration de différents systèmes d'auto-assemblage est explorée et leurs propriétés fonctionnelles sont étudiées. Il combine les concepts d'auto-assemblage et de tectonique moléculaire. Des substrats en film mince de copolymère séquence PS-*b*-PEO auto-assemblé et rayé ont été utilisés pour confiner et aligner l'auto-assemblage de S-layer, sans affecter la structure interne. De plus, la vitesse de nucléation et la croissance de la S-layer étaient grandement améliorées sur les substrats de PS-*b*-PEO, comparativement

aux constituants purs de PS ou de PEO. L'utilisation hiérarchique de différents systèmes d'auto-assemblage peut être considérée comme une approche fonctionnelle du concept de la tectonique moléculaire.

Les propriétés catalytiques des S-layers concernant la formation de CaCO_3 ont été étudiées. En effet, étude des propriétés catalytiques des S-layers *ex vivo* et leur rôle, peut être étudié indépendamment du métabolisme interne de leurs bactéries parentes. La spectroscopie d'absorption de rayons X (XAS), *in situ* et basée sur le synchrotron, et l'AFM sont combinées avec des conditions d'écoulement continu. Ceci a démontré la formation de CaCO_3 aux sursaturations naturelles. Les S-layers sont capables de stabiliser les formes amorphes de CaCO_3 et de catalyser la nucléation de la calcite à des sursaturations extrêmement faibles.

Mots-clés: Biomimétisme, Auto-assemblage, Tectonique moléculaire, Interface solide-liquide, Peptides, Couches minces de copolymères séquencés, S-layers, Microscopie à force atomique (AFM), Spectroscopie par absorption de rayons X (XAS), Dépôt par électronebulisation (ES-IBD).

Zusammenfassung

An der Schnittstelle zwischen Wissenschaft und Technik gibt es das Gebiet der Biomimikry: Innovationen, die von der Beobachtung natürlicher, evolutionär optimierter biologischer Strukturen und Prozesse inspiriert sind. Um die Herausforderungen der Biomimikry zu verstehen, ist das Konzept der "Molekulare Tektonik" besonders nützlich. Es beschreibt, wie verschiedene Selbstorganisationsprozesse räumlich und dynamisch integriert werden, um sukzessive komplexere Strukturen zu bilden. Diese Integration macht es schwierig, die zugrundeliegenden Mechanismen zu isolieren, die oft auf der Skala einzelner Moleküle liegen. Die molekulare Biomimikry hängt daher entscheidend von der Beobachtung natürlicher Systeme auf molekularer Ebene ab. Fortschritte in der Rastersondenmikroskopie haben die Untersuchung der molekularen Selbstorganisation in noch nie dagewesenem Detail ermöglicht. Viele dieser Fortschritte hängen jedoch entscheidend von der Verwendung von Ultrahochvakuum (UHV) -Bedingungen ab. Um natürliche Systeme auf molekularer Ebene zu studieren, ist ein Übergang von UHV zu solvatisierten Systemen erforderlich.

Im ersten Teil dieser Arbeit werden kleine synthetische Peptide als Modellsystem für die molekulare Selbstorganisation verwendet. Die Selbstorganisation von Peptiden an Grenzflächen wurde untersucht, indem die chemische Struktur und die Abscheidungsmethode systematisch variiert wurden. Durch die Verwendung der Electrospray-Ionenstrahl Deposition (ES-IBD) sowie des *in situ* "drop casting" wurde die Selbstorganisation an der Fest-Vakuum-Grenzfläche (UHV-Bedingungen) und an der Fest-Flüssig-Grenzfläche direkt verglichen. Diese umfassende Studie über die Wirkung von Lösungsmittel, Struktur und Abscheidungsmethode auf die Anordnung von Peptiden an Gas-Feststoff- und Fest-Flüssig-Biointerfaces hat gezeigt, dass sich das gleiche AcFA₅K-Peptid in verschiedenen Strukturen organisieren kann, von β -Faltblatt zu röhrenförmigen und globulären Ansammlungen, abhängig von ihrer lokalen Umgebung. Die Untersuchung der molekularen Selbstorganisation wurde auf 2D-Proteinkristalle erweitert. Durch die Verwendung von Hochgeschwindigkeits- und Hochauflösungs- Rasterkraftmikroskopie (AFM) war es möglich die S-layer Selbstorganisation an der Fest-Flüssig-Grenzfläche beteiligten Mechanismen räumlich und dynamisch aufzulösen, wie beispielsweise Monomeradsorption, Kondensation in Cluster mit hoher Dichte, Kristallisation und schließlich Konformationsänderungen vorhandener S-layer Kristalle.

Im zweiten Teil dieser Arbeit wird die Integration verschiedener selbstorganisierender Systeme untersucht und deren funktionelle Eigenschaften untersucht. Es kombiniert die Konzepte der Selbstorganisation und der molekularen Tektonik. Selbstorganisierte gestreifte PS-*b*-PEO Blockcopolymer (BCP) -Dünnschichtsubstrate wurden verwendet, um die Selbstorganisation der

S-layers einzuschränken und auszurichten, ohne die innere Struktur zu beeinflussen. Darüber hinaus war die Keimbildungsrate und das Wachstum der S-layers auf PS-*b*-PEO Substraten im Vergleich zu den reinen PS- oder PEO-Bestandteilen stark erhöht. Die hierarchische Verwendung verschiedener selbstassemblierender Systeme kann als ein funktionaler Ansatz für das Konzept der molekularen Tektonik gesehen werden.

Die katalytischen Eigenschaften von S-layers bezüglich der Bildung von CaCO₃ wurden untersucht. Durch Untersuchung der katalytischen Eigenschaften von S-layers *ex vivo* kann ihre Rolle unabhängig vom internen Metabolismus ihrer Elternbakterien untersucht werden. Synchrotron-basierte *in situ* Röntgenabsorptionsspektroskopie (XAS) und AFM werden mit kontinuierlichen Strömungsbedingungen kombiniert. Dies zeigte die Bildung von CaCO₃ bei natürlich vorkommenden Übersättigungen. S-layers sind in der Lage, amorphe Formen von CaCO₃ zu stabilisieren und die Keimbildung von Calcit bei extrem niedrigen Übersättigungen zu katalysieren.

Stichwörter: Biomimikry, Selbstorganisation, Molekulare Tektonik, Fest-Flüssig-Grenzflächen, Peptides, Block-Copolymerthinfilme, S-layers, Rasterkraftmikroskopie (AFM), Röntgenabsorptionsspektroskopie (XAS), Electrospray-Ionenstrahl Deposition (ES-IBD).

Contents

Acknowledgements	i
Abstract	ii
List of figures	xi
List of tables	xiii
Introduction	1
1 Fundamentals	8
1.1 Atomic Force Microscopy	8
1.1.1 Fundamentals of AFM	8
1.1.2 AFM Measurement Modes	12
1.1.3 Experimental Set-up	15
1.1.4 AFM probes	17
1.1.5 Software and Data Analysis	18
1.1.6 Workflow	19
1.2 Electrospray Ion Beam Deposition	21
1.2.1 Fundamentals of ES-IBD	21
1.2.2 Experimental set-up	21
1.3 X-ray Absorption Spectroscopy	22
1.3.1 Fundamentals of XAS	23
1.3.2 Experimental set-up	24
1.3.3 Software and Data Analysis	26
1.3.4 Workflow	27
2 Self-assembly of small peptides at the solid-liquid and solid-vacuum interface	29
2.1 External factors: The substrate and surrounding medium	31
2.1.1 Self-assembly at the solid-liquid interface	31
2.1.2 Self-assembly at the solid-air interface	36
2.2 Internal factors: Charge and internal structure of the peptide	39
2.2.1 The presence and position of the lysine residue	39
2.2.2 The charge states of the lysine residue	41
2.3 Thermal stability of peptide assemblies	42

2.3.1	Thermal stability at the mica-air interface	42
2.3.2	Thermal stability at the HOPG-air interface	43
2.4	Proposed model for the self-assembly of AcFA ₅ K	45
2.5	Influence of metal ions on the self-assembly of AcFA ₆ and AcFA ₅ K	48
2.5.1	Self-assembly of AcFA ₆ in the presence of Na ⁺ and Ca ²⁺	49
2.5.2	Self-assembly of AcFA ₅ in the presence of GdCl ₃	49
2.6	Summary & Conclusions	53
3	Bacterial surface layers	55
3.1	Non-classical crystallization of SbpA proteins into S-layers	56
3.2	Self-assembly of S-layers at the solid-liquid interface	57
3.2.1	Self-assembly of S-layers on mica	59
4	<i>In situ</i> dynamics of protein self-assembly on block copolymer thin films	64
4.1	Self-assembly of PS- <i>b</i> -PEO and PS- <i>b</i> -P2VP Block copolymer thin films	65
4.2	Self-assembly of S-layers on top of PS- <i>b</i> -PEO BCP thin films	68
4.3	<i>In situ</i> dynamics of S-layer self-assembly on PS- <i>b</i> -PEO BCP thin films	72
4.4	Chemical versus physical contrast	75
4.5	Directed collagen self-assembly	76
4.6	Conclusion and Outlook	77
5	S-layers as Biomimetic Template for Mineralization of CaCO₃	79
5.1	Biom mineralization of CaCO ₃	81
5.1.1	Amorphous Calcium Carbonate (ACC) as a transient precursor state	82
5.1.2	Prenucleation clusters	83
5.1.3	Organic-inorganic interfaces	83
5.2	Guidelines for controlled CaCO ₃ formation	84
5.3	Using optical microscopy to determine the nucleation rate of CaCO ₃ on S-layers	86
5.4	Using x-ray absorption spectroscopy to measure CaCO ₃ formation on S-layers	91
5.4.1	Specifics of CaCO ₃ absorption spectra	91
5.4.2	<i>Ex situ</i> XAS of CaCO ₃ on S-layers	93
5.4.3	Continuous flow <i>in situ</i> XAS of CaCO ₃ on S-layers	97
5.5	Using atomic force microscopy to image CaCO ₃ formation on S-layers	100
5.6	Conclusions	103
6	Summary & Outlook	104
6.1	Conclusions	108
A	Classical Nucleation Theory	109
A.1	Fundamentals of Nucleation Theory	109
A.2	Homogeneous Nucleation	111
A.3	Heterogeneous nucleation	112
A.4	Classical vs. Non-Classical Nucleation and Crystallization	113

Contents

B SbpA Purification and S-layer Growth Protocol	114
B.1 SbpA Purification	114
B.1.1 Cell Growth	114
B.1.2 Protein Purification	116
B.2 <i>Ex vivo</i> S-layer Crystallization	119
C Self-assembly of gas molecules at the HOPG-liquid interface	120
D AFM Probes	122
Bibliography	139

List of Figures

1	Top-down vs Bottom-up	2
2	Model systems featuring self-assembly	5
1.1	Interaction forces of AFM and STM	9
1.2	Different experimental setups of the AFM	11
1.3	Principle of PeakForce Mapping Mode	14
1.4	The experimental setup that is installed during this thesis	16
1.5	Schematic of the ES-IBD apparatus	22
1.6	X-ray fluorescence & the Auger effect	23
1.7	<i>In situ</i> x-ray absorption spectroscopy	25
2.1	Structure of the AcFA ₅ K peptide	30
2.2	Self-assembly of AcFA ₅ K at 0.1 mM at the mica-liquid interface	32
2.3	Self-assembly of AcFA ₅ K at 0.8 mM at the mica-liquid interface	33
2.4	Epitaxially vs solution grown fibers of AcFA ₅ K	34
2.5	The HOPG-liquid interface in the presence of AcFA ₅ K	35
2.6	Self-assembly at the HOPG-air interface after drop casting	36
2.7	Self-assembly of AcFA ₅ K at the HOPG-vacuum and HOPG-liquid interface	37
2.8	Self-assembly of AcFA ₅ K, AcFA ₆ and AcKFA ₅	40
2.9	Self-assembly of AcFA ₅ K at the mica-liquid interface at different pH	41
2.10	Thermal stability of AcFA ₅ assemblies at the mica-air interface	42
2.11	Thermal stability of AcFA ₅ K at the HOPG-air interface	43
2.12	Thermal induced changes of AcFA ₅ K assemblies at the HOPG-air interface	44
2.13	Proposed models for the self-assembly of AcFA ₅ K	46
2.14	Removal of AcFA ₅ K structures from the mica-liquid interface by GdCl ₃	50
2.15	<i>Ex situ</i> AFM image of AcFA ₅ K self-assembly in the presence of GdCl ₃	52
3.1	Self-assembly of S-layers	56
3.2	S-layers on mica, HOPG and Si ₃ N ₄	58
3.3	Pre-crystallized S-layers on mica, Si ₃ N ₄	59
3.4	AFM images of S-layer self-assembly at the mica-liquid interface	60
3.5	Dynamics of S-layer self-assembly at the mica-liquid interface	61
4.1	Principle of S-layer self-assembly on BCP thin films	64
4.2	PS- <i>b</i> -PEO and PS- <i>b</i> -P2VP BCP thin films	66

List of Figures

4.3	S-layer self-assembly on PS- <i>b</i> -PEO BCP thin films compared to mica and PS . . .	68
4.4	Directed S-layer self-assembly on PS- <i>b</i> -PEO BCP thin films	69
4.5	Preferential orientation of S-layers on striped PS- <i>b</i> -PEO BCP thin films	70
4.6	S-layer self-assembly on PS and PEO	71
4.7	SbpA adhesion on dot-patterned PS- <i>b</i> -PEO BCP thin films	71
4.8	Dynamics of S-layer self-assembly on dot-patterned PS- <i>b</i> -PEO BCP thin films .	72
4.9	S-layer self-assembly on reconstructed PS- <i>b</i> -P2VP BCP thin films	75
4.10	Directed collagen assembly on PS- <i>b</i> -PEO BCP thin films	77
5.1	Whiting event in Lake Michigan	79
5.2	Classical Nucleation Theory	81
5.3	Nucleation rate of CaCO ₃ on S-layers	88
5.4	CaCO ₃ reference spectra	92
5.5	<i>Ex situ</i> XAS of CaCO ₃ formation on S-layers	94
5.6	Change of ACC reference spectra during x-ray exposure	95
5.7	<i>In situ</i> XAS of CaCO ₃ formation on S-layers	98
5.8	<i>In situ</i> AFM of CaCO ₃ growth on S-layers	100
5.9	Amorphous CaCO ₃ removed by continuous AFM imaging	100
5.10	Calcite nucleation on amorphous CaCO ₃ sublayer	101
6.1	Controlled self-assembly of peptides	104
6.2	Dynamics of S-layer self-assembly on mica	105
6.3	Directed self-assembly of S-layers on PS- <i>b</i> -PEO BCP thin films	106
6.4	CaCO ₃ formation on S-layers	107
A.1	Free energy barriers according to nucleation theory	110
B.1	UV-VIS absorption curve of SbpA solution	118
B.2	Gel electrophoresis during SbpA preparation	118
C.1	Dynamics at the HOPG-liquid interface in the presence of AcFA ₅ K	121

List of Tables

1.1	Specifications of AFM probes used in this work.	18
4.1	Molecular weights and volume fractions of the block copolymers used in this work	67
5.1	Peak positions of the calcium L _{II} and L _{III} absorption edges for different calcium containing compounds	91
5.2	Properties related to CaCO ₃ nucleation for various concentrations of CaCl ₂ and NaHCO ₃	93
D.1	Specifications of AFM probes used in this work.	122

Introduction

The intellectual and practical activity encompassing the systematic study of the structure and behaviour of the physical and natural world through observation and experiment. – The New Oxford Dictionary of English.

This thesis starts with a general and arguably one of the most complete definitions of the practice of science. Interesting to note is that this definition implies that all knowledge that can be known scientifically is already present in the natural world, and only out of reach due to our inability to properly observe it. An argument can thus be made that the progress of science is primarily driven by the invention of new methods to observe the world around us. This is nicely exemplified by the creation of glass lenses that started the scientific disciplines of microscopy^[1] and astronomy, or the more recent invention of scanning probe techniques^[2,3] that enabled the observation of individual atoms on a regular basis.

Where science is focused on the collection of knowledge, engineering is primarily driven by the application of this knowledge to the creation of functional systems. In line with the scientific tradition of knowledge-through-observation, at the interface between these two disciplines there exists the field of biomimicry: Innovations inspired by the observation of natural, evolutionary optimized biological structures and processes^[4–10].

To understand the relevancy of biomimicry, it is important to realize that we are not the first to tackle design challenges through the appropriate use of the laws of chemistry and physics. In fact, the process of evolution has been optimizing living structures and processes in this manner for billions of years, compared to a mere few centuries for humanity.

Factors that contribute to the interest in evolutionary optimized systems are, for example, the search for and implementation of readily available energy sources, like the natural process of photosynthesis. Other interesting concepts are the modular approach to the structure of living systems that enables easy scalability with a limited number of unique components, the dynamic optimization that enables efficient functionality in highly diverse environments, the continued operation in the presence of defects and, last but not least, the self-organization and self-assembly that enables structural organization through a bottom-up approach^[7,11]. Unsurprisingly, the field of biomimicry has seen an explosive growth in the last few decades^[8]. Although natural systems and materials are often superior to their synthetic counterparts, the potential of the underlying design principles is not always reached in the natural world. This is not surprising, considering that natural systems have been optimized under conditions

that might not be compatible with useful technological applications. In certain systems it is therefore both feasible and desired to modify natural systems in order to increase their efficiency regarding technological applications. For example, efforts are made to develop more efficient synthetic counterparts to natural metalloenzymes^[12].

To understand what distinguishes these natural evolutionary optimized systems from artificially designed systems, the concept of “Molecular Tectonics” is particularly useful. Molecular tectonics describes the spatial and dynamic integration of hierarchical, often self-assembling or self-organizing, structures and processes^[5,13]. An analogy often used to clarify the importance of this concept is the construction of a house. Houses are built using a strict hierarchical approach, where each step depends strongly on the previous one. The building site is defined first (pre-organization), after which the foundations are laid within the building site (templating), and finally, the house is built following this predefined plan (assembly). Such a hierarchical organization of separate but interdependent processes is a central concept in evolutionary optimized systems and is closely related to the previously mentioned modularity and self-organization or self-assembly that is often observed in nature. The spatial and dynamic interdependence of such structures and processes makes it challenging to identify and isolate the underlying mechanisms, which are often on the scale of individual molecules. However, recent advances in molecular imaging techniques, in particular *in situ* Atomic Force Microscopy (AFM)^[3] and Scanning Tunneling Microscopy (STM)^[2], make it possible to follow individual biological molecules during assembly and thus, unravel the underlying mechanisms^[14–17].

Bottom-up fabrication through self-assembly

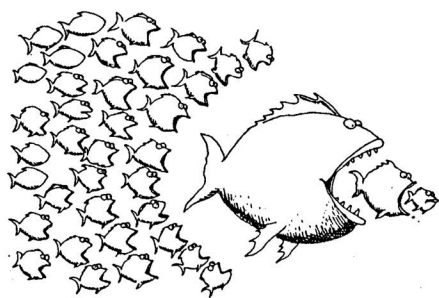


Figure 1 – Top-down vs Bottom-up.
(Source: *The Far Side* series by Gary Larson)

Top-down and bottom-up are two basic approaches to fabrication, both at the macro and the nanoscale. In a top-down approach, large pieces of material are reduced to obtain the desired pattern. In contrast, following a bottom-up approach means the desired pattern is instead composed of small building blocks. Most macroscopic fabrication techniques involve top-down techniques that remove material using external forces, similar to how a chisel is used in wood carving. Modern tools such as Electron Beam Lithography (EBL) have pushed the limits of top-down fabrication to reach a precision of tens of nanometers^[18]. However, there are several problems related to top-down fabrication. First, it becomes increasingly difficult when the precision required is on the order of individual molecules. And second, top-down fabrication is fundamentally limited because templates can only be created one at a time, limiting the ability to create large-scale patterns.

In contrast, a bottom-up approach to fabrication depends only on the forces that control the assembly of individual building blocks. In the special case where building blocks are designed such that these forces are inherent to the blocks themselves and do not require any external input, self-assembly will occur^[11,19]. In this case, the speed of fabrication is only limited by the availability and interaction kinetics of the individual building blocks.

At the nanoscale, the use of bottom-up fabrication through self-assembly is ubiquitous in natural systems and structures, ranging from the creation of complex enzymes from individual amino acids to the formation of membranes and lipid bilayers. A biomimetic approach to nanofabrication requires a deep understanding of the underlying forces and mechanisms that control the individual atoms or molecules. The secret to nanoscale fabrication is therefore the manipulation of molecular systems in order to control the intermolecular forces that in turn govern the assembly.

There are as many methods to control the self-assembly of molecules as there are forces acting on such molecules. One can roughly distinguish two approaches to controlling the self-assembly of individual molecules. The forces between molecules and their surroundings can be manipulated by controlling the local environment, something which is typically much easier than controlling the molecules directly. Alternatively, the forces between molecules can be manipulated by imposing changes directly to the molecular structure. Following, there are several examples of practical methods that are used to influence the self-assembly of molecules.

The assembly of molecules in solution often depends on the concentration. Consequently, a controlled evaporation of a solvent containing non-volatile molecules can influence the self-assembly of such molecules into ordered structures^[20].

By changing the medium in which molecules interact, one can induce different inter and intramolecular forces, and in this way drastically change the structure and self-assembly behavior for the same molecule. As an example, in vacuum, the forces acting on peptides are dominated by hydrogen bonds and van der Waals forces^[21,22]. However, in solution, the protonation or deprotonation of specific functional groups can change the self-assembly process completely^[23].

Self-assembly at the solid-liquid interface can be changed by manipulating the interactions between substrate and molecule. This can be done statically by changing the chemical or physical properties of the substrate in order to induce or inhibit adsorption of specific molecules. It is also possible to dynamically change the substrate-molecule interaction forces by changing the polarization of the substrate *in situ*^[24].

Finally, self-assembly can be influenced by changing the molecules themselves. Either by covalently linking together two independent molecules, or by removing from or adding specific parts to an existing molecule. The formation of block copolymers (BCPs) is a well established process that involves covalently linking two chemically different polymer blocks at the nanoscale. Under the right conditions, the different chemical properties contained within each molecule will induce self-separation of each block into well-defined domains at the nanoscale^[25]. This principle of self-separation of two covalently linked blocks is not limited to polymers. It is possible to combine the tunability of polymers with the functionality of

Introduction

proteins. Self-separation at the nanoscale then drives the organization of such molecules into patterns similar to the BCP system^[26,27].

Changing the self-assembly properties of molecules through the removal or addition of specific parts is a more subtle approach that implies an understanding of the forces governing molecular interactions at the level of specific functional groups within these molecules. The modular nature of peptides and proteins means that the structure depends directly on the amino-acid sequence. This makes them especially suited for molecular manipulation. A change in the amino acid sequence will result in a different tertiary three-dimensional structure, and thus influence the self-assembly properties of the system.

One of the most interesting features of self-assembled structures is the fact that their properties can go beyond those of the individual building blocks. Such emergent properties arise from the precise intramolecular structure and have been found in a variety of systems.

For example, patterned polystyrene-*block*-poly(methyl metacrylate) (PS-*b*-PMMA) BCP thin films create a chemically heterogeneous interface between PS and PMMA, which in turn induces an increased protein adhesion compared to either PS or PMMA alone^[28,29]. Also, the immobilization of catalytic enzymes through fusion with a self-assembling protein can extend its lifetime significantly, without loss of activity^[30].

Arguably the most studied topic related to emergent properties of organized structures is the interaction between organic and inorganic molecules during biomineralization^[31–33]. Natural systems have been shown to exhibit exceptional control over the mineralization process, such as polymorph selective crystallization^[34,35], control over the crystal orientation^[33,36], as well as spatially controlled dynamics of the mineralization process^[37–39]. All this is achieved using basic building blocks composed of readily available elements that, on their own, do not have special properties regarding mineralization.

A thorough understanding of how such emerging properties can influence mineralization would be of great interest for research areas such as the development of novel composite materials^[40,41] or the sequestration and storage of atmospheric CO₂ into carbonate minerals^[42,43].

As detailed above, the true strength of evolutionary optimized structures and systems lies with the seamless integration of different self-assembly mechanisms, i.e. molecular tectonics^[5,13,44]. Accordingly, a biomimetic approach to bottom-up fabrication would benefit from a similar hierarchical use of self-assembly systems^[45]. Integral to this methodology is the development and understanding of relatively simple self-assembly model systems and how such systems can be successfully integrated to create successively more complex structures.

Model systems to study molecular self-assembly

In this thesis, several model systems to study self-assembly *in situ* at the nanoscale have been investigated. These are the previously mentioned BCP thin films, modular peptides and Bacterial Surface Layers (S-layers), as shown in Figure 2.

One of the most versatile systems that can be used to study fundamental properties of self-

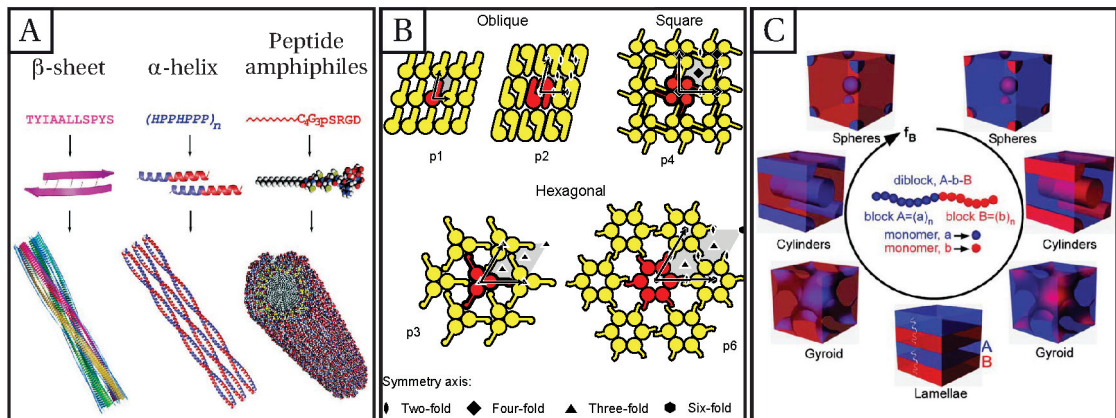


Figure 2 – Three different model systems that feature self-assembly properties at the nanoscale. **(a)** Peptide self-assembly pathways involving the formation of β -sheets and α -helices or through the preferential interaction with specific sub-units of peptide amphiphiles. Modified from reference [46]. **(b)** Schematic of the various S-layer lattice types found in nature. Modified from reference [47]. **(c)** Schematic of block copolymer phase separation in various microstructures. Modified from reference [48].

assembly is formed by peptides^[49,50]. This versatility originates from their modular structure, based on individual amino acids. Modern fabrication techniques allow for almost any combination of amino acids to be synthesized^[51,52]. This makes peptides a close-to-perfect model system to study the intermolecular forces resulting from the functional groups of the individual amino acid building blocks^[53–56]. By carefully choosing the sequence of amino acids, one can almost independently control various parameters of the peptide, such as size^[21,57], charge^[23,58,59], structure^[21] and hydrophilicity^[58,59].

Robust self-assembly can also be found in much more complex systems such as proteins. Bacterial Surface Layers (S-layers) are a good example. They form the outer cell membrane of many Gram-positive and Gram-negative bacterial species and almost all archaea^[60,61]. S-layers are composed of individual proteins, which self-assemble into two dimensional crystalline structures. Depending on the type of S-layer protein, the resulting crystalline structures have symmetries ranging from oblique (P1, P2), square (P4) to hexagonal (P6) and unit cell sizes from 3 nm to 30 nm. S-layer lattices are highly porous with uniform pores of 2 nm to 8 nm and porosities ranging from 30 % to 70 % of the total volume^[47,62–64]. The fact that individual monomers maintain their self-assembly properties *ex vivo*, and that the resulting S-layers even remain stable *ex situ*, makes S-layers extremely useful as self-assembly platform^[47,64–70]. S-layers have been used in a wide range of applications, such as templates that drive the ordered adhesion of nanoparticles^[71–73], immobilization matrices for functional biomolecules^[74–77], adsorption matrices for metal ions^[78,79] and even as bio-compatible coatings that inhibit the adhesion of cells^[80].

Self-assembly in block-copolymers (BCPs) happens through the spontaneous phase separation of chemically different but covalently linked polymer blocks. This can yield precisely

tuned structures with long-range nanoscale order^[48,81–83]. The phase separations is driven by a strong unfavorable mixing enthalpy in combination with only a small entropic penalty due to mixing. The covalent link between the two blocks prevents complete macroscopic separation. When the specific parameters that drive this process are understood, a relatively simple preparation protocol is sufficient to create high-quality and complex structures. For example, a simple spin coating with subsequent solvent annealing of BCP thin films composed of hydrophobic polystyrene and hydrophilic poly(ethylene-oxide) (PS-*b*-PEO) gives rise to chemically heterogeneous substrates. The precise nanoscale features of these BCP thin films depend on the mass-ratio between and molecular weight of each block^[84,85].

The high level of precision and versatility has lead to the use of BCP structures as templates for nanoscale structured inorganic materials^[86], immobilization matrices for nanoparticles^[87,88] and proteins^[89,90] as well as in more applied research areas such as drug delivery^[91] or fuel cell development^[92]. In this thesis, BCP substrates are primarily used as nanopatterned substrate to guide protein assemblies.

Structure of this thesis

In this thesis, 2D self-assembly of biological molecules at the solid-liquid interface has been investigated using the model systems introduced above.

The first chapter: *Fundamentals* introduces the various experimental techniques, such as AFM, X-ray Absorption Spectroscopy (XAS) and Electrospray Ion Beam Deposition (ES-IBD) that have been used throughout this thesis.

The following chapters have been arranged in a hierarchical order, where chapter 2: *Self-assembly of small peptides at the solid-liquid and solid-vacuum interface* is the most fundamental. It explores the underlying rules that govern self-assembly by using various small alanine based peptides. The self-assembly at solid-liquid and solid-vacuum interfaces was imaged using high resolution AFM techniques. It has been investigated how peptide self-assembly was affected by external factors such as medium and substrate as well as internal factors such as the amino acid sequence or protonation state of the functional groups within the peptides. Furthermore, the formation of metal-peptide complexes at the solid-liquid interface has been investigated.

The self-assembly of the more complex S-layer system is presented in detail in chapter 3: *Bacterial surface layers*. *In situ* AFM was used to determine the influence of the substrate on the self-assembly and continuous flow measurements were used to study in detail the dynamics of the different aspects of S-layer self-assembly at the mica-liquid interface.

Following this, the self-assembly of S-layers on patterned BCP thin films is detailed in chapter 4: *In situ dynamics of protein self-assembly on block copolymer thin films*. Here, the focus is on the hierarchical integration of different self-assembly systems to allow for greater control over the composite system and achieve novel functionality.

Chapter 5: *In situ dynamics of protein self-assembly on block copolymer thin films* looks at properties of self-assembled systems that originate from the precise arrangement of functional

groups, i.e. emergent properties. It has been suggested that crystalline S-layers have catalytic properties with regards to the formation of CaCO_3 . This is explored in depth by following the nucleation and growth of CaCO_3 with a variety of surface science techniques, that allow for *in situ* observation of CaCO_3 formation at naturally occurring supersaturations.

The final chapter concludes this thesis and combines the previous chapters in a short summary. It details the main conclusions presented in this thesis. Namely, that it is possible to control the self-assembly of small AcFA₅K peptides by precisely tuning the experimental conditions. How fast-scan and high resolution AFM in combination with continuous flow *in situ* conditions enables the imaging of the various stages of S-layer self-assembly in a single experiment. That by hierarchically integrating different self-assembly systems, it is possible to achieve unprecedented control over protein crystallization and bottom-up fabrication of nanoscale structures. And finally, how the combination of *in situ* continuous flow AFM and synchrotron based spectroscopies made it possible to show that bacterial surface layers exhibit catalytic properties with respect to the formation of CaCO_3 .

1 Fundamentals

The experimental work in this thesis has been performed using several state-of-the-art experimental techniques. This is the first PhD thesis that uses the FastScan AFM system in combination with *in situ* flow cells for both AFM and XAS. As such, the fundamentals and experimental details of these techniques are covered extensively and in detail. Apart from containing a thorough description of the experimental techniques in this thesis, this chapter will function as reference material for future studies in our laboratory that use the equipment installed during this PhD work.

1.1 Atomic Force Microscopy

Imaging materials at the atomic level on a regular basis remained elusive until the invention of the Scanning Tunneling Microscope (STM) by Binnig, Rohrer and Weibel^[2]. Even though STM provides exceptional spatial resolution, it has limitations that are inherent to this technique. For example, STM requires that the sample is electrically conductive so that a tunneling current can flow between a tip and surface.

In the early days of the STM, it was noticed that at the tip-sample distances achieved during regular STM operation, there were significant forces acting between tip and sample. This principle was later developed into the first working example of an Atomic Force Microscope (AFM) that used these tip-sample forces, instead of an electrical tunneling current, to detect the surface topography at the atomic level^[3]. Because no electrical conductivity is required during AFM operation, virtually any flat and solid sample can be imaged. This makes it possible to use AFM robustly under ambient atmospheric conditions and even at the solid-liquid interface.

1.1.1 Fundamentals of AFM

An AFM works by detecting the very small tip-surface forces that arise when a nanoscopic tip comes in very close proximity to a surface. The detection of this force, or properties derived from this force, can then be used as input for a feedback mechanism that is designed to keep

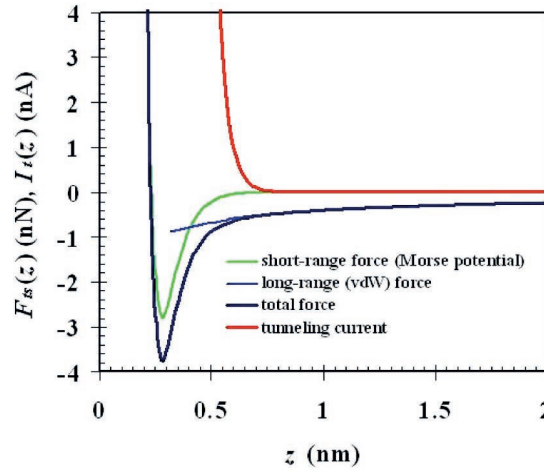


Figure 1.1 – Whereas the STM tunneling current is always positive, the interaction forces between AFM tip and sample can be attractive or repulsive, depending on tip-sample distance. Modified from reference [16].

the tip-surface distance constant. By recording the vertical movement that is required to keep the tip-surface distance constant, the surface morphology can be obtained. The fundamentals of the various aspects of AFM operation are described in more detail in the next paragraphs.

Interaction Forces

The main working principle of an Atomic Force Microscope relies on the interaction forces between a nanoscopic needle and the surface of a sample. This includes contributions from several sources.

Chemical forces are typically described by the *Morse Potential*, as shown in Equation 1.1, and have interaction distances of several angstrom. Depending on the tip-sample separation, the interaction force is either repulsive due to Pauli-repulsion, or attractive due to interaction of electron orbitals^[16].

$$V_{morse} = -E_{bond} (2e^{-\kappa(z-\sigma)} - e^{-2\kappa(z-\sigma)}) \quad (1.1)$$

With V_{morse} the chemical potential, E_{bond} the bond-energy, σ the equilibrium distance and κ the decay length^[16,93].

Van der Waals forces are caused by the fluctuations in the electric dipole moment of atoms. Their polarization with respect to one another causes an attractive force that has a $1/z^6$ dependence on distance. Due to the additive nature of these atom-atom interaction forces, the total van der Waals force depends on the geometry of the two interacting bodies. The potential in Equation 1.2 gives the Van der Waals potential in the case of a spherical tip in proximity to a flat plane, this results in a force that has a $1/z^2$ dependence on distance. In the case for a pyramidal or conical shaped tip, this reduces to a $1/z$ dependence. The relatively

Chapter 1. Fundamentals

weak dependence on distance makes interaction distances of up to 100 nm possible^[16,93].

$$V_{vdw} = -\frac{A_H R}{6z} \quad (1.2)$$

With V_{vdw} the van der Waals potential, A_H the Hamaker constant, R the radius of curvature of the tip and z the tip-sample distance^[16,93].

Electrostatic forces can be present when both tip and sample are conductive and have a non-zero potential difference. For very small distances the electrostatic force has a $1/z$ dependence, similar to the van der Waals force. However, in contrast to the additive nature of the van der Waals force, in the case of ionic crystals, the individual contributions of the electrostatic force cancel out at longer distances due to the fact that adjacent atoms have opposite charge^[16].

A graphical representation of the different forces acting on the AFM tip and the tunneling current between the STM tip and the sample, is shown in Figure 1.1^[16].

Force Detection

In order to detect the small tip-surface interaction forces, the detector must combine insensitivity to lateral forces with high sensitivity to normal forces. These requirements are fulfilled by using a cantilever where the thickness t is much smaller than the width w or length L . Such a cantilever behaves like a spring, with spring constant k given by Equation 1.3. The bending of the cantilever is thus directly proportional to the tip-surface interaction force^[3,94].

$$F = k \cdot d \quad , \quad k = \frac{Y w t^3}{4L^3} \quad (1.3)$$

With F the tip-surface interaction force, k the spring force and d the amplitude of the cantilever bending. Y is the Young's modulus of the material and w , t and L are the width, thickness and length of the cantilever, respectively.

In order to follow the topography of the sample, the cantilever bending is registered by measuring the angle with which a laser is reflected off its reflective backside, as schematically shown in Figure 1.2. This signal is then processed and used as feedback signal to maintain a constant tip-sample interaction force. Assuming that the force-profile, as shown in Figure 1.1, is constant over the entire sample surface, the constant-force image is directly proportional to the topography of the sample.

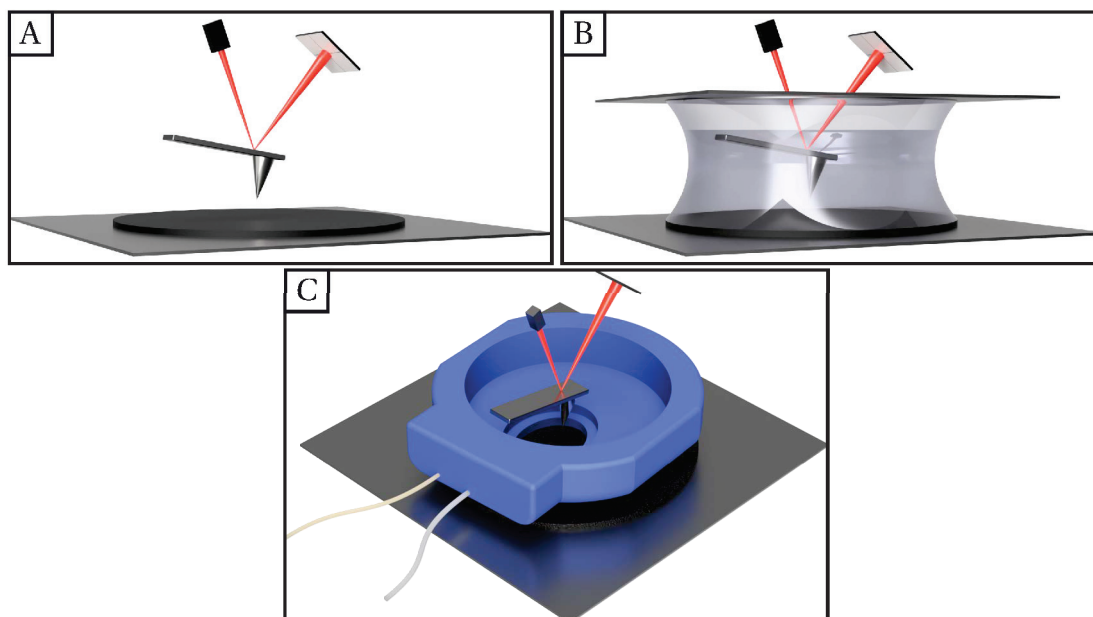


Figure 1.2 – Schematics that show the arrangement of the cantilever, laser source (left) and photodiode detector (right). The bending of the cantilever due to tip-surface interactions affects the reflection-angle, and thus moves the laser spot over the detector. (a) The standard operating setup is in ambient air. (b) By using the surface tension of aqueous solutions, it is possible to maintain a capillary bridge between sample and scan head and in this way achieve *in situ* imaging conditions. (c) When a liquid flow is required, when the working solution does not have sufficient surface tension or when evaporation of the solution must be prevented, it is possible to include a liquid flow cell. The cell creates an enclosed volume between sample and scan head. The addition of a dedicated inlet and outlet enables a liquid flow through the cell.

Feedback mechanism

To maintain a constant tip-sample distance, a feedback loop is used to relate the cantilever deflection or related properties to the physical tip-sample distance. Equation 1.4 shows how the two main feedback parameters, P and I , control the relation between error signal and vertical Z -piezo movement.

$$S_{piezo} = P \times S_{error} + I \times \int S_{error} dt \quad (1.4)$$

With S_{height} the extension of the Z -piezo, S_{error} the difference between the amplitude setpoint and the recorded cantilever amplitude, P the proportional gain value and I the integral gain value.

The proportional gain scales the error signal on which the feedback is based. A higher value will make the feedback loop more sensitive to small changes in the topography and will decrease the response time. The integral gain depends on the duration for which the error signal is maintained. In optimizing the feedback behavior, the integral gain is typically optimized first.

1.1.2 AFM Measurement Modes

The fundamentals of the AFM, as detailed in the previous section, allow for a variety of measurement modes with different feedback systems. Each measurement mode has specific benefits and problems, which will briefly be discussed in the following paragraphs.

Contact Mode

Contact Mode (CM-AFM) is by far the most simple measurement mode. First, the tip is brought in contact with the sample, i.e. in the repulsive regime of Figure 1.1. After this, the tip-sample interaction force is kept constant while the cantilever is moved in a line-by-line pattern over the sample surface. To prevent damage to the sample surface, the stiffness of the cantilever should be less than the inter-atomic spring constants of the atoms in the sample, which typically means $k \leq 10 \text{ N m}^{-1}$. For biological samples the allowed force is even lower at $k \leq 0.1 \text{ N m}^{-1}$.

The constant interaction between tip and sample results in a shear force, and thus relative quick wear and blunting of the tip. In practice, it is challenging to use this mode on fragile or soft samples without severely affecting the sample.

Dynamic Mode

In contrast to CM-AFM, Dynamic Mode AFM (DM-AFM) deliberately oscillates the cantilever so that the cantilever and tip can be viewed as a simple spring-mass system with a resonance frequency $f_0 \sim \sqrt{\frac{k}{m}}$. The tip is brought in close proximity to – but not in contact with – the sample surface, i.e. in the attractive regime in Figure 1.1. The tip-sample interaction forces then change the effective mass of the system, which shifts the resonance frequency of the system. Non-conservative forces, i.e. energy dissipation, can lead to an independent drop in oscillation amplitude and a phase shift with respect to the driving oscillation.

In Amplitude Modulated AFM (AM-AFM) the cantilever is oscillated close to the resonance frequency. Upon interaction with the surface, the resonance frequency shifts and the driving frequency is now further away from resonance, with a lower oscillation amplitude as a result. AM-AFM works by interpreting the change in amplitude as a frequency shift and thus tip-surface interaction force. By keeping the cantilever oscillation amplitude constant while the cantilever is moved in a line-by-line pattern over the sample surface, the topography of the sample is recorded. The phase-shift can be recorded simultaneously.

There are several problems inherent to AM-AFM. When non-conservative forces are present in the tip-sample system, this is recorded in the phase signal. However the change in oscillation amplitude due to the dissipation of energy is still interpreted by the feedback system as a change in tip-sample interaction force. Therefore, in the presence of non-conservative forces the amplitude change is no longer proportional to the tip-sample separation distance.

Furthermore, a sudden change in tip-surface separation can shift the interaction force from the attractive regime to the repulsive regime, as shown in Figure 1.1. Where in the attractive regime a decrease in separation results in a stronger attractive force, the opposite is true in

the repulsive regime. Upon such a change in separation, the normally negative feedback loop suddenly becomes a positive feedback loop. This results in large instabilities.

As AM-AFM uses the drop in amplitude to record a frequency shift, a sharp resonance peak in the frequency spectrum is beneficial, i.e. a high Q-factor. However, amplitude changes occur at timescales $\tau_{AM} \approx 2Q/f_0$ with Q the quality factor of the cantilever. Therefore, high Q-factor cantilevers behave rather slow, especially under vacuum conditions, where Q-factors typically reach values of 100000 this becomes problematic^[16].

To solve several of the problems associated with AM-AFM, Frequency Modulated AFM (FM-AFM) was developed. In FM-AFM, the frequency shift is used as feedback signal to keep the tip-sample force and thus distance constant. To do this, both the change in amplitude and frequency are recorded and kept constant by using two independent feedback loops. Conservative and non-conservative forces can now be separated and the frequency-shift remains proportional to the tip-sample separation distance. Additionally, the frequency change occurs at timescales $\tau_{FM} \approx 1/f_0$ and is now independent of the Q-factor^[16].

Similar to AM-AFM, a sudden change in tip-sample separation can result in a shift from the attractive to the repulsive regime, with severe instabilities as a result.

Under ambient conditions, almost any surface is typically covered in a few monolayers of water molecules due to the non-zero humidity in the air. Typical tip-surface distances are around 1 nm and oscillation amplitudes are usually less than 5 nm. Under these conditions, there is only a small region in which the tip is both close enough to the surface to feel the attractive forces, but far enough to prevent formation of a water meniscus between tip and surface. Such a water meniscus would abruptly prevent the cantilever from oscillating^[93,95].

Intermittent Contact Mode – Tapping Mode

CM-AFM has problems associated with the shear force between tip and sample, which makes it difficult to image delicate samples that are sensitive to deformation by the tip-sample interaction forces. DM-AFM has inherent instabilities related to the presence of both attractive and repulsive regimes in the tip-surface force-distance curve, as shown in Figure 1.1. In ambient conditions, the presence of surface liquid layers brings additional instabilities.

In order avoid these problems, intermittent contact mode or Tapping Mode AFM (TM-AFM) was developed. The cantilever is driven at large amplitudes in close proximity to the sample surface, such that the tip makes deliberate contact with the surface and is pulled away again each oscillation cycle^[95]. The interaction with the sample surface modifies the observed cantilever oscillation directly, which can thus be used as feedback signal to maintain a constant tip-sample separation distance. Similar to AM-AFM, both the topography and phase shift relative to the driving oscillation can be recorded simultaneously.

Although TM-AFM is more suitable than CM-AFM for the imaging of fragile samples under ambient conditions due to the lack of shear forces, the instantaneous normal forces can be large enough to trigger deformation of the sample surface^[96-98].

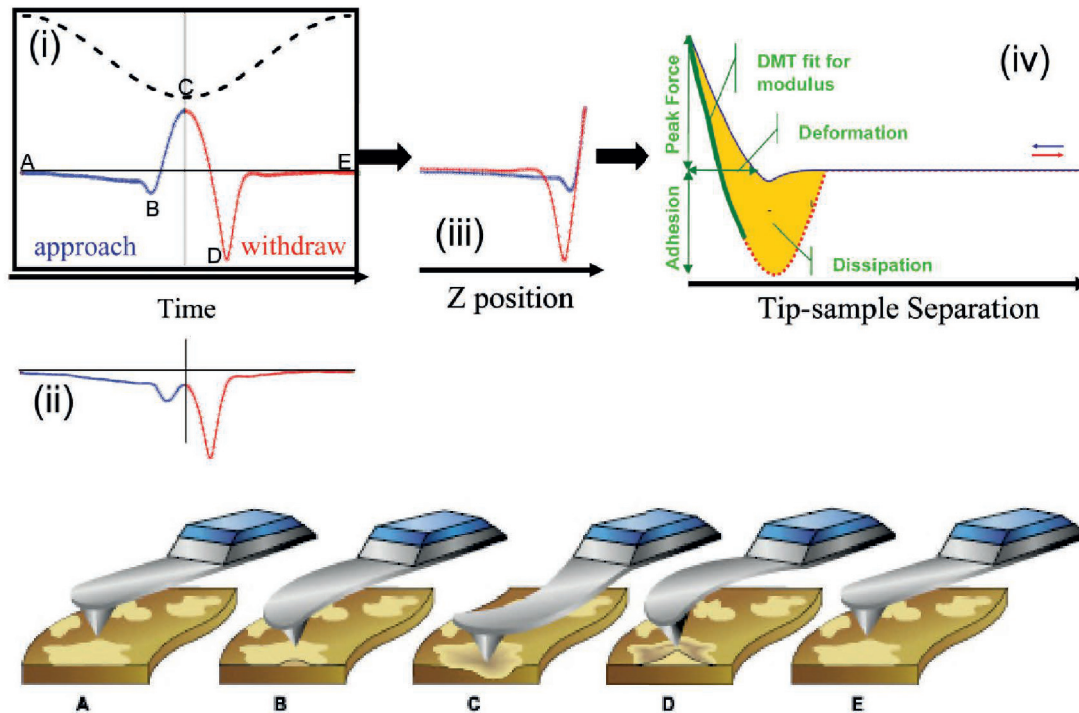


Figure 1.3 – Schematic representation of the probe motion during AFM PeakForce Mapping Mode.

(i) Force (red-blue line) and piezo Z-position (black dashed line) versus time. Points A-E in this graph correspond to the graphical cartoons shown below. In chronological order: Start (A), the jump-to-contact point (B), maximum applied force – Peak Force (C), maximum adhesion force (D) and end (E).

(ii) Same as (i). However, now with a small Peak Force.

(iii) Eliminating the time variable results in a plot of force versus Z piezo position.

(iv) Plot of force versus separation distance between tip and sample. From this, various sample features like adhesion, deformation and dissipation can be extracted.

(This figure is reproduced from figure 1 from Pittenger et al.^[99] and Bruker^[100]).

PeakForce Mapping Mode

Although TM-AFM shows robust imaging capabilities, the large instantaneous tip-sample interaction force can make it challenging to image fragile biological samples. Furthermore, it is challenging to extract quantitative mechanical information from either the topography or the phase-shift. The fact that the cantilever oscillates near the resonance frequency, in combination with large amplitudes, means that the tip is in contact with the sample only briefly each cycle. This also means that variations in the tip-sample force occur over time periods much smaller than the oscillation period of the cantilever. As the bandwidth of an oscillating cantilever is proportional to the resonance frequency of the bending mode that is used, these high-frequency variations in the tip-sample distance are difficult to extract from either the cantilever deflection amplitude or phase shift^[99]. The most straight-forward

method to overcome this, is by driving the cantilever at frequencies significantly lower than the resonance frequency, so that instantaneous changes in interaction forces result in immediate deflection changes. As the full tip-sample interaction history can now be recorded, material properties such as adhesion, deformation and stiffness are extracted.

PeakForce Mapping AFM (PFM-AFM) is a technique that oscillates the cantilever at a frequency of up to 8 kHz, i.e. well below resonance. For every oscillation cycle the complete force vs. time signal can be extracted, which makes it possible to isolate the maximum instantaneous force, or peak force – point C in Figure 1.3(i) – every time the tip interacts with the sample. This high level of control over the tip-sample interaction force, enables imaging at constant Peak Force, independent of adhesion forces that act on the tip^[99].

Compared to TM-AFM, this method has an increased acquisition time due to low oscillation frequency, the large amount of data that is collected and the requirement of real time processing. However, because the positive interaction forces can be controlled and multiple physical properties of the sample can be recorded simultaneously, this imaging method has clear benefits over other AFM measurement modes.

***In Situ* AFM**

Although high resolution imaging with AFM was reported as early as 1991^[101], high resolution imaging of soft organic materials and molecules remained elusive^[14,95,102].

Most biological macro molecules are extremely soft, with Young's Moduli in the range of 0.1 MPa to 1 MPa. This means that to image such molecules without deformation, tip-sample interaction forces should be less than 0.1 nN for tip radii of about 10 nm. While such small forces are readily achieved with soft cantilevers that can have spring constants as low as 0.01 N m⁻¹, operating them under ambient conditions is difficult.

In CM-AFM, the shear force easily surpasses the limit for deformation, and in TM-AFM, the presence of surface liquid layers^[93] requires tip-surface forces as much as tens of nN to prevent adhesion^[95,96].

By moving from *ex situ* imaging in air towards *in situ* imaging in liquid^[102], adhesion forces are reduced or even eliminated altogether. As tip and sample are both immersed in liquid, no capillary bridge is formed and the attractive van der Waals forces are shielded^[93].

This effectively eliminates the need for large TM-AFM amplitudes and stable TM-AFM can be achieved with amplitudes as small as 1 nm, whereas for PFM-AFM the amplitudes are only slightly larger at 3 nm to 10 nm, depending on the remaining adhesion force. Stable PFM-AFM with maximum tip-sample interaction forces of as little as 25 pN are possible^[99,103]. This is impossible for *ex situ* imaging under ambient conditions.

1.1.3 Experimental Set-up

The general AFM set-up consists of a combination of an AFM and a continuous flow system. The whole construction is placed on a damping system that shields the setup from mechanical vibrations that originate with the surroundings. The individual parts are shown in Figure 1.4

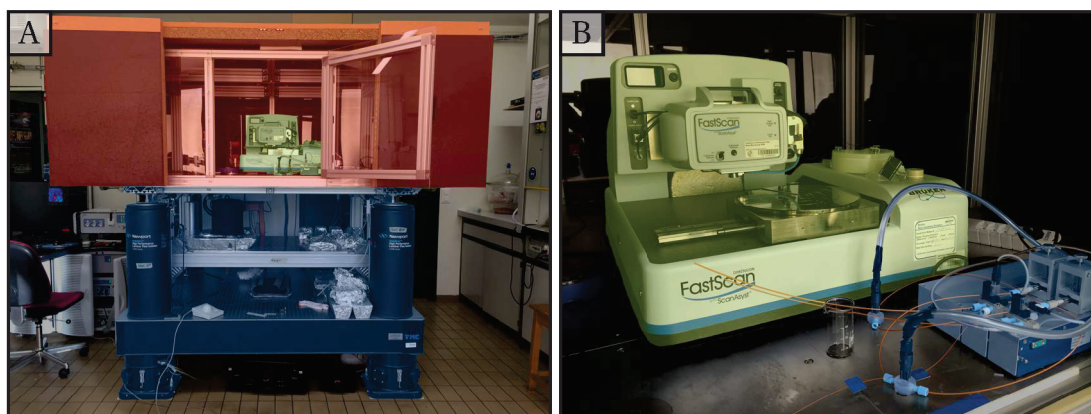


Figure 1.4 – The AFM setup that was installed during this thesis. **(a)** The setup consists of a damping system (blue), acoustic isolation box (red). The AFM (green) is located within the acoustic box. **(b)** The syringe pump (blue) that is used for continuous flow experiments is located next to the AFM (green).

and are described in more detail below.

Damping systems

In Figure 1.4a, the vibration isolation set-up is shown in blue. It is used to shield the AFM from environmental vibrations and consists of three parts, an active piezo electric damping system, a passive damping system based on air pressure and a box that shields the set-up from acoustic noise. The active vibration cancellation system consist of a three-part *STACIS*[®] 2100 system from *TMC*. Vibration sensors in combination with piezoelectric actuators are used to cancel out mechanical vibrations. The additional passive vibration cancellation system consist of a four-part *Newport I-2000* system that uses pressurized air to float the entire system on an air cushion which shields the set-up from mechanical vibrations.

The AFM and the flow system are placed within the acoustically shielded box, as shown in Figure 1.4. The acoustic box uses high-density foam, sandwiched between an inner acrylic box and an outer wooden box.

Dimension FastScan AFM

The AFM used in this work is a *Dimension FastScan AFM* with a *NanoScope V* controller from *Bruker*. This set-up is capable of scan speeds of up to 20 lines per second, making it possible to acquire about 2 images per minute at a 512×512 pixel resolution under ideal conditions. In Figure 1.2, the different AFM measurement setups are presented. The standard measurement environment is in ambient air. The scan-head of the FastScan AFM is compatible with *in situ* imaging conditions and can be used in non-flow conditions by using the surface tension of the solution to form a capillary between sample and scan head. The addition of a dedicated liquid-flow cell, as shown in Figure 1.2c, allows for *in situ* imaging during continuous flow conditions. Liquids that are not compatible with the formation of a capillary bridge due to a

low surface tension can be used in this set-up as well.

Continuous Flow Set-up

To achieve pulsation free continuous flow within the liquid cell, as shown in Figure 1.2, two *neMESYS* low pressure syringe pumps from *Cetoni* are each connected through an automatic three-way valve system. The syringe pump is placed inside the acoustic box, next to the AFM, as shown in Figure 1.4b.

The three-way switching valves are limited to 0.21 bar in pressure, whereas the syringe pumps are capable of generating pressures much higher than this. To prevent the valves from damage due to excessive pressures, additional pressure relief valves are installed that limit the pressure within the liquid flow system to 0.21 bar.

The AFM flow cell has a volume of 60 μl and the syringes each have a volume of 1 ml. The tubing between syringe and flow cell inlet has a volume of 220 μl and the total volume of both inlets and common outlet has a volume of 1.1 ml. Taking a minimum reservoir volume of 1 ml, this means that in order to establish a continuous flow through this system, a minimum of 3.1 ml of solution is required. If a single injection without subsequent flow is all that is required, a minimum of 300 μl is sufficient.

The presence of gas bubbles in the liquid flow poses a significant problem for *in situ* AFM imaging. Special care is required in the case of aqueous solutions that form gasses such as CO_2 formation from dissolved NaHCO_3 . This is solved by including a semi-permeable membrane within the liquid flow that is permeable to gas, but closed to liquid. In the system that is described here, a passive bubble trap from Omnifit is installed.

A portable *Jenco Model 6230* pH meter was connected in serial with the liquid flow system. This makes it possible to continuously read the pH of the liquid flow.

1.1.4 AFM probes

Several factors are important in choosing the right AFM probe. Not only do the various AFM imaging modes each have different requirements, also the imaging medium and sample properties greatly influence the choice of probe.

The main problem in CM-AFM is the shear force of the tip over the surface. To minimize the damage to the sample, it is important to use imaging probes with low spring constants. In contrast, for TM-AFM the most important probe feature is the Q-factor, which is typically higher for probes with high resonance frequencies and consequently higher spring constants. This makes probes that are suitable for CM-AFM, such as the SNL-D, unsuitable for TM-AFM, which needs high resonance frequencies such as the Tespa probes, see also Table 1.1.

The fact that the complete tip-sample interaction curve is recorded during PFM-AFM makes it possible to use a larger range of AFM probes than with either CM-AFM or TM-AFM. The tip-sample interaction can be controlled directly, largely independent from the spring force. The only constraint on the resonance frequency is that it must be larger than 8 kHz, which is the

Table 1.1 – Specifications of AFM probes used in this work.

Probe Name, Manufacturer	Imaging Mode	Spring Constant (N/m)	Resonance Frequency in Air (kHz)	Radius of Curvature (nm)
FastScan-D, Bruker	air/liq. – TM, PFM	0.25	200	5
ScanAsyst-Air, Bruker	air – PFM	0.4	70	2
ScanAsyst-Fluid, Bruker	liq. – PFM	0.7	150	20
PeakForce-HIRS-F-B, Bruker	air/liq. – PFM	0.12	100	1
SNL-D, Bruker	liq. – CM	0.06	18	2
Tespa, Bruker	air – TM, PFM	42	320	8

typical oscillation frequency used by the Dimension FastScan AFM when used in PFM-AFM. The *FastScan-D* probe from *Bruker* was experimentally found to be the most successful AFM probe that has been used during this work. This probe offers high resolution imaging conditions in either TM-AFM or PFM-AFM, both *in situ* and *ex situ*. The main reason for this is likely the non-standard tip geometry and the extremely small size compared to typical AFM probes. Where most AFM probes are either rectangular or triangular in shape, the FastScan-D has a paddle-like geometry, which allows for the combination of a high resonance frequency with a low spring force. The dimensions of the FastScan-D are with $4\ \mu\text{m} \times 16\ \mu\text{m}$ much smaller than the more usual $25\ \mu\text{m} \times 115\ \mu\text{m}$ of the ScanAsyst-Air. Especially in viscous liquids this greatly suppresses the creation of convection currents due to the cantilever oscillations. In Table 1.1 an overview is given of the most successful AFM probes used in this work. For a complete list, the reader is referred to Appendix D.

1.1.5 Software and Data Analysis

Typical imaging artifacts that occur during Fast Scan AFM operating procedures can easily be removed by correctly processing the obtained images. However, a thorough understanding of the underlying principles is required to avoid misinterpretation and over-processing of the data^[104].

The non-linearity of AFM piezos is usually compensated by correct and periodic calibration of the AFM. However, at larger scan-sizes, deviations between the observed and actual sample height are common. For example, the sample seems to have a bow-like curvature, while in fact it is flat. The most straight forward method of correcting such artifacts, is by fitting and subtracting to each image line a 2nd or 3rd order polynomial. This method works well for relatively homogeneous samples, however, in the presence of distinct protrusions or holes it can severely distort the AFM image. This can be fixed by either manually selecting the protrusions and holes and fitting only the flat parts of the surface, or by using an automated algorithm such as *flattening plus*, build into the WSxM software package^[105,106].

Another general image artifact is the presence of a periodic pattern resulting from ambient

vibrations that are not removed by the damping system. Such periodic patterns can be difficult to distinguish from periodic structures native to sample that is being measured. Two quick methods can be used to identify periodic ambient noise patterns. By comparing AFM images obtained by recording the trace and the retrace directions of the tip on the sample, one can often see that periodic structures resulting from ambient noise are differently oriented in the trace and retrace images. Alternatively, the scan speed can be changed. Periodic oscillations originating outside the sample will have a different spatial periodicity, depending on the line scan frequency. Patterns identified as noise can be filtered out using a 2D-FFT transformation, where periodic patterns show up as clearly identifiable points. Removing these points and using a reverse 2D-FFT transformation effectively removes the noise pattern.

In this work, two different software packages are used to process the AFM images. *WSxM version 5.0 develop 7.0* by *Nanotec Electronica* is used for detailed analysis of individual images^[105]. For batch processing of larger number of images, *NanoScope Analysis* software from *Bruker* is used.

1.1.6 Workflow

In the following section, the experimental AFM workflow is described in detail. The hypothetical case of imaging the adsorption of molecules at a mica-liquid interface under continuous flow conditions is used to describe the different aspects of sample preparation and imaging.

Preparation

To prevent drift, the sample has to be immobilized with respect to the movement of the scanning probe. During *ex situ* imaging, this often poses no problem. However, during *in situ* imaging, the presence of the liquid flow cell creates a mechanical connection between sample and scan head. To allow for high-resolution *in situ* imaging, the sample has to be thoroughly immobilized to a glass microscopy slide that fits in the AFM sample holder. Usually a two-component glue such as *Araldite Rapid* is used. Double sided tape is not sufficient to prevent movement of the sample at the nanoscale.

In the case of a mica sample, the top layer is removed using *Scotch Magic* tape. Simply applying the tape to the mica top surface and then removing it, gives an atomically flat and pristine sample surface. The sample-glass slide combination is then placed inside the AFM sample holder.

For *in situ* imaging, the liquid must be introduced to the liquid flow system. Typically, clean milliQ water with $18.2 \text{ M}\Omega \times \text{cm}$ is injected and bubbles are removed from the flow system by holding the syringes vertically, while vigorously flowing the liquid through the system. Once the bubbles are removed, the solution is exchanged for a different solution that contains the molecules that are to be adsorbed at the mica-liquid interface.

This exchange of solution is less trivial in the case of a limited volume of imaging liquid. The lateral movement of the syringes, in combination with a $200 \mu\text{l}$ internal volume of the flow

system, requires a specific sequence of syringe movements to replace the internal volume with as little solution as possible. For each syringe, a seven times repetition of 100 μl injection and withdrawal brings the internal concentration to more than 90 % of the injection liquid, with as little as 700 μl solution used (1.4 ml for both syringes). Fifteen repetitions are required to reach 100 %.

Starting the AFM experiment

A suitable choice of AFM probe must be loaded onto the scanning head of the AFM. In the case of *in situ* imaging, the liquid flow cell is placed on top of the scanning head and filled with solution. Typically, 60 μl is sufficient to immerse the cantilever. The exit tube should be closed to prevent the droplet from flowing away.

Once in place, the scan head is attached to the main AFM system. Note that the liquid droplet should remain in place during the 180° flip that is required for attachment. The built-in optical microscope is used to align the detection laser with the cantilever so that the total reflection onto the photodiode detector is maximized, Figure 1.2. In the case of TM-AFM, the cantilever must be oscillated close to the resonance frequency f_0 , which is found by recording the oscillation amplitude as function of the driving frequency and selecting the maximum. The probe is now ready to be brought in contact with the mica surface.

In close proximity to the sample, a capillary bridge will form between the hanging droplet in the liquid flow cell and the mica surface. At this point, it is often beneficial to double check the laser position and resonance frequency before making contact between the tip and the mica surface.

Tuning of imaging parameters

Now that the tip is in contact with the sample surface, it is important to minimize the interaction force as soon as possible. This is done by increasing the amplitude setpoint (TM-AFM) or decreasing the peakforce (PFM-AFM).

The feedback of the AFM (Equation 1.4) is then optimized by increasing the integral gain as much as possible, without introducing periodic patterns as a result of unstable feedback. The proportional gain is then increased using the same principle.

Lastly, other parameters such as the oscillation amplitude are optimized. By decreasing the amplitude, the tip-surface interaction time is increased. This is often beneficial for the resolution. However, in order to overcome adhesion, a minimum amplitude is required to generate the force required to break away from the surface. Trial-and-error, in combination with experience is used to arrive at an optimal value. As non-optimized parameters can result in high tip-surface forces, it is important to check for sample damage once imaging conditions are optimized by moving the tip to a new imaging area.

1.2 Electrospray Ion Beam Deposition

Conventional vacuum deposition of molecules uses sublimation and condensation techniques, such as Molecular Beam Epitaxy (MBE)^[107], as primary mechanism to transport molecules through UHV from solid form to individually deposited molecules on a substrate. Unfortunately, this technique is incompatible with larger molecules that become thermally unstable before the sublimation temperature is reached.

Electrospray Ionization (ESI) is a technique that was originally developed to make larger molecules available for mass spectroscopy^[108] and was later adapted as ion source for surface deposition^[109]. Electrospray Ion Beam Deposition (ES-IBD) overcomes the problems associated with thermal instability during MBE and allows for the deposition of large and fragile molecules under highly controlled conditions^[110,111].

1.2.1 Fundamentals of ES-IBD

To use ES-IBD, the molecules must be dissolved, usually at low or high pH to enhance ionization. The solution is then pumped through a needle-like emitter at high voltage with respect to the entrance of the ES-IBD system. The high voltage at the tip drives charge separation within the liquid jet that emerges from the emitter. This deforms the jet into a sharply tipped Taylor cone^[112]. The sharp curvature of this cone, in turn, locally enhances the electric field, which drives the separation into micrometer sized highly charged droplets.

In each droplet, there is a balance between the surface tension of the droplet and coulomb repulsion due to the charges contained within the droplet. When the solution evaporates, this balance drives the break-up of these micrometer sized droplets into what eventually become nanosized droplets or individual ionized molecules. The exact mechanism in which the nanosized droplets evaporate and leave individually charged molecules is still under debate and several mechanisms have been proposed, depending on the nature of the molecules^[113]. In the case of small chain-like molecules such as peptides, both the Ion Evaporation Model (IEM) and the Chain Ejection Model (CEM) are applicable.

1.2.2 Experimental set-up

Figure 1.5 shows the ES-IBD set-up that is used in this work. The apparatus is homebuilt and is part of a combined ES-EBD and STM system^[114]. ESI takes place under atmospheric conditions, however, in order to deposit under high vacuum (HV) conditions, the ion beam is directed through a series of differentially pumped chambers where the pressure is sequentially decreased to reach 10^6 mbar. In order to maintain the pressure difference between chambers, they are connected to one another only through a small pinhole. This requires that the ion beam is steered and focused precisely, which is done by using an ion funnel in combination with two quadrupoles. The second quadrupole is used as a bandpass filter to select specific m/z ratios. Finally, soft landing of the ionized molecules is achieved by applying a specific retarding voltage to the sample in order to decelerate the ions before impact.

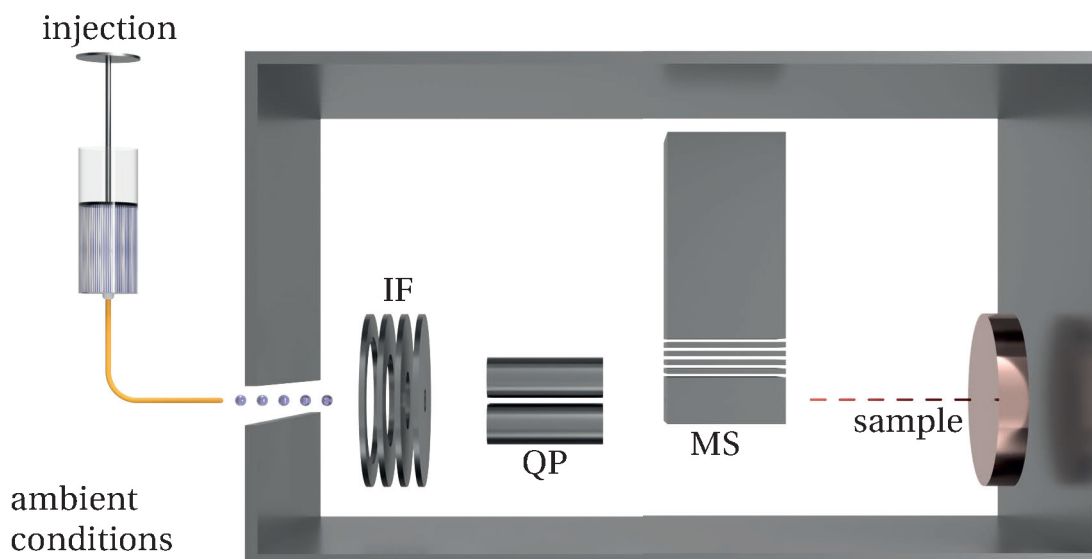


Figure 1.5 – The ES-IBD apparatus consists of several components that work together to transfer large molecules intact from a solvated phase to a solid-vacuum interface. A solution containing the molecules is injected. The presence of a custom made atmospheric interface facilitates the formation of a stable beam of micrometer sized droplets. An ion funnel (IF) and quadrupoles (QP) then collimate and transfer the ion beam to the high vacuum (HV) environment of the sample. During transfer to the HV environment, the microdroplets evaporate and break up to form individual charged molecules. The ion beam can be characterized in detail by mass spectroscopy (MS) before a controlled soft landing at the solid-vacuum interface of the sample.

1.3 X-ray Absorption Spectroscopy

X-ray Absorption Spectroscopy (XAS) refers to the absorption of x-rays due to the excitation of core-level electrons of atoms. From Equation 1.5 it can be seen that the absorption probability is highly dependent on both atomic number, Z , and x-ray photon energy E . For this reason XAS provides excellent sensitivity to, and contrast between, different chemical elements.

$$\mu \approx \frac{\rho Z^4}{AE^3} \quad (1.5)$$

With μ the absorption coefficient which determines the absorption probability, ρ the sample density, Z the atomic number, A the atomic mass and E the x-ray energy.

Furthermore, the absorption probability is modulated by the chemical and physical surroundings of the absorbing atom. This makes XAS highly sensitive to properties such as the distance to, coordination with, and species of the neighboring atoms^[115].

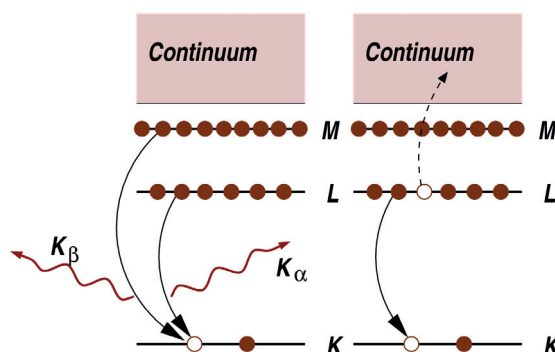


Figure 1.6 – Schematic representation of the two mechanisms through which the excited state can decay. X-ray fluorescence on the left, emission of electrons due to the Auger effect on the right. The probability of both mechanisms is directly proportional to the absorption probability of the x-ray photon (Figure 2.5 from *Fundamentals of XAFS* by Matthew Newville^[115]).

1.3.1 Fundamentals of XAS

When photons are absorbed, a core-level electron is excited and the absorbing atom is left with an unoccupied core energy-level. The probability of this depends on the difference in energy between the energy levels of the core electrons and the energy of the incoming photons. When the incoming photon energy surpasses the energy difference between a core electron and an empty state in the same atom, the absorption probability rises sharply. This is called an absorption edge.

In this work, the main absorption edge is the L-edge, which is defined as the excitation of the L electron shell. The L-edge is split between three different energy levels, L_I , L_{II} and L_{III} , respectively. Here L_I corresponds to the excitation of a 2s electron. Upon excitation of a 2p electron a $2p^5$ configuration is created, which, due to spin-orbit coupling, is split in a low and high energy state. The low energy state gives rise to the L_{III} edge and the high energy state to the L_{II} edge^[116].

This excited state can then decay using one of two possible mechanisms, through x-ray fluorescence or through the Auger effect, as is shown graphically in Figure 1.6^[115].

During x-ray fluorescence, the hole in the core-level created by the absorption event is filled by an electron from a higher energy level within the same atom. By moving to a lower level, the electron is left with excess energy, which is emitted in the form of an x-ray photon. The total number of x-ray fluorescent photons is called the Total Fluorescence Yield (TFY).

During the Auger effect, the core-level hole is again filled by an electron from a higher energy level within the same atom. However, unlike x-ray fluorescence, the excess energy is now transferred to yet another electron, which is subsequently emitted from the atom. The total number of emitted electrons is called the Total Electron Yield (TEY).

While both TFY and TEY signals are directly proportional to the X-ray absorption probability, they are not entirely interchangeable. Due to the fact that electrons have a much smaller inelastic mean free path in most materials compared to photons, the Auger electrons have a

higher surface sensitivity than the fluorescent photons.

XAS can be divided into two parts. X-ray Absorption Near-Edge Spectroscopy (XANES) is the part of the XAS spectrum within ~ 50 eV of the absorption edge and is most sensitive to the oxidation state and coordination chemistry of the absorbing atom. Extended X-ray Absorption Fine-structure Spectroscopy (EXAFS) is the part beyond the XANES region and is more sensitive to the distance, coordination number and species of the neighbors of the absorbing atoms^[117].

In this work, the XANES region is used to study noncrystalline as well as crystalline materials. Depending on the experimental constraints, the samples can be solid, liquid or gaseous.

Crystal Field Peaks

As stated before, the x-ray absorption probability depends on the difference in energy between the energy levels of the core electrons and the energy of the incoming photons. The presence of neighboring atoms can slightly affect the energy levels of the absorbing atom. Because of their non-spherical distribution, the d-orbitals are sensitive to the relative distribution of neighboring atoms.

In amorphous materials, all atoms are arranged randomly and the atoms do not have a specific orientation with respect to one another, i.e. all d-orbitals are affected equally. This is different for crystalline materials, where both position and orientation of the atom is fixed. In this case, some d-orbitals will be affected differently from others, and consequently will have specific energy levels that depend on the crystal structure of the solid. This is what is called crystal field splitting of the d-orbitals^[118-120].

The L_{II} and L_{III} edges can be affected by this effect because the split d-orbitals create extra energy levels available for the excited 2p electrons. This then shows up in the absorption spectrum as secondary peaks that precede the two main peaks at the L_{III} and L_{II} edges.

1.3.2 Experimental set-up

Liquid flow and static liquid experiments were exclusively performed at beamline 8.0.1, whereas solid state experiments were performed at beamline 7.0.1 as well. Both beamlines are located at the Advance Light Source (ALS) at the Lawrence Berkeley National Laboratory (LBNL).

The spot size of both beamlines is several thousand μm^2 ($100 \mu\text{m} \times 35 \mu\text{m}$) with photon intensities of 10^{11} - 10^{15} photons per second. The experimental setup is such that the x-rays come in at an angle with the sample surface so that the emitted fluorescent photons are emitted at an equal but opposite angle with respect to the normal.

The TFY signal is detected with a channeltron, which multiplies an incoming charge by means of secondary electron emission. The inside of a small glass tube is coated with a semiconducting metallic oxide coating. When an electron strikes this surface with enough energy, it will dislodge multiple secondary electrons. By applying a transverse electric field, the electrons will follow a zigzag pattern that results in an avalanche of outgoing electrons^[121]. The same

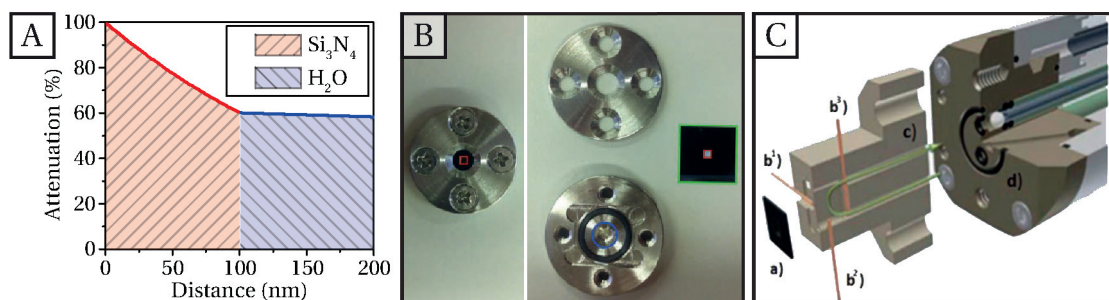


Figure 1.7 – *In situ* liquid cells enable the use of liquid samples under UHV conditions, which is required for XAS experiments. (a) The absorption of x-rays in a medium depends on the attenuation of the material. Here the attenuation through a Si_3N_4 window – (b) and (c) – is calculated following Equation 1.6. A single pass through 100 nm Si_3N_4 absorbs 77 % of photons. (b) A static liquid cell is displayed in closed and open configuration. The red square marks the optically transparent 100 nm thin Si_3N_4 window in the middle of the larger $1 \text{ cm}^2 \times 1 \text{ cm}^2$ silicon wafer, marked in green. The blue circle marks the hollow spacing where the liquid is confined. The four screws press the cover onto the silicon surface, which is therefore sealed against the black o-ring. (c) The flow cell that is shown here separates a continuous liquid flow, marked by the green curved arrow, from UHV condition with a 100 nm thin Si_3N_4 window, marked by the *a*. Image from reference^[122].

multiplication principle can be applied to incoming photons when a photo-emissive surface is placed in front of the channeltron.

The TEY detection is based on the fact that the emitted Auger electrons leave the sample in a charged state. This, in turn, creates a potential difference between the sample and its surroundings. By electronically connecting the sample to ground, the current along this potential can be recorded.

Difficulties arise when the source emits both photons and electrons, as is the case during standard XAS operation. The channeltron cannot distinguish between electron generated by a photon striking the photo-emissive surface, or electrons emitted directly from the source. To select only the fluorescent signal, a charged grid is placed in front of the channeltron and by applying a voltage to this grid just above the energy of the incoming electrons, the Auger electrons can be repelled without affecting the uncharged photons.

For both solid samples and static or liquid flow cells, Si_3N_4 membranes within a silicon frame are used as substrate. The membranes were purchased from *Silson Ltd* and *Ted Pella Inc.* and are $1.0 \text{ mm} \times 1.0 \text{ mm}$ in size, with a thickness of 100 nm on a silicon support frame with a thickness of $200 \mu\text{m}$. For the solid samples, the silicon support frame measured $5.0 \text{ mm} \times 5.0 \text{ mm}$, whereas for the static liquid and continuous flow cell, the support frame measured $10.0 \text{ mm} \times 10.0 \text{ mm}$.

***In situ* XAS**

As the channeltron is typically located at least several centimeters from the sample, the

medium between sample and detector must have an exceptionally low attenuation for photons in order to create a mean free path comparable to this distance. For regular solid samples, this is readily achieved by placing the samples in UHV conditions. However, for liquid samples or samples immersed in liquid, there is a strong attenuation of x-ray photons over these distances, which will make direct detection within this liquid impossible. This can be overcome by separating the liquid sample and detector by a medium with low attenuation.

In practice, this means that the liquid is physically separated from UHV conditions by a x-ray-transparent solid membrane such as Si_3N_4 ^[122–125]. The attenuation of photons with an energy of 350 eV through a Si_3N_4 window is calculated using Equation 1.6 and graphically shown in Figure 1.7a. At a thickness of 100 nm, the Si_3N_4 membrane has a transmission of 60 % for photons with an energy of about 350 eV. The attenuation of x-rays within pure water is much lower and several microns can be readily accessed.

$$P(x, E) = e^{-\alpha x} \quad (1.6a)$$

$$\alpha(E) = \tau(E) \cdot \rho \quad (1.6b)$$

$$\tau_{\text{Si}_3\text{N}_4, 350\text{eV}} = 1.48 \cdot 10^4 \text{ cm}^2/\text{g}$$

$$\tau_{\text{H}_2\text{O}, 350\text{eV}} = 3.01 \cdot 10^3 \text{ cm}^2/\text{g}$$

$$\rho_{\text{Si}_3\text{N}_4} = 3.44 \text{ g/cm}^3$$

$$\rho_{\text{H}_2\text{O}} = 1.00 \text{ g/cm}^3$$

With P the attenuation of the photon, E the photon energy, $\tau(E)$ the total attenuation (cm^2/g) at energy E and ρ the density of the material.^[126,127]

As the penetration depth of electrons in liquids is typically only a few nanometers^[128,129], compared to up to several microns for photons^[126], only x-ray fluorescence can be used to record absorption spectra of liquid samples or samples immersed in liquid^[122–125].

1.3.3 Software and Data Analysis

Once the TFY and TEY signals are recorded, specific software is used to analyze the data. A dedicated IgorPro package was available and was designed to work with data obtained from either beamline 7.0.1 or 8.0.1 at the ALS. The analysis of the x-ray data is based on several physical principles that are discussed here.

Each available absorption edge gives rise to stepwise increase in the total absorption intensity. Due to the degeneracy of the L_{II} and L_{III} edges, the jump in background intensity is twice as strong at the L_{III} edge compared to the L_{II} edge. Furthermore, spectra can be affected by charging or discharging of the sample surface, which would result in a continuously decreasing or increasing background intensity.

Based on these physical properties of the L_{II} and L_{III} edges, the flat pre-edge and post-edge regions of each spectrum are fitted with a 3^{rd} degree polynomial and two arctangent step-

functions. The positions of the two arctangent functions are fixed at the L_{II} and L_{III} edges and the step height at the L_{III} edge is set to double the height at the L_{II} edge.

The observed XAS spectra can have an energy shift related to the imprecision of the slit positioning. This shift can be corrected by collecting an XAS spectra of a known sample after each new position of the grating. The peak position of this reference spectra can then be related to its known literature value and the energy shift can be calculated. This energy shift is then applied to all consecutive spectra.

It can be useful to relate the absorption to the quantity of the absorbing atoms within the sample. It is therefore important to obtain both the intensity of the x-ray beam before absorption, and after absorption. This is typically done by dividing the absorption intensity, I , by the intensity of the incoming beam, I_0 .

1.3.4 Workflow

For solid samples, the Si_3N_4 membrane is attached with double sided sticky copper tape to a beamline-specific metal sample holder. The use of such sample holders is necessary to be compatible with the manipulation tools that are used to transfer the samples in UHV conditions from the load lock to the main XAS experimental chamber. The connection between sample and sample holder must be conductive to prevent sample charging and to enable the detection of the TEY signal.

For static liquid cells, Si_3N_4 membranes are placed inside the liquid cells that are shown in Figure 1.7. First, a specific volume of liquid is placed inside the liquid cell, after which the Si_3N_4 membrane is placed on top. The cover plate is fixed with four screws until a slight curving of the window is observed. If the volume of liquid is slightly too small, there is an additional air bubble trapped within the cell. If the volume is even a little bit too large, the membrane will rupture when the cover plate is screwed in place. The liquid cell is then attached to a sample holder using copper tape, similarly to the solid samples.

In the case of the continuous flow cell, the procedure is slightly different. As the cell must be connected to a liquid reservoir outside the UHV main chamber, the load lock cannot be used. Instead, the main chamber is vented to atmospheric pressures to allow the placement of the liquid flow cell. Once in place, the pressure in the main chamber is brought back to UHV conditions. Because the Si_3N_4 membrane is attached to the flow cell using glue, the system is prone to degassing when the pressure is lowered. This means it takes considerable time to reach UHV conditions.

After the samples are placed inside the measurement chamber, the XAS spectra are recorded by exposing the sample to the x-ray beam at an angle such that the reflected x-rays are directed towards the channeltron.

The position of the entrance slit with respect to the monochromater is slowly adjusted so that the sample is exposed to photons of varying energies. The intensity of the TFY and TEY signals

Chapter 1. Fundamentals

is then recorded as function of incoming photon energy.

2 Self-assembly of small peptides at the solid-liquid and solid-vacuum interface

Biointerfaces are ubiquitous in nature as well as in technological applications such as biosensors and medical implants. Their structure and response to stimuli are ultimately determined by intra- and intermolecular interactions at the nanoscale.

A biomimetic approach to bottom-up fabrication of biointerfaces requires a deep understanding of the underlying forces that drive the interactions between individual molecules and their surroundings. Their modular nature, in combination with established techniques for synthesis, make peptides well suited to the study of self-assembly at the nanoscale.

The goal of this part of the thesis is to add to this understanding through a systematic study of the self-assembly of peptides at various interfaces and in different environments. To elucidate the influence of the substrate, solvent and internal structure of the peptide on the self-assembly properties.

The main subject of this study is a small peptide composed of one phenylalanine, five alanine and one lysine residue and with an acetylated N-terminus (Ac-Phe-Ala-Ala-Ala-Ala-Lys or AcFA₅K). This combination of amino acids results in a peptide with a distinct hydrophobic N-terminus due to the phenylalanine residue and acetylation of the N-terminus. The C-terminus is hydrophilic due to the lysine residue and the fact that it is uncapped. The short backbone is composed of five alanine residues and is therefore hydrophobic. Due to its hydrophilic head and hydrophobic backbone, the AcFA₅K peptide is expected to have surfactant-like behavior. The length of a fully extended AcFA₅K peptide is about 25 Å and an additional 8 Å can be attributed to the lysine residue that extends away from the backbone, as is graphically displayed in Figure 2.1.

This particular peptide has been studied by Stearns et al.^[22], where its conformation in the gas phase was resolved. At low temperatures and in the gas phase, AcFA₅K exists in four major

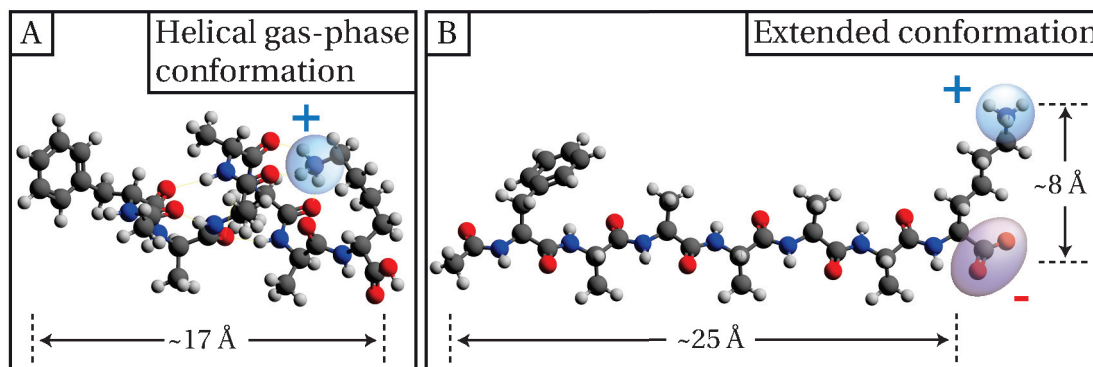


Figure 2.1 – A schematic representation of the peptide Ac-Phe-(Ala)₅-Lys (AcFA₅K). The N-terminus is capped with an acetyl group whereas the C-terminus is uncapped. (a) Individual AcFA₅K peptides in the gas-phase feature a helical structure^[22]. (b) A schematic representation of the AcFA₅K peptide in fully stretched conformation. Depending on the pH of the surrounding medium, the -NH₂ group can be protonated to become -NH₃⁺ (blue halo with +) whereas the -COOH group can be deprotonated to become -COO⁻ (red halo with -).

conformations, with all of them featuring a helical backbone structure as shown in Figure 2.1a. Furthermore, a direct comparison between the gas-phase structure of related peptides AcFA₁₀K and AcKFA₁₀ reveals that only AcFA₁₀K is helical, whereas AcKFA₁₀ is globular. It is thus thought that the helical structure is stabilized by the precise location of the lysine residue at the C-terminus^[21,22].

A careful look at the atomic structure of the AcFA₅K peptide shows that there are two functional groups that can be charged in solution, depending on the pH level. A rough estimate for the charged states can be made based on the pK_a values as found by titration experiments done by Qui et al. on similar peptides that lack the phenylalanine group. The pK_a value of the amino group was found to be 10.78 and can thus be considered positively charged for pH < 10.78. The pK_a of the carboxyl group is 2.46 and can thus be considered negatively charged for pH > 2.46^[23]. At neutral pH levels, this peptide is therefore expected to be in a zwitterionic state, with both a positively and negatively charged group at the C-terminus. This ionic self-complementary property enables self-assembly of AcFA₅K based on ionic interactions between the amine and carboxyl groups of neighboring peptides. For similar peptides that lack the hydrophobic phenylalanine group, it has been found that this results in the formation of fully cylindrical micelles^[23].

This chapter is divided into several sections that deal with different aspects of the self-assembly of AcFA₅K peptides. The first section revolves around the influence of external factors on the self-assembly behavior of AcFA₅K. By systematically studying the self-assembly of AcFA₅K at various interfaces and in different environments, we aim to elucidate the influence of the substrate and solvent on the self-assembly of AcFA₅K. The use of ElectroSpray Ion Beam Deposition (ES-IBD) and *in situ* drop casting techniques enables a direct comparison between self-assembly at the solid-vacuum interface (UHV conditions) and self-assembly at the solid-liquid interface. The second section investigates the influence of internal factors, such as

2.1. External factors: The substrate and surrounding medium

the charge and internal structure of the peptide. Following observations of Stearns et al., the influence of the lysine residue on the self-assembly is investigated. AcFA₅K is compared with AcKFA₅ and AcFA₆, which either have the lysine residue at the N-terminus or lack lysine completely. The thermal stability of the various self-assembled structures is analyzed in the third section. In order to present a thorough analysis of the various structures that have been presented throughout the first three sections, the discussion of their internal configuration is postponed until the fourth section, where the structural aspects of the various assemblies are compared and discussed. In the fifth section, the influence of metal ions on the self-assembly of AcFA₅K is investigated, with the aim of forming stable metal-peptide complexes at the solid-liquid interface. Such complexes have gathered interest as model structures for metalloproteins, which are often the most efficient and selective catalysts available^{[130][131]}. The final section contains the conclusions of this work and the implications for the field of peptide self-assembly in general.

2.1 External factors: The substrate and surrounding medium

External factors such as the substrate and the surrounding medium can have a profound effect on the self-assembly of peptides. For example, the surrounding medium can influence the self-assembly behavior of peptide through protonation or deprotonation reactions. For the previously introduced AcFA₅K peptide, the carboxyl group at the C-terminus can be deprotonated and thus become negatively charged, whereas the amine group at the end of the lysine residue can be protonated and become positively charged. These charged residues can in turn interact with surface charges at a solid-liquid interface.

By using ES-IBD to deposit AcFA₅ at the solid-vacuum interface, and drop casting to deposit the same peptides at the solid-liquid interface, a direct comparison can be made between the UHV and liquid environment.

2.1.1 Self-assembly at the solid-liquid interface

In this section, the influence of the solid-liquid interface on the self-assembly of AcFA₅K peptides is investigated. Negatively charged hydrophilic mica substrates are compared with neutrally charged hydrophobic HOPG substrates, while all other parameters are kept constant. Any difference in self-assembly behavior is therefore a result of the peptide-surface interaction forces.

The peptides are dissolved in H₂O and MeOH in a 50/50 volume ratio and subsequently deposited onto the substrate. The solid-liquid interface is then imaged using high resolution *in situ* AFM. Due to the low surface tension and vapor pressure of the H₂O/MeOH solution, a closed liquid flow cell is used to both confine the solution to the solid substrate and prevent evaporation.

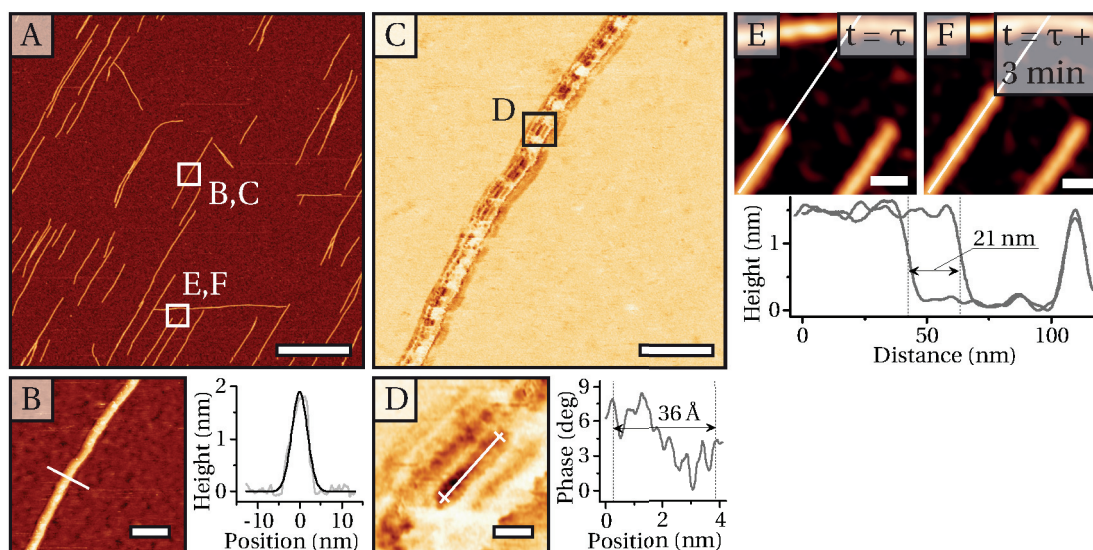


Figure 2.2 – The assembly of AcFA₅K at 0.1 mM at the mica-liquid interface, as observed by *in situ* AFM. (a-b) Peptides form fibers at the mica-liquid interface, which exhibit three preferential orientations separated by a 60° angle. The fibers have a height of about 2 nm and an apparent width of 4 nm to 5 nm. The scale bars represent 400 nm and 20 nm respectively. (c-d) Phase contrast images obtained simultaneously with the topography images from (a-b) show the presence of an internal structure. Bands that are aligned along the direction of the fibers have a 5 Å corrugation along their length. Scale bars represent 20 nm and 16 Å, respectively. (e-f) Zooms from (a) show the epitaxial growth of the fibers over the course of 3 min. The growth rate of the left fiber is about 4.6 nm/min, whereas the fiber on the right does not seem to exhibit any epitaxial growth during this time. Scale bars represent 20 nm.

Self-assembly at the mica-liquid interface

Due to the layered nature of mica substrates, their preparation is relatively easy, i.e. a simple procedure that uses *Scotch magic* tape to remove the top layer of the mica sample is sufficient to obtain atomically flat and pristine mica substrates. Mica is negatively charged in aqueous solutions due to desorption of K⁺, leaving a negatively charged [Si₃Al₁O₈]⁻ crystal surface^[132]. This high surface charge leaves mica extremely hydrophilic, with contact angles approaching 0°.

Figure 2.2a shows the self-assembly of AcFA₅K at 0.1 mM in 50/50 volume percentage H₂O and MeOH at the mica-liquid interface. Rigid fibers are present at the mica-liquid interface and a careful look at the orientations of the fibers reveals three principle orientations with a 60° angle with respect to one another. Although the crystal structure of the mica substrate could not be resolved at these conditions, the specific orientations suggest an alignment along the principal directions of the underlying atomic lattice of mica. Such directed epitaxial growth on mica has been widely reported for peptides featuring a positively charged N-terminus or other positively charged residues^[23,133–141]. It originates from a direct interaction with the negatively charged sites at the mica surface where K⁺ used to be absorbed^[132]. Figure 2.2b shows that the fibers have a uniform height of 2 nm. The phase contrast images shown in Figure 2.2c show

2.1. External factors: The substrate and surrounding medium

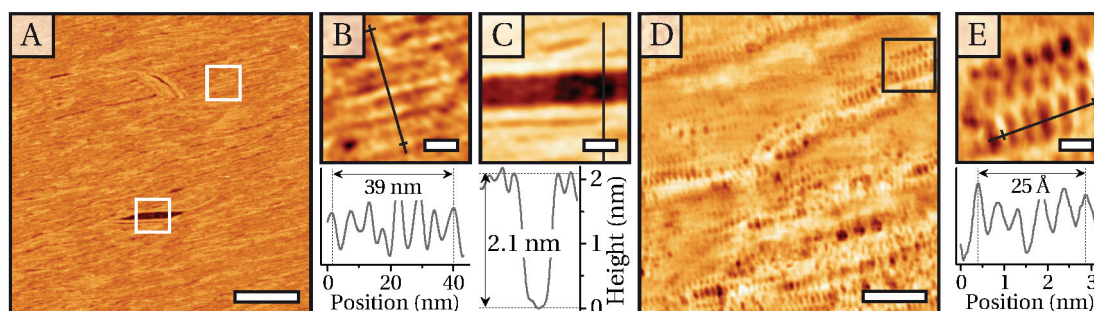


Figure 2.3 – The self-assembly of AcFA₅K at 0.8 mM at the mica-liquid interface as observed by *in situ* AFM. Images were made within 15 min after the peptides were brought in contact with the mica substrate. (a-c) Compared to Figure 2.2, the number of fibers at the mica-liquid interface is drastically increased, i.e. a full monolayer has formed. The height and separation are about 2 nm and 5.5 nm. Scale bars represent 100 nm and 10 nm, respectively. (d-e) Phase contrast images obtained simultaneously with the topography images from (a-c) clearly show an internal structure of the fibers, similar to what is observed in Figure 2.2. Dark bands are aligned along the direction of the fibers and have an internal periodicity of 5 Å. Separation between adjacent bands varies from 7 Å to 14 Å. Adjacent bands exhibit an antiparallel alignment, with peaks aligned with neighboring valleys so that at the interface a zig-zag pattern emerges. Scale bars represent 5 nm and 8 Å, respectively.

a banded internal structure. And Figure 2.2d identifies a 5 Å corrugation along the direction of the bands. Dynamics obtained from continuous AFM imaging in Figure 2.2e-f provide evidence for epitaxial growth, compared to deposition of fully formed fibers from solution. The same area has been imaged 3 min apart and clearly identifies the growth of the fibers at the mica-liquid interface. The growth rate of the fiber on the left is found to be approximately 7 nm min^{-1} . Interestingly, not all fibers show continuous growth. The reason for this is most likely related to the internal configuration around the endpoints. From Figure 2.2c it can be seen that the banded structure within the fiber has discontinuities. It is speculated that these discontinuities are local points of disorder and that when such disordered segments are located at the endpoints of the fiber, this can frustrate the attachment of additional peptides.

When the peptide concentration in solution is increased from 0.1 mM to 0.8 mM, the peptide assemblies at the mica-liquid interface form a full coverage, as is shown in Figure 2.3a. Here, AcFA₅K at 0.8 mM in 50/50 H₂O/MeOH is imaged *in situ* at the mica-liquid interface within 15 min after the peptides have come in contact with the substrate. Figures 2.3b and c show that the height and periodicity of these close-packed fibers is similar to what has been observed at lower concentrations. High resolution AFM phase contrast images in Figures 2.3d-e again show an internal periodicity of 5 Å along the direction of the fibers. Furthermore, adjacent bands show an interdigitated arrangement, such that the interface between two bands resembles a zig-zag pattern. The distance between bands varies from 7 Å to 14 Å, which is consistent with the distance between adjacent bands in Figure 2.2d.

In Figure 2.2a, the peptide assemblies were oriented at 60° angles with respect to one another. This pattern is not clearly visible at these elevated concentrations. This can either be due to

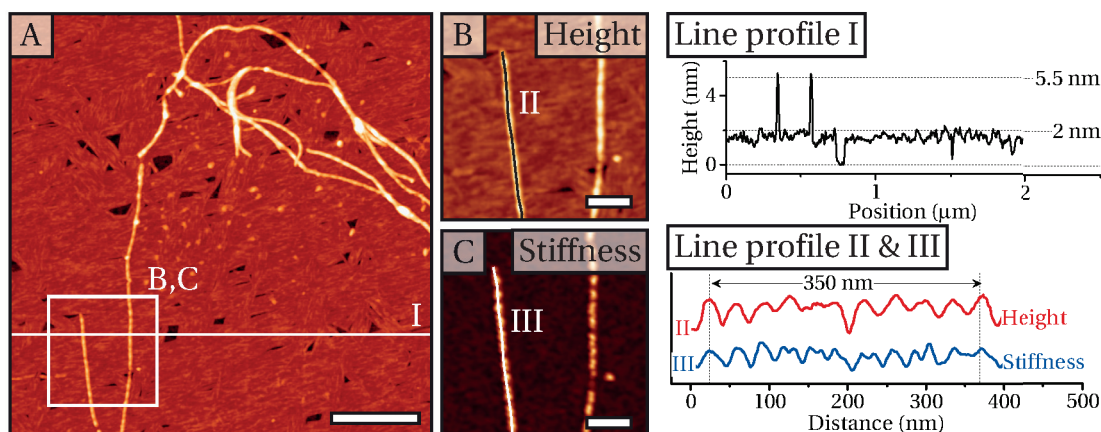


Figure 2.4 – The self-assembly of AcFA₅K at the mica-air interface, imaged with *ex situ* AFM. Mica is exposed to AcFA₅K at 0.8 mM in 50/50 volume ratio H₂O/MeOH. The solution is then evaporated in a semi-closed container over the course of several days. (a) The peptide fibers at the mica-air almost completely cover the mica surface, similar to Figure 2.3a. Flexible bundles have been deposited on top of the ordered sublayer. Line profile I shows that the height of the bundles is about double that of the ordered sublayer. The scale bar represents 400 nm. (b-c) There is a periodic corrugation with a period of about 35 nm in both height and stiffness along the length of the bundles. The scale bars represent 100 nm.

a more pronounced oriented growth at these higher concentrations, or, alternatively, due to re-alignment that occurs once the assemblies have formed. Unfortunately, the growth rate of the AcFA₅K assemblies is too fast at these concentrations to properly observe this process *in situ*.

In order to determine the stability of the AcFA₅K fibers *ex situ*, AcFA₅K at 0.8 mM in 50/50 H₂O/MeOH is deposited on a mica substrate, after which the solvent is evaporated over the course of several days. *Ex situ* AFM imaging shows that self-assembled fibers at the mica-liquid interface remain stable when the solution is removed, as shown in Figure 2.4.

Figure 2.4a shows that on top of the close-packed layer of well-aligned fibers, bundles are present that generally are both longer and more curved than the rigid fibers underneath. Line profile II in Figure 2.4b shows that these larger bundles have a periodic corrugation with a period of about 35 nm in their height. Line profile III in Figure 2.4c shows that the same periodic corrugation is observed in the 2D stiffness map of the same area. Similar periodically corrugated fibers have been reported by Adamcik et al. and were found to be indications for a double stranded coiled fiber^[142]. This corresponds well with the observation that these coiled fibers are twice as tall as the aligned rigid fibers at the mica surface. The fact that only a few bundles are observed, even after several days of incubation, indicates that fiber formation in solution is substantially slower than epitaxial growth at the mica-liquid interface.

Self-assembly at the HOPG-liquid interface

Similar to the preparation procedure for mica substrates, *Scotch magic* tape is used to remove

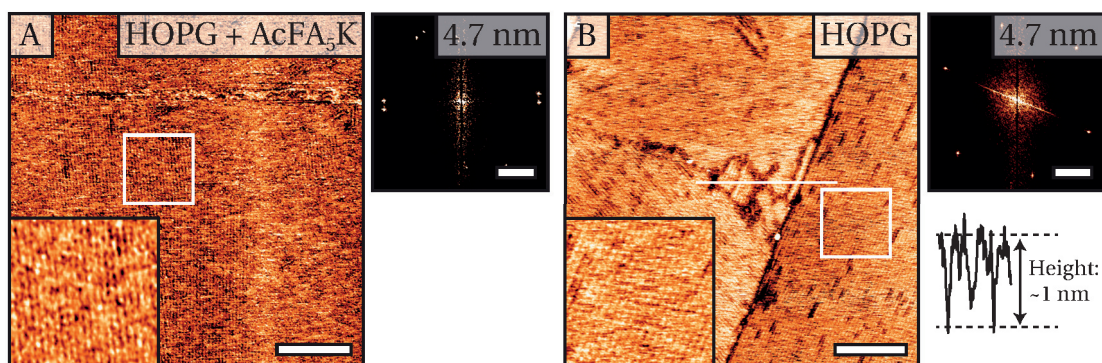


Figure 2.5 – A comparison between *in situ* AFM images of the HOPG-liquid interface with and without AcFA₅K peptides in solution. **(a)** In the presence of AcFA₅K at 0.8 mM, a line pattern is visible at the HOPG-liquid interface. A 2D fourier transform shows four distinct orientation, all with a periodicity of 4.7 nm and oriented at a 60° angle with respect to one another. Furthermore, there seem to be two sets of aligned lines, which are oriented at a 6° with respect to each another. Scale bars represents 100 nm and 0.1 nm⁻¹ respectively. **(b)** In the absence of any peptides, the same line pattern can be resolved at the HOPG-liquid interface. The height of the structures is about 1 nm. Scale bars are the same as in (a).

the top layer of the HOPG sample to obtain atomically flat and pristine substrates. Pristine HOPG does not have any functional groups which can dissociate in solution and has therefore a very low surface charge. Consequently, the HOPG surface is naturally hydrophobic.

AcFA₅K at 0.1 mM in 50/50 volume percentage H₂O and MeOH is deposited on a freshly cleaved HOPG substrate. Analysis of the resulting *in situ* AFM topography and phase contrast images in Figure 2.5 shows extended linear patterns at the HOPG-liquid interface. Careful comparison with HOPG imaged in the absence of any peptides suggests that these patterns cannot be composed of AcFA₅K, as the same linear line patterns are observed on bare HOPG. Similar patterns at the HOPG surface have been reported before and it has been suggested that these patterns are in fact regularly ordered gas molecules of atmospheric O₂ and N₂ adsorbed at the hydrophobic HOPG-liquid interface^[143–150]. The patterns remain present when the solution is removed by evaporation or when peptides are deposited in by ES-IBD in the absence of a solvent. For additional experimental data on the HOPG-liquid interface in the presence of AcFA₅K peptides, the reader is referred to appendix C.

When the H₂O/MeOH solvent is allowed to evaporate over the course of several hours, the peptide concentration continuously increases, until no solvent remains and the peptides have been adsorbed at the HOPG surface. The resulting structures at the HOPG-air interface can be imaged by low-force *ex situ* AFM, as shown in Figure 2.6. It shows that under these conditions the peptides assemble into small rigid rods that, at first sight, are very similar to the fibers observed at the mica-liquid interface in Figure 2.2 and 2.3. However, a careful comparison shows that the height of the rods at the HOPG-air interface is 13 Å. Significantly lower than the 20 Å height of the fibers at the mica-liquid and mica-air interface.

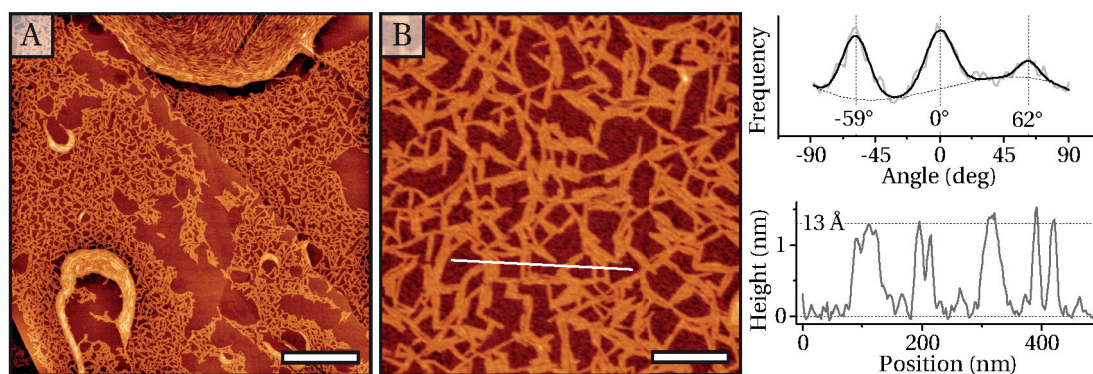


Figure 2.6 – The self-assembly of AcFA₅K at the HOPG-air interface imaged with *ex situ* AFM. HOPG is exposed to AcFA₅K at 0.8 mM in 50/50 volume ratio H₂O/MeOH. The solution is then evaporated in a semi-closed container over the course of several days. **(a)** Rigid rods are found at the HOPG-air interface, either in a close or open packed configuration. The scale bar represents 1 μm . **(b)** A Fourier component analysis clearly shows that the rods within the open packed configuration have three preferential orientations with a 60° difference. The height of the structures is about 13 Å, significantly lower than the fibers that formed at the mica-liquid interface. Scale bar represents 200 nm.

A thorough discussion of the structural details is given in section 2.4, within the context of the other structures that will be presented further in this chapter.

2.1.2 Self-assembly at the solid-air interface

To investigate the role of the solvent in the self-assembly of peptides at the solid interface, the previously described drop casting method is compared with ES-IBD deposition, where individual peptides are deposited individually in the absence of a solvent^[109].

ES-IBD deposition uses an electric field in combination with ion optics and as such requires charged molecules^[109]. This makes it difficult to deposit the peptides at neutral pH conditions, because in that case, the negatively charged carboxyl group in combination with the positively charged amino group would make for a neutrally charged peptide. At low pH conditions however, the peptide as a whole is positively charged^[23].

A non-conductive surface will turn into a capacitor when charged molecules are deposited at its surface. Thus, the accumulated charge will prevent the deposition of additional molecules. This means that only conductive substrates can be used for ES-IBD deposition. It is therefore impossible to directly compare ES-IBD deposition and drop casting on mica substrates. Instead, ES-IBD deposition is limited to conductive HOPG substrates. Note that the conductive properties of HOPG will neutralize the charged peptides upon contact. Assuming the mass/charge ratio of the peptides is known, this makes it possible to determine the number of peptides that has been deposited. Here, a coverage of 17.5 pAh/mm² is used. With one charge per peptide and assuming a homogeneous coverage over the sample, this translates to about 4×10^5 peptides/ μm^2 . Using a rough estimate of the surface area per peptide of 1.5 nm², this

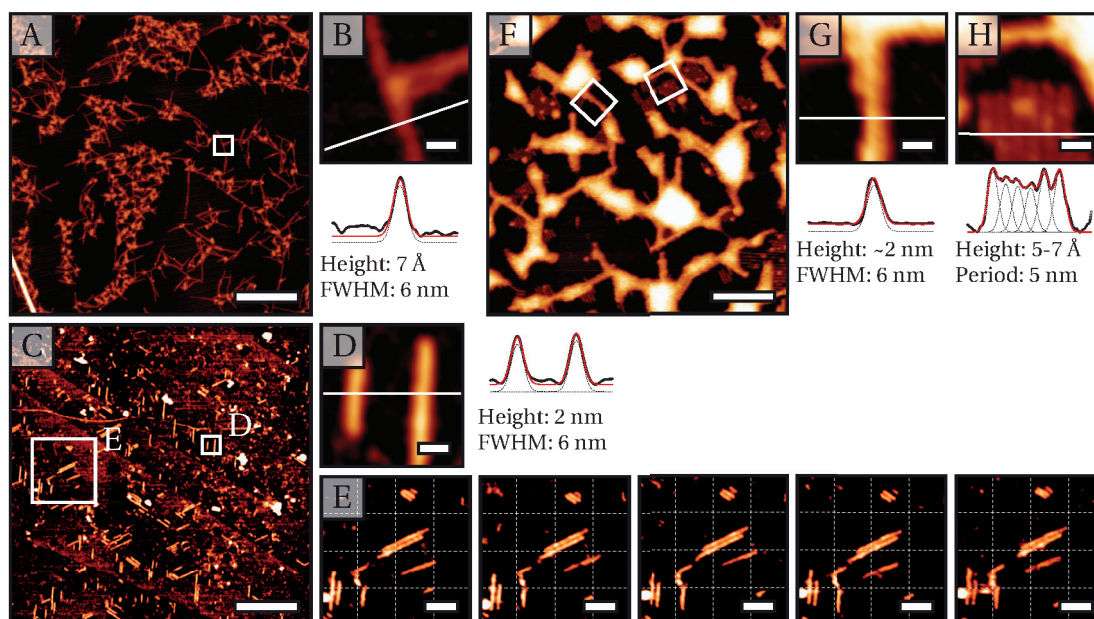


Figure 2.7 – Supramolecular structures formed by AcFA₅K peptides at the HOPG surface. (a) AcFA₅K has been deposited at the HOPG-vacuum interface by ES-IBD. The sample is then transferred out of the HV deposition chamber and imaged *ex situ* with AFM. Globular deposits are connected by rigid fibers. The scale bar represents 200 nm. (b) The rigid fibers have a height of 6 nm and apparent width of 0.7 nm. The scale bar represents 10 nm. (c) The peptide structures at the HOPG-air interface are immersed in 50/50 H₂O/MeOH and imaged at the HOPG-liquid interface using *in situ* AFM. Neither globular deposits nor connecting fibers are stable at the HOPG-liquid interface. Instead, small rigid rods are present with a typical height and apparent width of 2 nm and 6 nm, respectively. Scale bars are the same as in (a-b). (e) Continuous *in situ* AFM with 9 min between consecutive frames. Whereas some rods are slightly mobile at the HOPG-liquid interface, none of the rods shows growth. The scale bar is 40 nm. (f-h) The solvent is removed through controlled evaporation over the course of several days. The resulting HOPG-air interface is imaged *ex situ* with AFM. Now, both low (0.7 nm by 6 nm) and high (2 nm by 6 nm) structures are present simultaneously. Scale bars represent 100 nm and 10 nm, respectively.

corresponds to a surface coverage of about 60 %.

Mass/charge selection, in combination with a soft landing, ensures that only individual and intact peptides reach the HOPG-vacuum interface. After the peptides have been deposited, the sample is transferred out of the HV deposition chamber and imaged in air using *ex situ* AFM, as shown in Figure 2.7a-b.

Figure 2.7a shows that the atomically flat HOPG surface is covered in structures that can only be composed of AcFA₅K. Two different features can be distinguished, i.e. straight and rigid fibers are connected by taller and more globular structures. The height profile in 2.7b shows that the rigid fibers have a height of about 7 Å, with an apparent width of about 6 nm. As the apparent width is a convolution between the actual width of the structure with the radius of

Chapter 2. Self-assembly of small peptides at the solid-liquid and solid-vacuum interface

curvature of the tip, it is expected that the actual width is slightly less.

The straight and rigid fibers are much larger than individual peptides, and their uniform width and height therefore indicate a specific internal structure. It is interesting to note that the dimensions are clearly different from the peptide assemblies on mica, indicating that the presence of a solvent has a significant impact on the self-assembly.

It was previously found that self-assembled structures of AcFA₅K at the mica-liquid interface were found to be stable, both *in situ* and *ex situ*. Furthermore, no AcFA₅K self-assembly was observed at the HOPG-liquid interface. Surprisingly, Figures 2.7a and b indicate that ES-IBD does result in AcFA₅K self-assembly at the HOPG-air interface. Furthermore, the resulting structures are markedly different from the self-assembled structures found on mica.

The following experiments are designed to learn more about these structures and to determine their stability in the presence of a solvent.

The AcFA₅K peptides that were deposited with ES-IBD onto the HOPG-vacuum interface are covered in a droplet that contains 50 % H₂O and 50 % MeOH. The HOPG-liquid interface is imaged *in situ* using AFM.

In Figure 2.7c-d, *in situ* AFM imaging at the HOPG-liquid interface shows that the pre-existing ES-IBD AcFA₅K assemblies underwent a conformational change from a low configuration of 7 Å, as shown in Figure 2.7b, to a high configuration of 2 nm, as shown in Figure 2.7d. The structures that are present at the HOPG-liquid interface have dimensions that are similar to what has been observed at the mica-liquid and mica-air interfaces in Figure 2.2 and 2.4, respectively. This strongly suggests that both structures have similar internal conformations. As mentioned before, direct drop casting on HOPG does not result in AcFA₅K self-assembly at the HOPG-liquid interface. Therefore, the presence of peptide assemblies here must be related to the ES-IBD deposition that preceded the addition of liquid. Although peptides do not spontaneously adsorb to the HOPG-liquid interface, these results show that pre-existing peptide structures at the HOPG-air interface undergo a conformational change in contact with solution and remain stable at the HOPG-liquid interface.

The fact that the peptide fibers at the mica-liquid and HOPG-liquid interface seem to be identical, makes it interesting to compare their dynamics as well. In order to probe the dynamics of the AcFA₅K assemblies at the HOPG-liquid interface, the surface is imaged continuously with *in situ* AFM. The results in Figure 2.7e show that, in contrast to what has been found at the mica-liquid interface, some of the rigid structures are mobile at the HOPG-liquid interface. The main difference between the mica-liquid and HOPG-liquid interface is the strong surface charge, and therefore hydrophilic properties, of the mica substrate. The mobility of the peptide fibers at the HOPG-liquid interface therefore suggests that the strong negative surface charge of mica facilitates a stronger physisorption, compared to HOPG.

In order to determine whether the peptide assemblies at the HOPG-liquid interface are stable *ex situ*, the solvent is removed through controlled evaporation in atmospheric conditions over the course of several days. The resulting HOPG-air interface is imaged using *ex situ* AFM. The results in Figure 2.7f-h show that two different kind of structures are now present at the

2.2. Internal factors: Charge and internal structure of the peptide

HOPG-air interface. 2 nm High rod-like fibers, associated with peptide self-assembly at the solid-liquid interface (2.7g), and 7 Å high rod-like fibers, associated with peptide self-assembly at the HOPG-air interface after ES-IBD (2.7h). These results show that both structures remain stable *ex situ*.

The results presented in this section used a unique combination of high resolution *in situ* AFM to study self-assembly at the solid-liquid interface, and ES-IBD with *ex situ* AFM to study the self-assembly at the solid-air interface. This enabled a direct comparison of the same peptide in a variety of local environments, i.e. mica-liquid, mica-air, HOPG-liquid and HOPG-air.

The self-assembly of AcFA₅K at the mica-liquid interface results in fibers with a uniform height of 2 nm and a width of 5 nm to 6 nm, with an internal corrugation of 5 Å parallel to the fiber direction. These structures remain stable once the solvent is removed.

On HOPG however, the self-assembly depends strongly on the presence of a solvent during deposition and re-assembly of the peptides. Deposition using ES-IBD initially results in fibers with a height of 6 Å to 7 Å and width of 5 nm to 6 nm. Subsequent exposure to solution triggers a conformational change into fibers that are similar to what has been observed at the mica-liquid interface with a height of 2 nm and width of about 6 nm. When peptides are deposited at the HOPG surface through drop casting with subsequent drying, the resulting peptide assemblies are 13 Å in height.

2.2 Internal factors: Charge and internal structure of the peptide

Self-assembly is governed by external factors such as substrate and solvation, which are explored in the previous section, as well as by internal factors such as the structure of the molecule itself. Due to their modular nature it is possible to precisely control the internal structure of peptides.

In this section, the influence of the internal structure of the peptide on the self-assembly behavior is explored. Both by directly changing the order and presence of the lysine residue and by changing the charged state of the amine and carboxyl functional groups.

2.2.1 The presence and position of the lysine residue

At near neutral pH, the AcFA₅K peptide has both a positive and negatively charged group near the C-terminus. In contrast, AcFA₆ has only a negatively charged group at the C-terminus. AcKFA₅ has both positive and negative groups, but at opposing ends of the peptide backbone.

In Figure 2.8, the self-assembly at the mica-liquid interface of all three different peptides is presented. For AcFA₅K and AcFA₆, the self-assembly at the HOPG-air interface is compared as well.

The self-assembly at the HOPG-air interface is identical for both AcFA₅K and AcFA₆. The difference in coverage between Figure 2.8d and 2.8e is due to fact that ES-IBD results in an inhomogeneous coverage that decreases towards the edge of the ion beam. Figure 2.8d is

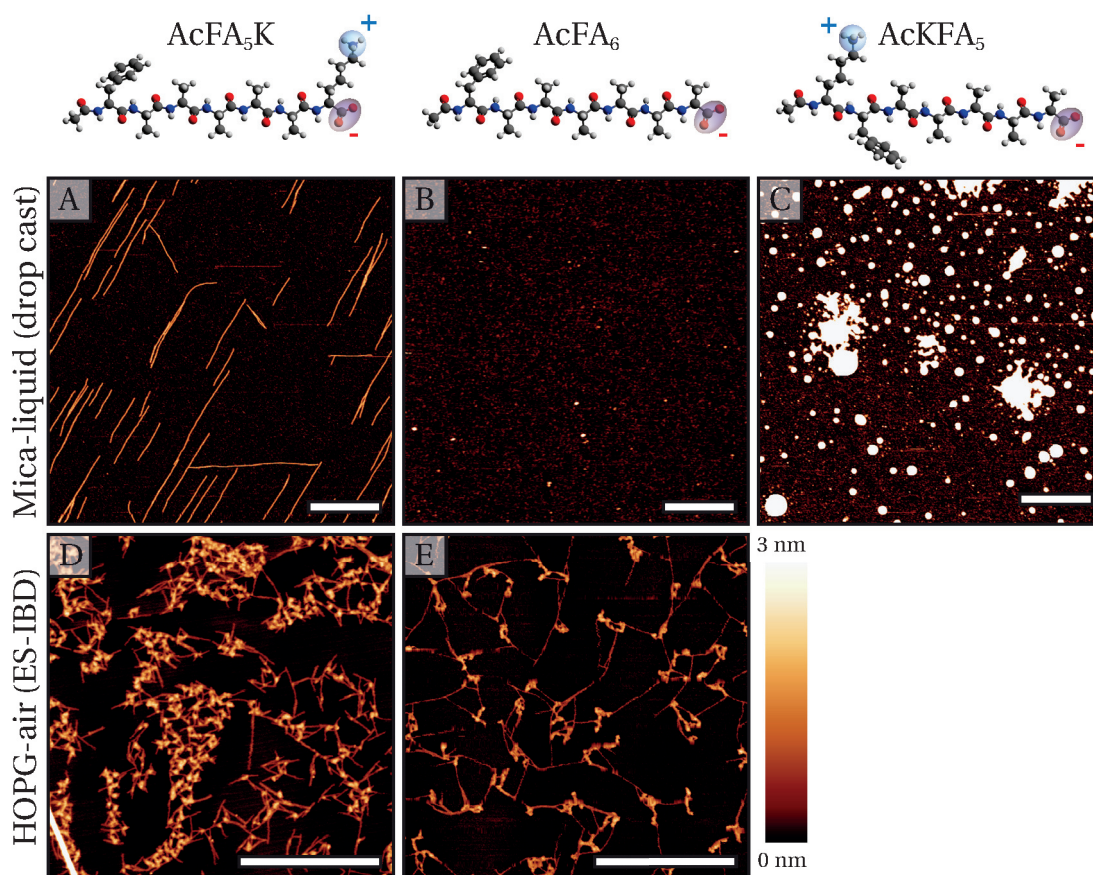


Figure 2.8 – Self-assembly of AcFA₅K, AcFA₆ and AcKFA₅ at the mica-liquid and HOPG-air interface, imaged with *in situ* and *ex situ* AFM, respectively. (a) AcFA₅K at 0.1 mM in 50/50 volume percent H₂O/MeOH forms regular fibers at the mica-liquid interface, which are oriented along the underlying mica lattice. (b) AcFA₆ at 0.1 mM in 50/50 volume percent H₂O/MeOH does not assemble at the mica-liquid interface. (c) AcKFA₅ at 0.1 mM in 50/50 volume percent H₂O/MeOH forms globular assemblies at the mica-liquid interface. Scale bars in (a)-(c) represent 400 nm. (d) AcFA₅K deposited using ES-IBD forms a semi-organized network at the HOPG-air interface. The network is composed of globular nodes and connecting fibers that are aligned along the underlying HOPG atomic lattice. (e) The self-assembly of AcFA₆, when deposited using ES-IBD at the HOPG-air interface, is similar to that of AcFA₅K. Scale bars in (d) and (e) represent 200 nm. Color scale is as indicated and equal in all images.

located closer to the respective center of the ion beam than Figure 2.8e.

In contrast, the self-assembly at the mica-liquid interface is markedly different for AcFA₅K and AcFA₆. Where AcFA₅K forms long fibers, AcFA₆ shows no sign of any self-assembly at all. Because the only difference between these peptides is the presence of the lysine residue with its positive charge, these results suggest that it is the positively charged amine group that drives adhesion and self-assembly at the mica-liquid interface.

Lastly, the mica-liquid interface in the presence of AcKFA₅ shows large globular structures that do not seem to have any internal structure. This is in line with conclusions of Stearns

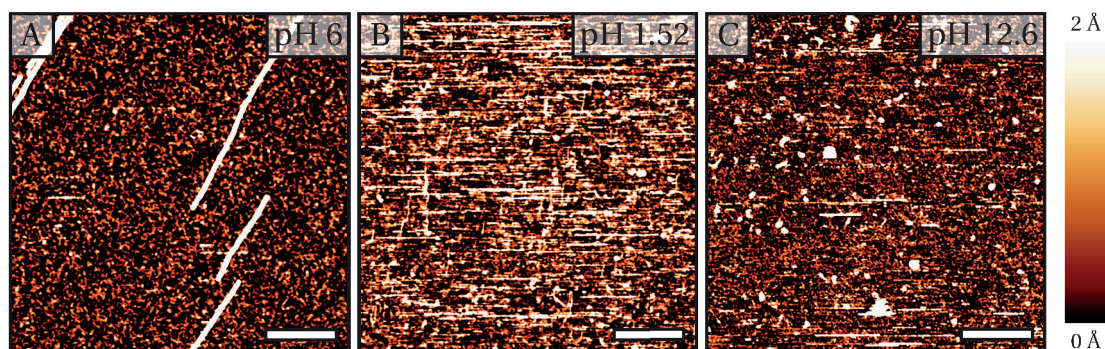


Figure 2.9 – Self-assembly of AcFA₅K at 0.1 mM at the mica-liquid interface under different pH conditions. Imaged with *in situ* AFM. (a) At near neutral pH 6.0, the AcFA₅K peptides form fibers, as is described previously. (b) At pH 1.52, no such assemblies are observed, and instead small ribbon-like structures are observed at the mica-liquid interface. (c) At pH 12.6, there is less adsorption of individual AcFA₅K peptides at the mica-liquid interface, as is indicated by the smoother background. However, globular structures are present at the mica-liquid interface. Scale bars represent 100 nm and the color scale is as indicated and equal in all images.

et al.^[22], which state that the lack of a lysine residue at the C-terminus results in a globular conformation in the gas phase. It is thus suggested that AcKFA₅ is globular or transient in solution, which would prevent a directional self-assembly and instead would drive the adsorption into amorphous structures at the mica-liquid interface. This is consistent with the structures observed in Figure 2.8c.

2.2.2 The charge states of the lysine residue

The different pK_a values of the carboxyl and amino groups within the AcFA₅K peptide (~ 2.5 and ~ 10.8, respectively^[23]) mean that the charged state of the peptide can be influenced by adjusting the pH of the surrounding H₂O/MeOH solution. It must be noted that this invariably changes the surface charge of the mica substrate as well. Negatively charged surface sites are in equilibrium with cations and protons in solution, and as such are subject to bulk concentrations of the species. This behavior is reflected in a pK_a value of 2.94 for mica^[151]. The pK_a of mica and the carboxyl groups within the AcFA₅K peptides are similar and therefore both carboxyl groups and substrate will be neutrally charged at pH < 2.

In Figure 2.9a, the self-assembly of AcFA₅K at the mica-liquid interface is imaged under near neutral conditions at pH 6, at acidic conditions (pH 1.52) in Figure 2.9b and at basic conditions (pH 12.6) in Figure 2.9c.

Interestingly, structured self-assembly into fibers was only observed at neutral pH where both amine and carboxyl groups are charged, Figure 2.9a.

At acidic conditions, shown in Figure 2.9b, the AcFA₅K peptide is positively charged. Neither globular nor fiber-like structures are present at the mica-liquid interface. This can be explained

Chapter 2. Self-assembly of small peptides at the solid-liquid and solid-vacuum interface

by the fact that the lack of both positively and negatively charged groups within a single AcFA₅K peptide prevents intermolecular ionic interactions. Furthermore, in an acidic environment, the mica surface assumes a more neutral surface charge^[151], which limits the ionic interaction between the mica surface and the positively charged AcFA₅K peptides. The resulting higher mobility of peptides at the mica-liquid interface is observed as a more noisy background compared to either pH 6 in 2.9a or pH 12.6 in 2.9c.

At basic conditions, where both the mica substrate and the AcFA₅K peptide are negatively charged, globular structures are present at the mica-liquid interface. The negative charge of the peptide prevents both intermolecular assembly and adsorption to the mica substrate. The lack of adsorption is observed as a smoother background compared to pH 6 in 2.9a or pH 1.52 in 2.9b. The observation of globular deposits at pH 12.6 indicates the formation of non-organized peptide aggregates.

2.3 Thermal stability of peptide assemblies

Additional experiments were performed to assess the stability of the peptide assemblies. The thermal stability of fibers at the mica-air interface is compared with fibers at the HOPG-air interface.

2.3.1 Thermal stability at the mica-air interface

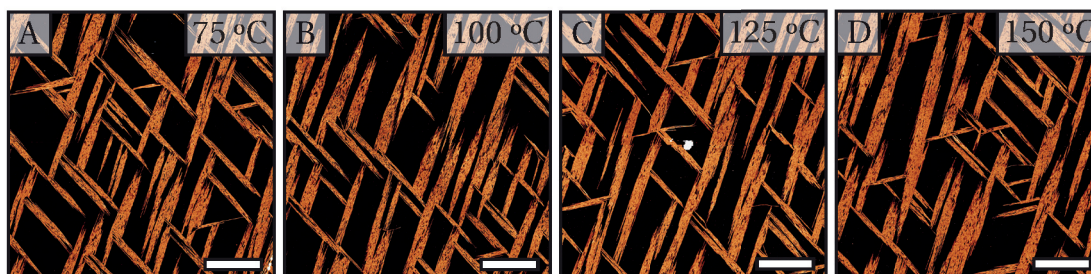


Figure 2.10 – AcFA₅K supramolecular assemblies imaged with *ex situ* AFM. Mica substrates are exposed to a solution containing AcFA₅K at 0.8 mM in 50/50 volume ratio H₂O/MeOH, after which the solvent is allowed to evaporate within a laboratory atmosphere. The mica sample is subsequently heated incrementally to 75 °C, 100 °C, 125 °C and 150 °C. After the required temperature is reached, it is maintained for 15 min. The sample is then cooled to room temperature and imaged *ex situ*. All scale bars represent 1 μm.

The preparation of peptide assemblies at the mica-air interface followed a drop casting procedure of AcFA₅K at 0.8 mM in 50/50 volume ratio H₂O/MeOH, with subsequent evaporation of the solvent. An area of the sample was selected where the peptide structures did not fully cover the surface so that possible lateral movement due to an increased mobility could easily be observed.

The samples were heated incrementally to 75 °C, 100 °C, 125 °C and 150 °C. Once the required temperature was reached this was maintained for 15 min, after which the sample was cooled

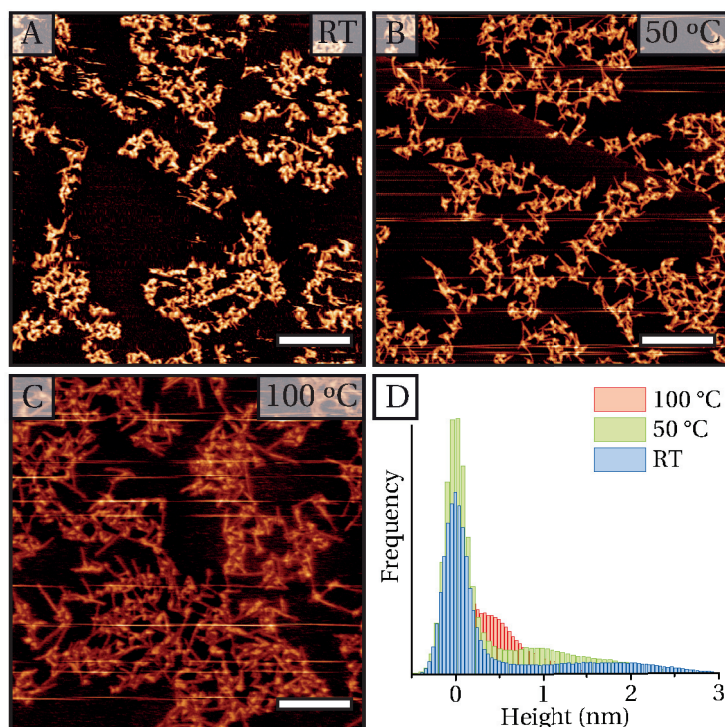


Figure 2.11 – Thermal stability of AcFA₅K at the HOPG-air interface, imaged with *ex situ* AFM. (a) AcFA₅K is deposited onto HOPG substrates using ES-IBD to reach a coverage of 7.5 pA/mm². (b) The sample is subsequently heated to 50 °C for 30 min and imaged at RT. (c) The sample is heated again to 100 °C for 30 min and imaged at RT. Images (a)-(c) are taken within 100 μm of one another, so that the coverage can be considered equal. (d) The histogram shows that the increased temperature results in the decrease of tall structures, in favor of low structures. Furthermore, the rod-like structures increase in length when heated. The scale bars represent 200 nm.

to RT and imaged *ex situ* using AFM as shown in Figure 2.10. Due to the fact that the samples were positioned manually, the exact location of the four measurements is different.

As can be seen in Figure 2.10, the general structure of the peptide assemblies at the mica-air interface remains the same, even after heating to 150 °C. Neither the coverage nor the alignment of the fibers is affected by the increased temperature.

2.3.2 Thermal stability at the HOPG-air interface

Similar to the samples shown in Figures 2.7a and 2.8d-e, AcFA₅K peptides were deposited at the HOPG-vacuum interface by ES-IBD to reach a coverage of 7.5 pA/mm². The samples were subsequently transferred to ambient conditions and imaged with AFM *ex situ*, see Figure 2.11. The thermal stability of these assemblies was determined by controlled sequential heating to 50 °C for 15 min, 70 °C for 15 min and lastly to 100 °C for 30 min. In between each heating cycle, the HOPG substrate was cooled to room temperature and imaged *ex situ* with AFM. The

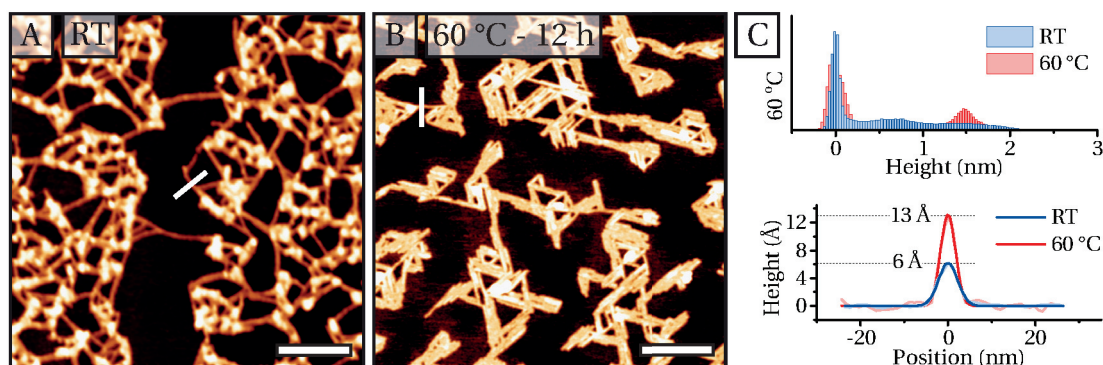


Figure 2.12 – Thermal stability of AcFA₅K at the HOPG-air interface. AcFA₅K is deposited onto HOPG substrates using ES-IBD to reach a coverage of 5.6 pA/mm² and imaged with *ex situ* AFM at RT in (a). In (b), the sample is heated to 60 °C for 12 h. Images are taken within 100 μm of one another so that the coverage can be considered equal. (c) The histogram and line profiles show that after the annealing procedure, the structures in (b) all have comparable heights, which is double that of the rod-like structures in (a). The scale bars represent 100 nm.

images obtained before heating, after heating to 50 °C and after heating to 100 °C are shown in Figure 2.11a-c.

As described before, the AcFA₅ assemblies at the HOPG-air interface are composed of two distinct structures, i.e. globular deposits that are connected by rigid nanofibers. Sequential heating to a maximum of 100 °C shows that the increased temperature and associated mobility at the HOPG-air interface resulted in both a reduction in globular deposits and an increase in the length of the nanofibers. This is reflected in the histogram in Figure 2.11d, and suggests a direct transformation from a disordered to an organized structure.

From Figure 2.11c it can be seen that although the sample is heated to 100 °C for 30 min, globular deposits remain present at the HOPG-air interface. This suggests that the transformation to the rigid nanofiber structures was not yet complete. For this reason, a second series of experiments was performed. A similarly prepared substrate (Figure 2.12a) is now heated to 60 °C for up to 12 h.

The results shown in Figure 2.12b show that this procedure resulted in the complete removal of globular deposits. Only rigid and well-aligned nanofibers are observed at the HOPG-air interface. The histogram in 2.12c shows that the fibers are nearly identical in height and a comparison between line profiles of the rigid fibers before and after the annealing procedure shows that the fibers after annealing have doubled in height. Furthermore, the orientation along three principal axes that are separated by almost exactly 60° suggests an alignment along the underlying HOPG atomic lattice.

Interestingly, a comparison between Figures 2.12b and 2.6b shows that the structures that form at the HOPG-air interface after ES-IBD deposition with subsequent annealing are nearly identical to the ones that form at the HOPG-air interface after drop casting with subsequent evaporation of the solvent. Both structures show an alignment along three principal axes with

a 60° angle separation and both are about 13 Å in height.

The observation in Figure 2.12 of a direct transformation from 6 Å high fibers to 13 Å high fibers, strongly suggests that the 13 Å fibers are in fact composed of two layers. The next section contains a more thorough analysis of this transformation, see also Figure 2.13a-b.

2.4 Proposed model for the self-assembly of AcFA₅K

As detailed in Figure 2.1, the length of the AcFA₅K peptide in a helical conformation is about 17 Å, whereas the fully extended conformation is about 25 Å.

The experimental data presented in this chapter clearly shows that individual peptides self-assemble into extended structures. One of the most common structures for peptide assemblies are β -sheets. They form when individual peptides, in an extended configuration, are connected laterally through hydrogen bonds between the N-H and C=O groups of neighboring peptides. Depending on the configuration of the side chains, a typical β -sheet adsorbed at an interface has a height of 6 Å to 8 Å and the distance between two adjacent peptides within such a β -sheet is about 5 Å^[138].

Another common theme in peptide self-assembly in aqueous solution, is the segregation of polar and non-polar residues. This segregation drives the formation of micellar structures, which can take the form of tubes, cylinders or spheres, depending on the geometry of the peptides^[50].

The AcFA₅K and AcFA₆ assemblies at the HOPG-air interface in Figure 2.7a-b and 2.8d-e are all 6 Å to 7 Å high and about 6 nm wide. This corresponds well with two β -sheets arranged face-to-face, parallel to the surface. The uncapped -COOH C-terminus is likely involved in the previously mentioned face-to-face interactions, as the carboxyl group in one peptide can readily form hydrogen bonds with opposing carboxyl groups. This is not likely for the capped -CH₃ N-terminus. A schematic representation of such a β -sheet assembly is given in Figure 2.13a.

Results presented in Figure 2.12 show that when β -sheet ribbons at the HOPG-air interface are heated, their height doubles from 6 Å to 7 Å to 13 Å. Interestingly, this is exactly the same as what has been found for self-assembled structures of AcFA₅K at the HOPG-air interface after drop casting and subsequent evaporation of the solvent.

This suggest an internal structure that consists of two β -sheets on top of one another, as is schematically shown in Figure 2.13b. Such stacked β -sheet structures have been reported before, and are stabilized by formation of a hydrophobic core that shields the alaine and phenylalaine residues^[152].

The absence of such stacked β -sheets in Figure 2.7a-b, suggests that single layered β -sheets occupy a local energetic minimum. The presence of a solvent (Figure 2.6) or increased kinetic energy through heating (Figure 2.12) can overcome this energetic barrier and allow for the formation of the thermodynamically more favorable stacked β -sheet configuration.

The external dimensions of the peptide assemblies at the mica-liquid, mica-air and HOPG-

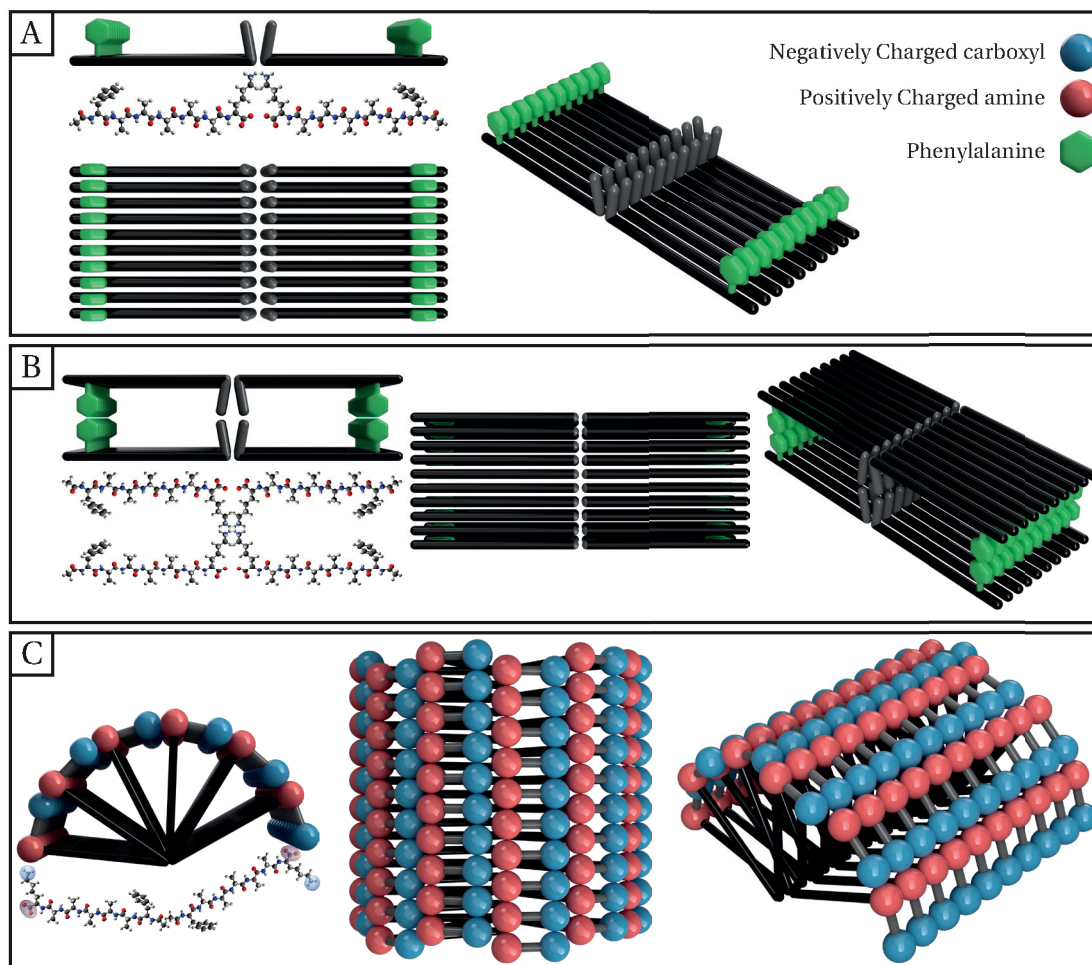


Figure 2.13 – Proposed model for the self-assembly of AcFA₅K at interfaces. **(a)** A schematic representation of the self-assembly of AcFA₅K at the HOPG-air interface. Two β -sheets are positioned such that hydrogen bonding between their C-termini is possible. The phenylalanine residues indicated in green further stabilize the β -sheet structure through $\pi - \pi$ stacking of the phenyl rings. **(b)** A double-layered structure that combines two structures such as shown in (a). The structure is stabilized by a hydrophobic core that consists of alanine and phenylalanine side chains. **(c)** A schematic representation of a half-cylindrical micelle at the solid-liquid interface. The positively and negatively charged groups are indicated by a red and blue sphere, respectively. β -Sheet formation stabilizes the structure in the lateral direction and the arrangement of β -sheets in a circularly stacked structure will stabilize the charged groups by combining them with opposing charges in the neighboring β -sheet. For simplicity, the phenylalanine residues are omitted from this schematic representation.

air interface are, with 2 nm high by 5 nm to 6 nm, significantly different from the previously described β -sheet structure. However, structures in Figure 2.2 and 2.3 show a 5 Å periodicity. This suggests the presence of β -sheets, which have a reported distance between adjacent peptides of about 4.5 Å to 5 Å^[136,138,153]. With 2 nm, the height of the structures is much more than the 6 Å to 8 Å expected for a single β -sheet parallel to the mica substrate^[138] and, instead,

2.4. Proposed model for the self-assembly of AcFA₅K

is similar to the length of a fully extended peptide. Furthermore, the observed epitaxial growth along the mica crystal lattice, suggests that the positively charged lysine residue binds to the negatively charged K⁺ vacancy in the mica crystal lattice^[132].

The proposed model in Figure 2.13c combines both the presence of β -sheet formation with the formation of half-cylindrical micelles. The hydrophilic head groups are directed toward the solvent, while simultaneously shielding the hydrophobic alanine and phenylalanine groups. Initial adsorption is triggered by the interaction of the positively charged lysine with the negatively charged lattice positions in the mica substrate. This is followed by the sequential adsorption of additional peptides until a half-cylindrical micelle has formed.

When individual β -sheets of AcFA₅K are considered, all positively charged amino and negatively charged carboxyl groups are stacked. Because the backbone of the lysine residue prevents these opposing charges from interacting, the electrostatic repulsion caused by the close proximity of identical charges has a destabilizing effect on the β -sheet. However, by adsorbing onto a negatively charged surface in the form of half-cylindrical micelles, the opposing charges are brought in close proximity to one another. This, in turn, stabilizes the individual β -sheets and the micellar structure as a whole.

This model is consistent with the observed self-assembly of AcFA₅K at extreme pHs in Figure 2.9. The absence of positive charges would make the C-terminus of the peptides negatively charged, whereas the absence of negative charges at the C-terminus would make it positively charged. In either case, this would prevent the ionic interaction between separate β -sheets. Indeed, no ordered peptide assemblies have been observed at the mica-liquid interface at either pH 1.52 or pH 12.6.

The comparison between AcFA₅K, AcFA₆ and AcKFA₅ further stresses the importance of both a positively and a negatively charged functional group at the same end of the peptide backbone. Only then can both surfactant-like and catanionic properties be combined.

In the case of AcFA₆, the peptide is surfactant-like due to the presence a distinct polar head and a non-polar backbone. However, the lack of positively charged functional groups prevents ionic interaction between peptides.

In the case of AcKFA₅, the peptide has both positive as well as negative charges. However, due to the placement of the lysine residue at the N-terminus, there is no distinct polar side to the peptide. Furthermore, the flexible nature of the alanine backbone makes it likely that the oppositely charged ends of the peptide can interact directly, resulting in a globular shape that would be incompatible with β -sheet formation.

During ES-IBD deposition, the peptides are initially positively charged. After adsorption on a grounded and conductive HOPG substrate, this charge is neutralized. This prevents any ionic interaction of the peptides and instead limits the self-assembly to simple β -sheet formation as discussed above and schematically represented in Figure 2.13a.

However, when these β -sheets are subsequently exposed to a H₂O/MeOH solution, some of the amine and carboxyl groups are expected to be protonated and deprotonated, respectively. Figure 2.7c-d indeed shows that ES-IBD deposition in combination with subsequent exposure

Chapter 2. Self-assembly of small peptides at the solid-liquid and solid-vacuum interface

to H₂O/MeOH solution results in structures at the HOPG-liquid interface that correspond with half-cylindrical micelles that are similar to what is observed at the mica-liquid interface. In Figure 2.5e-g the H₂O/MeOH solution has been removed through evaporation. The fact that now both β -sheet ribbons as well as cationic half-cylinders are present is consistent with the existence of two different self-assembly mechanisms. One that is stabilized by hydrogen bonding and $\pi - \pi$ stacking in the absence of solution, and one that includes ionic interactions due to the presence of charged functional groups in solution.

Self-assembly of AcFA₅K is readily observed at the HOPG-liquid interface after ES-IBD deposition, as shown in Figure 2.7c-d. This is not the case in Figure 2.5a, where direct drop casting is used. This suggests a requirement of initial direct adsorption to the substrate.

At the mica-liquid interface, this is facilitated by the ionic interaction between the positively charged lysine group and the negatively charged mica surface. At the HOPG-liquid interface, with prior ES-IBD of peptides at the HOPG-vacuum interface, this is facilitated by the presence of pre-existing of peptides in β -sheet formation, resulting from the ES-IBD. At the HOPG-liquid interface without prior ES-IBD deposition, neither mechanism is available and therefore no self-assembly takes place.

Interestingly, the work presented here shows a surprising lack of fully-cylindrical micelles. It can be speculated that the phenylalanine groups interact with one another through $\pi - \pi$ stacking, and as such would occupy a significant volume within the half-cylindrical micelles. This could frustrate the formation of fully cylindrical micelles.

2.5 Influence of metal ions on the self-assembly of AcFA₆ and AcFA₅K

In this section, the interaction between metal ions and self-assembling peptides is investigated. Metal-peptide complexes have gathered interest as model structures for metalloproteins, which are often the most efficient and selective catalysts available^{[130][131]}.

Combining within one system, the self-assembling properties of small peptides with the functionality of coordinated metal ions^[154], would open up possibilities for metal-organic complexes in solution or immobilized at the solid-liquid interface. In order to combine self-assembly with metal coordination, two approaches are explored.

From work done by Stearns et al.^[22], it is known that metal-peptide complexes composed of Na⁺ or Ca²⁺ with AcFA₆ are formed in the gas-phase. By introducing NaCl or CaCl₂ to a solution of AcFA₆, we aim to induce self-assembly of AcFA₆-Na or AcFA₆-Ca, similar to the self-assembly of AcFA₅K.

A different approach is to use AcFA₅K, which already has robust self-assembling properties, and include metal ions to this system. The metal ion Gadolinium(III) is chosen based on its large coordination number of 8-10^[155]. This means that Gd³⁺ can interact with multiple peptides at once, possibly enabling the formation of extended metal-peptide networks.

2.5.1 Self-assembly of AcFA₆ in the presence of Na⁺ and Ca²⁺

Following the model as shown in Figure 2.13c, the self-assembly of AcFA₅K at the mica-liquid interface is driven by ionic interactions between the individual peptides, which have both a positive and negative charge. In contrast, AcFA₆ only has a negative charge and as such does not exhibit self-assembly behavior at the mica-liquid interface.

In this section, it is explored whether the addition of positive charge to the AcFA₆ peptide will trigger self-assembly behavior similar to what has been observed for AcFA₅K. Gas-phase spectroscopy of AcFA₆ in the presence of Na⁺ as done in the group of Prof. Thomas Rizzo at the EPFL has indicated that AcFA₆-Na and AcFA₆-Ca complexes are stable in the gas-phase. Extrapolating these gas-phase observations to the solution phase, it is expected that positively charged Na⁺ and Ca²⁺ ions form complexes with AcFA₆ peptides, which have a negative charge at neutral pH. In the case for Na⁺, this would result in a neutral AcFA₆-Na complex. The double oxidation state of Ca²⁺ could result in either positive AcFA₆-Ca⁺ complexes or neutral AcFA₆-Ca-AcFA₆ complexes.

The self-assembly behavior of AcFA₆, AcFA₆Na and AcFA₆Ca at 0.1 mM in 50/50 H₂O/MeOH at the mica-liquid interface was compared. Apart from small globular features that are present regardless of the presence of metal ions, there are no self-assembling structures visible at the mica-liquid interface for pure AcFA₆, AcFA₆Na complexes or AcFA₆Ca complexes. From this, it can be concluded that the addition of positive charge to AcFA₆ in the form of separate charged ions is not sufficient to mimic the self-assembly behavior observed for AcFA₅K.

It is likely that the positively charged metal ions bind to the negatively charged C-terminus of the AcFA₆ peptide, thus forming globular complexes. This is different from AcFA₅K peptides, which are overall neutrally charged, but have distinct positively and negatively charged sites that are physically separated by the C6 lysine backbone. This suggests that the presence of distinct positive and negative sites is required for self-assembly.

2.5.2 Self-assembly of AcFA₅ in the presence of GdCl₃

In this section, it is explored whether existing peptide assemblies can be used to capture or incorporate metal ions, effectively creating peptide-metal complexes.

In Figure 2.14, AcFA₅K assemblies are formed *in situ* at the mica-liquid interface through drop casting of AcFA₅K at 0.8 mM in 50/50 H₂O/MeOH. The AFM liquid flow cell is then used to replace the solution with 50 mM GdCl₃ in 50/50 H₂O/MeOH. A sequence of images is created using continuous *in situ* AFM and reveals that the added GdCl₃ removes the pre-existing AcFA₅K assemblies. After about 1 h, all assemblies have been removed from the mica-liquid interface. The insets in Figures 2.14a,c show that as long as the peptide assemblies remain at the mica-liquid interface, their internal structure does not change.

The observation that the presence of Gd³⁺ ions can remove pre-existing AcFA₅K assemblies from the mica-liquid interface, either suggests that Gd³⁺ directly interacts with the AcFA₅K peptides and as such interferes with intermolecular interactions within the assemblies, or that

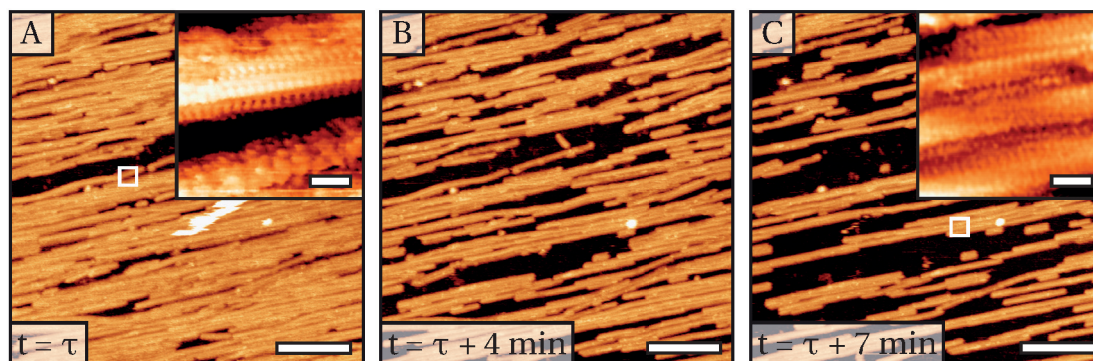


Figure 2.14 – *In situ* AFM shows how pre-existing assemblies of AcFA₅K peptides are removed from the mica-liquid interface in the presence of GdCl₃. (a) Exposure of a mica substrate to AcFA₅K at 0.8 mM in 50/50 H₂O/MeOH results in half-cylindrical micelles of AcFA₅K at the mica-liquid interface. The inset shows the typical 5 Å corrugation along the direction of the micelles. (b) Exposure of the pre-existing assemblies to GdCl₃ at 50 mM in 50/50 H₂O/MeOH results in the disappearance of the peptide assemblies from the mica-liquid interface. (c) The AcFA₅K assemblies continue to be removed from the mica-liquid interface in the presence of GdCl₃ at 50 mM. The inset shows that the internal structure of the remaining assemblies is not affected. The scale bars represent 50 nm and 2 nm, for the main images and insets, respectively.

Gd³⁺ competes with the AcFA₅K assemblies for adhesion to the mica substrate.

In Figure 2.15, both AcFA₅K at 0.6 mM and GdCl₃ at 50 mM in a 50/50 H₂O/MeOH solution are deposited simultaneously on a mica substrate. The solution is then removed through evaporation within a semi-closed container over the course of several days. The resulting structures that are observed at the mica-air interface are different from what was observed in the absence of GdCl₃, shown in Figure 2.3.

The overview in Figure 2.15a shows several different structures. Some of the tall and curved bundles that are sparsely covering the surface show a configuration in which a bundle intersects and curves over itself. This suggests that these structures were already fully formed before adsorption to the mica-liquid interface. Another feature that can be seen in Figure 2.15a is an almost complete coverage of the surface with a slightly curved line pattern. 2.15b shows that, surprisingly, this line pattern is present on top of the taller bundles. Furthermore, the fact that the lines within the line pattern do not intersect, suggests that they have formed at the solid-liquid interface and not in solution. Figure 2.15c shows that the line pattern consists of two distinct line structures. There are taller lines that are generally more continuous, and there are shorter lines that cover the majority of the mica surface. Note that the ‘empty’ space between the lines is too rough to be considered pure mica. For this reason, it is difficult to determine the absolute height of the lines. However, the height difference between the short and tall lines is approximately 7 Å. A 2D FFT of an area covered completely by the shorter lines, shown in 2.15d, indicates a line spacing of 4.2 nm. The width of the taller lines is approximately 5 nm.

2.5. Influence of metal ions on the self-assembly of AcFA₆ and AcFA₅K

In 2.15e, an ultra high-resolution AFM probe is used to determine the internal structure of the lines. Line profile I follows the length of the taller lines and shows an internal corrugation of 5 Å. This is exactly the same as what has been observed for the half-cylindrical micelles shown in Figure 2.13c. Surprisingly, line profile II, which follows the length of the shorter lines, shows an internal corrugation of 1 nm. This has not been observed in the absence of GdCl₃.

Figure 2.14 suggests that GdCl₃ either interacts directly with AcFA₅K assemblies, or that it replaces peptide assemblies at the mica-liquid interface. The observation of intact AcFA₅K assemblies in Figure 2.15 suggests that Gd³⁺ does not interact with AcFA₅K directly, but that, instead, the mica-Gd³⁺ interaction is preferred over mica-AcFA₅K interactions. This is consistent with the absence of alignment of the lines along the mica lattice, as seen in Figure 2.15c. The rod-like assemblies would not, in fact, interact with the mica substrate itself, but instead form on top of a layer of adsorbed Gd³⁺.

Figure 2.15b shows that the line pattern, which is formed at the solid-liquid interface, is deposited on top of the large AcFA₅K bundles, which are associated with bulk formation. This suggests a specific sequence of events, i.e. the adsorption of AcFA₅K bundles from bulk solution to the mica-liquid interface takes place before the formation of AcFA₅K structures at the solid-liquid interface. This suggests that the line pattern indicated by profile II is only formed when large AcFA₅K bundles have already been deposited at the solid-liquid interface, i.e. when most solvent has been evaporated and thus at extreme concentrations of AcFA₅K and GdCl₃.

Line profile I in Figure 2.15e indicates that the tall lines have the same internal structure as the half-cylindrical micelles that have been observed at the mica-liquid interface and are schematically shown in Figure 2.13c. The shorter lines are clearly different, with a lower height of 1.3 nm instead of 2 nm, smaller width of 4.2 nm instead of 5 nm and a larger internal corrugation of 1 nm instead of 5 Å. These structures have not been observed in the absence of GdCl₃ and therefore might represent AcFA₅K-Gd complexes. This is consistent with the conclusion that these structures only form at extreme concentrations of AcFA₅K, and only on top of Gd³⁺ that has been adsorbed to the mica-liquid interface beforehand.

In summary, the presence of GdCl₃ affects the self-assembly of AcFA₅K at the mica-liquid interface. When existing AcFA₅K assemblies are exposed to a solution containing GdCl₃, the assemblies disappear from the mica-liquid interface. In contrast, when a mica substrate is exposed to AcFA₅K and GdCl₃ simultaneously, novel assemblies are observed. The specific internal structure of these novel assemblies suggests the formation of AcFA₅K-Gd complexes.

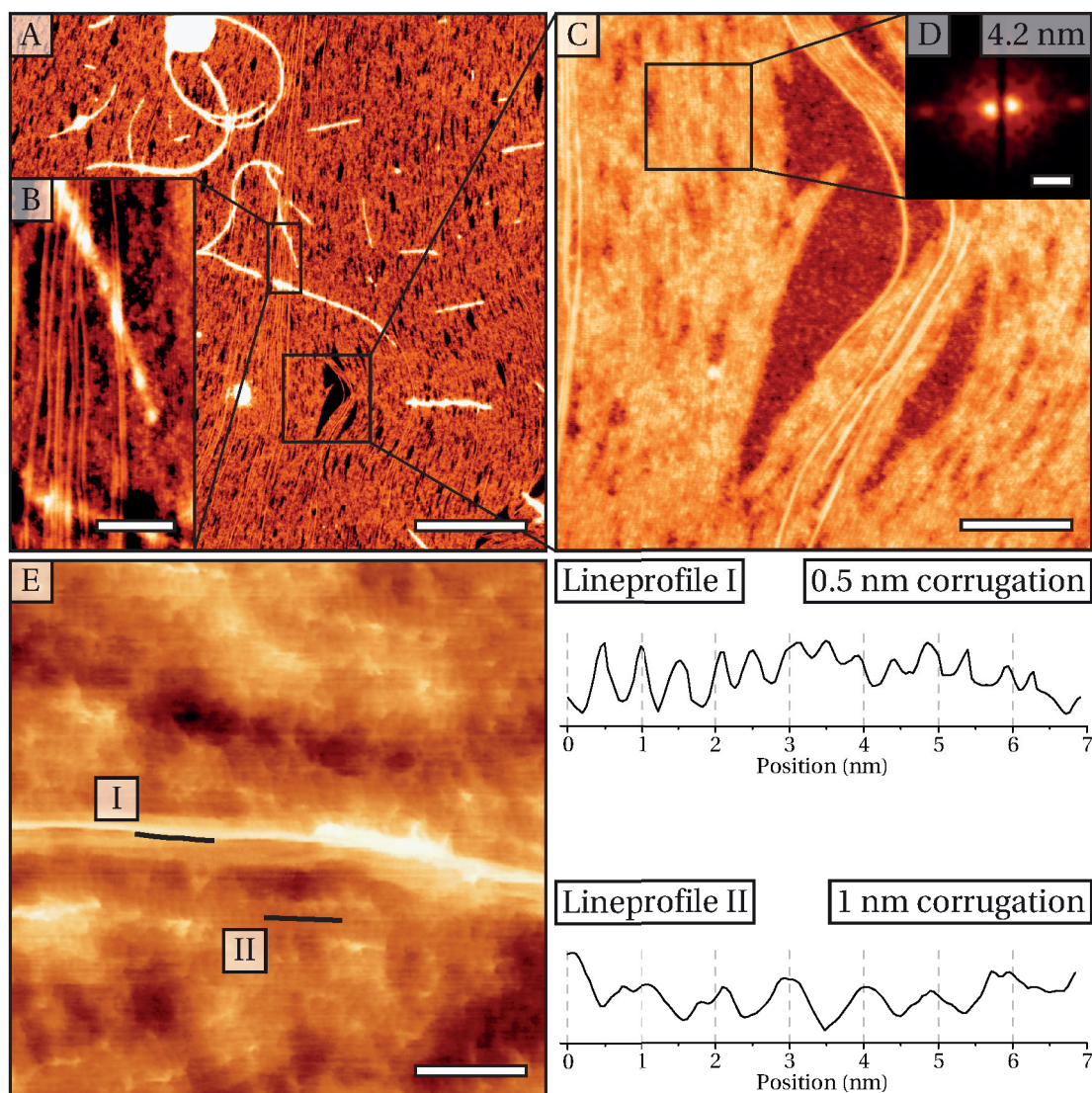


Figure 2.15 – *Ex situ* AFM images of the mica-air interface after simultaneous deposition on mica of AcFA₅K at 0.6 mM and GdCl₃ at 50 mM in 50/50 H₂O/MeOH. The solvent was slowly evaporated over the course of several days. (a) An overview of the mica-air interface shows the presence of different structures. Tall, curved bundles are present on the surface. Their curved and self-intersecting configuration suggests that the bundles were fully formed before adsorption to the mica-liquid interface. Additionally, a curved line pattern is visible across the whole surface. The scale bar represents 600 nm. (b) The inset shows that the curved line pattern is positioned on top of the taller bundles. The scale bar is 80 nm. (c) The curved line pattern is composed of two distinct line structures. Taller, continuous lines and shorter lines that cover the majority of the surface. The scale bar is 100 nm (d) A 2D FFT of an area covered by the short lines indicates a line spacing of 4.2 nm. The scale bar represents 0.12 nm⁻¹. (e) A high-resolution AFM probe is used to resolve the internal structure of the tall and short lines at the mica-air interface. For the taller lines, line profile I shows a corrugation of 5 Å, similar to AcFA₅K assemblies on mica in the absence of GdCl₃. However, line profile II shows that the shorter lines have an internal corrugation that is closer to 1 nm, which was never observed in the absence of GdCl₃. The scale bar is 10 nm.

2.6 Summary & Conclusions

Traditionally, ESI is almost exclusively used to bring large molecules in the gas-phase to study their properties, using UHV based techniques such as mass spectroscopy, IR spectroscopy^[21,22] and ion mobility techniques^[156]. All these techniques are limited in that they only probe the gas-phase conformation. ES-IBD has been developed to extend the functionality of ESI to include the deposition of large molecules at interfaces, where their collective self-assembly can be studied^[114]. To our knowledge, this work is the first example of a direct comparison between the gas-phase conformation (UHV) and the conformation of peptides within self-assembled structures at solid-air and solid-liquid interfaces.

At the HOPG-liquid interface, AcFA₅K peptides do not exhibit self-assembly. However, when the same AcFA₅K peptides are deposited at the HOPG-vacuum interface using ES-IBD, tightly packed β -sheets are formed. Subsequent heating of these β -sheets enables the relaxation into a thermodynamically more stable configuration, composed of two stacked β -sheets. The same stacked configuration can be achieved directly by depositing AcFA₅K peptides onto HOPG through dropcasting with subsequent slow evaporation of the H₂O/MeOH solvent.

When peptides are dissolved in a H₂O/MeOH solvent, the contrasting hydrophobicity between the non-polar backbone and the polar lysine residue and C-terminus, enables surfactant-like behavior. Furthermore, at near neutral pH, the amine group in the lysine residue is positively charged, whereas the carboxyl group at the C-terminus is negatively charged. These opposing charges enable ionic interactions between individual peptides. At the mica-liquid interface, the combination of surfactant-like and catanionic interactions drives the formation of half-cylindrical micelles.

All these structures point to a building block that consists of an individual peptide in the extended conformation. In contrast, Stearns et al. thoroughly showed that individual AcFA₅K peptides in vacuum have a helical conformation that is stabilized by the formation of hydrogen bonds between the positively charged lysine group and the peptide backbone^[21,22].

This means that, although spectroscopic studies of individual peptides under UHV conditions can reliably be used to identify the structure of the peptide in that particular environment^[21,22], this conformation can be drastically altered by the presence of interfaces and solvent molecules.

Numerous studies have addressed the influence of the substrate^[157] or presence of specific functional groups^[59] on the self-assembly of peptides. However, this is the first comprehensive study that includes all of the above, and additionally makes an effort to probe the influence of the deposition method on the self-assembly of peptides. Thus, it is possible to make a direct comparison between self-assembly at the solid-vacuum interface (UHV conditions) and the solid-liquid interface.

Results presented here have shown that the technique used to bring the peptides to the solid substrate, drastically influences the self-assembly of AcFA₅K peptides. This indicates that a rational choice of the deposition method can be used as an additional parameter to tune the self-assembly of peptides at interfaces, thus promising an increased control over the functional

Chapter 2. Self-assembly of small peptides at the solid-liquid and solid-vacuum interface

properties at the bio-interface.

A novel and promising approach that has been presented in this thesis, combines ES-IBD in HV with *in situ* self-assembly. Results have shown that the transfer of peptide assemblies to a different local environment, can drastically alter the structure, and therefore the functional properties of the peptide assemblies. A comprehensive comparison between different substrates and variations in the amino acid sequence, point to a direct relation between this conformational change and the sequence of specific functional groups within the peptide itself. This suggests that it is possible to program specific dynamical behavior through rational design of the peptide.

Lastly, high-resolution *in situ* AFM shows that the self-assembly of AcFA₅K in the presence of GdCl₃ is different from the self-assembly of pure AcFA₅K. The periodic arrangement at the mica-liquid interface suggests a structured arrangement of metal-peptide complexes.

These results indicate a straightforward, *in situ* method to achieve structural ordering of peptides and metals. This is of particular interest because metal-peptide complexes have been used to model the structures and reactions of natural metalloenzymes, a class of proteins that is known for their profound catalytic activity and selectivity^[131,158].

Because the results on the structure of AcFA₅K-metal complexes has been obtained by using high-resolution *in situ* AFM, they are limited to the topography of the self-assembled structures. Future work could therefore focus on complementary spectroscopic techniques like XPS that are able to probe the chemical properties of these complexes.

A factor that has not been explored in this work, is the effect of the different solvents or solvent compositions on the self-assembly of AcFA₅K peptides at the solid-liquid interface. This could form a promising road to further understand the self-assembly and conformational changes that have been described here.

3 Bacterial surface layers

Bacterial Surface Layers (S-layers) are two-dimensional crystalline protein layers that make up the outer cell membrane of many Gram-positive and Gram-negative bacteria and almost all archaea^[60,61]. An electron micrograph of such an organism is displayed in Figure 3.1a^[66]. S-layers are composed of individual proteins, which self-assemble into regularly ordered lattices that can have symmetries ranging from oblique (P1,P2), square (P4) to hexagonal (P3, P6), as can be seen in Figure 2b, depending on the originating organism^[70,159].

The fact that S-layer proteins are the most abundant molecules in their respective organisms points to a significant biological importance and various functions have been ascribed to S-layers. Although no single function is found to be applicable to all instances of S-layer expressing organisms, structural integrity, permeability of the cell envelope and cell adhesion have all been related to the presence of S-layers^[160].

S-layers have been used in a wide range of applications, such as templates that drive the ordered adhesion of nanoparticles^[71–73], immobilization matrices for functional biomolecules^[74–77], adsorption matrices for metal ions^[78,79] and even as coatings that inhibit the adhesion of cells^[80]. S-layers can be patterned using top-down techniques like deep UV radiation^[161] to obtain a specific configuration of regularly spaced S-layer unit cells^[74]. However, because UV patterning cannot be employed *in situ*, this scheme is largely incompatible with fragile organic proteins.

This limitation can be overcome by using a biomimetic approach such as described in chapter 4: *In situ dynamics of protein self-assembly on block copolymer thin films*, in which inherent properties of the self-assembling molecules are used to direct the self-assembly of S-layers to specific locations.

In this chapter, different substrates are compared in order to elucidate the effect of sample surface properties on the self-assembly of S-layers at the solid-liquid interface. Furthermore, the nucleation and growth of S-layer at the mica-liquid interface is continuously imaged and compared with theoretical models for the non-classical crystallization of SbpA proteins into S-layers. This chapter contains the basics on S-layer self-assembly, which is used as a platform for the chapters that follow.

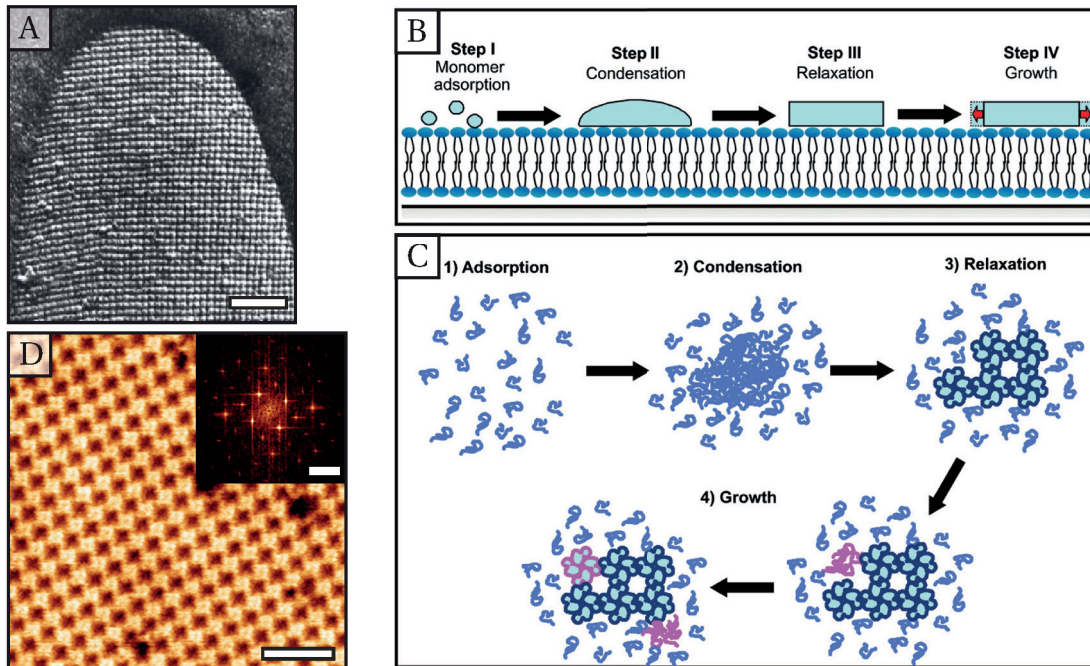


Figure 3.1 – (a) Electron micrograph of a Gram-positive organism that features crystalline S-layers at its outer surface. Reproduced from reference [66]. (b) The formation of S-layer self-assembly on Supported Lipid Bilayers (SLBs) goes through four distinct steps: adsorption, condensation, relaxation and finally growth. (c) A schematic top view shows the appearance of crystalline order during the relaxation step. Crystalline S-layers are self-catalyzing and grow through the addition of individual monomers that form tetrameric unit cells. Both (b) and (c) are reproduced from reference [162]. (d) *In situ* AFM image which shows that *ex vivo* recrystallization of S-layers on mica reproduces the native P4 symmetric structure. The tetrameric structure of the S-layer unit cell is clearly visible. Scale bar of the AFM image is 40 nm and for the FFT image in the top right corner 0.12 nm^{-1} .

3.1 Non-classical crystallization of SbpA proteins into S-layers

Chung et al.^[162] have shown that the self-assembly of S-layers follows a non-classical multi-stage crystallization pathway. The actual crystallization of the individual proteins is preceded by a distinct condensation step as is detailed in Figure 3.1b-c. Once formed, the crystalline S-layer is self-catalyzing and subsequent growth happens through the direct attachment of monomers.

Furthermore, Chung et al. found that once crystalline S-layer crystals have formed, only growth is observed and existing crystals never disappear, regardless of size. This indicates that there is no bi-directional exchange between the crystalline S-layers and the SbpA monomers in solution, and thus that classical nucleation theory cannot be applied here^[162].

The self-assembling properties of S-layers originate from the individual protein building blocks. As such, it is possible to isolate and purify S-layer proteins and trigger re-assembly into crystalline layers *ex vivo*^[163,164]. The resulting structures are robust and remain stable

3.2. Self-assembly of S-layers at the solid-liquid interface

ex situ^[47,66]. This robust self-assembling behavior enables their investigation with surface science techniques like electron microscopy, as shown in Figure 3.1a^[62,66] and high-resolution *in situ* and *ex situ* AFM, as shown in Figure 3.1d. In this chapter, the self-assembly of the S-layer proteins (SbpA) from the bacterium *Lysinibacillus sphaericus* has been investigated in detail using *in situ* AFM techniques.

For detailed protocols that describe the synthesis of SbpA proteins and recrystallization at the solid-liquid interface, the reader is referred to appendix B.

3.2 Self-assembly of S-layers at the solid-liquid interface

As mentioned in the previous sections, S-layers readily self-assemble on a variety of substrates. In this section, a comparison is made between self-assembly of S-layers on mica, HOPG and Si₃N₄. The SbpA monomers were purified from live *Lysinibacillus sphaericus* cultures, following the protocol detailed in appendix B. Mica, HOPG and Si₃N₄ were exposed to an S-layer growth solution that contains SbpA at 50 µg ml⁻¹, 10 mM Tris buffer at pH 7.2, 50 mM CaCl₂ and 100 mM NaCl. S-layer self-assembly on mica is relatively fast and a 3 h exposure to the S-layer growth solution results in a full coverage, as shown in Figure 3.2a. S-layer self-assembly at the HOPG-liquid interface is much slower and even an overnight exposure does not result in a full coverage, as shown in Figure 3.2b. Overnight exposure of Si₃N₄ to S-layer growth solution gives a full coverage of crystalline S-layers as shown in Figure 3.2c. The sample is imaged *ex situ*, because the small sample size of 4 mm × 4 mm prevents *in situ* imaging.

The results in Figure 3.2 show that the structure at the micrometer scale differs between mica, HOPG and Si₃N₄. However, a high-resolution zoom at the nanoscale shows that the internal crystalline structure of the S-layers has a 13.1 nm periodicity within a P4 symmetric configuration, regardless of which substrate is used.

Figure 3.2a shows that on mica, the S-layer patches formed in two different conformations, with the low domains about 5 nm to 6 nm in height and the high domains about 8 nm to 9 nm in height. N.B. realistic S-layer heights are measured *in situ* because the presence of capillary bridges between AFM tip and sample under ambient conditions, i.e. *ex situ*, requires higher imaging forces, which can result in deformation of soft materials such as S-layers. The presence of these two different conformations has been reported and described in detail by Shin et al. The energy barrier from adsorbed SbpA monomers to the high conformation islands was found to be 1.6 kJ/mol lower than the barrier from adsorbed SbpA monomers to the low conformation islands. In contrast, the energy barrier that separates the low and high conformations is about 40 times larger, at 61 kJ/mol. The low conformation therefore forms a kinetic trap that can be easily reached, but from which relaxation into the thermodynamically more favorable high conformation is much harder.

S-layers on HOPG were found to nucleate and grow at a much lower rate, and consequently could grow to larger sizes until competition with neighboring S-layer islands occurred. Fur-

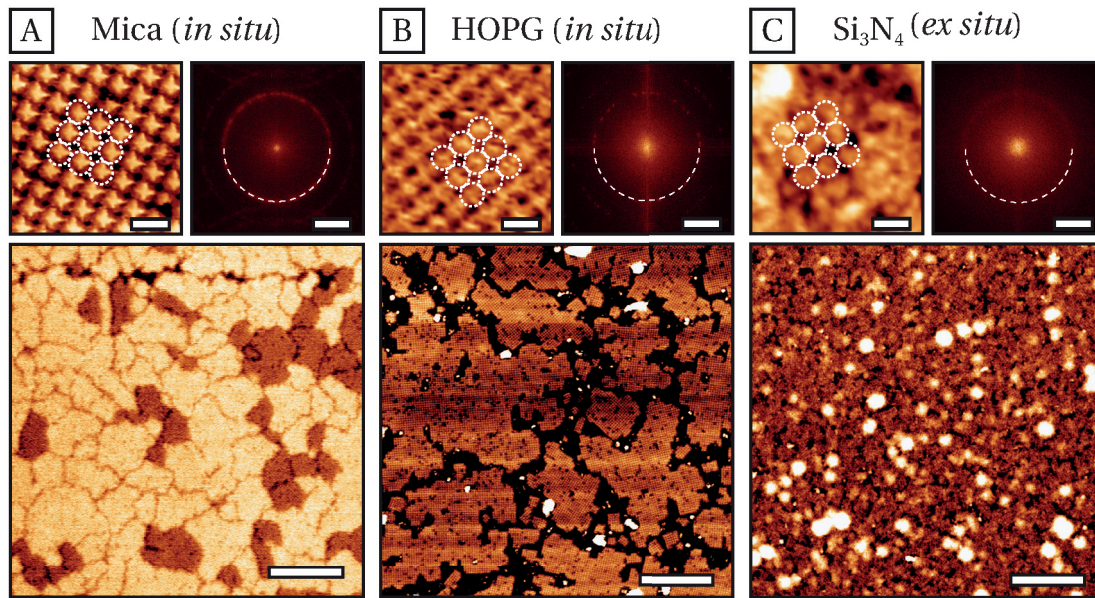


Figure 3.2 – S-layers can be recrystallized on various inorganic substrates such as mica, HOPG and Si_3N_4 . Whereas the size and shape of the individual monocrystalline S-layer patches differs among substrates, the internal P4 periodicity remains the same. The half-circle in each FFT image indicates a periodicity of 13.1 nm. (a) *In situ* AFM image of S-layers at the mica-liquid interface. (b) *In situ* AFM image of S-layers at the HOPG-liquid interface. (c) *Ex situ* AFM image of S-layers at the Si_3N_4 -air interface after the S-layer growth solution has been removed. Scale bars in the overviews indicate 400 nm. In the zoomed images, the scale bars indicate 20 nm and in the FFT images $50 \mu\text{m}^{-1}$.

thermore, the average height of the S-layer crystals on HOPG was about 12 nm. This is about double the height of the low S-layer conformation on mica and therefore suggests a structure composed of two layers. This corresponds well with observations by Pum et al.^[164], who showed that the two faces of S-layer crystals have a different affinity for hydrophilic and hydrophobic substrates. The outer face (compared to the native configuration at the bacterial cell membrane) is charge neutral, whereas the inner face has a net positive or negative charge, depending on the pH level of the solution. On hydrophilic substrates, S-layers therefore form single layers in their native orientation that directs the neutral face outward. On hydrophobic substrates, the neutral S-layer face is oriented towards the substrate and the charged inner face is directed outward. This then enables the formation of a second S-layer on top of the first one, which creates a double layer configuration with a height twice that of a single layer. On hydrophilic Si_3N_4 , the S-layer patches are both smaller and more numerous compared to either mica or HOPG. This points to a fast nucleation process relative to the subsequent growth of the S-layer patches. The height of the S-layer patches is about 4 nm to 5 nm. As the Si_3N_4 is imaged *ex situ*, the tip-substrate interaction forces are typically higher than comparable *in situ* measurements, which can lead to a slight compression of the S-layers. The reported height of about 4 nm to 5 nm is therefore consistent with the expected height of a single S-layer. By increasing the concentration of SbpA in solution to about 1 mg ml^{-1} , it is possible to trigger

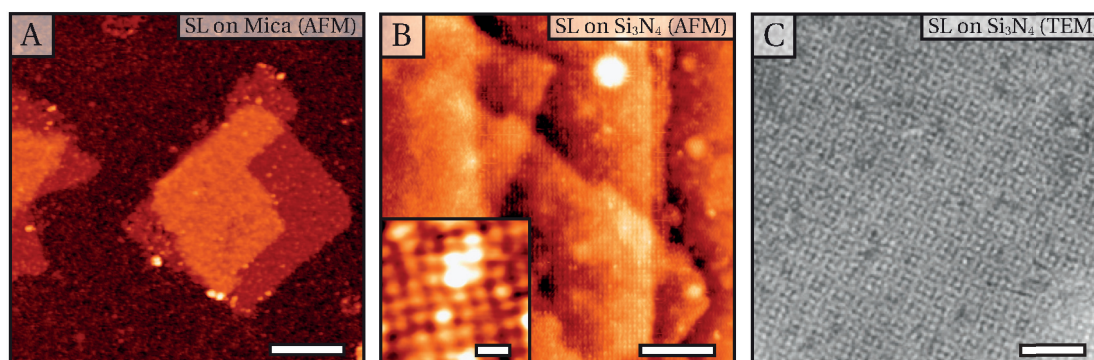


Figure 3.3 – S-layers can be crystallized in solution and deposited directly on the sample by drop casting. **(a)** Large single-crystal S-layer sheets can be formed at the mica-liquid interface. Often, different S-layer sheets overlap. The scale bar represents 800 nm. **(b)** The same procedure can be used to deposit large S-layer crystals at the Si₃N₄-liquid interface. Scale bars represent 200 nm and 20 nm (inset). **(c)** Transmission Electron Microscopy (TEM) can be used to image larger areas and produce high-quality images that clearly show the crystalline structure of the S-layer. The scale bar represents 100 nm.

S-layer self-assembly into large sheets within the bulk solution. Drop casting can then be used to deposit these large sheets onto a sample such as mica or Si₃N₄, as shown in Figure 3.3.

3.2.1 Self-assembly of S-layers on mica

The previously mentioned self-assembly of S-layers on mica is especially interesting because it combines three different processes. First, protein monomers adsorb to the solid-liquid interface, second, the adsorbed monomers undergo self-assembly, and finally, the self-assembled S-layers undergo a conformational change from a low conformation into a high conformation. The dynamics of S-layer self-assembly have been studied in detail by Chung et al.^[162] and the dynamics of the conformational change have been analysed by Shin et al.^[165].

The different time scales of each process make it challenging to observe all dynamics in one single experiment, i.e. the adsorption of SbpA to the mica-liquid interface takes place within minutes, whereas the conformational change of the fully formed S-layer crystals can take several hours. This experimental challenge can be overcome by using the high resolution and fast scanning speeds of our Dimension FastScan AFM system, in combination with a continuous flow through the *in situ* flow cell. This enables the detailed observation of all three processes in a single experiment, as is shown in Figure 3.5.

The models from Chung et al.^[162] and Shin et al.^[165] have been modified to be compatible with the specific experimental conditions in this experiment. This enabled their combination into a single model, which accurately describes both S-layer formation and subsequent conformational change.

Chung et al. studied the self-assembly of S-layers on supported lipid bilayers (SLBs) and

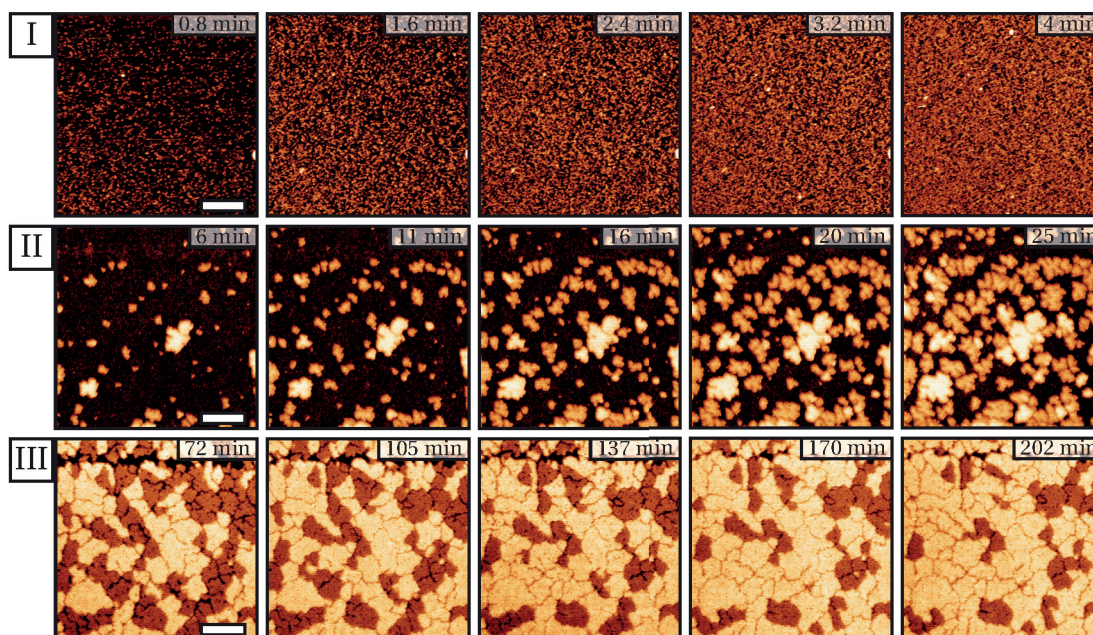


Figure 3.4 – The mica-liquid interface in the presence of SbpA at $50 \mu\text{gml}^{-1}$ is continuously imaged for over 8 h. Three distinct regimes can be distinguished. **(I)** Consecutive images recorded in the first 4 min after introduction of the SbpA proteins to the solution. The adsorption of individual SbpA proteins was resolved at several frames per minute. Over the course of 4 min, the surface was fully covered in SbpA proteins. **(II)** Consecutive images recorded from 6 min to 25 min after introduction of SbpA. Individual S-layer crystals begin to form and grow until the surface is fully covered. They are formed in two different conformations, with conformation α slightly higher and thermodynamically more stable than conformation β ^[165]. **(III)** Consecutive images recorded from 72 min to 202 min after introduction of SbpA. At a time scale much slower than either SbpA adsorption or S-layer self-assembly, conformation β transformed into conformation α . The scale bars represent 400 nm.

accurately predicted the S-layer island size over time by using a perimeter driven growth model. This model defines the growth of an S-layer island as the number of tetrameric unit cells that is added per unit time, i.e. $\frac{dN_T}{dt}$. The growth is linearly proportional to the number of available unit cells along its border, $\sqrt{N_T}$, and an experimentally determined tetramer attachment rate, R , i.e. $\frac{dN_T}{dt} \sim \sqrt{N_T} \cdot R$. Under their specific experimental conditions, the nucleation (condensation and relaxation steps in Figure 3.1) and growth of the S-layer crystals did not overlap, i.e. no nucleation was observed once S-layer crystals had formed at the solid-liquid interface. Furthermore, the use of SLBs as substrate and the absence of liquid mixing within the liquid cell resulted in a slow diffusion of SbpA monomers to the solid-liquid interface, which led to a depletion in SbpA concentration during S-layer growth. This depletion of the SbpA concentration at the solid-liquid interface limited the S-layer growth, even before competition with neighboring S-layer crystals became apparent. Both factors are markedly different for S-layer self-assembly on mica under continuous flow conditions. Depletion of the SbpA monomer concentration at the mica-liquid interface has

3.2. Self-assembly of S-layers at the solid-liquid interface

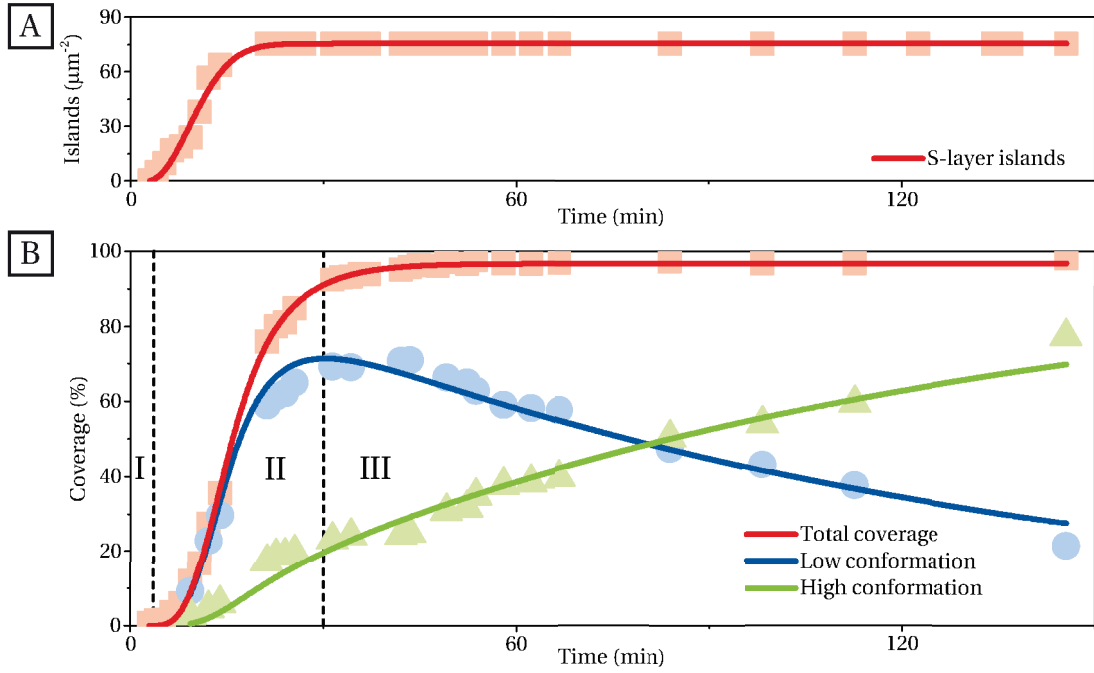


Figure 3.5 – The mica-liquid interface in the presence of SbpA at $50 \mu\text{gml}^{-1}$ is continuously imaged for over 8 h. **(a)** S-layer islands only start to appear after a short period of time because SbpA monomers need time to adsorb to the mica-liquid interface, see Figure 3.4I. After this, the number of S-layer islands start to increase faster over time, before reaching a steady state that corresponds with a full coverage. The experimental data is fitted with the model shown in Equation 3.7. **(b)** The coverage of the S-layer islands, in percentage of the total area, is tracked over time and displayed in red. A distinction is made between S-layer islands in a low (blue) or high (green) conformation. The experimental data for the total coverage is fitted with the mathematical model shown in Equation 3.8, the coverage of the low conformation is fitted with the model in Equation 3.9 and the coverage of the high conformation is fitted with the model in Equation 3.10. The three regimes, i.e. I, II and III, correspond with the series of AFM images in Figure 3.4.

not been observed, i.e. R is constant. Furthermore, the growth of S-layer patches at the solid-liquid interface only continues until the mica surface is fully covered. This is included in the model by the term $\frac{N_{T,m} - N_T}{N_{T,m}}$ in Equation 3.1, where $N_{T,m}$ is the average size of the S-layer islands when the surface is fully covered.

$$\frac{dN_T}{dt} = \sqrt{N_T} \cdot R \cdot \frac{N_{T,m} - N_T}{N_{T,m}} \quad (3.1)$$

$$N_T(t) = N_{T,m} \cdot \tanh^2 \left(\frac{R \cdot t}{2\sqrt{N_{T,m}}} \right) \quad (3.2)$$

Here N_T is the number of tetrameric unit cells within the S-layer island, with $N_{T,m}$ the av-

Chapter 3. Bacterial surface layers

erage number of unit cells at the point where the surface is fully covered. R is the tetramer attachment rate per unit cell along the borders of the existing S-layer islands.

Furthermore, S-layer nucleation has been observed well after existing S-layer crystals have started to grow, which is incorporated in the model by multiplying the perimeter driven growth model (Equation 3.2) with the number of S-layer crystals $N_{SL}(t)$. Through careful consideration of the mechanism of S-layer self-assembly, as shown in Figure 3.1, a model for the S-layer nucleation rate can be extracted. The number of S-layer islands depends both on the number of high density monomer globules, N_g , and on the ratio with which these globules undergo relaxation into crystalline S-layers, k_2 , i.e. $\frac{dN_{SL}}{dt} = N_g \cdot k_2$. In turn, the number of globules will increase over time, i.e. $N_g \equiv N_g(t)$. Although the time dependency of N_g is not exactly known, the most basic assumption that can be made is a linear approximation, i.e. $N_g(t) = k_1 \cdot t$. The fact that only a limited number of S-layer islands can fit within the measurement volume is included as a factor $\frac{N_{SL,m} - N_{SL}}{N_{SL,m}}$. The number of S-layer islands over time is then described by Equation 3.4.

$$\frac{dN_{SL}}{dt} = k_1 \cdot k_2 \cdot t \cdot \frac{N_{SL,m} - N_{SL}}{N_{SL,m}} \quad (3.3)$$

$$N_{SL}(t) = N_{SL,m} \left(1 - e^{-\frac{k_1 \cdot k_2 \cdot (t - t_c)^2}{2 \cdot N_{SL,m}}} \right) \quad (3.4)$$

N_{SL} is the total number of S-layer crystals at the mica surface, with $N_{SL,m}$ the maximum number that is reached when S-layer crystals fully cover the surface. t_c reflects the time it takes to form the first dense monomer globules (step I in Figure 3.1). k_1 is the number of dense monomer globules that form per unit time (step II in Figure 3.1). k_2 is the ratio of dense monomer globules that undergo relaxation into crystalline S-layers per unit time (step III in Figure 3.1).

Shin et al.^[165] found that during the conformational change of the S-layers, the coverage of the low conformation followed a simple exponential decay. This is incorporated into the model by multiplying the total coverage by an expression for exponential decay, as is shown in Equation 3.6. The experimentally observed coverage for the low and high configurations are thus described by the models in Equation 3.9 and 3.10, respectively.

$$\frac{dA_{low}}{dt} = -A_{low} \cdot R_{conf} \quad (3.5)$$

$$A_{low}(t) = A \cdot e^{-R_{conf} t} \quad (3.6)$$

A_{low} is the total area of the S-layer crystals in the low conformation and R_{conf} reflects the rate at which S-layers with low conformation relax to the high conformation.

3.2. Self-assembly of S-layers at the solid-liquid interface

$$N(t) = N_{SL,m} \left(1 - e^{-\frac{k_1 \cdot k_2 \cdot (t-t_c)^2}{2 \cdot N_{SL,m}}} \right) \quad (3.7)$$

$$A_{tot}(t) = N_{SL,m} \left(1 - e^{-\frac{k_1 \cdot k_2 \cdot (t-t_c)^2}{2 \cdot N_{SL,m}}} \right) \cdot N_{T,m} \cdot \tanh^2 \left(\frac{R \cdot (t - t_c)}{2 \sqrt{N_{T,m}}} \right) \quad (3.8)$$

$$A_{low}(t) = N_{SL,m} \left(1 - e^{-\frac{k_1 \cdot k_2 \cdot (t-t_c)^2}{2 \cdot N_{SL,m}}} \right) \cdot N_{T,m} \cdot \tanh^2 \left(\frac{R \cdot (t - t_c)}{2 \sqrt{N_{T,m}}} \right) \cdot (e^{-R_{conf}(t-t_c)}) \quad (3.9)$$

$$A_{high}(t) = N_{SL,m} \left(1 - e^{-\frac{k_1 \cdot k_2 \cdot (t-t_c)^2}{2 \cdot N_{SL,m}}} \right) \cdot N_{T,m} \cdot \tanh^2 \left(\frac{R \cdot (t - t_c)}{2 \sqrt{N_{T,m}}} \right) \cdot (1 - e^{-R_{conf}(t-t_c)}) \quad (3.10)$$

The models from Equations 3.7 to 3.10 were applied to the experimental data in Figure 3.5 by first fitting Equation 3.7 to the experimentally determined number of S-layer crystals per unit area. The parameters $N_{SL,m}$, $k_1 \times k_2$ and t_c obtained from this fitting were then used as fixed input values in order to fit Equation 3.8 to the total coverage of S-layers over time. The two additional parameters $N_{T,m}$ and R obtained from this fit were then used as fixed input values to fit Equation 3.9 and 3.10 to the experimentally obtained values for the coverage of the low and high conformations, respectively. As shown in Figure 3.5, the models accurately fit the experimental data.

This chapter shows how the self-assembly of S-layers can be manipulated relatively easily by changing the substrate. Single-layer structures are formed on hydrophilic substrates, whereas on hydrophobic substrates, a double-layer structure is observed. However, regardless of the substrate, the unit cell of the S-layer remains the same.

Using dynamically resolved AFM data, it has been shown that the self-assembly of S-layers can be separated into several processes, with distinct dynamics. The nucleation of S-layers follows an exponential growth, as presented in Equation 3.7. The growth of existing S-layer crystals can be described by a perimeter driven growth model, as shown in Equation 3.2. And the relaxation from a low conformation to a high conformation follows a simple exponential decaying function, as presented in Equation 3.9.

Furthermore, the high resolution dynamic AFM data presented here shows the benefits of this high speed *in situ* continuous flow AFM setup. A single experiment has been shown to be sufficient to accurately resolve the dynamics of S-layer self-assembly at three vastly different time scales.

It has been shown that S-layers retain their internal crystalline structure on a variety of substrates, which suggests that it is possible to control S-layer self-assembly by manipulating the properties of the solid-liquid interface. This has been build upon in the next chapter, where the self-assembly of S-layers on chemically heterogeneous block-copolymer thin films is studied in depth.

4 *In situ* dynamics of protein self-assembly on block copolymer thin films

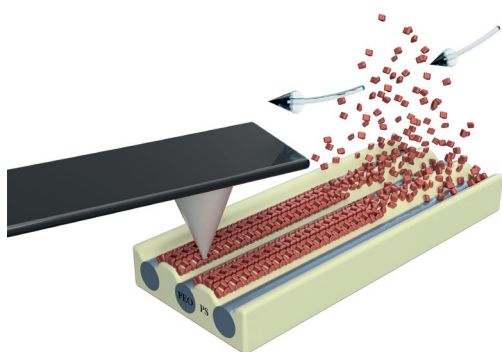


Figure 4.1 – *In situ* AFM is used to image directed self-assembly of proteins at chemically heterogeneous substrates during continuous flow conditions.

formed by block copolymers (BCPs). The spontaneous separation of the chemically different polymer blocks at the nanoscale can yield precisely tuned structures with long-range order^[48]. Solvent annealing of BCP thin films composed of polystyrene and polyethylene oxide (PS-*b*-PEO) gives rise to chemically heterogeneous substrates with precise nanoscale features, depending on the composition and molecular weight of the BCP^[81,82,85]. Interestingly, the surface of BCP films can be modified by a simple solvent reconstruction process. For example, cylinder-forming poly(styrene-*block*-2-vinylpyridine) (PS-*b*-P2VP) BCPs were shown to form a nanoscale trench pattern in thin films, with most of the P2VP blocks located at the surface.

A bottom-up approach that uses self-assembly of biological molecules can result in nanostructures that exceed synthetic counterparts in both complexity and functionality^[6–8]. In contrast to most top-down techniques, this is done without the use of expensive machinery or the consumption of large amounts of energy^[166]. One of the key challenges in this field is the rational use of existing self-assembling systems, while maintaining the level of control required for actual applications.

In this chapter, a hierarchical and entirely bottom-up approach is used to control the self-assembly of S-layers.

Promising and extensively studied examples of self-assembling nanostructures are

4.1. Self-assembly of PS-*b*-PEO and PS-*b*-P2VP Block copolymer thin films

This reconstruction occurs after an immersion of the BCP film in ethanol, a good solvent for the minority P2VP cylinders and a bad solvent for the PS matrix^[167]. This versatility and tunability makes the BCP system useful as building block in a hierarchical bottom up approach to nanofabrication of functional structures.

For the next stage, the robust self-assembling properties of bacterial surface layers (S-layers) are used. It has been shown that S-layers form practical and easy to use adhesion templates for proteins and nanoparticles alike^[30,47,87,161,168,169]. S-layers are composed of individual monomers that, through a non-classical pathway involving high-density amorphous clusters, form highly ordered 2D crystalline structures, as shown in the previous chapter^[162]. Genetic modification of the S-layer protein can result in the expression of specific allergens, without affecting the self-assembling properties. In this way, regularly spaced specific adhesion sites for functional molecules can be created at the nanoscale through an entirely bottom-up approach^[74].

This chapter shows the hierarchical use of self-assembling systems. BCP thin films are used as platform for the adhesion and subsequent self-assembly of S-layers as well as for the adhesion and bundling of collagen molecules. The tunability of chemically heterogeneous PS-*b*-PEO BCP thin films enables a high level of control over the position and orientation of crystalline S-layers. The self-assembly of S-layers can be confined to the hydrophobic PS nanodomains, with their internal structure unaffected and their crystalline orientation aligned along the principal direction of the underlying BCP pattern. Furthermore, the total protein loading at the (PS-*b*-PEO)-liquid interface is drastically increased compared to its pure PS or PEO constituents. A comparison with physically similar, but chemically homogeneous substrates such as reconstructed PS-*b*-P2VP BCP films, makes it possible to distinguish between the relative effects of chemical and physical contrasts within the BCP thin film.

In situ FastScan Atomic Force Microscopy (AFM), combined with continuous flow conditions, enables the dynamics of self-assembly at the solid-liquid interface to be tracked in real time with molecular resolution. This is used to explore at the nanoscale the influence of chemical vs physical confinement in 2D protein crystallization.

4.1 Self-assembly of PS-*b*-PEO and PS-*b*-P2VP Block copolymer thin films

Figure 4.2 shows typical patterns observed in PS-*b*-PEO and PS-*b*-P2VP BCP thin films. For PS-*b*-PEO, hexagonal arrays of PEO cylinders oriented perpendicular to the substrate give rise to hexagonal dot patterns with a periodicity of about 41 nm. PEO cylinders oriented parallel to the substrate result in the formation of striped patterns with a line spacing of about 55 nm and a FWHM of about 32 nm. Note that these patterns were often found to coexist across the surface of a solvent annealed PS-*b*-PEO film, as can be seen in Figure 4.4a.

Cylinder-forming PS-*b*-P2VP BCPs were annealed in the vapor of tetrahydrofuran (THF), a near-neutral solvent for PS and P2VP, resulting in the formation of substrate-parallel P2VP-cylinders embedded in a PS-matrix. The surface of solvent annealed PS-*b*-P2VP films was

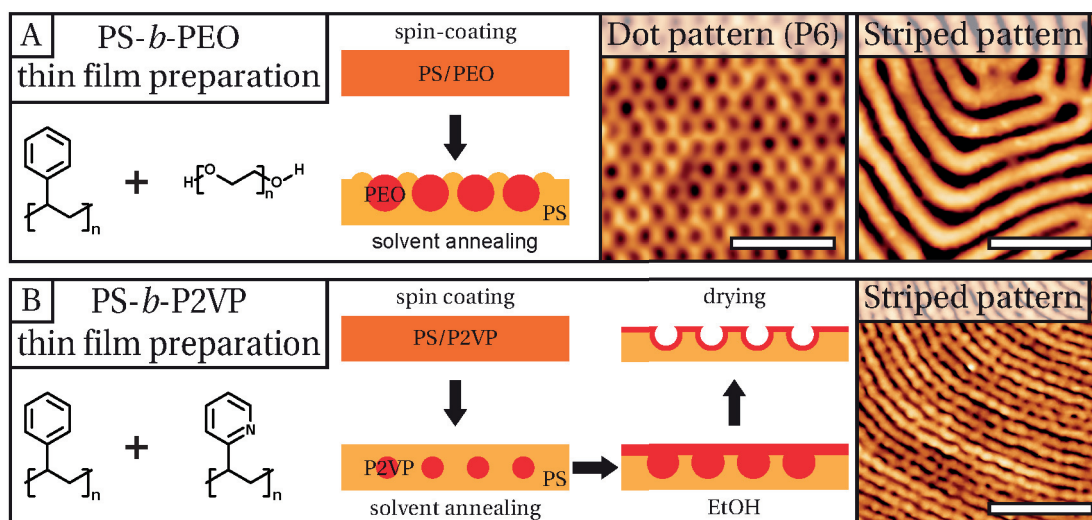


Figure 4.2 – The preparation methods for PS-*b*-PEO and PS-*b*-P2VP BCP thin films with AFM images showing the typical patterns that were used. **(a)** Dot and striped patterns in PS-*b*-PEO (43 kg/mol) films obtained after solvent annealing in mixed vapors of THF and H₂O. Note that the PEO blocks appear as the lower (darker) domain in the AFM height images. The scale bars represent 200 nm **(b)** Typical PS-*b*-P2VP (34 kg/mol) patterns have a lamellar pattern, similar in shape to the PS-*b*-PEO patterns. However, annealing in ethanol selectively dissolves the P2VP blocks which subsequently form a closed layer on top of the PS matrix. The scale bar represents 200 nm

reconstructed by immersing the films in ethanol to form trench patterns as can be seen in Figure 4.2b. Reconstructing the films at elevated ethanol temperatures was found to increase both the depth and width of the trenches.

All BCP thin films were prepared by Dr. Ilja Gunkel at the Lawrence Berkeley National Laboratory, United States. The protocols that were used are described in the following paragraphs. The samples were all used as received.

Preparation of PS-*b*-PEO Thin Film Patterns

Polystyrene-*block*-poly(ethylene oxide) (PS-*b*-PEO) with a total molecular weight of $M_n = 32.0$ - 11.0 kg/mol and a PEO volume fraction of $f_{PEO} = 0.240$ (see Table 4.1) was purchased from *Polymer Source Inc.* and used as received. Thin films with a thickness of (34 ± 1) nm were prepared by spin coating a 1.0% (w/v) solution of PS-*b*-PEO in toluene and THF (both purchased from *Sigma-Aldrich*) at a volume ratio of 4:1 onto silicon (15 mm \times 15 mm) at 3500 rpm for 20 s. Solvent vapor annealing was carried out using sealed glass containers with a volume of 45 ml. 100 μ l H₂O and 300 μ l THF was added to maintain a constant surface area of the solvents during the annealing process. The PS-*b*-PEO thin films were first annealed in H₂O vapor for 10 min, and secondly, at a temperature of (21 ± 1) °C in mixed vapors of THF and H₂O.

By slightly changing the preparation procedure, different morphologies in the PS-*b*-PEO films could be obtained. The shape of the pattern, i.e. dotted or striped, depends on the ratio

4.2. Self-assembly of S-layers on top of PS-*b*-PEO BCP thin films

Table 4.1 – Molecular weights M_n , volume fractions f of the minority component and polydispersity indices (PDI) of the homopolymers and block copolymers, as provided by *Polymer Source Inc.*

Polymer	M_n [kg/mol]	$f_{PEO/P2VP}$	PDI
PS	25	-	1.05
PEO	10	-	1.05
PS- <i>b</i> -PEO, 43k	32.0- <i>b</i> -11.0	0.240	1.06
PS- <i>b</i> -P2VP, 27k	18.0- <i>b</i> -9.0	0.315	1.08
PS- <i>b</i> -P2VP, 43k	30.0- <i>b</i> -12.5	0.277	1.06

of molecular weights of the components. The periodicity is related to the absolute weight of the molecules, with a larger period for longer polymer chains, and to the annealing time. Especially for line patterns, the line width and spacing is increased for increasing annealing times.

Reconstructed PS-*b*-P2VP Thin Film Patterns

Polystyrene-block-poly (2-vinyl pyridine) (PS-*b*-P2VP) BCPs of different molecular weights and composition (see Table 4.1 for details) were purchased from *Polymer Source Inc.* PS-*b*-P2VP BCPs were dissolved in mixtures of toluene and THF at a 4:1 volume ratio to form 1.5 % (w/v) solutions (for $M_n = 27 \text{ kg mol}^{-1}$ this was 1.0 % (w/v)). The mixtures were then spin-coated onto either a flat silicon wafer or a faceted sapphire surface at 3000 to 4000 rpm for 20 s. The faceted surface was generated by annealing M-plane sapphire from *Precision Micro-Optics* at temperatures between 1200 °C and 1300 °C in air for 24 h. Faceted sapphire substrates provide directional guidance to the PS-*b*-P2VP thin film, which results in a laterally ordered striped pattern^[170].

PS-*b*-P2VP films were annealed in THF vapor at room temperature using a custom-designed chamber^[84], with a reservoir of THF located inside the annealing chamber. The degree of swelling of a film was controlled by adjusting the flow rate of dry N₂ into the chamber with a variable area flow meter from *Cole Parmer* to obtain a flow rate of 150 sccm. The thickness of the swollen film was measured in real-time with a spectroscopic white light reflectometer from *Filmetrics*. Swollen films were rapidly dried by removing the chamber cover, which resulted in instantaneous evaporation of the solvent in the chamber.

The surface of the solvent-annealed PS-*b*-P2VP film was reconstructed by immersing the film in ethanol for 10 min, at a temperature between 25 °C and 45 °C, followed by a thorough drying of the film with a nitrogen gun. The temperature of ethanol was controlled to within 1 °C with a hot plate and temperature sensor.

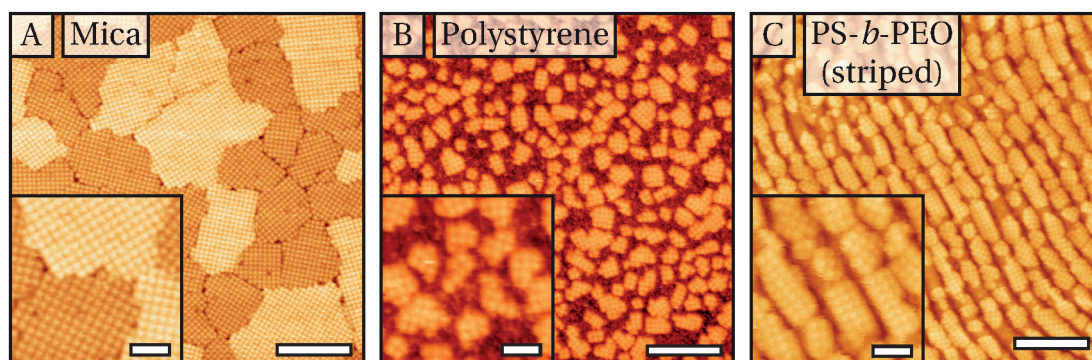


Figure 4.3 – The self-assembly of S-layers is compared between mica, striped patterned PS and PS-*b*-PEO. **(a)** S-layer self-assembly at the mica-liquid interface results in a full coverage of S-layer islands that have hundreds of unit cells. The typical high and low conformations introduced in chapter 3 are clearly visible. **(b)** On homogeneous PS, S-layers self-assemble into smaller islands, typically tens of unit cells in size. The islands are homogeneously scattered over the surface and do not have any preferential orientation. **(c)** The self-assembly of S-layers on a linearly patterned PS-*b*-PEO substrate results in a striking confinement of the S-layer islands to the PS matrix. A detailed analysis of this system is given in Figures 4.4 and 4.5. The scale bars represent 200 nm (50 nm for the insets).

4.2 Self-assembly of S-layers on top of PS-*b*-PEO BCP thin films

The self-assembly of S-layers on patterned PS-*b*-PEO thin films was imaged *in situ* by AFM, similar to the study of S-layer self-assembly at the mica-liquid interface, as detailed in chapter 3. Results in Figure 4.3 show that the self-assembly is strongly affected by the underlying pattern of the PS-*b*-PEO thin film.

From a comparison between Figures 4.3b, d and f it follows that, unlike on mica, on PS-*b*-PEO substrates, S-layers only exist in one conformation. On dot patterned PS-*b*-PEO BCP substrates, the S-layer islands are markedly smaller than on mica and do not form a full coverage. A more striking result is obtained for the self-assembly of S-layers on striped PS-*b*-PEO BCP thin films, such as shown in Figure 4.3c. The crystalline S-layer islands are strongly confined to the PS matrix. Furthermore, there seems to be a preferential alignment of the S-layer crystals along the underlying BCP pattern. In the following sections, the self-assembly of S-layers on PS-*b*-PEO thin films is investigated further.

In Figure 4.4, striped PS-*b*-PEO BCP thin films were used as a substrate for S-layer self-assembly at the solid-liquid interface. In Figure 4.4a-b, a comparison of the same area before and after SbpA exposure reveals that the self-assembly of the S-layers is clearly confined to the hydrophobic PS lines, while avoiding the PEO areas. This clearly shows that the self-assembly of S-layers depends on the local properties of the substrate.

Figure 4.4c indicates a preferential orientation parallel to the underlying PS lines. However, a more quantitative analysis is used to corroborate this. For each unit cell, the orientation of the parent S-layer crystal with respect to the principal direction of the PS-*b*-PEO substrate

4.2. Self-assembly of S-layers on top of PS-*b*-PEO BCP thin films

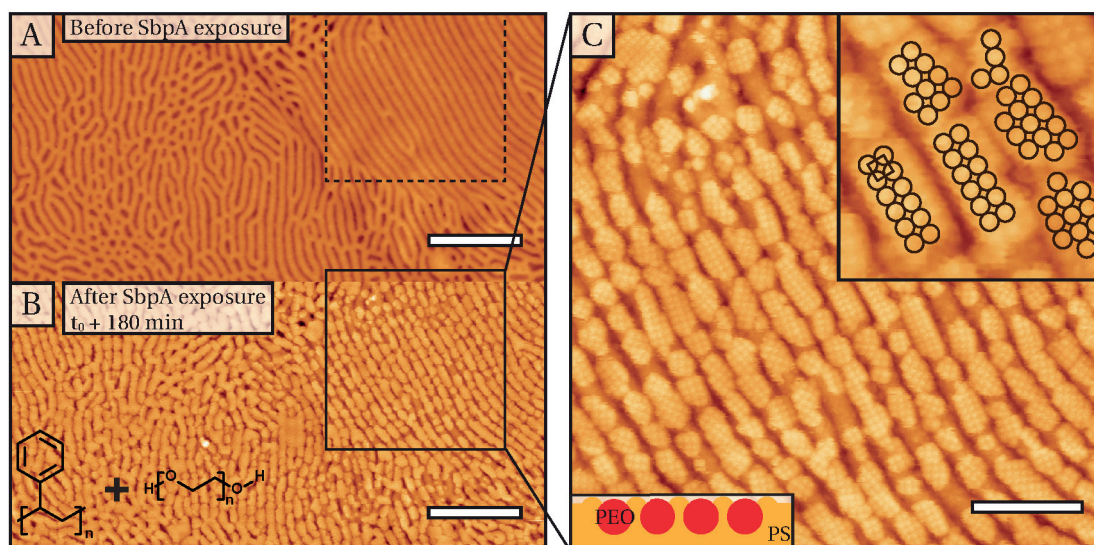


Figure 4.4 – (a) *In situ* AFM image at the solid-liquid interface of striped PS-*b*-PEO thin films in H₂O. (b) AFM image of the same region after exposure to SbpA at 50 μgml^{-1} in S-layer growth solution. Note that the S-layer crystals are confined to the underlying PS matrix. Scale bars in (a) and (b) represent 500 nm. (c) A magnification of (b), which shows that the internal structure of the S-layer crystals remains intact. Scale bar represent 200 nm.

was recorded. The same analysis was performed for crystalline S-layer islands on homogeneous substrates such as mica and PS (Figure 4.5a). Results in Figure 4.5b show that whereas chemically homogeneous substrates have randomly oriented crystals, on the chemically heterogeneous PS-*b*-PEO thin film there is a preferential orientation at 0° (parallel) to the underlying PS line direction. In Figure 4.5c-d a detailed analysis is performed on the distribution of sizes and orientations of the S-layer crystals on PS-*b*-PEO BCP substrates. Figure 4.5c shows that S-layer crystals that are aligned at 0° (parallel) to the underlying PS-*b*-PEO line direction, can grow larger in size than the S-layer crystals oriented differently. It is possible that this is due to an increased mobility of SbpA monomers along the PS-PEO interface. When S-layer crystals are aligned such that their principle crystal growth direction matches the direction of highest SbpA mobility, they will experience an increased growth speed.

Figure 4.5d shows that not only are these parallel aligned islands larger, they are also more numerous compared to other orientations. As no re-alignment of crystalline S-layer islands has been observed during continuous *in situ* AFM observations, it is suggested that this preferred orientation is imposed during nucleation.

In order to determine whether the local properties originate from the individual constituents PS and PEO, or whether they are a result of emergent effects due to their combination into a block copolymer, these PS-*b*-PEO samples were compared with homogeneous polystyrene (PS) and poly(ethylene oxide) (PEO) samples. Both PS and PEO substrates are exposed to S-layer growth solution and the solid-liquid interface is imaged using *in situ* AFM.

In Figure 4.6, a comparison is made of SbpA adhesion and subsequent S-layer formation

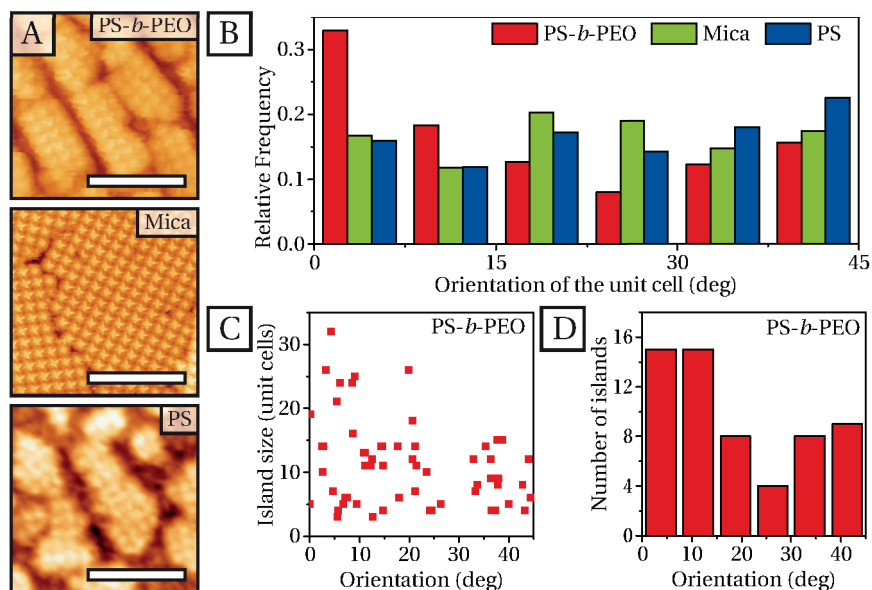


Figure 4.5 – (a) S-layer self-assembly depends strongly on the substrate. Confinement to PS lines on PS-*b*-PEO block copolymer substrates, a full coverage of randomly oriented crystals on mica and scattered small crystals on polystyrene. Scale bars represent 100 nm. (b) Histogram that shows for thousands of S-layer unit cells the orientation of their parent crystal with respect to the principal direction of the underlying substrate. For chemically heterogeneous PS-*b*-PEO BCP, homogeneous mica and PS. (c) Scatter plot that shows the relation between S-layer crystal size and the orientation with respect to the underlying line direction of the PS-*b*-PEO substrate. (d) The number of S-layer crystals as function of the orientation with respect to the underlying line direction of the PS-*b*-PEO substrate.

between PS and PEO. On PS, the adhesion of SbpA prior to S-layer crystallization is clearly visible, whereas for PEO, this is not the case. The PEO-liquid interface remains empty, even in the presence of SbpA in solution. S-layer ‘formation’ on PEO was found to occur not through self-assembly at the solid-liquid interface, but instead through adsorption of fully formed S-layer crystals that ‘drop’ from solution. There is no subsequent growth of these fully formed S-layer islands once adsorbed. Furthermore, these S-layer islands at the PEO-liquid interface have double the height compared to the S-layer crystals at the PS-liquid and mica-liquid interfaces. This suggests the presence of double layered S-layer crystals at the PS-PEO interface, in line with reported behavior of SbpA self-assembly on hydrophilic substrates^[164,171]. In conclusion, the different S-layer adsorption affinities of PS and PEO seem to be preserved when both polymers are combined within a nanostructured BCP thin film. This is corroborated by an *ex situ* experiment in which a hexagonal dot patterned PS-*b*-PEO thin film is exposed to an S-layer growth solution containing SbpA at $6 \mu\text{gml}^{-1}$. The solution is left in contact with the BCP substrate for 1 h, after which the solution is removed and the substrate is gently dried in a nitrogen flow. The resulting substrate is then imaged *ex situ* with AFM. The results shown in Figure 4.7 show that SbpA adsorbed exclusively to the PS matrix, avoiding the PEO dots.

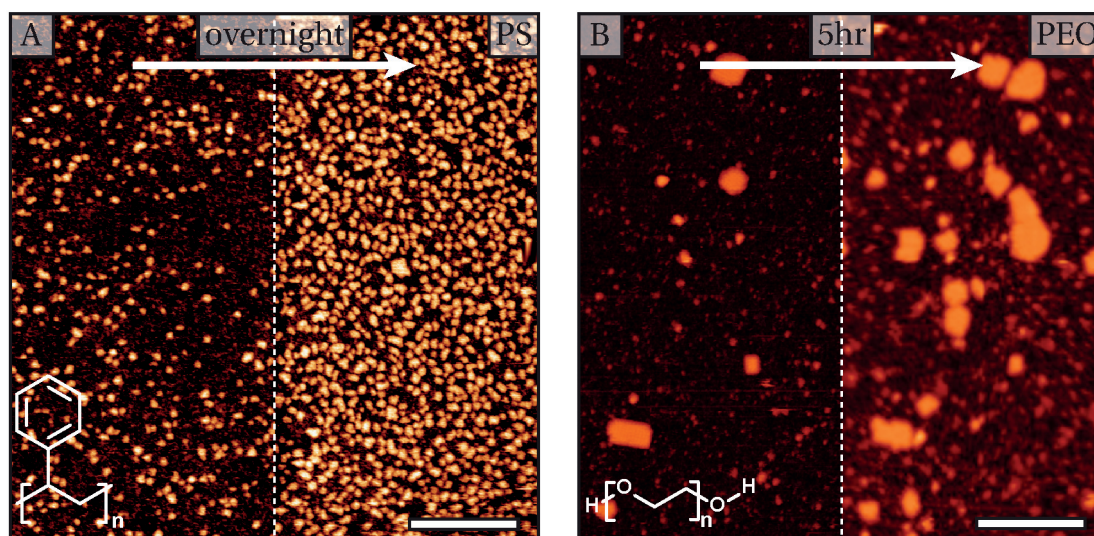


Figure 4.6 – S-layer self-assembly on PS and PEO. (a) S-layer self-assembly on a homogeneous polystyrene (PS) substrate after 4 h of exposure to S-layer growth solution during a continuous flow of $20\ \mu\text{s}^{-1}$. The S-layer growth solution consists of 100 mM NaCl, 50 mM CaCl_2 and 10 mM Tris buffer at pH 7.2. (b) S-layer self-assembly on a homogeneous poly(ethylene oxide) PEO substrate after exposure to S-layer growth solution for 1 h on the left and 6 h on the right. A continuous flow of $20\ \mu\text{s}^{-1}$ was maintained during this time. Over time, more S-layers appear at the PEO-liquid interface, however existing S-layer islands present on the left, do not show further growth in the image on the right. Scale bars in both (a) and (b) represent 500 nm.

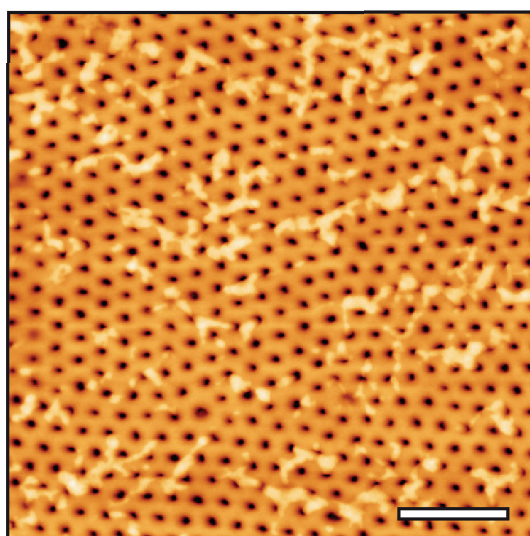


Figure 4.7 – *Ex situ* AFM image of a PS-*b*-PEO hexagonal dot pattern with adsorbed SbpA protein. The PS-*b*-PEO sample has been exposed to an S-layer growth solution containing SbpA at $6\ \mu\text{gml}^{-1}$ for 1 h. After this, the S-layer growth solution is gently washed away with milliQ water and the sample is dried in a nitrogen stream. This reveals that SbpA is only adsorbed to the PS matrix, while avoiding the PEO dots. The scale bar represents 200 nm.

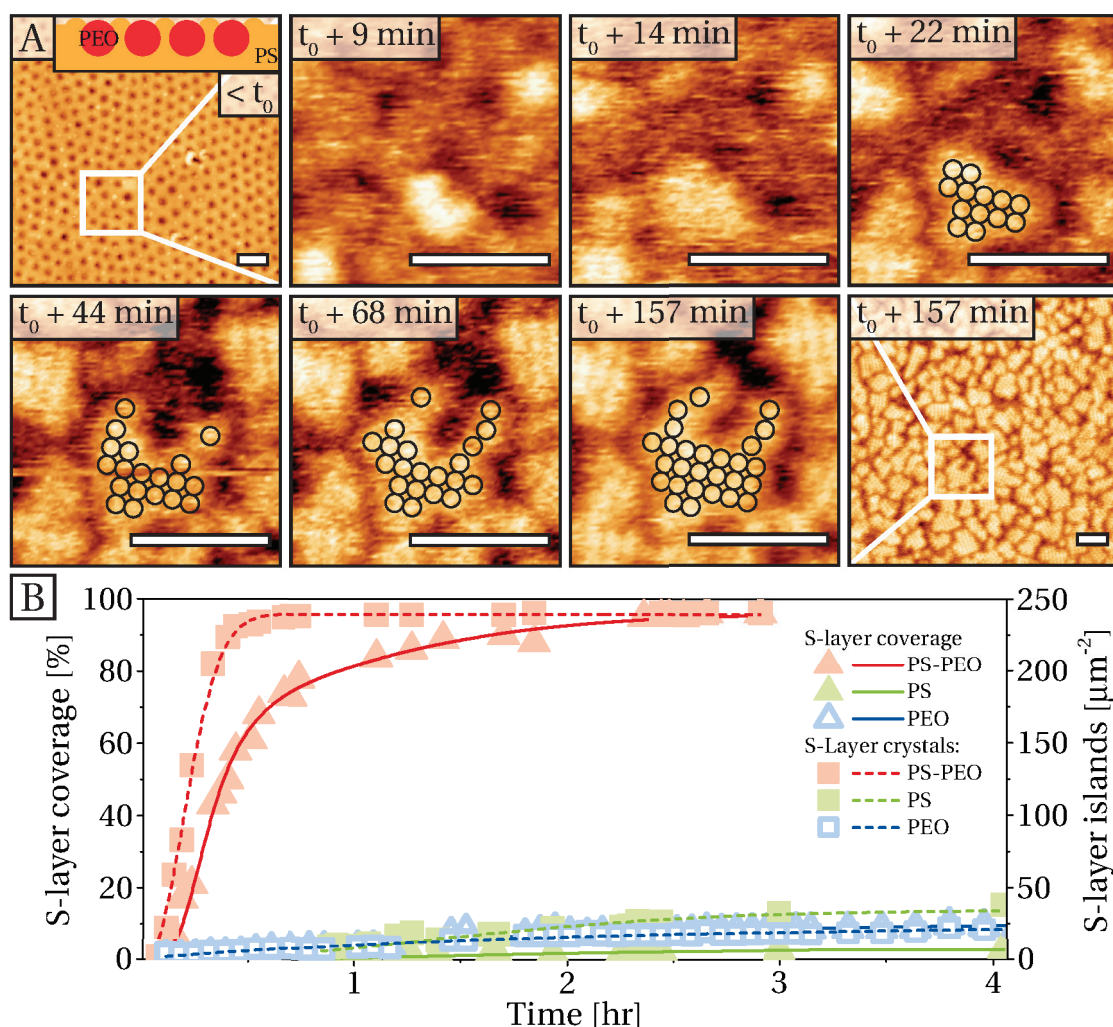


Figure 4.8 – (a) Snapshots of continuous *in situ* AFM measurements show the nucleation and subsequent growth of the S-layers on the PS-*b*-PEO substrates. The nucleation and growth is concentrated on the PS areas, while avoiding the PEO areas. The scale bars represent 100 nm. (b) Graphical representation of the dynamics of S-layer nucleation and growth on PS, PS-*b*-PEO and PEO. Note that S-layers do not, in fact, nucleate and grow on PEO substrates, but instead originate in solution.

4.3 *In situ* dynamics of S-layer self-assembly on PS-*b*-PEO BCP thin films

To get a better understanding of the observed confinement effect in Figure 4.4, the dynamics of self-assembly have been resolved using high speed *in situ* AFM, as shown in Figure 4.8a. The snapshots are a selection of images taken continuously during the self-assembly process. The images show that crystalline S-layers began nucleation solely on PS regions and that throughout the subsequent growth of the islands, the hydrophilic PEO regions were mostly avoided. However, note that the final S-layer coverage exceeds the total surface area comprised

4.3. *In situ* dynamics of S-layer self-assembly on PS-*b*-PEO BCP thin films

of PS, which means that the S-layer islands eventually extend onto the unfavorable PEO domains.

The blurred nature of the substrate in the first several snapshots is due to the mobility of the adsorbed SbpA monomers at the solid-liquid interface. The darker spots indicate areas of low protein adsorption and they correlate with the PEO regions of the PS-*b*-PEO BCP template. The observation that SbpA monomers do not adsorb onto the PEO domains indicates a strong preferential adsorption of SbpA on PS domains, in line with *ex situ* and *in situ* observations in Figures 4.6 and 4.7.

The adsorption of SbpA proteins from bulk solution to the solid-liquid interface is generally a much slower process than the incorporation of already adsorbed proteins into existing crystalline S-layers. Growth of crystalline S-layers therefore occurs almost exclusively through surface transport of SbpA monomers and subsequent attachment to existing crystalline S-layers^[162]. The difference in SbpA adsorption on the nanoscale PS and PEO blocks is thus proposed as the main driving force behind the confinement of S-layers to the PS domains.

In Figure 4.8b, the self-assembly of SbpA proteins on PS-*b*-PEO dot patterns is compared with the self-assembly on pure PS and PEO. The total S-layer coverage and the number of S-layer islands are compared independently, indicated by the solid and dashed lines, respectively. The experimental data is fitted using the same models as presented in the previous chapter. The number of S-layer islands is fitted with the model from Equation 3.7. The parameters $N_{SL,m}$, $k_1 \times k_2$ and t_c obtained from this fit, are used as fixed input parameters for the fit of the total S-layer coverage. For the PS-*b*-PEO BCP substrate, the number of S-layer islands is well described by the theoretical model, however, the total coverage is not well described by the model from Equation 3.8. This is most likely due to the non-homogeneous nature of the substrate, where the initial growth rate on the PS domains is different from the growth on the PEO domains in a later stage. Instead, the experimental data is fitted with the model from Equation 4.1, which is still based on Equation 3.8 from the previous chapter, but incorporates two different growth rates, i.e. R_1 and R_2 . From the fit to the experimental data, the relative contributions of both growth rates, indicated by $N1_{T,m}$ and $N2_{T,m}$, are 73 % and 27 %, respectively. This corresponds very well with coverage of the PS and PEO domains, which is approximately 75 % and 25 %, respectively.

$$A_{tot}(t) = N_{SL,m} \left(1 - e^{-\frac{k_1 \cdot k_2 \cdot (t-t_c)^2}{2 \cdot N_{SL,m}}} \right) \cdot \left(N1_{T,m} \cdot \tanh^2 \left(\frac{R1 \cdot (t-t_c)}{2\sqrt{N1_{T,m}}} \right) + N2_{T,m} \cdot \tanh^2 \left(\frac{R2 \cdot (t-t_c)}{2\sqrt{N2_{T,m}}} \right) \right) \quad (4.1)$$

A comparison of the total S-layer coverage over time (solid line in Figure 4.8b) clearly shows that the rate of self-assembly is enhanced on PS-*b*-PEO, compared to its homogeneous constituents. The enhanced rate of self-assembly can be either due to an increased rate of nucleation or an increased growth rate of existing S-layer islands. In order to distinguish between these two

Chapter 4. *In situ* dynamics of protein self-assembly on block copolymer thin films

factors, the number of S-layer islands is compared independently, indicated by the dashed lines in Figure 4.8b.

On PS-*b*-PEO BCP thin films, the steady state nucleation rate is ~60 times higher than on homogeneous PS. By dividing the total coverage by the number of crystals within that area, the area per crystal is calculated. From this, the maximum growth rate per crystal can be obtained. On PS-*b*-PEO, the maximum growth rate is ~100 times higher than on homogeneous PS. This shows that both nucleation and growth of S-layer islands is enhanced by about two orders of magnitude on PS-*b*-PEO BCP thin films compared to homogeneous PS, which is its most favorable constituent.

Note that S-layers do not in fact nucleate at the PEO-liquid interface, but originate in solution and adsorb fully formed on the PEO surface, see also Figure 4.6b. Consequently, the rate of nucleation and growth of S-layer islands on PEO is not considered in the analysis presented above.

Kumar et al. found a similar enhanced adsorption for large biomolecules such as bovine immunoglobulinG (IgG) and fluoresceinon isothiocyanate (FITC) on PS-*b*-PMMA substrates^[28,29,90,172–174]. Furthermore, the enhanced adsorption was localized to the PS regions close to the chemical interface between the PS and PMMA domains, with the local concentration inversely proportional to the distance from the PS-PMMA interface. This was interpreted as a flux of molecules from an unfavorable substrate with high interfacial energy, towards a favorable substrate where the interfacial energy is lower. It was thus concluded that the enhanced adsorption of proteins was related to the chemical contrast between the PS and PMMA domains.

The observed difference in SbpA adsorption affinity between PS and PEO domains indicates a similar chemical contrast. And a similar enhanced SbpA concentration near the PS-PEO interface is proposed. Given the high density of PS-PEO interfaces within the PS-*b*-PEO dot pattern and the exponential dependency of the rate of S-layer self-assembly on the local SbpA surface concentration, even a moderate concentration enhancement near the interface would result in a drastically increased rate of S-layer self-assembly. Furthermore, the resulting gradient in the rate of S-layer nucleation perpendicular to the PS-PEO interface will favor parallel alignment of the S-layer crystals, because an orientation parallel to the PS-PEO interface maximizes the number of nuclei per S-layer crystal that are located within the area of enhanced concentration.

The experimental results in this study are therefore in line with an enhanced surface concentration near the PS-PEO interface, as both an increased rate of S-layer self-assembly (Figure 4.5) and a preferential orientation parallel to the PS-PEO interface (Figure 4.4) have been clearly observed.

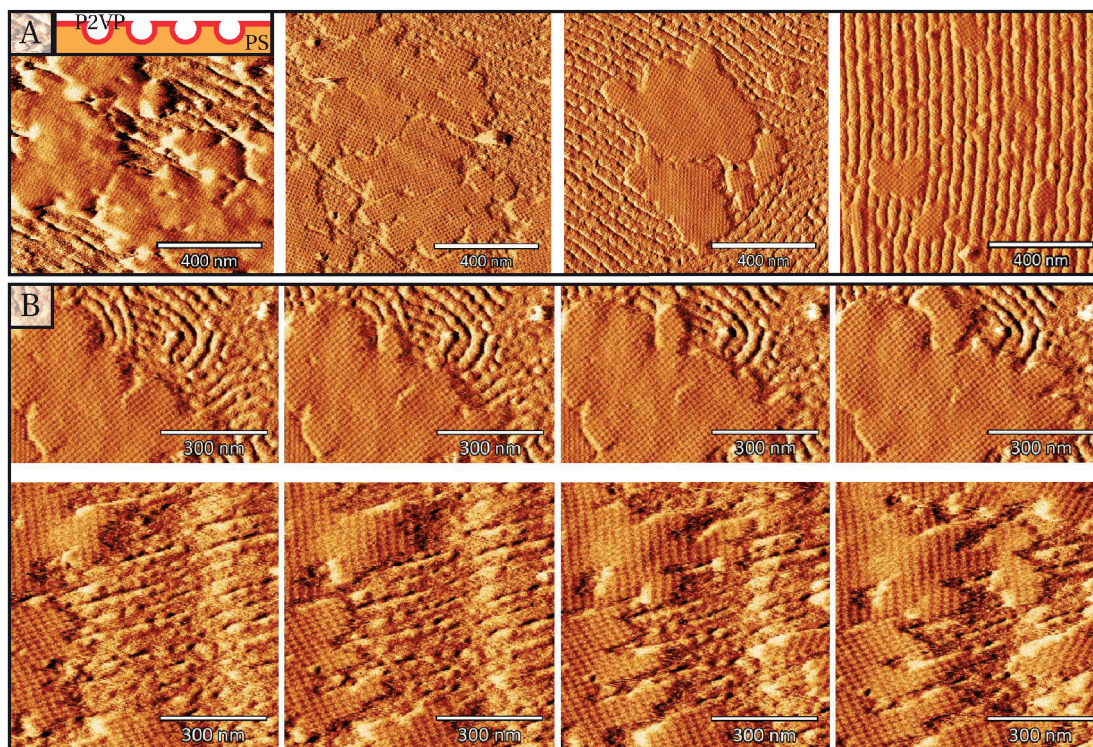


Figure 4.9 – (a) *In situ* AFM amplitude error images of S-layers on PS-*b*-P2VP striped patterns. There is a preferred crystal orientation of 0° and 45° with respect to the underlying striped pattern. (b) Real-time series of *in situ* AFM amplitude error images of S-layers on top of PS-*b*-P2VP curved striped patterns on silicon. The bottom row shows S-layers on PS-*b*-P2VP linearly striped patterns on faceted sapphire (top: PS-*b*-P2VP, 27k; bottom: PS-*b*-P2VP, 58k). An increased growth rate of the S-layer islands along the direction of the underlying striped patterns leads to “finger-shaped” S-layer assemblies.

4.4 Chemical versus physical contrast

The PS-*b*-PEO samples in Figures 4.2a, 4.4a (top) and 4.8b have a strong hydrophilic-hydrophobic chemical contrast as well as a slight physical height difference of 3 nm to 6 nm (*in situ*) between the PS and PEO areas. In order to determine the relative importance of the chemical and physical contrast between PS and PEO, a second series of experiments was designed.

The growth of S-layers was studied on reconstructed PS-*b*-P2VP patterns, which have a more pronounced physical contrast of 15 nm to 25 nm (*in situ*) between domains, but lack the associated chemical contrast. Figure 4.9 shows *in situ* AFM images of S-layers on PS-*b*-P2VP striped patterns. Since no confinement of the S-layer crystals is observed, one can conclude that a chemical contrast between the polymer blocks is necessary to achieve complete confinement of the S-layer crystals. This is in line with our hypothesis that the confinement of S-layers is driven by a difference in non-specific adsorption of SbpA due to the contrasting hydrophobicity of the BCP domains. Since the PS-*b*-P2VP surface is chemically homogeneous,

it is not expected that SbpA adsorption rates will vary over the surface.

Although the S-layer crystals are not confined to specific domains of the substrate, an analysis of the growth dynamics reveals that most S-layers exhibit a preferential orientation and growth direction parallel to the direction of the trenches, Figure 4.9c. However, the low nucleation rate on PS-*b*-P2VP substrates results in insufficient S-layer islands to allow for a statistical approach as is applied to the PS-*b*-PEO substrates in Figure 4.5.

4.5 Directed collagen self-assembly

In the previous sections, it has been shown that chemically nanopatterned substrates can be used to control protein crystallization at the nanoscale. Such a bottom-up approach to control position and orientation of individual molecules is of great general interest. Especially in the field of tissue engineering the challenge is to control the assembly of functional molecules at the nanoscale, over macroscopic areas.

In this section it is shown that nanopatterned PS-*b*-PEO striped patterns can be used to direct the self-assembly of collagen molecules. Collagen is the main structural protein in vertebrates and collagen films have been widely used as substrate to facilitate cell adhesion or as adhesion matrix for specific collagen-binding proteins^[175–177]. For this reason, a high level of local control over the position and orientation of collagen fibers is desired.

Self-organization of collagen at the solid-liquid interface was achieved by drop casting collagen growth solution (100 mM KCl, 10 mM Na₂HPO₄ and collagen at 1 or 3 μg ml⁻¹, pH of 4.1) on top of a horizontally placed substrate, following Narayanan et al.^[178]. The collagen (*PureCol-S, Advanced BiomatrixA*) contains 97 % collagen type I with a remainder of 3 % collagen type III at a total concentration of 3.1 mg ml⁻¹. This stock solution was diluted to 36 μg ml⁻¹ in a phosphate buffer (10 mM Na₂HPO₄, pH 4.1) and stored at 4 °C until further use. Previously described PS-*b*-PEO BCP thin films and freshly peeled mica (Grade V-1 Muscovite, *Electron Microscopy Sciences*) were used as substrate and incubation took place in a sealed container containing MilliQ water to prevent evaporation of the growth solution. Subsequent *in situ* AFM imaging was carried out using the *Dimension FastScan* AFM from with *FastScan-DAFM* probes (both from *Bruker*).

The adsorption of collagen to chemically homogeneous mica substrates was compared with chemically heterogeneous PS-*b*-PEO substrates. The samples were exposed to collagen for several hours and the resulting collagen arrangement at the solid-liquid interface is shown in Figure 4.10.

On the PS-*b*-PEO thin films, the collagen molecules assembled into bundles that were aligned along the local direction of the underlying BCP film. In contrast, at the same experimental conditions, the collagen molecules formed loose bundles at the mica-liquid interface that were relatively mobile. At higher concentrations of 3 μl ml⁻¹, the collagen self-organized into unidirectional bundles at the mica-liquid interface.

Based on this, it can be concluded that linearly patterned PS-*b*-PEO BCP thin films can be

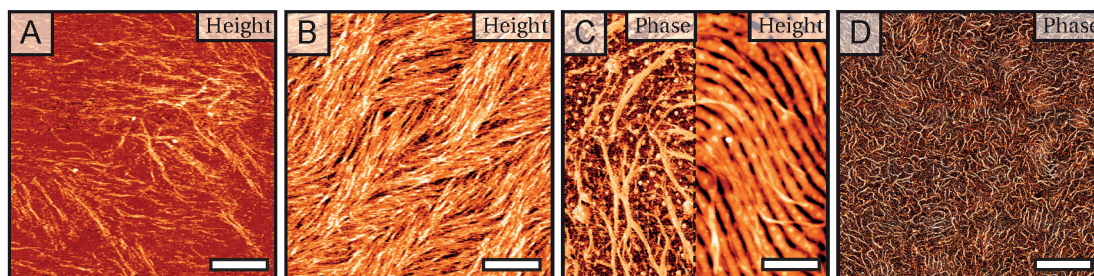


Figure 4.10 – (a-b) *In situ* AFM images of collagen at $1 \mu\text{gml}^{-1}$ (a) and $3 \mu\text{gml}^{-1}$ (b) on mica. Collagen fibers show self-assembly into interconnected bundles with a clear preferential direction. The directionality arises from the interaction between individual collagen molecules and is not related to the underlying substrate. The scale bars represent 200 nm. (c-d) *In situ* AFM images of collagen at $1 \mu\text{gml}^{-1}$ on PS-*b*-PEO BCP thin films. The collagen bundles align themselves along the local direction of the underlying PS-*b*-PEO film. The scale bar in (c) represent 200 nm and in (d) 2 μm .

used to immobilize and impose a predetermined directionality on the organization of collagen molecules into extended bundles. The templating effect of chemically heterogeneous BCP thin films is thus not limited to small self-assembling molecules, but is as well applicable to long flexible molecules such as collagen.

4.6 Conclusion and Outlook

The hierarchical bottom-up approach that has been presented here, can be used to direct the self-assembly of crystalline S-layers through non-specific interaction with nanostructured block copolymer thin films. Self-assembled PS-*b*-PEO BCP thin films feature ordered, chemically distinct nanodomains, which can be used to control both position and orientation of self-assembled crystalline S-layers. A comparison between chemically heterogeneous PS-*b*-PEO and chemically homogeneous reconstructed PS-*b*-P2VP BCP thin films has shown that a chemical heterogeneity is required to confine the self-assembly of S-layers to specific areas. Furthermore, whereas the internal crystalline structure of the self-assembled S-layers is not affected by the confinement provided by the PS-*b*-PEO BCP thin film substrate, the orientation of the S-layer crystals shows a preference for parallel alignment along the underlying PS lines. *In situ* results on the dynamics of S-layer self-assembly show that the protein adhesion and subsequent nucleation rate is significantly enhanced on substrates exhibiting chemically contrasting nanodomains such as PS-*b*-PEO BCP thin films. The contrasting adsorption affinity of SbpA proteins onto PS and PEO areas and the resulting local concentration increase on PS areas, has been proposed as the driving force behind the increased rate of self-assembly.

Experiments with collagen self-assembly on chemically heterogeneous PS-*b*-PEO BCP thin films have shown that collagen fibers closely follow the underlying pattern. The hierarchical bottom-up approach presented in this chapter is thus more generally applicable, as it can be extended to large flexible molecules.

Chapter 4. *In situ* dynamics of protein self-assembly on block copolymer thin films

This opens up new possibilities for the control of protein crystallization and patterning using readily available and low-cost materials. In contrast to established techniques for collagen alignment^[177,179], the versatility of nanostructured BCP thin films can provide local control over the collagen assembly. This could provide macroscopic adhesion templates for tissue engineering with local nanoscale control over the adhesion and migration of live cells^[175].

The directed self-assembly of S-layers, in combination with genetic programming, opens up possibilities for the bottom-up fabrication of high-density nanoscale scaffolds, that can be used to periodically express specific binding sites at predetermined areas. This is especially useful in the field of protein detection arrays and the functional enhancement of surface immobilized enzymes, where precise control over density and binding site spacing is important^[172,173,180,181].

5 S-layers as Biomimetic Template for Mineralization of CaCO_3

S-layers have been introduced in chapter 3: *Bacterial surface layers*, where their self-assembly properties were discussed in detail. In this chapter, the focus is shifted instead to their functional properties. Not only are S-layers known for their robust self-assembly, it is speculated that S-layers have catalytic properties with regards to the nucleation of CaCO_3 and that they play a role in natural CO_2 sequestration processes.

The reasoning that precedes this assumption starts with the observation of so called whiting events in fresh water lakes and marine environments^[182–185]. These events are named after the milky haze caused by massive CaCO_3 precipitation over the course of several months. A typical whiting event in Lake Michigan, USA in 2001 is shown in Figure 5.1.

There are three schools of thought on the origin of these events. Whiting events are driven either by direct precipitation of CaCO_3 from supersaturated concentrations of Ca^{2+} and CO_3^{2-} ^[186,187], by the re-suspension of pre-existing sediment^[183,185] or by a biologically medi-

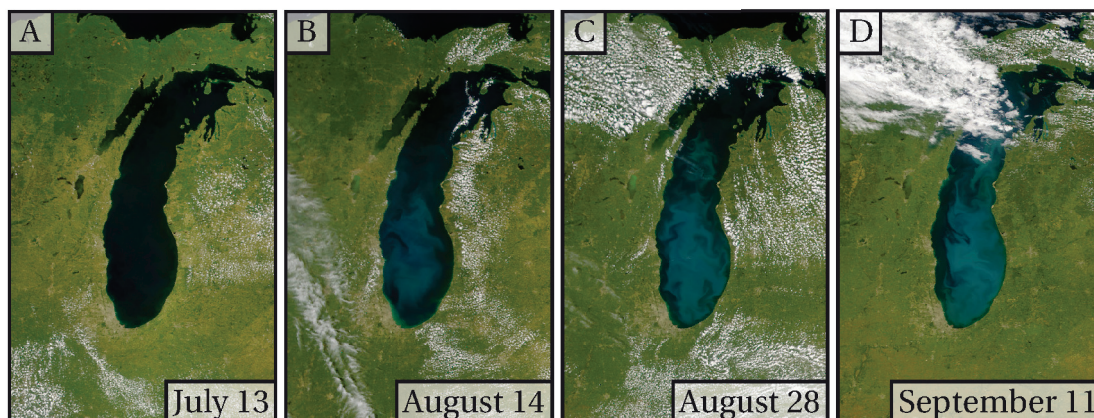


Figure 5.1 – Satellite imagery of a whiting event in Lake Michigan, USA in 2001. Source: NASA Earth Observatory.

Chapter 5. S-layers as Biomimetic Template for Mineralization of CaCO₃

ated process^[43,182,184,188–190].

In nutrient poor marine environments such as the Bahama Banks, whiting events are thought to originate through a re-suspension mechanism^[185]. However, in nutrient rich environments such as the fresh water North American Great Lakes (Figure 5.1), the formation of CaCO₃ has been found to coincide both in time and location with blooms of cyanobacteria^[43,182,184,188–190] and a biologically mediated mechanism is thought to be involved.

The main mechanism through which cyanobacteria trigger the precipitation of CaCO₃ is thought to involve their photosynthetic capabilities. The synthesis of organic material within the cells involves the uptake of HCO₃⁻ from the aquatic environment, which is internally dissociated into CO₂ and OH⁻. The CO₂ is used in the photosynthesis process whereas the OH⁻ is actively removed from the interior. This drives a pH increase in the local environment surrounding the bacteria, which in turn increases the supersaturation of Ca²⁺ and CO₃²⁻ with respect to CaCO₃^[43,190].

Obst et al.^[191] investigated the nucleation rate of calcite in the absence and presence of cyanobacteria and under light and dark conditions. It was found that the nucleation rate in the presence of cyanobacteria under dark conditions was still increased compared to the reference where no cyanobacteria were present^[191]. This suggests a passive mechanism that facilitates the formation of CaCO₃. It is thought that the catalytic properties are related to the structural and chemical properties of the S-layers that encompasses the bacteria. Understanding the passive role that S-layers play in the precipitation of CaCO₃ could help elucidate the archeological record of carbonate sediments^[192] and open up novel methods of atmospheric CO₂ sequestration^[42].

To further study the specific catalytic properties of S-layers, it is important that they are isolated from the effects of the internal bacterial metabolism. This is done by isolating the S-layer proteins and trigger recrystallization *ex vivo*.

In this work the formation of CaCO₃ on S-layers is studied using a set of novel and complementary techniques. Structural information about the S-layer and the biomineralization products is obtained by *in situ* AFM. This makes it possible to track at the nanoscale in real time the formation of CaCO₃ structures at the S-layer-liquid interface. *In situ*, as well as *ex situ*, X-ray Absorption Spectroscopy (XAS) is used to provide a chemical analysis of the mineralization products^[193]. This technique is extremely sensitive to the chemical composition and different polymorphs of the mineralization products^[194]. Moreover, by maintaining a continuous flow of liquid over the sample surface at one side, and Ultra High Vacuum (UHV) conditions at the other^[115,117,195], it is possible to directly observe the formation of CaCO₃ under naturally occurring supersaturations, i.e. far below the experimental concentrations that are obtainable with traditional techniques.

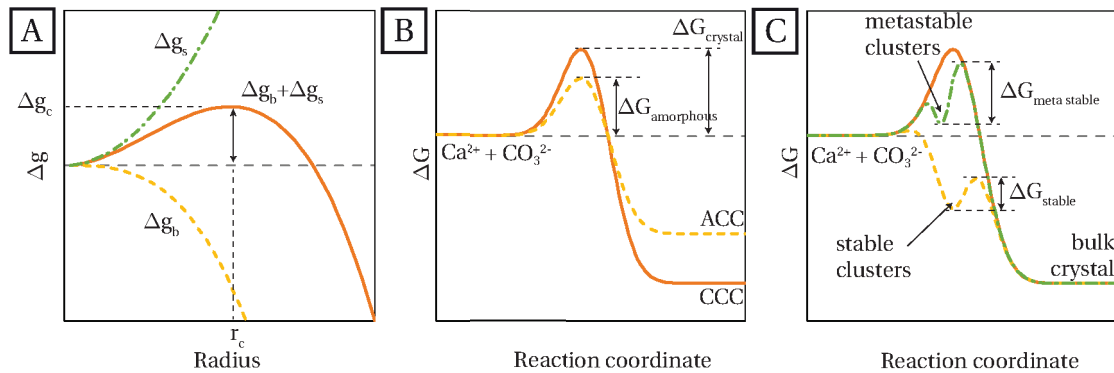


Figure 5.2 – (a) The opposing terms of the bulk and surface terms leads to a maximum in free energy when the pre-nucleation embryo reaches the critical radius. Only then a continuing growth of the nucleus will lead to a decrease in total free energy. (b) The free energy barrier to nucleation can differ among polymorphs of the same material. Whereas Amorphous Calcium Carbonate (ACC) can have a lower barrier to nucleation, Crystalline Calcium Carbonate (CCC) is typically thermodynamically more stable. (c) Variations in the surface free energy with size can lead to local and global minima in the free energy diagram. A combination of (b) and (c) can lead to a variety of reaction pathways.

5.1 Biomineralization of CaCO₃

Although the formation of CaCO₃ has been thoroughly studied and the number of research papers related to this topic is enormous, the exact mechanism of nucleation and crystallization remains elusive. In this section, a brief overview is given of Classical Nucleation Theory (CNT) and the latest research into the biomineralization of CaCO₃. The experimental results are then discussed in view of the current understanding of CaCO₃ mineralization.

The phase transition of matter through the formation of small pre-nucleation embryos of a new low free energy phase (CaCO₃), within the bulk of an old high free energy phase ($\text{Ca}^{2+} + \text{CO}_3^{2-}$), is called nucleation. The formation of an interface between these phases carries an interfacial free energy penalty, Δg_s , that is only compensated by the bulk free energy, Δg_b , after a certain critical radius is reached. This is graphically depicted in Figure 5.2a.

The existence of a critical radius creates an energy barrier to nucleation, as shown in Figure 5.2b. This energy barrier depends on the properties of the bulk phases α and β , as well as on the nature of the interface between the two. For this reason, different polymorphs of the same mineral can have different barriers to nucleation.

Lastly, the growth from solute ions into particles can involve structural changes. These structural changes can, in turn, affect both the bulk free energy and the interfacial free energy of the particle. This creates local energy minima, as shown in Figure 5.2c.

For a more detailed analysis on the fundamentals of nucleation theory, the reader is referred to appendix A.

5.1.1 Amorphous Calcium Carbonate (ACC) as a transient precursor state

CaCO₃ exists in several different polymorphs that have different crystalline structures^[194]. However, Ca²⁺ and CO₃²⁻ can be prevented from fully crystallizing by a number of factors. For example, a very rapid nucleation and growth, the incorporation of other species or the presence of a specific interface. What results is Amorphous Calcium Carbonate (ACC) that has a non-crystalline internal structure.

ACC can form prior to the formation of Crystalline Calcium Carbonate (CCC), and this has been reported in many biomineralization systems^[35,196-204]. By using free energy diagrams such as shown in Figure 5.2b, this can be understood as a lower energy barrier to nucleation, ΔG , for ACC compared to crystalline polymorphs. Subsequent transformation to thermodynamically more stable crystalline phases occurs either by direct crystallization^[196,204], or indirectly through a dissolution and reprecipitation reaction^[33]. It is also possible that multiple pathways to crystallization occur simultaneously^[205].

Control over the stability of ACC can proceed through confinement^[201,202]. When the curvature of the confining volume is of the same order as the critical radius of the nucleus, the increased solid-crystal interface has a stabilizing effect. Alternatively, the presence of cavities much larger than the critical radius of the nucleus can, under the right circumstances, inhibit nucleation. This can be used to favor the transformation of ACC into a single calcite crystal, as opposed to numerous small crystals^[200].

Alternatively, the interaction with organic molecular additives or substrates can provide control over the transition of ACC into crystalline polymorphs through the selective stabilization of a specific polymorph^[206] or amorphous state itself^[203]. Considering Figure 5.2a, this can be seen as the polymorph-selective lowering of Δg_s or Δg_b . This will lower the barrier to nucleation for that specific polymorph, as is shown in Figure 5.2a. Again, multiple pathways can occur simultaneously. For example, ACC is first stabilized using confinement, with subsequent crystallization controlled through the specific interaction with organic substrates^[199].

The structural nature of ACC has been subject of many studies and numerous structures have been proposed, ranging from semi-ordered^[207-209] to fully amorphous^[210] or even liquid-like^[211-213].

The notion of semi-ordered ACC originates with the observation of distinct ACCs that have low-level ordering at length scales similar to the three dominant anhydrous crystalline polymorphs, i.e. calcite, vaterite and aragonite. This order could be related to the presence of molecular additives as explained before. Alternatively, the specific structure of ACC can originate with prenucleation clusters that have a specific structure related to the conditions under which they formed. ACC then forms through aggregation of these prenucleation clusters and thus inherits the structural properties of these clusters^[207-209]. When ACC is completely amorphous, this is usually attributed to the extreme supersaturations at which such ACC is often produced, i.e. the ACC nucleates at time scales that prevent even moderate ordering to occur^[210].

Recent studies have predicted the presence of an ion-dense liquid phase within an ion-poor solution phase, that forms through liquid-liquid separation^[213,214]. When the nucleation of

crystalline phases can be suppressed until the concentration reaches levels that enable the decomposition into the ion-dense and ion-poor solution phase, subsequent ACC formation can take place within the liquid-like ion-rich phase. Suppression of crystallization can be achieved by stabilization of the liquid-like precursor states through a polymer-induced liquid-precursor (PILP) process^[211,215].

Both the presence of semi-ordered ACC and the presence of liquid-like states of CaCO₃ have been related to the presence of stable prenucleation clusters in solution. However, the observed stability of such clusters is in contrast with the metastability of the nucleus, as predicted by CNT^[207-209,216]. In the following section this will be discussed in more detail.

5.1.2 Prenucleation clusters

Prenucleation clusters are observed for the formation of CaCO₃ from supersaturated solutions of Ca²⁺ and CO₃²⁻^[208,217]. Ion potential measurements indicate a negligible energy barrier between clusters and free ions and as such identified these clusters as true solutes^[208,216]. Aggregates of such ACC clusters have properties that are inherited from the consisting prenucleation clusters. Depending on the solution equilibria that existed during prenucleation cluster formation, these ACC aggregates crystallize into either calcite or vaterite^[207]. This is the basis for the notion of semi-ordered ACC as discussed before.

Theoretical work has been done in order to identify the nature of these stable non-classical solutes. It has been proposed that such solute clusters are, in fact, liquid-like ionic polymers of Ca²⁺ and CO₃²⁻^[218]. Work by Wallace et al.^[214] has taken this one step further and shows that a dense liquid phase can coexist with an ion-poor solution phase and that both phases are metastable with respect to solid CaCO₃^[214]. Simulations show that the coexistence of these two phases results in liquid-like ion clusters that are similar to the experimentally observed pre-nucleation clusters. It also corresponds well with the observations of liquid-like precursor states to crystallization.

An alternative and more classical description of prenucleation clusters revolves around the influence of solvation layers around these nanoscopic particles and the water content within. The rough surface of these particles is thought to disturb the structured solvation layers and, in this way, reduces the interfacial free energy to the level of thermal energy fluctuations. Furthermore, the size-dependent water content of these particles results in a barrier to the formation of ACC compared to its crystalline bulk counterparts at radii less than about 4 nm^[217].

5.1.3 Organic-inorganic interfaces

Interfaces can have a pronounced influence on nucleation reactions. It is known that neutral molecules are often present in higher concentrations at interfaces, compared to charged and strongly hydrated ion species. Recently, it has been shown that this is also the case for doubly charged CO₃²⁻ ions, which have been found to accumulate in the region near the air-water interface^[219]. Such a local concentration enhancement near interfaces could have significant

implications for the heterogeneous nucleation of carbonate species.

Furthermore, the presence of organic substrates are known to influence biomineralization^[34]. It is known that certain charged groups can affect the nucleation rate. Special interest has been given to polysaccharides, which have been found on numerous biomineralizing substrates. Based on a systematic comparison of different polysaccharide species, the effective surface charge emerged as the determining factor for the nucleation rate of CaCO₃ through a lowering of the thermodynamic barrier to nucleation^[39].

The rate of nucleation depends both on a thermodynamic and a kinetic barrier to nucleation. The latter of which is, among other factors, also subject to the presence of specific functional groups at the solid-liquid interface. Preferential ion binding at the interface can affect the kinetic barrier to nucleation and trigger the nucleation of ACC in place of thermodynamically more stable calcite^[220].

Adding complexity to the picture of heterogeneous nucleation at organic interfaces, it has been found that the interaction between functional groups at the organic substrate is of importance as well. Specific arrangements of functional groups at the solid-liquid interface can facilitate better binding transport of molecules from the solvent to the interface, and thus lower the kinetic barrier to nucleation. Important is that such emergent behavior, arising from the interaction of multiple distinct and possibly individually less important functional groups, can have profound effects on the total rate of nucleation^[32].

Clearly, the heterogeneous nucleation at interfaces can greatly enhance the rate of nucleation. By introducing a favorable surface geometry, this effect can be further increased. Specifically, for the case of cylindrical pores, there is an optimal pore width that can dramatically maximize the rate of nucleation^[221,222]. The existence of such a maximum pore size is a result of two opposing mechanisms that govern the total nucleation rate. The barrier to nucleation within a pore will increase for a larger pore width, whereas the barrier to nucleate out of a pore has an opposite relation to the pore width.

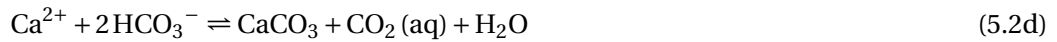
5.2 Guidelines for controlled CaCO₃ formation

In natural environments, CaCO₃ formation starts with the absorption of CO₂ into water according to Equation 5.1. From there, the now dissolved CO₂ reacts with water to form H₂CO₃, which can then dissociate into HCO₃⁻ and CO₃²⁻ (Equation 5.2). Finally, carbonate ions can react with calcium ions in solution to form CaCO₃.

$$\frac{P_{\text{CO}_2}}{[\text{CO}_2](\text{aq})} = k_H = 29.76 \text{ atm/mol} \times 1 \quad @ \quad 25^\circ\text{C} \quad (5.1)$$

5.2. Guidelines for controlled CaCO₃ formation

The amount of dissolved CO₂ depends on the partial pressure of CO₂ in the atmosphere and is governed by the Henry constant, k_H ^[223].



Dissolved CO₂ reacts with H₂O to form CO₃²⁻ through intermediates of H₂CO₃ and HCO₃⁻. CO₃²⁻ then combines with Ca²⁺ to form CaCO₃^[223].

Thus, these precipitation reactions have the counter-intuitive result that CaCO₃ mineralization results in an equal amount of CO₂ formation^[42,224].

Controlled nucleation at the S-layer-liquid interface requires exposure to precise concentrations of both Ca²⁺ and CO₃²⁻ ions. There are two experimental methods that can be used to achieve this.

CaCl₂ can be introduced to an aqueous solution which is then exposed to an atmosphere of CO₂, similar to the natural process of CaCO₃ formation. In practice, this can be done by confining in a closed environment the Ca²⁺ containing solution together with solid (NH₄)₂CO₃ (ammonium carbonate), which decomposes in ammonia and CO₂^[33]. This method is easy to use and allows for a slow increase in the CO₃²⁻ concentration.

However, in this process the CO₂ partial pressure of the air is not directly controlled and will quickly reach high concentrations. It is therefore difficult to mimic low natural atmospheric CO₃²⁻ concentrations.

An alternative is to introduce CaCl₂ together with NaHCO₃ directly to the solution. This enables direct control over the final concentration, and the absence of solid and gaseous components makes it compatible with a continuous flow setup. An equilibrium with atmospheric conditions can be achieved by imposing a continuous flow, which connects the measurement volume with a reservoir in contact with air.

Sample preparation

Depending on the sample size, a droplet containing CaCl₂ is either deposited on top of the sample, or the sample is suspended on top of a sitting droplet on a hydrophobic substrate such as fresh parafilm.

At concentrations below the homogeneous nucleation limit of calcite, these two methods are interchangeable. However, this is not the case once homogeneous nucleation takes place, i.e. gravity will pull the nuclei that form in solution towards the bottom. In order to distinguish between homogeneous and heterogeneous nucleation, the sample surface must therefore be

facing downwards, i.e. be suspended upside down on top of a sitting droplet.

Alternatively, the homogeneous nucleation can be suppressed in favor of heterogeneous nucleation by working at very small supersaturations. The ratio between heterogeneous and homogeneous nucleation rate can be expressed as $\frac{J_{het}}{J_{hom}}$, as shown in Equation 5.3.

$$\frac{J_{het}}{J_{hom}} = \frac{Ae\left(-\frac{1}{k_B T} \cdot \frac{\alpha_{het}^3}{\sigma^2}\right)}{Ae\left(-\frac{1}{k_B T} \cdot \frac{\alpha_{hom}^3}{\sigma^2}\right)} = e^{\frac{1}{k_B T} \left(\frac{\alpha_{hom}^3 - \alpha_{het}^3}{\sigma^2}\right)} \quad (5.3)$$

For a constant interfacial energy ($\alpha_{hom} - \alpha_{het}$), this ratio sharply increases with decreasing supersaturation σ . At low supersaturations, heterogeneous nucleation is therefore increasingly favorable compared to homogeneous nucleation.

In order to measure *ex situ* the mineralization products that originate at the sample-liquid interface, the liquid containing the Ca²⁺ and CO₃²⁻ ions has to be removed without interfering with the CaCO₃ present at the sample surface. To prevent any solution from drying, and in the process create additional CaCO₃ at the sample surface, the liquid is removed quickly by absorption with tissue paper. The residual liquid film is diluted by adding ultrapure milliQ water, which is then immediately removed in the same manner. This procedure is typically repeated three times.

Although bulk crystalline CaCO₃ is insoluble and should therefore remain unaffected by the washing procedure, it is possible that transient or more soluble polymorphs of CaCO₃ are inadvertently removed from the sample surface. For this reason, direct *in situ* observation is preferable whenever possible.

5.3 Using optical microscopy to determine the nucleation rate of CaCO₃ on S-layers

As mentioned in the introduction, S-layers are thought to have catalytic properties with regards to the formation of CaCO₃. In this section, the ability of S-layers to catalyze the nucleation of CaCO₃ is determined using nucleation rate experiments. These experiments are performed in collaboration with Dr. Mina Hong and Prof. Jim de Yoreo (Physical Sciences Division, PNNL, United States). The results shown in Figure 5.3 enable a direct comparison with other organic interfaces^[39].

S-layers are recrystallized on mica substrates following the protocol from appendix B.2. For a more fundamental description of S-layer self-assembly, the reader is referred to chapter 3: *Bacterial surface layers*.

The steady state nucleation rate of CaCO₃ on S-layer is then determined by placing recrystallized S-layers on mica in a custom-build liquid flow cell and by exposing the solid-liquid

5.3. Using optical microscopy to determine the nucleation rate of CaCO₃ on S-layers

interface to equal concentrations of CaCl₂ and NaHCO₃ at a steady flow rate. The affinity of the S-layer substrate is determined by optically identifying the number of nuclei as function of time^[33,39].

The flow rate is set sufficiently high, so that the nucleation of CaCO₃ at the S-layer surface is not limited by mass transport from solution. Furthermore, the samples were placed upside down in the flow cell to prevent homogeneously nucleated nuclei to land on the surface.

An inverted optical microscope is used to collect a series of sequential optical images from which the number of calcite nuclei as function of exposure time can be determined using general image recognition software. From this, the steady state nucleation rate J (number of nuclei per unit area per unit time) is calculated.

Classical Nucleation Theory (CNT) relates the kinetic, E_A , and thermodynamic, ΔG_c , barriers to nucleation to the steady state nucleation rate J :

$$J = A e^{\frac{-E_A}{k_B T}} e^{\frac{-\Delta G_c}{k_B T}} \quad (5.4)$$

Here, the barrier to heterogeneous nucleation, ΔG_c , is defined as:

$$\Delta G_c = B \alpha_{het}^3 / \sigma^2 \quad (5.5)$$

$$\alpha_{het} = C_{cs}(\alpha_{cs} - \alpha_{sl}) + C_{cl}\alpha_{cl} \quad (5.6)$$

$$B = f \cdot \frac{\Omega^2}{k_B^2 T^2} \quad \text{with } f = \frac{4C_a^3}{27C_v^2} \quad (5.7)$$

With $\sigma = \ln[\frac{\{Ca^{2+}\}\{CO_3^{2-}\}}{K_{sp}}]$ the supersaturation of the solution relative to the nucleating solid. K_{sp} is the solubility product and $\{Ca^{2+}\}$ and $\{CO_3^{2-}\}$ are the activities for calcium and carbonate ions respectively which are calculated from the molar concentrations of CaCl₂ and NaHCO₃ using the software package *Visual MINTEQ v3.1*^[225].

The total interfacial free energy α_{het} depends on the surface-ratio between the interfacial free energies of the various interfaces, i.e. the crystal-solid interface (α_{cs}), the solid-liquid interface (α_{sl}) and the crystal-liquid interface (α_{cl}), as shown in Equation 5.6. C_{cs} is defined as the relative part of the surface in contact with the substrate, and C_{cl} is defined as the relative part that is in contact with the liquid.

The constant B depends on the shape and orientation of the nucleating crystal, where C_a is a constant that relates the surface of the nucleus to r^2 , and C_v is a constant that relates the volume of the nucleus to r^3 , i.e. $A = C_a \cdot r^2$ and $V = C_v \cdot r^3$.

A straightforward method to determine the thermodynamic barrier to nucleation ΔG_c is to make a linear regression of $\ln(J)$ versus σ^{-2} , which, according to CNT, gives a slope equal to $B \cdot \alpha_{het}^3$. Thus, the difference in free energy between the substrate-liquid and substrate-calcite interfaces ($\alpha_{cs} - \alpha_{sl}$) can be determined:

$$\alpha_{cs} - \alpha_{sl} = \left(\sqrt[3]{-\text{slope} \cdot \frac{1}{f} \cdot \frac{k_B^3 T^3}{\Omega^2} - C_{cl}\alpha_{cl}} \right) / C_{cs} \quad (5.8)$$

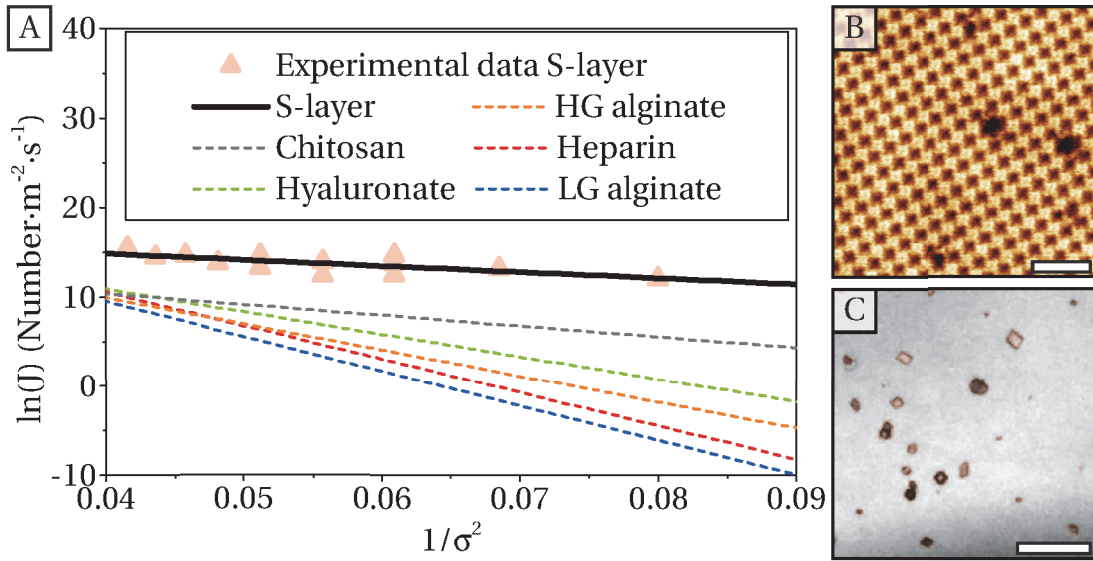


Figure 5.3 – Nucleation rate experiments of calcite on S-layers. (a) The steady-state nucleation rate J of CaCO_3 on S-layers as function of supersaturation σ is shown in red triangles (experimental data) and the black line (linear regression) and is compared to a variety of organic substrates. Steady state nucleation rates for Heparin, LG alginate, HG alginate, Hyaluronate and Chitosan are reproduced from Giuffrè et al.^[39]. Experimentally feasible nucleation rates limit the accessible supersaturations to equimolar solutions of CaCl_2 and NaHCO_3 from about 9 mM to 34 mM, $1/\sigma^2$ of 0.09 and 0.04, respectively. (b) A high-resolution AFM image that shows the P4 crystalline structure of the S-layers at the mica-liquid interface. The scale bar represents 40 nm. (c) Optical microscopy image on which the steady-state nucleation rates from (a) are based. The crystals are marked in red. The scale bar represents 50 μm . Note that even the smallest crystals shown in (c) are many times larger than the entire AFM image in (b).

Discussion of results

In Figure 5.3a, $\ln(J)$ is plotted versus σ^{-2} . A linear regression of the data gives a slope of -69 ± 21 . However, in order to calculate $\alpha_{cs} - \alpha_{sl}$, the shape and orientation of the calcite nuclei must be known, i.e. C_a , C_v , C_{cl} and C_{sl} .

From Figure 5.3c it can be seen that the heterogeneously nucleated calcite crystals have the same shape as during homogeneous nucleation, i.e. rhombohedral. From the calcite unit cell parameters, the angle of these rhombohedral shapes is known to be approximately 120° and 60° . As a first approximation, it is assumed that upon nucleation, these crystals already possess such a rhombohedral crystalline shape and that all sides are equal. Deviations from this approximation will be discussed later.

A rhombohedral calcite crystal with 60° angles gives $C_{cl} = 5/6$, $C_{cs} = 1/6$, $C_v = \sqrt{1/2}$ and $C_a = 3\sqrt{3}$. With this information, and using literature values $\Omega = 6.13 \times 10^{-23} \text{ cm}^3$ and $\alpha_{cl} = 109 \text{ mJ/m}^2$, $\alpha_{cs} - \alpha_{sl}$ is calculated using Equation 5.8 and found to be -345 mJ/m^2 .

This means that, at a concentration of 10 mM for both CaCl_2 and NaHCO_3 , the thermodynamic barrier to heterogeneous nucleation is $5.6 k_B T$, compared to a barrier to homogeneous

5.3. Using optical microscopy to determine the nucleation rate of CaCO₃ on S-layers

nucleation of 234 k_B T.

As $\alpha_{het}^3 \propto 1/f$ and $\Delta G_{c,het} \propto \alpha_{het}^3 \& f$, in this analysis, the obtained barrier to heterogeneous nucleation is independent of f and remains at 5.6 kT for any shape or orientation. However, it follows that the difference between α_{cs} and α_{sl} depends strongly on C_{cl} and C_{cs} , and thus the choice of nuclei shape and orientation. By approximating the shape of the nuclei as an equal sided rhombohedral, α_{sl} was found to be 345 mJ/m² larger than α_{cs} . This means that S-layers strongly prefer to be in contact with calcite crystals instead of water and that this is the main driving force behind the increased nucleation rate on S-layers.

An alternative assumption for the nucleus shape could be that, upon nucleation, the particles are shaped like half spheres on top of the substrate. Using the same analysis for this alternative assumption, $f \approx 28$ and $\frac{C_{cs}}{C_{cl}} = 0.5$. What follows is that the interfacial free energy of the solid-liquid interface is only 111 mJ/m² larger than α_{cs} .

Considering the porous nature of the S-layers, it would be interesting to consider the fact that nucleation originates within the S-layer pores and as such creates the peculiar geometry where the crystal-solid interface is larger than the crystal-liquid interface. Considering for example $\frac{C_{cs}}{C_{cl}} = 2$, would lead to the situation in which the solid-liquid interfacial free energy is about equal to the crystal-solid interfacial free energy. In this case, the increased nucleation rate would be solely driven by a reduction solid-liquid interface.

This short example shows that in order to have a good understanding about the underlying mechanisms that drive nucleation, high resolution data of the nucleation events is necessary to determine the shape and orientation of the nuclei.

In Figure 5.3a the nucleation rate on S-layers is compared with nucleation rates on various polysaccharide substrates obtained by Giuffre et al.^[39]. An increased nucleation rate on Chitosan compared to Heparin or Alginate was explained by the near neutral surface charge of Chitosan, which is unfavorable to water and thus favors crystal interfaces instead, i.e. $\alpha_{cs} < \alpha_{sl}$. In case of Heparin or Alginate, their negative surface charge favors hydration, resulting in a much lower α_{sl} .

S-layers from *B. Spaericus* CCM 2177 are charge neutral at the outer face while positively charged at the inner surface with which it is bound to the bacterial cell wall^[72,164,181]. This orientation is mimicked by reassembling S-layers on mica substrates, which are negatively charged^[132] and thus bind the positively charged side of the S-layer, exposing the charge neutral side of the S-layer to the solution. Following the same reasoning from Giuffre et al., this explains the enhanced nucleation of CaCO₃ on S-layers through a large α_{sl} .

Obst et al.^[191] have studied the formation of CaCO₃ on live cyanobacteria of the strain *Synechococcus leopoliensis* PCC 7942 that express S-layers at their outer cell surface. Their analysis suggested a lowering of α_{cs} on S-layers, driven by Ca²⁺ adsorption by carboxylate and phosphodiester surface groups^[191,226]. This was independently corroborated with chemically sensitive force probe measurements by Obst et al.^[227], which show that S-layers preferentially adsorb calcium ions.

Chapter 5. S-layers as Biomimetic Template for Mineralization of CaCO₃

Although the S-layers expressed by these cyanobacteria are not the same as the S-layers that have been studied in this work, it is likely that the mechanism underlying the formation of CaCO₃ is similar.

Where the work from Obst et al. focussed on the absorption of Ca²⁺, the preferential ion adsorption or accumulation at or near interfaces can also include CO₃²⁻, as was shown by Lam et al.^[219]. Smeets et al. showed that such preferential ion binding at interfaces can influence not only the interfacial free energy, and thus the thermodynamic barrier to nucleation, but the kinetic barriers to nucleation as well^[220]. This follows as well from the results shown in Figure 5.3, where the value of the nucleation rate at the y-intercept, i.e. at infinite supersaturation, is a measure for kinetic barrier to nucleation.

This shows that, although the underlying reason for the increased nucleation rate on S-layers is not yet fully understood, there are several mechanism that can explain the experimentally observed nucleation rates of CaCO₃ on S-layers in Figure 5.3. Independent of the underlying mechanism is the fact that the excess free energy for calcite nucleation on S-layers is exceptionally low. The resulting relatively weak dependency on the supersaturation means that especially at low – i.e. naturally occurring – concentrations, S-layers catalyze the nucleation of calcite remarkably well. These results therefore demonstrate that S-layers catalyze the formation of CaCO₃, even when removed from the *in vivo* environment and immobilized on inorganic substrates.

There are several limitations to the technique used here, which should be discussed. First, the nucleation rate depends strongly on the concentration that is used, i.e. the nucleation rate J depends exponentially on the barrier to nucleation, which in turn depends inversely quadratic on the supersaturation. This means that the direct determination of the nucleation rate at low concentrations becomes increasingly problematic. For example, at naturally occurring concentrations of 10 mM Ca²⁺ and 3.2 mM CO₃²⁻, the nucleation rate J would approach only 10 /mm²/day nucleation events. Secondly, the use of an optical microscope limits the size of the observable crystals as all structures below the resolution limit of the microscope remain invisible. It is therefore not possible to directly observe the shape of the CaCO₃ nuclei in their initial stages, which is necessary to understand the underlying mechanism that drives the nucleation of CaCO₃.

As discussed in section 5.1, recent observations of CaCO₃ formation at the nanoscale have reported both the existence of stable prenucleation clusters^[207–209,214,216–218] and a variety of non-equilibrium amorphous precursor phases^[33,35,196–215]. This brings into question the applicability of CNT when it comes to biomineralization at the nanoscale and simple extrapolation of observed nucleation rates beyond the originally used range of concentrations should be avoided.

To reach concentration regimes that more closely resemble naturally occurring values, the high sensitivity of AFM and XAS techniques can be used. As discussed in section 1.1, AFM can distinguish topographical changes on the S-layer surface at the nanoscale, both *ex situ*

5.4. Using x-ray absorption spectroscopy to measure CaCO₃ formation on S-layers

Table 5.1 – Peak positions of the calcium L_{II} and L_{III} absorption edges for different calcium containing compounds. With a₂ the L_{III} edge, b₂ the L_{II} edge and a₁, b₁ the crystal field peak of each edge^[194,203,232,233].

Compound	a ₁	a ₂	b ₁	b ₂
Calcite	347.4 & 348	349.3	351.4	352.6
Vaterite	347.5 & 348.1	349.3	351.4	352.6
Aragonite	347.7 & 348.5	349.3	351.2 & 351.5 & 351.8	352.6
CaCl ₂	348.1	349.1	351.4	352.4

as well as *in situ*. The lack of chemical contrast, however, prevents direct identification of CaCO₃ and its various polymorphs such as calcite, vaterite and aragonite^[194]. The unique properties of XAS, as discussed in section 1.3, make this technique sensitive to the local atomic environment and therefore the crystalline structure of the sample. By combining the complementary techniques of AFM and XAS, it is possible to characterize the topography as well as the internal atomic configuration of mineralizing CaCO₃ structures at the nanoscale and at naturally relevant concentrations.

Using *in situ* continuous flow conditions, the environment of marine lakes can be simulated, while maintaining compatibility with aforementioned techniques. The concentration of Ca²⁺ and HCO₃⁻ in natural lake water is reported to be around 10 mM and 3.2 mM, respectively, at a pH of around 7.5 and 10 °C^[228–230]. This corresponds to a supersaturation $\sigma \approx 2.4$ relative to calcite and $\sigma \approx -2.4$ relative to ACC^[225,231].

5.4 Using x-ray absorption spectroscopy to measure CaCO₃ formation on S-layers

The nature of X-ray Absorption Spectroscopy (XAS) makes this technique extremely sensitive and able to distinguish between different polymorphs of the mineralization products. The fundamentals of this technique have been discussed in section 1.3.

5.4.1 Specifics of CaCO₃ absorption spectra

The XAS spectrum of the calcium L_{II} and L_{III} edge from CaCO₃ containing compounds is especially feature rich. This is due to the relative small energy difference between the L_{II} and L_{III} transitions in combination with pronounced crystal field splitting, as detailed in section 1.3.1: *Fundamentals of XAS*. For the case of CaCO₃ containing compounds, this produces a very characteristic L_{III} and L_{II} XANES spectrum as is shown in Figure 5.4 and Table 5.1.

The sensitivity of the spectra with respect to the local environment around the absorbing calcium atom makes XANES measurements a very effective tool to identify the crystal structure of CaCO₃ containing compounds^[34,203,233–235].

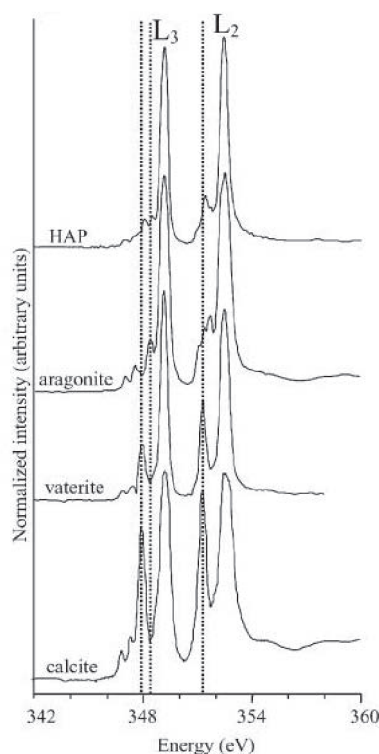


Figure 5.4 – XAS spectra of various CaCO₃ polymorphs and hydroxyapatite (HAP). Modified from reference [194].

The lack of a detailed theoretical description of the XANES region limits the quantitative interpretation of the XANES spectra. The agreement between experimental data and simulations remains relatively poor compared to the EXAFS region. However, it is not always necessary to have a full understanding of the numerous and often complex features of the XANES spectra. In many cases, it is sufficient to compare the shape and peak positions of the XANES spectrum with reference spectra from known materials in order to identify the compounds within the sample^[116,234,236]. This “fingerprinting” provides a straightforward analysis method, which, in combination with the high sensitivity of XANES for the coordination chemistry, makes it a robust method to obtain chemical information of CaCO₃, *ex situ* as well as *in situ*.

From Figure 5.4, several observations can be made. Calcite and aragonite can be distinguished rather easily due to the different calcium coordination number originating from the different crystal structure of the two polymorphs. The aragonite XANES spectrum has additional peaks preceding the main *a*₂ and *b*₂ absorption peaks. The calcite and vaterite spectra are relatively similar and can only be distinguished by a slight variation in the crystal field peaks preceding the main L_{III} peak.

Alternatively, the peak intensity of the various absorption peaks can be used to differentiate between spectra. However, this is less reliable because the intensity depends in part on the analysis and background subtraction.

5.4. Using x-ray absorption spectroscopy to measure CaCO₃ formation on S-layers

Table 5.2 – Properties related to CaCO₃ nucleation for various concentrations of CaCl₂ and NaHCO₃: The concentration of CaCl₂, the concentration of NaHCO₃, the supersaturation with respect to calcite, the thermodynamic barrier to homogeneous nucleation, the thermodynamic barrier to heterogeneous nucleation on S-layers, the nucleation rate on S-layers, the ratio between the homogeneous nucleation rate and the nucleation rate on S-layers.

CaCl ₂ (mM)	3.5	10	50
NaHCO ₃ (mM)	3.5	3.2	50
σ_{calcite}	2.11	2.44	5.46
$\Delta G_{c,\text{homogeneous}}$ (k _B T)	518	386	77
$\Delta G_{c,S\text{-layer}}$ (k _B T)	15.6	11.6	2.32
$J_{S\text{-layer}}$ (m ⁻² s ⁻¹)	8.15	417	4.54 · 10 ⁶
$J_{\text{homogeneous}}/J_{S\text{-layer}}$	9.80 · 10 ⁻²¹⁹	1.60 · 10 ⁻¹⁶³	3.50 · 10 ⁻³³

Experimental procedures

The samples are exposed to three different concentrations. At natural concentrations (10 mM CaCl₂ and 3.2 mM NaHCO₃), slightly below natural concentrations (3.5 mM CaCl₂ and 3.5 mM NaHCO₃), and at high concentrations where instantaneous homogeneous nucleation is expected (50 mM CaCl₂ and 50 mM NaHCO₃). The values for the nucleation rate on S-layers and thermodynamic barriers to homogeneous and heterogeneous nucleation are calculated for each of these concentrations in Table 5.2.

5.4.2 *Ex situ* XAS of CaCO₃ on S-layers

Ex situ XAS experiments are performed to detect CaCO₃ formation on S-layer substrates that are exposed to various concentrations of CaCl₂ and NaHCO₃. The extreme sensitivity of this technique makes it possible to detect CaCO₃ at less than the equivalent of a monolayer. Furthermore, the ability to discriminate between the various crystalline polymorphs of CaCO₃, allows for the precise chemical identification of the mineralization products on the S-layer substrate.

In contrast to the optical nucleation rate experiments from the previous section, XAS is not limited by a minimum crystal size in order to detect the CaCO₃ products. This makes it possible to investigate CaCO₃ formation below the nucleation limit for macroscopic crystals, i.e. at naturally occurring concentrations.

CaCO₃ is detected by recording the Total Fluorescence Yield (TFY) and Total Electron Yield (TEY), as described in section 1.3. For samples measured *ex situ*, the TEY signal usually gives a better signal-to-noise ratio, whereas for *in situ* measurements the x-ray absorption can only be recorded by detecting the TFY signal.

Sample preparation

For a detailed description of the purification of S-layers and the composition of the S-layer

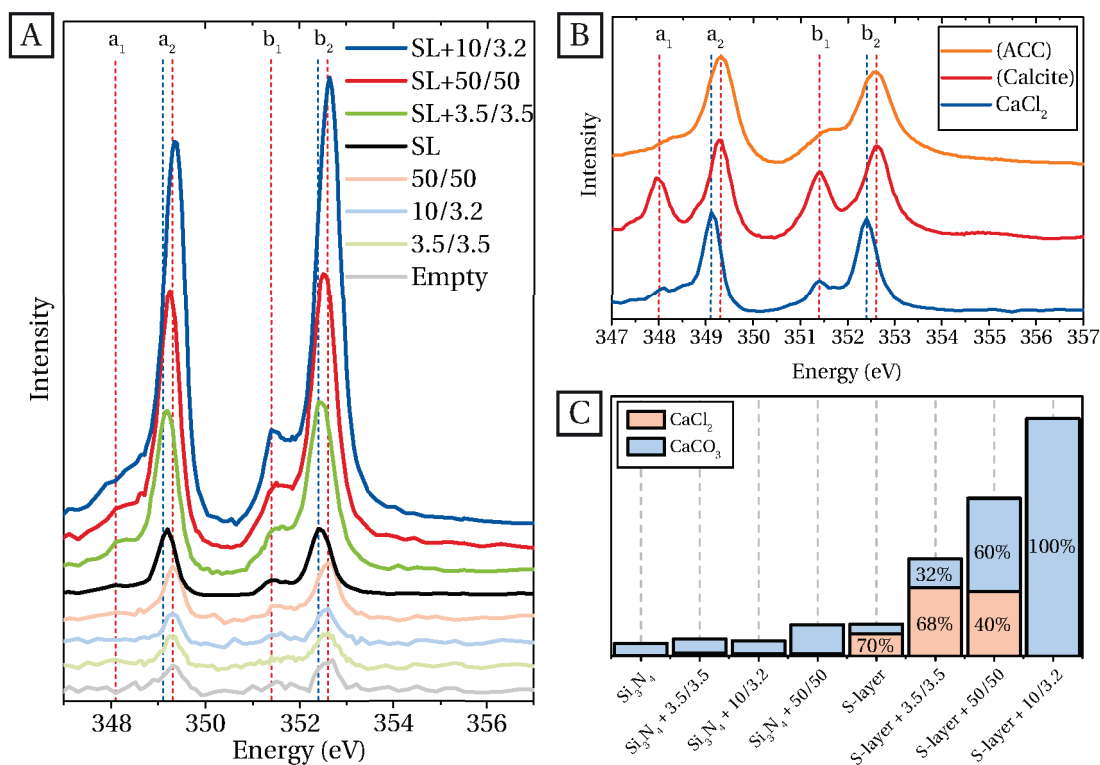


Figure 5.5 – TEY x-ray absorption spectra of samples exposed for 1 h to concentrations of CaCl₂ and NaHCO₃ as indicated, i.e. 10/3.2 corresponds to 10 mM CaCl₂ mixed with 3.2 mM NaHCO₃. The L_{III} and L_{II} absorption edge energies are compared with reference spectra of calcite and CaCl₂. The main and crystal field peak positions of the CaCl₂ and CaCO₃ reference spectra are marked by the dashed lines. **(a)** The spectra are shown without normalization so that the relative intensities can be compared. **(b)** Reference spectra that were used to determine the main and crystal field peak positions corresponding to CaCl₂ and CaCO₃. **(c)** A histogram that shows for the spectra shown in (a) the relative contributions of CaCO₃ and CaCl₂. The substrate and the concentration of Ca²⁺ and CO₃²⁻ are indicated on the x-axis. The total amount of CaCO₃ was determined by integrating the absorption peaks in Figure 5.5a. The CaCl₂/CaCO₃ ratio was determined by dividing the area of the peaks at 349.1 eV and 352.4 eV by the area of the peaks at 349.3 eV and 352.6 eV.

growth solution, the reader is referred to Appendix B.

For S-layer formation on the Si₃N₄ membranes, the support frames are placed on top of a sitting drop of about 50 μ l, which is placed on clean parafilm. This prevents any contaminating particles in solution from falling down to the sample surface.

The samples are kept in contact with the S-layer growth solution for 5 h, after which the samples are gently washed three times with Milli-Q water (18.2 M Ω cm at 25 $^{\circ}$ C). This is done by placing a droplet on top of the sample and subsequently removing it through absorption with a piece of tissue paper that is gently touched to the side of the droplet.

Exposure to CaCl₂ and NaHCO₃ to induce CaCO₃ formation follows the protocol as described

5.4. Using x-ray absorption spectroscopy to measure CaCO₃ formation on S-layers

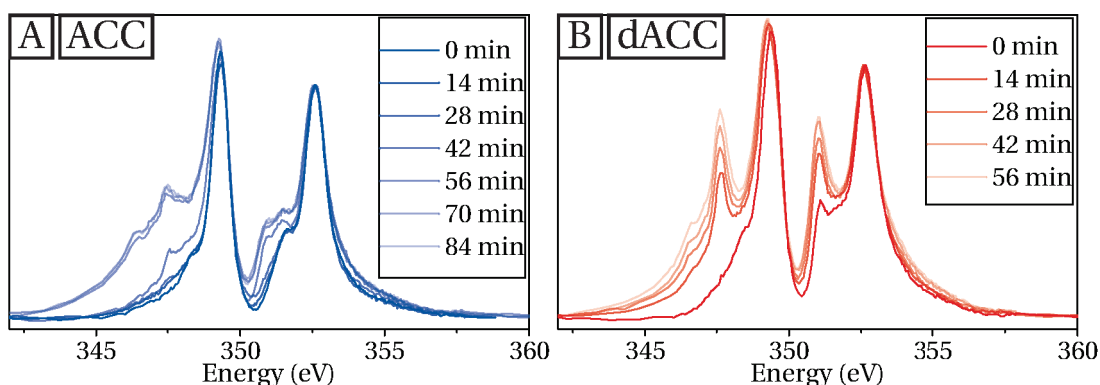


Figure 5.6 – Change of ACC reference spectra during x-ray exposure.

in section 5.2.

Discussion of results

S-layer samples and pristine Si₃N₄ reference substrates are exposed to varying concentrations of CaCl₂ and NaHCO₃ for 1 h. The resulting XAS of the calcium L_{II} and L_{III} absorption edges are displayed in Figure 5.5. The data is displayed non-normalized so that the absolute intensities, and therefore total calcium content, can be compared.

In all calcium absorption spectra, one can distinguish several features with different physical origins. The main peaks at a₂ and b₂ are related to the absorption at the L_{III} and L_{II} edges, respectively. These peaks are preceded by a set of smaller peaks indicated by a₁ and b₁, which are related to the crystal field that arise from the symmetry of the atoms that surround the absorbing Ca²⁺ ion^[118,232]. Using these spectroscopic features, it is possible to distinguish between different polymorphs of CaCO₃. Variations in the local crystal structure affect the crystal field and result in different positions of the crystal field peaks, as is shown in Table 5.1^[194,203,232,233]. The absence of crystalline structure, i.e. ACC, can be identified by the lack of crystal field peaks.

From the spectra in Figure 5.5a it quickly becomes clear that the intensity and energy position of the absorption peaks depends strongly on both the presence of S-layers and the concentration of CaCl₂ and NaHCO₃ to which the sample is exposed. There are several observations to be made from these spectra, as shall be discussed in detail in the next paragraphs.

The pristine Si₃N₄ sample, without S-layer and which is not exposed to any CaCl₂ or NaHCO₃, still has two absorption peaks at positions corresponding to CaCO₃. This indicates that the extreme sensitivity of this technique is able to identify trace amounts of CaCO₃ due to contamination of the samples. Possibly from trace contamination originating from the phosphor powder used to identify the location of the x-ray beam.

When looking at the Si₃N₄ samples that do not contain S-layers, the calcium L_{II} and L_{III} absorption peaks do not increase in intensity after exposure to 3.5 mM CaCl₂ and 3.5 mM

Chapter 5. S-layers as Biomimetic Template for Mineralization of CaCO₃

NaHCO₃ or 10 mM CaCl₂ and 3.2 mM NaHCO₃, indicating that all Ca²⁺ ions are removed from the sample during the washing procedure and none of it is immobilized at the sample surface. When a Si₃N₄ sample without S-layers is exposed to 50 mM CaCl₂ and 50 mM NaHCO₃, the L_{II} and L_{III} absorption peak intensity is slightly increased. This indicates that now some calcium is immobilized at the sample surface, i.e. not removed during the washing procedure. Although the nucleation rate of calcite on Si₃N₄ is not known, it is expected that once the concentration is increased to the point where even homogeneous nucleation occurs instantaneously, which is the case for 50 mM CaCl₂ and 50 mM NaHCO₃, heterogeneous nucleation will take place as well. This would then result in calcite crystals immobilized at the Si₃N₄ surface, which corresponds well with the slight increase in the observed calcium absorption spectrum on Si₃N₄ samples without S-layers exposed to these concentrations.

The nucleation rate experiments discussed in the previous section and shown in Figure 5.3 and Table 5.2, indicate a nucleation rate of calcite on S-layers of only hundreds of events per m² per second when exposed to 10 mM CaCl₂ and 3.2 mM NaHCO₃. This means that for an XAS spot size of 100 μm × 100 μm, only about 0.02 calcite crystals are to be expected after 1 h of exposure to 10 mM CaCl₂ and 3.2 mM NaHCO₃. However, from Figure 5.5a, it is clearly visible that the intensity of the calcium L_{II} and L_{III} absorption peaks is much higher when S-layers are exposed to these concentrations, compared to the S-layer reference sample. Furthermore, the main peak at b₂ is shifted, from an adsorption energy similar to the bare S-layer sample, towards an absorption energy more similar to the CaCO₃ references in Figure 5.5b. Taken together, this points towards the formation of CaCO₃ on S-layers during exposure to even minute concentrations of CaCl₂ and NaHCO₃, which cannot be explained by simple nucleation rate experiments.

Interestingly, when S-layers are exposed to 10 mM CaCl₂ and 3.2 mM NaHCO₃, a larger amount of CaCO₃ is present at the sample surface as compared to when S-layers are exposed to the higher initial concentration of 50 mM CaCl₂ and NaHCO₃. This could be explained by the fact that, similar to what was observed on the bare Si₃N₄ samples, only concentrations of 50 mM CaCl₂ and NaHCO₃ trigger homogeneous nucleation. Instead of increasing the amount of calcium at the sample surface, this actually has the opposite effect. Once nucleation of calcite occurs, the concentration of Ca²⁺ and CO₃²⁻ quickly drops to the solubility limit of calcite, which is about 0.9 mM CaCl₂ and NaHCO₃. This then inhibits the formation of CaCO₃ at the S-layer surface.

For the S-layer samples in Figure 5.5a that are exposed to CaCl₂ and NaHCO₃, there is no crystal field peak at position a₁. At position b₁, there is the presence of a shoulder, or, in the case of S-layers exposed to 10 mM CaCl₂ and 3.2 mM NaHCO₃, a small peak. This is very similar to the ACC reference spectrum in Figure 5.5b. In contrast, Figure 5.4 shows that all crystalline CaCO₃ polymorphs have clearly identifiable crystal field peaks around the a₁ and b₁ positions. This shows that the CaCO₃ formation on S-layers at these low concentrations is not in the form of crystalline CaCO₃, but instead has an amorphous structure.

Gong et al.^[203] have studied the biomineralization of CaCO₃ on sea urchins with *ex situ* XAS.

5.4. Using x-ray absorption spectroscopy to measure CaCO₃ formation on S-layers

Their analysis found two distinct types of ACC. One type was characterized by the absence of any peak or shoulder at the a₁ position and a shoulder at the b₁ position, and was identified as typical ACC. The other type had no peak or shoulder at the a₁ position, but had a defined peak at the b₁ position. This type was identified as a transitional phase between ACC and crystalline calcite and labeled dehydrated ACC (dACC).

In an effort to further characterize the difference between ACC and dACC, both compounds were synthetically prepared by Dr. Alejandro Fernandez-Martinez (former researcher at the Lawrence Berkeley National Laboratory and currently at the Institut des Sciences de la Terre (ISTerre), Université de Grenoble, France). Their spectra are shown in Figure 5.6. Interestingly, both ACC and dACC are found to be unstable during x-ray exposure. ACC was stable for about 60 min, after which the absorption spectrum started to change significantly. dACC is even more unstable and shows dramatic changes within about 15 min. The initial XAS spectra are characteristic of ACC and dACC. However, a detailed analysis of the peak shapes and positions suggests a subsequent decomposition of CaCO₃ into CaO.

Importantly, no such unstable behavior has been observed for any of the samples where CaCO₃ is present on top of S-layers. It can therefore be concluded that S-layers stabilize the structure of CaCO₃ and prevent it from decomposition during x-ray exposure.

In order to determine the amount of CaCO₃ formation on top of the S-layers, an effort was made to quantify the shift of the L_{II} and L_{III} peaks from absorption energies corresponding to CaCl₂ (349.1 eV and 352.4 eV) to energies corresponding to CaCO₃ (349.3 eV and 352.6 eV). The peak at the a₂ position was fitted with two voigt peaks at 349.1 eV and 349.3 eV and the peak at the b₂ position was fitted with two voigt peaks at 352.4 eV and 352.6 eV. The total area of the peaks at 349.1 eV and 352.4 eV is related to the amount of CaCl₂, whereas the total area of the peaks at 349.3 eV and 352.6 eV is related to the amount of CaCO₃ in the sample. The relative contributions are indicated by the different colors in Figure 5.5c.

This histogram clearly shows how pristine S-layers have a spectroscopic signature similar to CaCl₂. This is most likely due to the porous nature of S-layers, which prevents the CaCl₂ used in S-layer preparation to be removed completely. However, upon exposure to Ca²⁺ and CO₃²⁻, the absorption spectrum starts to resemble CaCO₃. With an increased concentration of Ca²⁺ and CO₃²⁻ directly related to more CaCO₃ formation.

In summary, these *ex situ* XAS measurements show that S-layers are able to both catalyze and stabilize the formation of amorphous forms of CaCO₃.

5.4.3 Continuous flow *in situ* XAS of CaCO₃ on S-layers

During the *ex situ* experiments discussed in the previous section, there exists the possibility that during the drying process additional CaCO₃ has formed or that structural changes in existing CaCO₃ deposits occur. To eliminate this variable, a liquid flow cell system is employed to track the evolution of CaCO₃ formation on S-layers directly *in situ*. The absorption spectrum of the calcium L_{II} and L_{III} peaks is recorded as function of exposure time to 3.5 mM equimolar

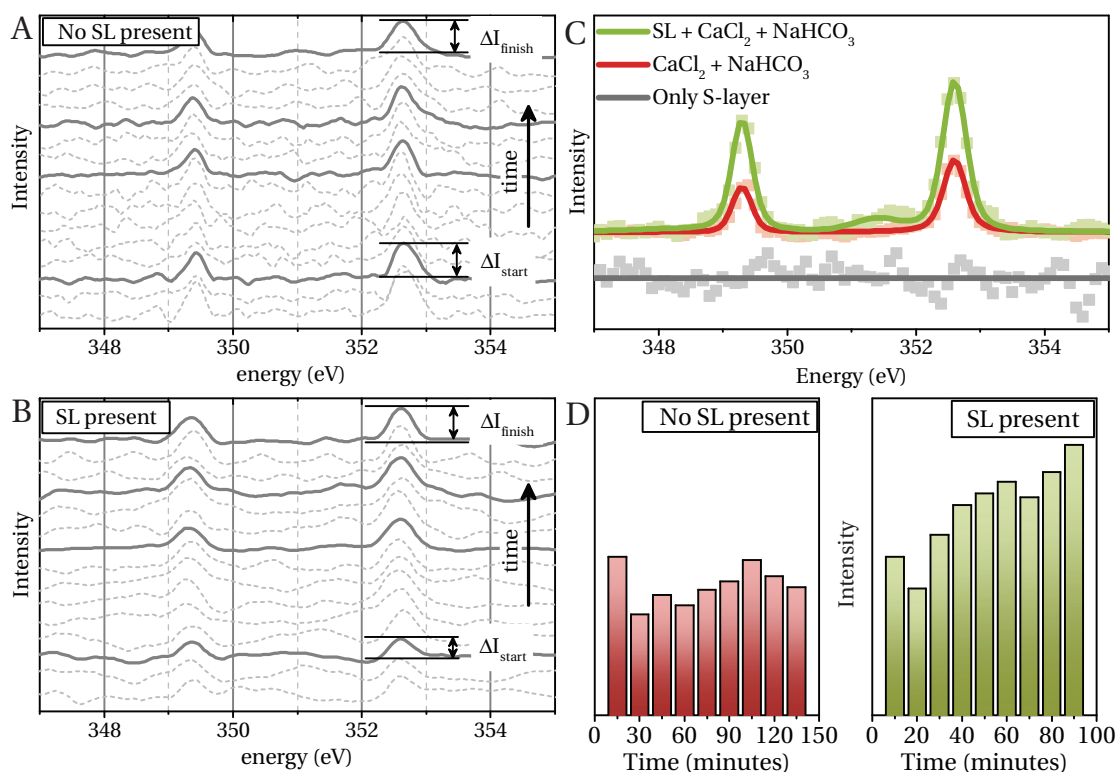


Figure 5.7 – Recording of the TFY signal during continuous flow conditions shows the evolution of the calcium L_{III} and L_{II} absorption edge. Dashed lines indicate individual recorded spectra, solid lines indicate averages of the preceding spectra up to the last average. **(a)** When no S-layers are introduced to the continuous flow, the calcium L_{III} and L_{II} absorption edge remains at constant intensity. The time interval between individual spectra is about 15 min. **(b)** When S-layers are introduced to the continuous flow, the calcium L_{III} and L_{II} absorption edge increased in intensity over time. The time interval between individual spectra is about 10 min. **(c)** Comparison of the average spectrum in the presence and absence of S-layers with a reference spectrum of only S-layers. The intensity is not normalized so that the intensities can be compared. **(d)** Histogram that shows the average intensity of the L_{III} and L_{II} peaks over time for the case where S-layers are present and when they are absent. Each histogram is scaled so that the intensity of the first spectrum is equal to 1.

concentrations of CaCl₂ and NaHCO₃.

The continuous flow setup in combination with the high sensitivity of XAS makes it possible to observe in real time the formation and immobilization of CaCO₃ within the measurement volume. The absorption intensity around the L_{III} and L_{II} edges is recorded continuously for several hours, while simultaneously a flow is maintained at the liquid side of the Si₃N₄ membrane.

Sample preparation

Si₃N₄ membranes must be mounted at least one to two days prior to the start of the liquid flow

5.4. Using x-ray absorption spectroscopy to measure CaCO₃ formation on S-layers

experiment. This is because the glue with which the membranes are kept in place must harden overnight. After this, the liquid flow cell is loaded inside the XAS measurement chamber. Lastly, the pressure inside the measurement chamber is lowered to UHV conditions, which can take up to 6 h.

Due to the delicate nature of the Si₃N₄ membranes, and the likelihood that up to 80 % will break during this process, it was decided to load bare Si₃N₄ membranes and add pre-crystallized S-layers to the solution flow once the required experimental conditions were achieved.

The use of pre-crystallized S-layers in solution made it possible to remove all Ca²⁺ ions from solution, prior to the *in situ* XAS measurements. The S-layers were crystallized in solution following the protocol that is detailed in appendix B. After this, ultra-centrifugation was used to remove the S-layers from the buffer solution that includes Ca²⁺ and resuspended in a new buffer solution that contained no Ca²⁺ ions.

Discussion of results

When 3.5 mM CaCl₂ is mixed with 3.5 mM NaHCO₃ during more than 2 h of continuous exposure, no increase in the calcium L_{II} or L_{III} absorption edges occurs at the Si₃N₄ membrane. Similar to what was expected based on the *ex situ* experiments in Figure 5.5. From Figure 5.7a and the red histogram in 5.7d it can be seen that the absorption intensity at the L_{III} and L_{II} edge remains constant over time, indicating that no heterogeneous nucleation of CaCO₃ occurs at the Si₃N₄ window.

Previous experiments shown in Figure 3.3 in section 3.2 show that pre-crystallized S-layers readily adsorb to Si₃N₄ membranes. When the solution includes 200 µgml⁻¹ pre-crystallized S-layers, Figure 5.7b and the green histogram in 5.7d clearly show an increase of about 60 % in the L_{III} and L_{II} absorption edges. This indicates the formation and immobilization of CaCO₃ within the measurement volume.

The average spectra in the absence and presence of S-layers, and the pure S-layer reference spectra are shown in Figure 5.7c. Note the absence of any calcium absorption signal for the pure S-layer reference signal. This indicates that all Ca²⁺ is removed from the S-layer samples. Therefore, addition of S-layers alone cannot explain the increase in calcium absorption signal. Furthermore, Figure 5.7c shows that the average absorption signal in the presence of S-layers has an increase in intensity just before the L_{II} peak, compared to the spectrum recorded in the absence of S-layers. This corresponds well with the *ex situ* XAS results that indicate the presence of amorphous forms of CaCO₃ at the S-layer surface in the presence of CaCl₂ and NaHCO₃. It shows that the observed crystal field peak at position b₂ in the *ex situ* XAS experiments is not a result of the drying process, but is an actual feature of the CaCO₃ formations at the S-layer-liquid interface.

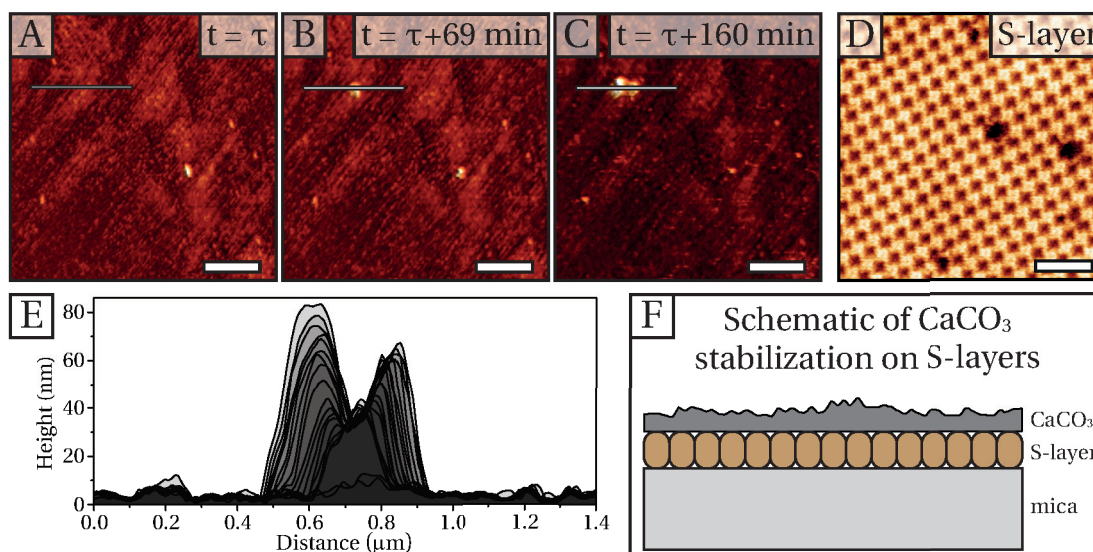


Figure 5.8 – (a-c) *In situ* continuous flow atomic force microscopy shows the growth of CaCO₃ formations on S-layers during continuous exposure to 10 mM CaCl₂ and 3 mM NaHCO₃ (equilibrated with atmospheric CO₂ levels). Scale bars represent 750 nm. (d) A high-resolution AFM image that shows the P4 crystalline structure of the S-layers at the mica-liquid interface. The scale bar represents 40 nm. (e) Line profiles of consecutive AFM images show the continuous growth of the CaCO₃ particle. The time between images is about 7.5 min. (f) Schematic that shows the layered nature of the mica-S-layer-CaCO₃ structure.

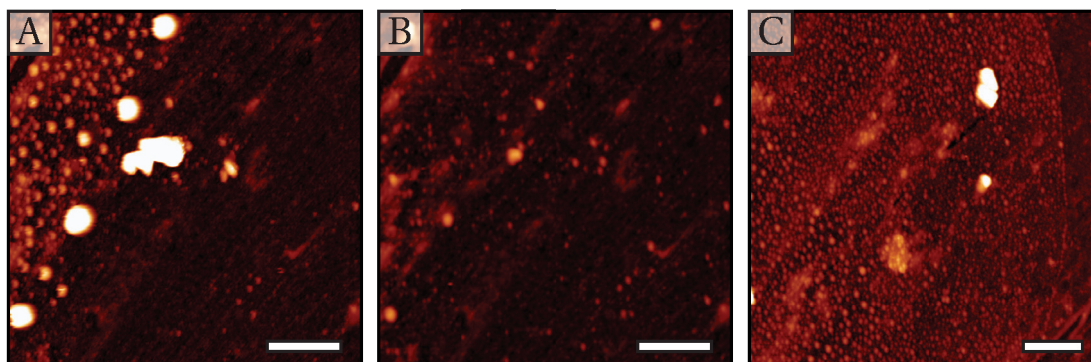


Figure 5.9 – S-layers are imaged using *in situ* Tapping Mode AFM during continuous flow conditions of 10 mM CaCl₂ and 3 mM NaHCO₃ (equilibrated with atmospheric CO₂ levels) at a rate of 5 μs^{-1} . (a) After 8 h of continuous exposure, globular CaCO₃ structures have formed on the S-layer substrate. (b) Continuous interaction with the AFM probe triggers the removal of the metastable CaCO₃ structures. (c) Similar CaCO₃ structures remain present outside the affected area. The scale bar equals 1.5 μm .

5.5 Using atomic force microscopy to image CaCO₃ formation on S-layers

A limitation of the XAS experiments that are discussed here is the large spot size of the x-ray beam, typically tens of thousands of μm^2 . The result is that only an average signal can be

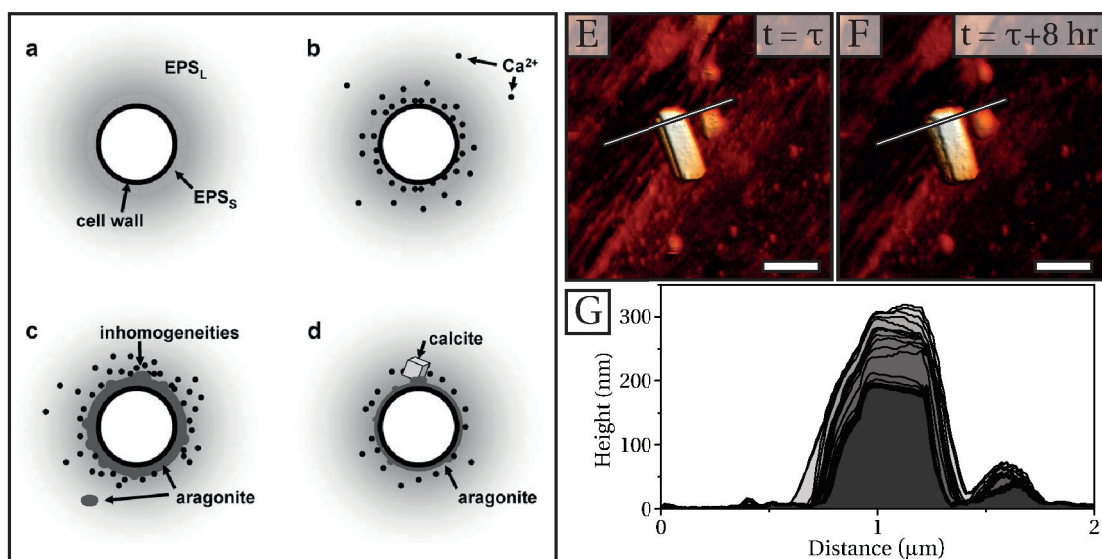


Figure 5.10 – Direct observation of calcite nucleation on top an amorphous CaCO₃ sublayer. (a-d) A schematic by Obst et al. outlining how the nucleation of an aragonite sublayer precedes the nucleation of crystalline calcite at the surface of live S-layer expressing cyanobacteria. Image reproduced from Obst et al.^[237]. (e-f) *In situ* AFM images of the S-layer-liquid interface *ex vivo* during continuous flow conditions at a rate of $5\mu\text{s}^{-1}$ of 10 mM CaCl₂ and 3 mM NaHCO₃ equilibrated with atmospheric CO₂ levels. Over the course of 8 h a rhombohedrally shaped particle is found to increase in size, consistent with the growth of a calcite nucleus as detailed in the schematic on the left. The scale bars represent 800 nm. (g) Line profiles of consecutive AFM images show the continuous growth of the calcite crystal.

obtained and specific information of individual CaCO₃ particles is unavailable.

By using *in situ* AFM techniques as described in section 1.1.2, it is possible to obtain topographical data on the CaCO₃ structures during growth at the S-layer-liquid interface.

Experimental procedures

S-layers are formed on mica substrates following the procedures from appendix B and exposed to a continuous flow of 10 mM CaCl₂ and 3 mM NaHCO₃. During this time the S-layer surface is imaged continuously by AFM using the *in situ* continuous flow cell as described in section 1.1.3.

The mica substrates were purchased from *Electron Microscope Sciences* and qualified as *muscovite mica, v-1 quality*. The original size of the mica pieces was 25 mm × 75 mm, with a thickness of 0.26 mm to 0.31 mm. From this, discs were cut with a diameter of 25 mm.

Discussion of results

As the S-layer surface is exposed only to CaCl₂ and NaHCO₃, all structures that differ from the crystalline S-layer substrate must be composed of insoluble CaCO₃.

In Figure 5.8 the nucleation and subsequent growth of a single particle is observed continu-

ously for a period of 3 h. The absence of clearly defined crystalline facets and the spherical nature of the particle suggests that it is composed of amorphous material, i.e. ACC. The initial nucleus is about 100 nm in diameter and appears within the timespan of one image. With an imaging frequency of about 7.5 min per frame, this puts an upper limit to the time it takes to form a stable nuclei. Alternatively, the particle is deposited from bulk solution during this time window. During the 3 h period, in which the same area is imaged continuously, the initial particle grows and develops from a single globular particle into a two-lobed particle. It can be speculated that the gradual nature of this transition into two distinct regions is due to a Crystallization by Particle Attachment (CPA) process where a secondary nucleation site develops on top of the existing particle.

Interesting to note is that the substrate on which the particle grows is not consistent with the typical structure of S-layers as is shown in Figure 5.8c for reference. This is evident from the lack of distinct S-layer islands as is normally clearly visible at this scale for S-layers on mica. For this reason, it is assumed that an amorphous layer of CaCO₃ has formed at the S-layer-liquid interface. This is consistent with the *ex situ* and *in situ* XAS data that point to the presence of amorphous forms of CaCO₃ on the S-layers, as well as with observations by Obst et al.^[237] of an amorphous aragonite-like layer on live cyanobacteria.

In Figure 5.9, S-layer samples are imaged after an 8 h period of exposure to 10 mM CaCl₂ and 3 mM NaHCO₃, at rate of 5 μs^{-1} . After this 8 h incubation period, the area shown in Figure 5.9a is imaged for the first time. It shows the presence of globular particles on top of an amorphous layer.

In Figure 5.9b, the same area is shown after it has been imaged several times. The interaction with the scanning probe has triggered removal of a majority of globular particles. This is consistent with the fact that such globular particles are unaffected and still present in areas not previously imaged by the AFM, as is shown in Figure 5.9c.

According to the model for amorphous aragonite-like CaCO₃ formation on top of live cyanobacteria, as proposed by Obsts et al.^[237], nucleation of calcite occurs on top of this pre-existing layer. This is schematically shown in Figure 5.10a-d. This behavior has been reproduced during continuous flow *in situ* AFM measurements, as shown in Figure 5.10e-g. On top of an amorphous layer, a rhombohedrally shaped calcite crystal is imaged continuously over the course of several hours. During this time, the crystal is found to grow in size by about 50 %.

These *in situ* AFM images unambiguously show that the mechanism that has been proposed for CaCO₃ formation on S-layers *in vivo* is also applicable *ex vivo* where S-layers have been immobilized on inorganic substrates. S-layers therefore have innate catalytic qualities regarding the formation of CaCO₃ that are preserved *ex vivo*.

5.6 Conclusions

Based on the nucleation rate data presented in this chapter, it can be concluded that S-layers have catalytic properties regarding the nucleation of CaCO_3 . The low thermodynamic barrier to nucleation results in a relatively weak dependence of the nucleation rate on supersaturation. This makes S-layers especially efficient at CaCO_3 formation at low supersaturations.

Furthermore, XAS and AFM have shown that prior to the macroscopic nucleation of calcite, a layer of amorphous CaCO_3 is formed at the S-layer-liquid interface. Both methods haven been able to detect this CaCO_3 formation *in situ* at naturally occurring supersaturations. The layer is amorphous in nature and is stable under extended continuous flow conditions as well as prolonged x-ray exposure.

In summary, we have used a surface science approach to investigate the catalytic properties of S-layers regarding the formation of CaCO_3 at naturally occurring concentrations. We have shown that at these low concentrations, S-layers facilitate the formation of an amorphous layer of CaCO_3 and that subsequent nucleation of calcite crystals occurs on top of the layer.

It is thus likely that there is a causal relationship between blooms of S-layer expressing bacteria and whiting event, where bacteria catalyze the nucleation of CaCO_3 . Here we have shown that these catalytic properties are at least in part due to the S-layers at the outside of the bacteria and do not originate solely with their internal metabolism.

6 Summary & Outlook

This thesis hierarchically explores different aspects of self-assembling systems. In chapter 2: *Self-assembly of small peptides at the solid-liquid and solid-vacuum interface*, the underlying rules that govern self-assembly were investigated by using synthetic peptides as a model system. In chapter 3: *Bacterial surface layers*, more complex self-assembling systems were investigated using high speed *in situ* AFM during continuous flow conditions. This was build upon further in chapter 4: *In situ dynamics of protein self-assembly on block copolymer thin films*, where different self-assembling systems were hierarchically combined to improve the control of bottom-up assembly. In the last chapter 5: *S-layers as Biomimetic Template for Mineralization of CaCO₃*, emergent functionality of self-assembled systems, i.e. catalytic properties, were analyzed in detail.

The fundamentals of self-assembly have been investigated by using synthetic peptides as a model system. The peptides AcFA₅, AcFA₆ and AcKFA₅ have been studied systematically and the final self-assembly products have been imaged by AFM, both *ex situ* and *in situ*. The influence of external factors such as the presence of a liquid medium or chemical properties

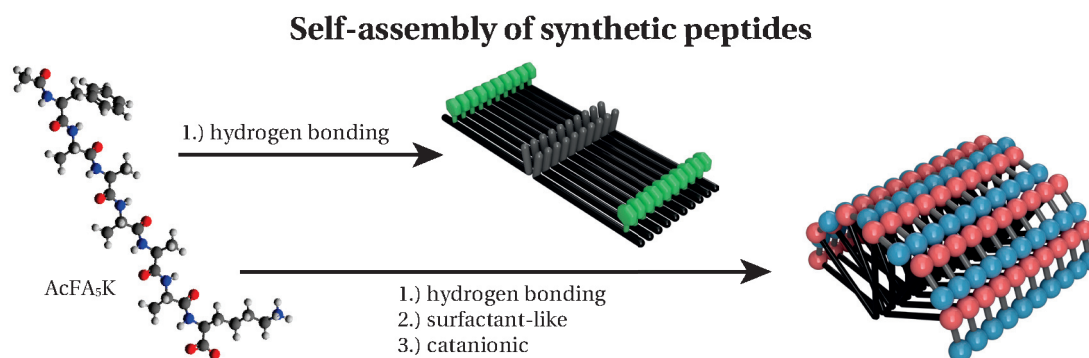


Figure 6.1 – The self-assembly of AcFA₅K is governed by various intermolecular forces such as hydrogen bonding, hydrophobic/hydrophilic interactions and electrostatic interactions. The availability of these intermolecular forces depends on the local environment of the peptide. By controlling this environment, different self-assembled structures can be obtained.

Dynamics of protein-based self-assembly systems

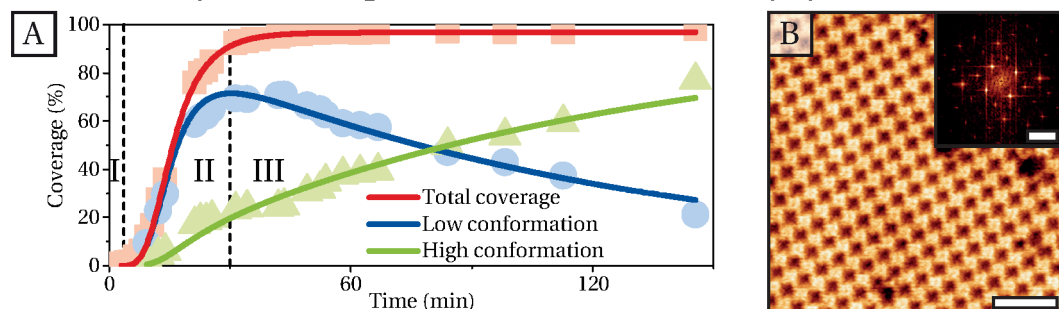


Figure 6.2 – (a) The self-assembly of S-layers at the mica-liquid interface can be divided in three domains, where different aspects of the self-assembling process dominate. First, SbpA monomers adsorb to the mica-liquid interface and form crystalline S-layers. Secondly, growth of the S-layer islands can be modeled using a perimeter driven growth model. Thirdly, the conformational change of the final 2D protein crystals can be modeled using an exponentially decaying function. (b) The internal structure of the S-layer islands can be resolved using *in situ* AFM. Each unit cell is composed of four SbpA monomers. The scale bars of the AFM and corresponding FFT represent 40 nm and 0.12 nm^{-1} , respectively.

of the solid-liquid interface have been explored independently. Internal factors such as the sequence of amino acid residues within the peptide or the protonation state of functional groups have been investigated as well.

It has been shown that the same AcFA₅K peptide can self-assemble into different structures, i.e. different intermolecular forces dominate the self-assembling process, depending on the local environment, as is graphically shown in Figure 6.1.

In the presence of a solution composed of 50 % H₂O and 50 % MeOH, the AcFA₅K peptide has both surfactant-like and catanionic properties that drive the self-assembly into half-cylindrical micelles. Depending on the surface charge of the solid-liquid interface, these micelle structures exhibit epitaxial growth.

In the absence of a liquid environment, the self-assembly of AcFA₅K is dominated solely by hydrogen bonding. β Sheets are formed through hydrogen bonding between the alanine backbones, whereas hydrogen bonding between the carboxyl groups at the C-termini of the peptides assembles β sheets face-to-face. Double layered structures, i.e. two β sheets aligned face-to-face on top of another two β sheets aligned face-to-face, are found to be more stable than single layered structures.

There has been extensive work on Metal-Organic Coordination Networks (MOCNs) on surfaces^[238]. These networks form promising examples of rationally designed complex nanosystems with specific functional properties. Because it is difficult to form stable MOCNs outside highly controlled UHV conditions, technological applications are limited. In contrast, this work has shown that peptides can form highly stable assemblies at the solid-liquid interface. Furthermore, spectroscopy studies have identified individual metal-peptide complexes in the gas-phase^[22]. This suggests that it might be possible to form coordinated metal-peptide assemblies at the solid-liquid interface, i.e. an *in situ* MOCN analogue.

Hierarchical use of self-assembling systems to enable control over

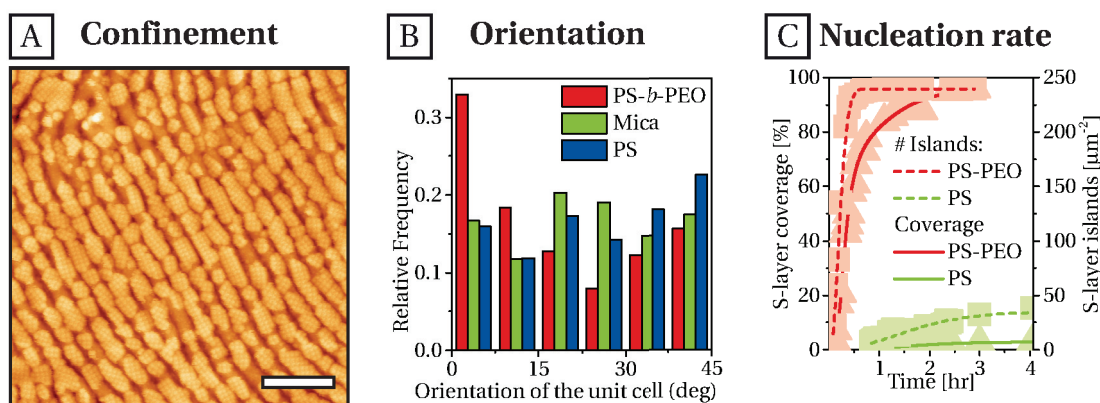


Figure 6.3 – The use of PS-*b*-PEO BCP thin films as nanopatterned substrate for the self-assembly of S-layers creates novel functionality. S-layers are confined to the PS matrix and oriented along the underlying striped PS-*b*-PEO pattern. Furthermore, the nucleation and growth rate of S-layers on PS-*b*-PEO dot patterns is enhanced, compared to pure PS or PEO substrates.

This idea was explored by using AcFA₅K peptides and Gd³⁺ ions. High-resolution *in situ* AFM data has found indications for the formation of organized structures composed of both AcFA₅K peptides and Gd³⁺ ions. This suggests that, under the right conditions, AcFA₅K peptides can indeed be used to immobilize metal ions in an organized fashion.

Suggestions for future work include the investigation of the influence of different liquid environments on the self-assembly at the solid-liquid interface. And the observation of possible metal-peptide complexes at the mica surface warrants further investigation as well. Spectroscopic analysis using XPS might be able to determine the nature of the metal-peptide bond.

The investigation of molecular self-assembly using *in situ* AFM was extended to more complex protein self-assembling systems. The self-assembly of bacterial surface layers at the mica-liquid interface was imaged using high speed AFM in combination with *in situ* continuous flow conditions. This enabled a detailed investigation of the dynamics of the self-assembling process, from the relatively fast adsorption of individual proteins to the slow conformational change of the final 2D protein crystals. Figure 6.2 shows how the dynamics of the different processes involved in self-assembly could successfully be resolved.

The self-assembly of S-layers was further controlled through the use of a second self-assembling system. The self-assembly of PS-*b*-PEO BCP thin films can be controlled, such that nanoscale patterns are formed over macroscopic sized areas. These high-quality thin films were then used as a template to control the self-assembly of S-layers. The hierarchical use of self-assembly can be seen as a functional approach to the concept of molecular tectonics. Following the analogy of building a house, as introduced in the introduction, the foundations of the house are formed through the self-assembly of block copolymer thin films into

Catalytic properties of naturally self-assembled 2D protein layers

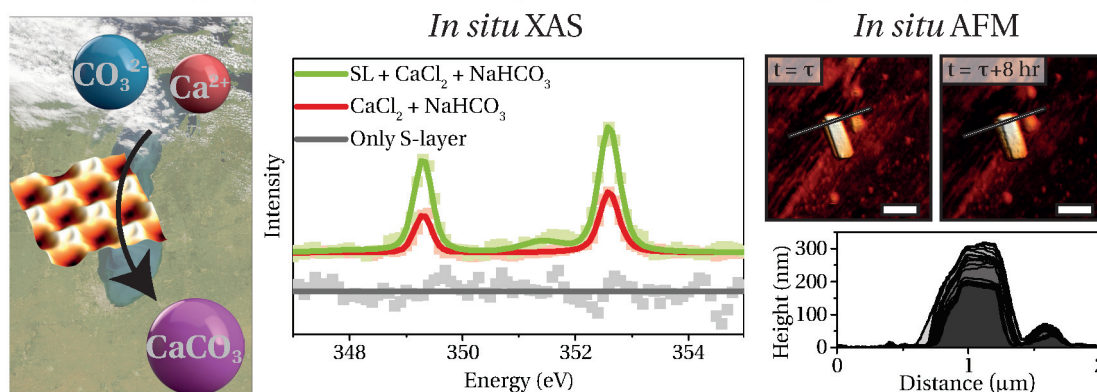


Figure 6.4 – The formation of CaCO_3 on S-layers has been investigated using *in situ* continuous flow XAS and AFM. Both complementary techniques show the formation of CaCO_3 on S-layers at naturally occurring supersaturations of CaCl_2 and NaHCO_3 . No CaCO_3 formation is observed in the absence of S-layers. Under these conditions, calcite has been found to nucleate on top an amorphous-like CaCO_3 layer. The scale bars in the AFM images on the right represent 800 nm.

nanoscale chemically heterogeneous patterns. The house that is then build on top of these foundations, is formed by the self-assembly of SbpA proteins into crystalline S-layers or other functional protein assemblies such as collagen fibers. In this way, both location and orientation of the S-layer crystals can be controlled at the nanoscale, as is shown in Figure 6.3a-b. For long and flexible molecular assemblies such as collagen molecules, their shape closely follows the underlying PS-PEO interfaces.

Furthermore, *in situ* AFM recordings of the dynamics of this process have revealed that the rate of self-assembly of S-layers on PS-*b*-PEO BCP thin films is drastically enhanced compared to homogeneous PS or PEO substrates, as shown in Figure 6.3c. A detailed analysis has shown that the contrasting adsorption affinities of PS and PEO with respect to SbpA proteins is responsible for a locally enhanced concentration of SbpA on the PS nanodomains of the PS-*b*-PEO substrate. The exponential dependency of the rate of self-assembly on the concentration translates even a moderate concentration enhancement into drastically increased rates of self-assembly.

This work could be further extended through the use of genetically modified SbpA proteins that, once assembled into S-layers, expose specific functional domains at the S-layer surface. These functional domains can be designed such that they form anchoring points for a variety of molecules or nanoparticles. Remaining within the analogue for molecular tectonics, this can be interpreted as if the house that is represented by the S-layer crystals will now have inhabitants. This is especially interesting for the use of enzymatic systems, where it has been shown that the precise organization of the functional domains greatly benefits the turnover rate^[30].

Emergent properties of self-assembling systems were investigated by considering the catalytic

properties of S-layers with regards to the formation of CaCO_3 . Based on previous observations reported by Thompson et al.^[182], it has been suspected that S-layers play a role in natural CO_2 sequestration processes where CaCO_3 is formed from dissolved CO_2 .

The *ex vivo* recrystallization and immobilization of S-layers at inorganic substrates enabled the use of established surface science techniques such as AFM and XAS. Whereas the use of continuous flow compatible cells made it possible to investigate the formation of CaCO_3 at the S-layer-liquid interface at naturally occurring supersaturations of CaCl_2 and NaHCO_3 .

By combining these experimental techniques, it was shown that S-layers indeed have catalytic properties regarding the formation of CaCO_3 . Furthermore, it was shown that under these conditions, calcite nucleation is preceded by the formation of a layer of amorphous forms of CaCO_3 at the S-layer surface. Nucleation of calcite on top of this amorphous layer was directly observed. See also Figure 6.4. Therefore, the catalytic properties of cyanobacteria originate, at least in part, from the specific surface properties of S-layers. This strongly suggests a causal relationship between blooms of S-layer expressing bacteria and the appearance of whitening events.

6.1 Conclusions

AFM and XAS have been successfully combined with novel *in situ* continuous flow techniques. Furthermore, ES-IBD was used to bridge the gap from *in situ* to *ex situ* environments. This made it possible to obtain novel and unique experimental conditions, which were applied to study the 2D self-assembly of biological molecules and their functional properties.

Various self-assembling systems have been studied in detail, ranging from simple peptides to complex multi-component protein assemblies, which made it possible to elucidate the underlying process that governs self-assembly. In turn, this knowledge was used to manipulate, and ultimately control, the self-assembling process via a bottom-up approach. This principle was successfully extended to include multiple self-assembling systems, where the emergent properties of one system (BCP) were used to control the self-assembly of a second system (proteins).

The catalytic properties of self-assembled S-layers were studied in detail *ex vivo* and the unique experimental setup used in these studies made it possible to directly detect the mineralization of CaCO_3 at naturally occurring supersaturations. Thus proving that the mineralizing properties of S-layer expressing cyanobacteria are, at least in part, due to the functional properties of S-layers.

A Classical Nucleation Theory

The phase transition of matter through the formation of small embryos of a new low free energy phase β , within the bulk of an old high free energy phase α , is called nucleation. Equation A.1 defines the change in the free energy, or Gibbs free energy, of a system. A phase change from phase α to β that has a negative free energy change therefore indicates a total entropy increase of the combined system and surroundings, and will thus occur spontaneously.

$$\Delta G = \Delta H - T\Delta S \quad (\text{A.1})$$

With ΔG the Gibbs free energy, ΔH the change in enthalpy or heat flux into the system at constant pressure, ΔS the change in entropy and T the absolute temperature of the system.

A.1 Fundamentals of Nucleation Theory

Intuitively, the Gibbs free energy of a solution is related to the concentration. Something which is more precisely described in Equations A.2 and A.3 which relate the activity products of the reactants of a precipitation reaction, AP , to the change in free energy, $\Delta\mu$, of molecules moving from the bulk of phase α to the bulk of phase β .



With the actual activity product:

$$AP = [A]^a [B]^b [C]^c \dots [N]^n \quad (\text{A.2b})$$

And the activity product at equilibrium:

$$K_{sp} = [A]_e^a [B]_e^b [C]_e^c \dots [N]_e^n \quad (\text{A.2c})$$

Appendix A. Classical Nucleation Theory

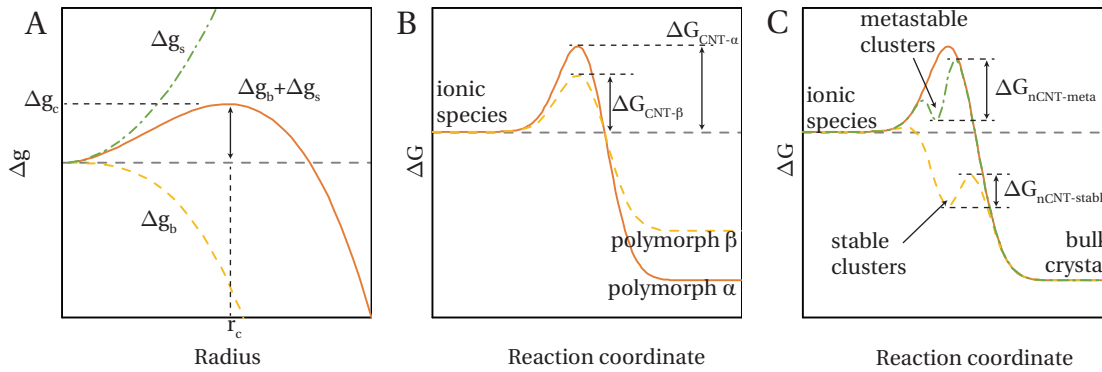


Figure A.1 – (a) The opposing terms of the bulk and surface terms lead to a maximum in free energy when the embryo reaches the the critical radius. Only then a continuing growth of the nucleus will lead to a decrease in total free energy. (b) The free energy barrier to nucleation can differ among polymorphs of the same material. (c) Variations in the surface free energy with size can lead to local and global minima in the free energy diagram. A combination of (b) and (c) can lead to a variety of reaction pathways.

The activity product AP is defined as the product of the concentrations and activity coefficients of all the reactants. It determines the direction and rate of the reaction. The activity product at equilibrium is defined as K_{sp} .

$$\Delta\mu = \Delta g_{\text{phase } \beta} - \Delta g_{\text{phase } \alpha} \quad (\text{A.3a})$$

$$\Delta\mu = k_B T \ln(AP) - k_B T \ln(K_{sp}) \quad (\text{A.3b})$$

$$\Delta\mu = k_B T \ln(AP/K_{sp}) \quad (\text{A.3c})$$

$$\Delta\mu = k_B T \sigma \quad \text{with} \quad \sigma \equiv \ln(AP/K_{sp}) \quad (\text{A.3d})$$

$\Delta\mu$ is defined as the change in free energy of molecules moving from phase α to phase β . It depends linearly on the supersaturation σ , which in turn depends on the difference between the actual and equilibrium activity products.

While the free energy of the new phase can be lower for bulk molecules, this is not necessarily the case for molecules confined to the surface, which carry an additional energy term. As they cannot make as many intermolecular bonds as their bulk counterparts, these surface molecules have a higher free energy. The difference between the bulk and surface free energy per molecule is called the interfacial free energy. Because the free energy of the surface-bound molecules of phase β is generally higher than that of the bulk of phase α , the interfacial free energy acts as a destabilizing factor. Only when the free energy contribution of all the bulk molecules exceeds the total free-energy penalty of the surface molecules, the pre-nucleation embryos of phase β become stable. This size-dependent stability is called the Gibbs-Thomson effect and is the reason behind the existence of a thermodynamic energy barrier to nucleation

and the related critical size of the nuclei.^[31,239]

A.2 Homogeneous Nucleation

For a simple nucleus, the critical size and free energy barrier can be derived from the relative bulk and surface contributions, Δg_b and Δg_s , to the total change in free energy per molecule, Δg , as is done in equation Equation A.4.

$$\Delta g = \Delta g_b + \Delta g_s \quad (\text{A.4a})$$

$$\Delta g = -\frac{V}{\Omega} k_B T \sigma + A \alpha \quad (\text{A.4b})$$

$$\Delta g = -\frac{C_v r^3}{\Omega} k_B T \sigma + C_a r^2 \alpha \quad (\text{A.4c})$$

$$(\text{A.4d})$$

Setting $d\Delta g / dr = 0$ gives:

$$r_c = \frac{2C_a}{3C_v} \cdot \frac{\Omega}{k_B T} \cdot \frac{\alpha}{\sigma} \propto \alpha / \sigma \quad (\text{A.4e})$$

Substituting $r = r_c$ gives:

$$\Delta g_c = \frac{4C_a^3}{27C_v^2} \cdot \frac{\Omega^2}{k_B^2 T^2} \cdot \frac{\alpha^3}{\sigma^2} \propto \alpha^3 / \sigma^2 \quad (\text{A.4f})$$

With C_v and C_a depending on the shape of the nucleus, Ω the volume per molecule, σ the supersaturation of the solution and α the interfacial free energy of the crystal-liquid interface.

The relation between the critical radius and the solution supersaturation derived in Equation A.4e, shows that at sufficiently high supersaturation the critical size can be reduced to only one molecule, i.e. the Gibbs-Thompson effect disappears and there is no more thermodynamic barrier to nucleation. In this regime the transition of phase α to phase β is called spinodal decomposition and is only limited by the mass transport of the nucleating species.

There are two major barriers to nucleation: the thermodynamic barrier to nucleation, ΔG_c , arising from a change ΔG in the free energy as discussed previously, and a kinetic barrier to nucleation E_A that arises from a limited transport of molecules and energy from the solvent to the interface between phase α and phase β . The rate of nucleation J therefore depends exponentially on both barriers, as is shown in Equation A.5.

$$J = A e^{\frac{-E_A}{k_B T}} e^{\frac{-\Delta G_c}{k_B T}} \quad (\text{A.5})$$

The rate of nucleation J depends exponentially on the thermodynamical barrier to nucleation ΔG_c and the kinetic barrier to nucleation E_A . The prefactor A depends on the geometric

material dependent parameters.

The fact that the interfacial free energy appears as a cubic term (Equation A.4f) within an exponential term of the nucleation rate shows the incredibly strong dependency of nucleation rate, J , on the interfacial energy, α .

A.3 Heterogeneous nucleation

When nucleation happens at a solid-liquid interface, the molecules can form bonds with the solid surface. As those bonds are typically stronger than the bonds with the solvent that they replace, the interfacial energy associated with the substrate-crystal interface, α_{sc} is typically smaller than the interfacial free energy associated with the liquid-crystal interface, α_{lc} . By including the various interfacial energies, the total change in free energy per molecule, Δg , can be derived following Equation A.4.

$$\Delta g = \Delta g_b + \Delta g_s \quad (\text{A.6a})$$

$$\Delta g = -\frac{V}{\Omega} k_B T \sigma + C_{cs} A (\alpha_{cs} - \alpha_{sl}) + C_{cl} A \alpha_{cl} \quad (\text{A.6b})$$

$$\Delta g = -\frac{V}{\Omega} k_B T \sigma + A \cdot [C_{cs} (\alpha_{cs} - \alpha_{sl}) + C_{cl} \alpha_{cl}] \quad (\text{A.6c})$$

$$\Delta g = -\frac{V}{\Omega} k_B T \sigma + A \cdot \alpha_{het} \quad \text{with} \quad \alpha_{het} = C_{cs} (\alpha_{cs} - \alpha_{sl}) + C_{cl} \alpha_{cl} \quad (\text{A.6d})$$

$$\Delta g = -\frac{C_v r^3}{\Omega} k_B T \sigma + C_a r^2 \alpha_{het} \quad (\text{A.6e})$$

Setting $d\Delta g/dr = 0$ gives:

$$r_c = \frac{2C_a}{3C_v} \cdot \frac{\Omega}{k_B T} \cdot \frac{\alpha_{het}}{\sigma} \propto \alpha_{het}/\sigma \quad (\text{A.6f})$$

$$\Delta g_c = \frac{4C_a^3}{27C_v^2} \cdot \frac{\Omega^2}{k_B^2 T^2} \cdot \frac{\alpha_{het}^3}{\sigma^2} \propto \alpha_{het}^3/\sigma^2 \quad (\text{A.6g})$$

With C_{cs} the part of surface of the nucleus in contact with the substrate and , C_{cl} the part that is in contact with the liquid. C_a is a constant relating the surface of the nucleus to r^2 and C_v a constant relating the volume of the nucleus to r^3 . α_{cs} , α_{sl} and α_{cl} are the free energy of the crystal-substrate, substrate-liquid and crystal-liquid interface respectively.

If $\alpha_{cs} < \alpha_{sl}$, then $\alpha_{het} < \alpha_{cl}$, and following Equations A.6f to A.6g, both the critical radius and the thermodynamic barrier to nucleation will be reduced compared to homogeneous nucleation. Even in the case where the solid-crystal and liquid-solid interfacial energies are equal, i.e. $\alpha_{cs} = \alpha_{sl}$, the total interfacial energy is still reduced by a factor of 1.5 (a half-spherical nucleus on a flat plane) simply because the interface between nucleus and solid carries no energy penalty, i.e. $C_{cl} < 1$. This shows that in almost all cases, heterogeneous nucleation will have a lower barrier to nucleation than homogeneous nucleation.

A.4. Classical vs. Non-Classical Nucleation and Crystallization

By introducing a surface curvature similar to the size of the nucleating particle, half of the surface of the nucleus is now in contact with the substrate and the interfacial energy is reduced by a factor of 2. Indeed, theoretical studies suggest that the rate of nucleation in pores is maximized when the pore size is in the same order as the critical size of the nucleating particle^[221,222].

The strong dependence of the nucleation rate on the total interfacial energy means that the presence of solid-liquid interfaces can completely change the nucleation pathway and dynamics compared to homogeneous nucleation.

A.4 Classical vs. Non-Classical Nucleation and Crystallization

The assumption that the nucleation and growth happens solely through the addition of individual ions or molecules is called the Classical Nucleation Theory (CNT). Furthermore, the “capillary approximation” made in CNT states that the molecular arrangement of the growing pre-nucleation embryo is the same as for macroscopic crystals, i.e. the change in chemical potential for the bulk molecules, $\Delta\mu$, as well as the interfacial free energy, α , is the same^[31,216]. In contrast, by avoiding the “capillary approximation”, one includes the possibility of variations in both μ and α as function of particle size.

A molecular arrangement at the solid-liquid interface that depends on the particle size will result in variations in α^3 and $(\Delta\mu)$. As $\Delta g_c \propto \alpha^3, (\Delta\mu)^2$ these variations can result in pronounced changes to the thermodynamic barrier to nucleation. Local minima in the total free energy vs. size diagram then give rise to metastable prenucleation clusters, lowering the barrier to nucleation compared to that of single ions and favoring Crystallization by Particle Attachment (CPA). Alternatively, when the minima are global, the kinetically most favorable growth process would depend on which barrier to nucleation is smaller. If the barrier from solvated ions to the bulk crystalline phase is smaller, then classical nucleation theory (CNT) can be applied. When the barrier from the stable prenucleation clusters to the bulk crystalline phase is the smallest, then non-classical pathways will dominate (nCNT).

Furthermore, crystalline materials often have several stable or meta-stable polymorphs and amorphous phases and the heterogeneous solid-crystal interfacial free energy can be different for each one. This means that heterogeneous nucleation can favor one structure over another even when in solution this is not thermodynamically favorable. Nucleation of the stable phase occurs then in, on top or even completely independent of this metastable phase.

B SbpA Purification and S-layer Growth Protocol

The individual SbpA proteins can be purified from live *Lysinibacillus sphaericus*, recrystallization can then occur through addition of Ca^{2+} .

In this section, protocols for *ex vivo* S-layer crystallization and SbpA purification are detailed. The protocols are based on work by Norville et al.^[62] and Rad et al.^[162,165].

B.1 SbpA Purification

The growth of a cell culture of *Lysinibacillus sphaericus* is a two-step process. First, a 20 ml seed solution is prepared, which is then expanded to a 500 ml volume. After this, the cell wall is purified.

B.1.1 Cell Growth

1.) Preparation of the growth solution (SVIII):

The growth solution that is required for the growth of *Lysinibacillus sphaericus* is prepared by following the steps below:

- SVIII ingredients:
 - 10 g/l peptone
 - 5 g/l meat extract
 - 0.2 mM MgSO_4 – $M_w = 120.37 \text{ g mol}^{-1}$ gives 12 mg for 0.5 l
 - 1.8 mM sucrose – $M_w = 342.3 \text{ g mol}^{-1}$ gives 308 mg for 0.5 l
 - 7 mM K_2HPO_4 – $M_w = 174.2 \text{ g mol}^{-1}$ gives 609.7 mg for 0.5 l
- Fill a ~2 l Erlenmeyer flask with 470 ml SVIII.

- Fill a 250 ml Erlenmeyer flask with 18.8 ml SVIII.
- Close off the Erlenmeyers with aluminum foil, then place both in an autoclave set to 121 °C for about 50 min.
- Leave to cool to room temperature for about 1.5 h.

Simultaneously, the following solutions can be prepared:

- 17 mM glucose ($M_w = 180.16 \text{ g mol}^{-1}$)
- 50 mM HEPES at pH 7.2
- 50 mM Tris, pH 7.2 (Keep the solution cold by placing it in an ice bath or refrigerator.)
- 10 % Triton X-100 (*Thermo Scientific*, # 28314)
- 1 M HEPES at pH 7.2 (Use filter sterilization.) – A minimum of 26 ml for 500 ml final culture.
- 1.67 M glucose (Use filter sterilization.) – A minimum of 5.2 ml for 500 ml final culture.

2.) Preparation of the 20 ml seed solution:

Get the sterilized 250 ml Erlenmeyer with 18.8 ml SVIII from step 1 and follow the steps below:

- Add 1.0 ml of 1 M HEPES at pH 7.2
- Add 0.20 ml of 1.67 M glucose
- Combine this solution with scrapings from a glycerol stock of *Lysinibacillus sphaericus*. The glycerol stock has been prepared by growing *Lysinibacillus sphaericus* overnight (~16 h) in SVIII medium. 1 ml is extracted, and 250 µl of 80 % glycerol is added. After a 1 h inoculation period, the glycerol stock is placed in a –80 °C freezer.
- The Erlenmeyer is closed with aluminum foil and placed in a 32 °C environment for about 16 h.
- After a 16 h period, the culture has become cloudy.

3.) The 20 ml seed solution is expanded to a 500 ml culture:

Take the ~2 l Erlenmeyer flask with 470 ml SVIII from step 1 and follow the steps below:

- Add the solution of the 250 ml Erlenmeyer from step 2.
- Add 25 ml of 1 M HEPES at pH 7.2
- Add 5 ml of 1.67 M glucose
- Leave for about 6 h to 7 h at 32 °C until it reaches an optical density (OD_{600}) of ~0.7 to 1.0. (The important aspect is that the growth medium has become cloudy due to bacteria growth.)

Appendix B. SbpA Purification and S-layer Growth Protocol

- Centrifuge the solution at 15000 ×g at 4 °C for 20 min. (*Beckman JLA 8.1 Fixed-angle Rotor.*)
- Re-suspend each pellet in 30 ml solution containing 50 mM Tris at pH 7.2 and transfer it to an Oakridge Tube.
- Centrifuge the resulting solution at 16000 ×g at 4 °C for 15 min. (*Beckman Coulter JA-20 Fixed-Angle Rotor*)
- Measure the weight of the wet cell pellet and discard the supernatant.
- When the cell wall purification is postponed to a later time, store the cell pellet at –80 °C.

B.1.2 Protein Purification

1.) Lysing of cells:

- Re-suspend the cell pellets in 28 ml of 50 mM Tris at pH 7.2, which is kept cold. (28 ml Will work for up to 8 g of cell material. For more than 8 g, add the buffer in a ratio of 100 g cell material to 350 ml buffer.)
- Lyse the suspended cells in ice by sonication with 2 s pulses and 2 s pauses at an output power ~21 W. (This corresponds to power level 7 for a *Misonix sonicator 3000.*) Repeat this procedure three times with a 1 min cooling period between each cycle.
An alternative and preferred Lysis method uses the *EmulsiFlex-C3 homogenizer* from *Avestin*. The cells are passed 3 times through the system at a pressure of 20000 psi (1.4 kbar) and with a cooling loop through an ice bath.
- When Lysed, centrifuge the cells at 28000 ×g at 4 °C for 15 min. (*Beckman Coulter JA-20 Fixed-Angle Rotor*)

2.) Purification of cell wall:

- Use a disposable plastic spatula to separate the cell wall (the white outer ring of the pellet) from the unbroken cells (the tan inner ring).
- Add 18 ml of Tris at pH 7.2
- Sonicate the solution in an ice bath for ~1 min with 1 s pulses separated by 1 s pauses.
- Add 1.8 ml of 10 % Triton X-100
- Stir the solution for 10 min at room temperature at 300 rpm (The suspension is initially pale pink and becomes white cloudy as it is washed).
- Spin the suspension at 40000 ×g for 10 min at 4 °C. (*Beckman Coulter JA-20 Fixed-Angle Rotor*)

This purification procedure is repeated four to five times, see also Figure B.2. The final pellet is the purified cell wall and can be stored at $-20\text{ }^{\circ}\text{C}$ until the next step.

3.) Denaturing of purified cell wall:

- The pellet containing the purified cell walls is dissolved in 10 ml of 50 mM Tris at pH 7.2 and 5 M Guanidinium Chloride (CH_6ClN_3). This is then incubated for 30 min at room temperature while slowly shaking.
- The resulting solution is centrifuged at $100\,000 \times g$ at $4\text{ }^{\circ}\text{C}$ for 45 min. (*SW28Ti rotor, Beckman coulter, Optima L-100XP*)
- The supernatant is decanted and dialyzed against 2 l of deionized water at $4\text{ }^{\circ}\text{C}$ for 2 h. Place the dialysis tube into 2 l fresh deionized water after every 40 min.
- The final solution ($\sim 12\text{ ml}$) is centrifuged again at $100\,000 \times g$ at $4\text{ }^{\circ}\text{C}$ for 30 min.

4.) Measuring the concentration:

The concentration is determined using a visible light absorption measurement, as is shown in Figure B.1. The concentration of SbpA is then calculated using Beer's law and the absorption coefficient for SbpA at a wavelength of 280 nm, Equation B.1a^[240].

By following this protocol, usually a concentration of 1.5 mgml^{-1} to 2.0 mgml^{-1} is obtained. In order to reduce aggregation and for consistency, the concentration is adjusted to $\sim 1.5\text{ mgml}^{-1}$

$$A = \epsilon \cdot c \cdot l \tag{B.1a}$$

$$\epsilon_{280} = 0.5978 / (\text{mg/ml}) / \text{cm} \tag{B.1b}$$

Beer's law relates the absorption, A , to the concentration, c , and optical path length, l , through the absorption coefficient, ϵ ^[240]. For SbpA proteins from the *Lysinibacillus sphaericus*, the absorption coefficient at a wavelength of 280 nm (ϵ_{280}) is known and can be used to determine the concentration by measuring the absorption and optical path length.

Appendix B. SbpA Purification and S-layer Growth Protocol

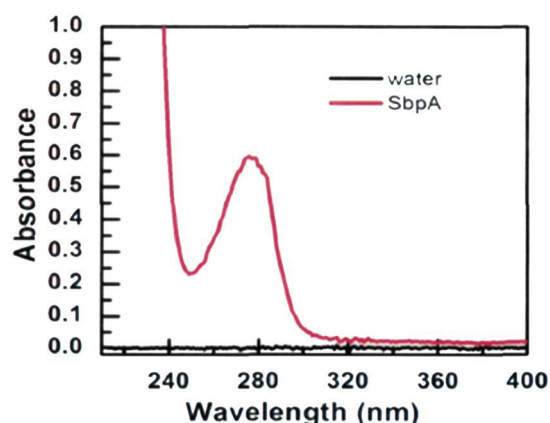


Figure B.1 – The absorbance of a solution that contains SbpA proteins and a reference solution that only contains deionized water. The absorbance of water is set to zero so that the absorbance of the solution that contains SbpA only depends on the protein concentration. Equation B.1a can be used to determine the concentration of SbpA. The SbpA protein has a strong absorption around 280 nm, contaminants like DNA or aggregates have absorption peaks around 260 nm and 340 nm respectively. $A_{260}/A_{280} = 0.6$ indicates very little DNA contamination, $A_{340}/A_{280} < 0.05$ indicates little scattering and therefore few aggregates.

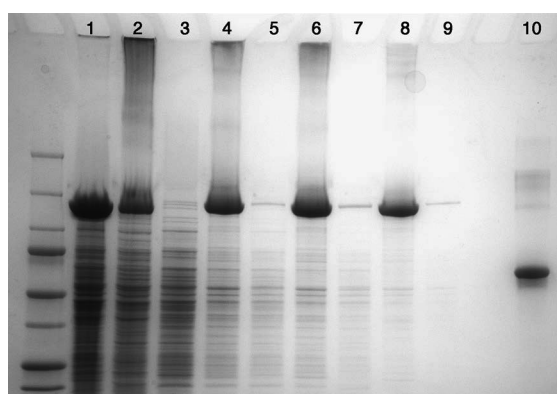


Figure B.2 – Gel electrophoresis taken at different steps in the SbpA protocol. 1.) The crude cell lysate. 2.) The first wash before centrifugation. 3.) The first supernatant. 4.) The second wash before centrifugation. 5.) The second supernatant. 6.) The third wash before centrifugation. 7.) The third supernatant. 8.) The final wash before centrifugation. 9.) The final supernatant. 10.) 5 µg BSA (Bovine Serum Albumin) reference. It is clear that after four washes, the supernatant contains few contaminants, indicating that the cell wall is sufficiently purified.

B.2 *Ex vivo* S-layer Crystallization

S-layers can be recrystallized *ex vivo* from previously purified SbpA monomers. Based on the concentration of SbpA used in this procedure, the S-layers either form immobilized on the surface or also free floating in solution.

For immobilized S-layers the following protocol is used, based on in-situ AFM S-layer measurements by Chung et al.^[162].

- Prepare SbpA at a concentration of $50\ \mu\text{gml}^{-1}$ in a buffer solution containing:
 - 50 mM CaCl_2
 - 100 mM NaCl_2
 - 10 mM Tris at pH 7.2
- A drop is placed on the sample surface and left to incubate for ~5 h.
When a mica substrate is used, it is preferred to use an incubation time of at least 10 h. This in order to allow the monocrystalline S-layer domains to relax to a thermodynamically stable state^[165].
- To remove excess SbpA protein and possible S-layers that have formed in solution, the drop on the surface is replaced by milliQ water for several times.

In some instances, a higher concentration of S-layers is required. This can be achieved by crystallizing S-layers free floating in solution and subsequently centrifuging them to a pellet, which can be dissolved in a smaller volume to increase the concentration.

- Prepare SbpA at a concentration of up to $1\ \text{mgml}^{-1}$ in a buffer solution containing:
 - 50 mM CaCl_2
 - 100 mM NaCl_2
 - 10 mM Tris at pH 7.2
- Let the solution incubate overnight, the solution will turn slightly opaque during S-layer crystallization.
- Centrifuge the resulting solution at $20000 \times g$ for 10 min. (*General eppendorf tabletop centrifuge.*)
- Discard the supernatant and redissolve the S-layer to obtain the desired concentration.

C Self-assembly of gas molecules at the HOPG-liquid interface

Figure 2.5 from chapter 2: *Self-assembly of small peptides at the solid-liquid and solid-vacuum interface* shows the HOPG-liquid interface in 50 % H₂O and 50 % MeOH. In Figure 2.5a AcFA₅K is present at 0.8 mM whereas in Figure 2.5b no peptides are present. The fact that regular line patterns are observed in both cases rules out the possibility that these lines are composed of AcFA₅K peptides.

As discussed in section 2.1.1, similar line patterns at the HOPG surface have been reported in a number of research papers^[143–150] and are thought to be a result of dissolved gas molecules that self-assemble into regular structures at the solid-liquid interface.

Additional experimental data on this phenomenon is presented in Figure C.1. There are two sets of features that are worth noting.

In Figure C.1a, the presence of a parallel line patterns similar to what is seen in Figure 2.5 are again observed. However, in this experiment, different areas are found to have line patterns with different periodicity and orientation, i.e. 4.1 nm at 158°, 4.7 nm at 158° + 30° and 5.3 nm at 158° + 60°. Interestingly, the periodicities vary with exactly 6 Å, whereas the angles vary with exactly 30°.

In Figure C.1b, a 2D non-structured layer is seen to grow over time. It exist simultaneously with the periodic structures in Figure C.1a and has a height of about 7 Å above the underlying substrate.

A comparison with results published by Lu et al.^[146] shows that similar structures have been observed at the HOPG-H₂O interface and were attributed to the adsorption of N₂ molecules at the HOPG-liquid interface. Furthermore, the presence of varying periodicities for different orientations was attributed to a tip anisotropy that resulted in a different tip-interaction profile in each direction. This is consistent with the fact that high imaging resolutions resulting from exceptionally sharp AFM probes, as shown in Figure 2.5, resulted in the same observed periodicity for all patterns. In contrast, lower resolutions, which are probably due to

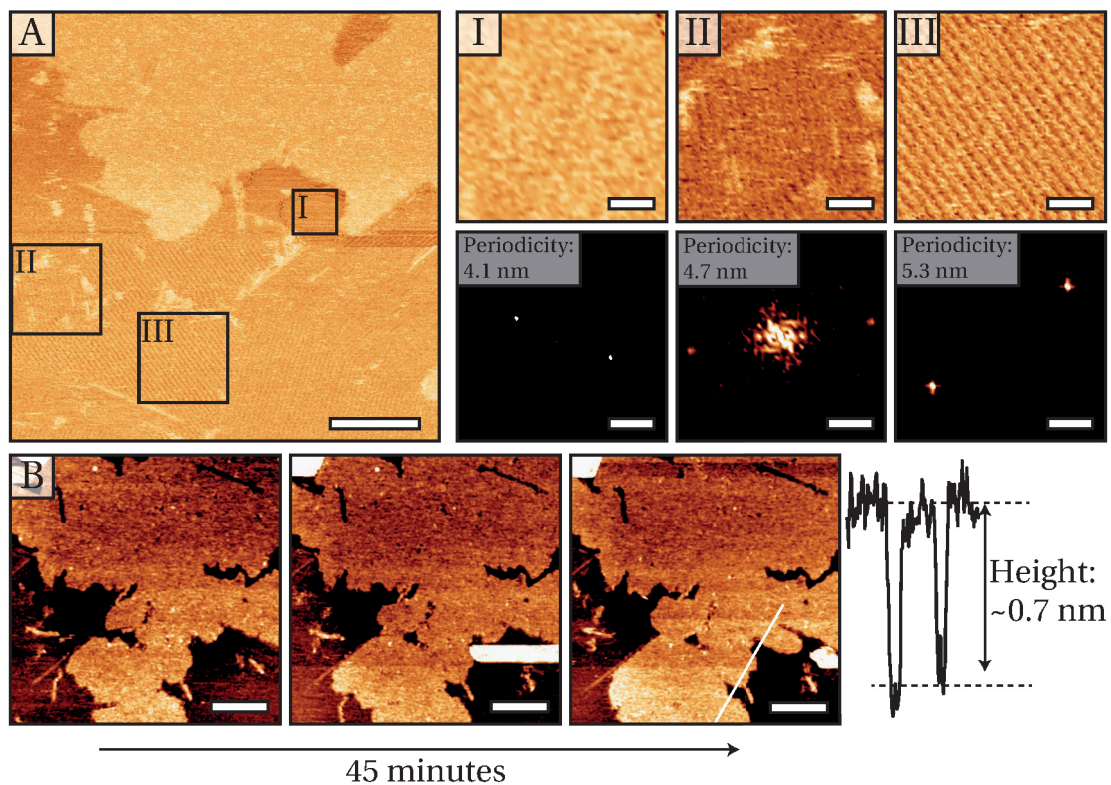


Figure C.1 – (a) The HOPG-liquid in the presence of AcFA₅K at 0.8 mM shows line patterns with different periodicity (I, II and III) and an amorphous layer that grows over time. 2D fourier transforms of the respective areas reveal periodicities of 4.1 nm, 4.7 nm and 5.3 nm. Scale bars represent 100 nm, 10 nm and 0.2 nm⁻¹ for image I and 20 nm and 0.1 nm⁻¹ for image II and III. (b) Snapshots taken over the course of 45 min show the evolution of the 2D layer at the HOPG-liquid interface. The height of the layer is about 0.7 nm. Scale bars represent 90 nm.

slightly contaminated AFM probes, resulted in varying periodicities for differently oriented line patterns, as shown in Figure C.1.

These additional results form further evidence that the observed periodic line patterns are not composed of AcFA₅K peptides. It can thus be concluded that AcFA₅K does not adsorb at the HOPG-liquid interface when a direct drop casting method is used.

D AFM Probes

Table D.1 – Specifications of AFM probes used in this work.

Probe Name, Manufacturer	Imaging Mode	Spring Constant (N/m)	Resonance Frequency in Air (kHz)	Radius of Curvature (nm)
FastScan-A, Bruker	air/liq. – TM	18	1400	5
FastScan-B, Bruker	air/liq. – TM	1.8	450	5
FastScan-C, Bruker	air/liq. – TM, PFM	0.8	300	5
FastScan-D, Bruker	air/liq. – TM, PFM	0.25	200	5
ScanAsyst-Air, Bruker	air – PFM	0.4	70	2
ScanAsyst-Air-HR, Bruker	air – PFM	0.4	130	2
ScanAsyst-Fluid, Bruker	liq. – PFM	0.7	150	20
ScanAsyst-Fluid+, Bruker	liq. – PFM	0.7	150	2
PeakForce-HIRS-F-A, Bruker	air/liq. – PFM	0.35	165	1
PeakForce-HIRS-F-B, Bruker	air/liq. – PFM	0.12	100	1
SNL-A, Bruker	air – TM, PFM	0.35	65	2
SNL-B, Bruker	liq. – CM, PFM	0.12	23	2
SNL-C, Bruker	liq. – TM, PFM	0.24	56	2
SNL-D, Bruker	liq. – CM	0.06	18	2
MSNL-C, Bruker	liq. – CM	0.01	7	2
Tespa, Bruker	air – TM, PFM	42	320	8
NCLR, NanoWorld	air – TM	42	320	8
NCHR, NanoWorld	air – TM	48	190	8

Bibliography

- [1] Anton van Leeuwenhoek. "The Selected Works of Antony van Leeuwenhoek Containing His Microscopical Discoveries in Many of the Works of Nature". *Arno Press* (1977).
- [2] G. Binnig et al. "Surface Studies by Scanning Tunneling Microscopy". *Physical Review Letters*, vol. 49, no. 1 (July 5, 1982), pp. 57–61.
- [3] G. Binnig; C. F. Quate, and Ch. Gerber. "Atomic Force Microscope". *Physical Review Letters*, vol. 56, no. 9 (Mar. 3, 1986), pp. 930–933.
- [4] Otto H. Schmitt. "Some interesting and useful biomimetic transforms". Third International Biophysics Congress. Boston, 1969, p. 297.
- [5] Stephen Mann. "Molecular tectonics in biomineralization and biomimetic materials chemistry". *Nature*, vol. 365, no. 6446 (Oct. 7, 1993), pp. 499–505.
- [6] Yoseph Bar-Cohen. "Biomimetics – using nature to inspire human innovation". *Bioinspiration & Biomimetics*, vol. 1, no. 1 (2006), p. 1.
- [7] Arnim Gleich et al. *Potentials and Trends in Biomimetics*. Heidelberg: Springer, 2010.
- [8] Nathan F. Lepora; Paul Verschure, and Tony J. Prescott. "The state of the art in biomimetics". *Bioinspiration & Biomimetics*, vol. 8, no. 1 (2013), p. 013001.
- [9] Janine M. Benyus. *Biomimicry: Innovation Inspired by Nature*. New York: Harper Perennial, Sept. 17, 2002.
- [10] Dora Lee. *Biomimicry: Inventions Inspired by Nature*. In collab. with Margot Thompson. Toronto: Kids Can Press, Aug. 1, 2011.
- [11] Julianne. D. Halley and David A. Winkler. "Consistent concepts of self-organization and self-assembly". *Complexity*, vol. 14, no. 2 (Nov. 1, 2008), pp. 10–17.
- [12] Fiora Rosati and Gerard Roelfes. "Artificial Metalloenzymes". *ChemCatChem*, vol. 2, no. 8 (Aug. 9, 2010), pp. 916–927.
- [13] Stephen Mann. "Biomineralization and biomimetic materials chemistry". *Journal of Materials Chemistry*, vol. 5, no. 7 (Jan. 1, 1995), pp. 935–946.
- [14] Zhifeng Shao et al. "Biological atomic force microscopy: what is achieved and what is needed". *Advances in Physics*, vol. 45, no. 1 (Feb. 1, 1996), pp. 1–86.

Bibliography

- [15] Andreas Engel and Daniel J. Müller. “Observing single biomolecules at work with the atomic force microscope”. *Nature Structural & Molecular Biology*, vol. 7, no. 9 (Sept. 2000), pp. 715–718.
- [16] Franz J. Giessibl. “Advances in atomic force microscopy”. *Reviews of Modern Physics*, vol. 75, no. 3 (July 29, 2003), pp. 949–983.
- [17] T. J. Young et al. “The use of the PeakForce TM quantitative nanomechanical mapping AFM-based method for high-resolution Young’s modulus measurement of polymers”. *Measurement Science and Technology*, vol. 22, no. 12 (2011), p. 125703.
- [18] C. Vieu et al. “Electron beam lithography: resolution limits and applications”. *Applied Surface Science. Surface Science in Micro & Nanotechnology*, vol. 164, no. 1 (Sept. 1, 2000), pp. 111–117.
- [19] George M. Whitesides and Bartosz Grzybowski. “Self-Assembly at All Scales”. *Science*, vol. 295, no. 5564 (Mar. 29, 2002), pp. 2418–2421.
- [20] C. Jeffrey Brinker et al. “Evaporation-Induced Self-Assembly: Nanostructures Made Easy”. *Advanced Materials*, vol. 11, no. 7 (May 1, 1999), pp. 579–585.
- [21] Jaime A. Stearns; Oleg V. Boyarkin, and Thomas R. Rizzo. “Spectroscopic Signatures of Gas-Phase Helices: Ac-Phe-(Ala)₅-Lys-H⁺ and Ac-Phe-(Ala)₁₀-Lys-H⁺”. *Journal of the American Chemical Society*, vol. 129, no. 45 (Nov. 1, 2007), pp. 13820–13821.
- [22] Jaime A. Stearns et al. “Spectroscopy and conformational preferences of gas-phase helices”. *Physical Chemistry Chemical Physics*, vol. 11, no. 1 (Dec. 10, 2008), pp. 125–132.
- [23] Feng Qiu; Yongzhu Chen, and Xiaojun Zhao. “Comparative studies on the self-assembling behaviors of cationic and catanionic surfactant-like peptides”. *Journal of Colloid and Interface Science*, vol. 336, no. 2 (Aug. 15, 2009), pp. 477–484.
- [24] Shern-Long Lee et al. “Reversible Local and Global Switching in Multicomponent Supramolecular Networks: Controlled Guest Release and Capture at the Solution/Solid Interface”. *ACS Nano*, vol. 9, no. 12 (Dec. 22, 2015), pp. 11608–11617.
- [25] Sébastien Lecommandoux; Massimo Lazzari, and Guojun Liu. “An Introduction to Block Copolymer Applications: State-of-the-Art and Future Developments”. *Block Copolymers in Nanoscience*. Ed. by Massimo Lazzari Faculty of Chemistry; Guojun Liu, and Sébastien Lecommandoux. Wiley-VCH Verlag GmbH & Co. KGaA, 2006, pp. 1–7.
- [26] Carla S. Thomas; Matthew J. Glassman, and Bradley D. Olsen. “Solid-State Nanostructured Materials from Self-Assembly of a Globular Protein–Polymer Diblock Copolymer”. *ACS Nano*, vol. 5, no. 7 (July 26, 2011), pp. 5697–5707.
- [27] Dongsook Chang et al. “Effect of polymer chemistry on globular protein–polymer block copolymer self-assembly”. *Polymer Chemistry*, vol. 5, no. 17 (July 29, 2014), pp. 4884–4895.
- [28] Nitin Kumar and Jong-in Hahm. “Nanoscale Protein Patterning Using Self-Assembled Diblock Copolymers”. *Langmuir*, vol. 21, no. 15 (July 1, 2005), pp. 6652–6655.

- [29] Nitin Kumar et al. "Elucidation of Protein Adsorption Behavior on Polymeric Surfaces: Toward High-Density, High-Payload Protein Templates". *Langmuir*, vol. 24, no. 6 (Mar. 1, 2008), pp. 2688–2694.
- [30] Christina Schäffer et al. "Novel Biocatalysts Based on S-Layer Self-Assembly of *Geobacillus Stearothermophilus* NRS 2004/3a: A Nanobiotechnological Approach". *Small*, vol. 3, no. 9 (Sept. 3, 2007), pp. 1549–1559.
- [31] James J. De Yoreo and Peter G. Vekilov. "Principles of Crystal Nucleation and Growth". *Reviews in Mineralogy and Geochemistry*, vol. 54, no. 1 (Jan. 3, 2003), pp. 57–93.
- [32] Adam F. Wallace; James J. DeYoreo, and Patricia M. Dove. "Kinetics of Silica Nucleation on Carboxyl- and Amine-Terminated Surfaces: Insights for Biomineralization". *Journal of the American Chemical Society*, vol. 131, no. 14 (Apr. 15, 2009), pp. 5244–5250.
- [33] Q. Hu et al. "The thermodynamics of calcite nucleation at organic interfaces: Classical vs. non-classical pathways". *Faraday Discussions*, vol. 159 (2012), pp. 509–509.
- [34] P. U. P. A. Gilbert; Mike Abrecht, and Bradley H. Frazer. "The Organic-Mineral Interface in Biominerals". *Reviews in Mineralogy and Geochemistry*, vol. 59, no. 1 (Jan. 1, 2005), pp. 157–185.
- [35] Lia Addadi et al. "Mollusk Shell Formation: A Source of New Concepts for Understanding Biomineralization Processes". *Chemistry – A European Journal*, vol. 12, no. 4 (Jan. 23, 2006), pp. 980–987.
- [36] Boaz Pokroy; Victoria Fay Chernow, and Joanna Aizenberg. "Crystallization of Malonic and Succinic Acids on SAMs: Toward the General Mechanism of Oriented Nucleation on Organic Monolayers". *Langmuir*, vol. 25, no. 24 (Dec. 15, 2009), pp. 14002–14006.
- [37] Joanna Aizenberg; Andrew J. Black, and George M. Whitesides. "Control of crystal nucleation by patterned self-assembled monolayers". *Nature*, vol. 398, no. 6727 (Apr. 8, 1999), pp. 495–498.
- [38] E. Loste et al. "Precipitation of Calcium Carbonate in Confinement". *Advanced Functional Materials*, vol. 14, no. 12 (Dec. 1, 2004), pp. 1211–1220.
- [39] Anthony J. Giuffre et al. "Polysaccharide chemistry regulates kinetics of calcite nucleation through competition of interfacial energies". *Proceedings of the National Academy of Sciences of the United States of America*, vol. 110, no. 23 (June 4, 2013), pp. 9261–9266.
- [40] Francois Barthelat. "Biomimetics for next generation materials". *Philosophical Transactions of the Royal Society of London A: Mathematical, Physical and Engineering Sciences*, vol. 365, no. 1861 (Dec. 15, 2007), pp. 2907–2919.
- [41] P. Calvert and A. Azhari. "Biomimetic Materials: Properties and Processing". *Reference Module in Materials Science and Materials Engineering*. Elsevier, 2016.
- [42] Christer Jansson and Trent Northen. "Calcifying cyanobacteria—the potential of biomineralization for carbon capture and storage". *Current opinion in biotechnology*, vol. 21, no. 3 (June 2010), pp. 365–71.

Bibliography

- [43] Nina Kamennaya et al. "Cyanobacteria as Biocatalysts for Carbonate Mineralization". *Minerals*, vol. 2, no. 4 (Oct. 2012), pp. 338–364.
- [44] Mir Wais Hosseini. "Molecular Tectonics: From Simple Tectons to Complex Molecular Networks". *Accounts of Chemical Research*, vol. 38, no. 4 (Apr. 1, 2005), pp. 313–323.
- [45] Helmut Cölfen and Stephen Mann. "Higher-Order Organization by Mesoscale Self-Assembly and Transformation of Hybrid Nanostructures". *Angewandte Chemie International Edition*, vol. 42, no. 21 (May 30, 2003), pp. 2350–2365.
- [46] Derek N. Woolfson and Zahra N. Mahmoud. "More than just bare scaffolds: towards multi-component and decorated fibrous biomaterials". *Chemical Society Reviews*, vol. 39, no. 9 (Aug. 18, 2010), pp. 3464–3479.
- [47] Uwe B. Sleytr et al. "S-layers: principles and applications". *FEMS Microbiology Reviews*, vol. 38, no. 5 (Sept. 1, 2014), pp. 823–864.
- [48] Hanqiong Hu; Manesh Gopinadhan, and Chinedum O. Osuji. "Directed self-assembly of block copolymers: a tutorial review of strategies for enabling nanotechnology with soft matter". *Soft Matter*, vol. 10, no. 22 (May 15, 2014), pp. 3867–3889.
- [49] Shuguang Zhang. "Emerging biological materials through molecular self-assembly". *Biotechnology Advances*, vol. 20, no. 5 (Dec. 2002), pp. 321–339.
- [50] Shuguang Zhang. "Fabrication of novel biomaterials through molecular self-assembly". *Nature Biotechnology*, vol. 21, no. 10 (Oct. 2003), pp. 1171–1178.
- [51] R. B. Merrifield. "Solid Phase Peptide Synthesis. I. The Synthesis of a Tetrapeptide". *Journal of the American Chemical Society*, vol. 85, no. 14 (July 1, 1963), pp. 2149–2154.
- [52] Fernando Albericio. "Developments in peptide and amide synthesis". *Current Opinion in Chemical Biology*, vol. 8, no. 3 (June 2004), pp. 211–221.
- [53] Ian W. Hamley. "Peptide Nanotubes". *Angewandte Chemie International Edition*, vol. 53, no. 27 (July 1, 2014), pp. 6866–6881.
- [54] Thomas M. Hermans. "Self-assembly: Materials from a peptide soup". *Nature Nanotechnology*, vol. 11, no. 11 (Nov. 2016), pp. 920–921.
- [55] Xiaojun Zhao and Shuguang Zhang. "Molecular designer self-assembling peptides". *Chemical Society Reviews*, vol. 35, no. 11 (Oct. 23, 2006), pp. 1105–1110.
- [56] Xiaojun Zhao and Shuguang Zhang. "Designer Self-Assembling Peptide Materials". *Macromolecular Bioscience*, vol. 7, no. 1 (Jan. 5, 2007), pp. 13–22.
- [57] Çelen Çağrı Cenker; Seyda Bucak, and Ulf Olsson. "Aqueous Self-Assembly within the Homologous Peptide Series AnK". *Langmuir*, vol. 30, no. 33 (Aug. 26, 2014), pp. 10072–10079.
- [58] Valeria Castelletto et al. "Influence of End-Capping on the Self-Assembly of Model Amyloid Peptide Fragments". *The Journal of Physical Chemistry B*, vol. 115, no. 9 (Mar. 10, 2011), pp. 2107–2116.

- [59] Christopher R. So et al. "Controlling Self-Assembly of Engineered Peptides on Graphite by Rational Mutation". *ACS Nano*, vol. 6, no. 2 (Feb. 28, 2012), pp. 1648–1656.
- [60] Uwe B. Sleytr. "Regular Arrays of Macromolecules on Bacterial Cell Walls: Structure, Chemistry, Assembly, and Function". *International Review of Cytology*. Ed. by G. H. Bourne {and} J. F. Danielli. Vol. 53. Academic Press, 1978, pp. 1–64.
- [61] Sonja-Verena Albers and Benjamin H. Meyer. "The archaeal cell envelope". *Nature Reviews Microbiology*, vol. 9, no. 6 (June 2011), pp. 414–426.
- [62] Julie E. Norville et al. "7 Å projection map of the S-layer protein sbpA obtained with trehalose-embedded monolayer crystals". *Journal of Structural Biology*. *Electron Crystallography of Membrane Proteins*, vol. 160, no. 3 (Dec. 2007), pp. 313–323.
- [63] Christine Horejs et al. "Atomistic Structure of Monomolecular Surface Layer Self-Assemblies: Toward Functionalized Nanostructures". *ACS Nano*, vol. 5, no. 3 (Mar. 22, 2011), pp. 2288–2297.
- [64] Uwe B. Sleytr and Margit Sára. "Bacterial and archaeal S-layer proteins: structure-function relationships and their biotechnological applications". *Trends in Biotechnology*, vol. 15, no. 1 (Jan. 1, 1997), pp. 20–26.
- [65] Uwe B. Sleytr et al. "Crystalline Bacterial Cell Surface Layers (S Layers): From Supramolecular Cell Structure to Biomimetics and Nanotechnology". *Angewandte Chemie International Edition*, vol. 38, no. 8 (Apr. 19, 1999), pp. 1034–1054.
- [66] Uwe B. Sleytr et al. "S-Layers as a basic building block in a molecular construction kit". *FEBS Journal*, vol. 274 (2007), pp. 323–334.
- [67] Uwe B. Sleytr et al. "Nanobiotechnology with S-Layer Proteins as Building Blocks". *Progress in Molecular Biology and Translational Science*. Ed. by Stefan Howorka. Vol. 103. *Molecular Assembly in Natural and Engineered Systems*. Academic Press, 2011, pp. 277–352.
- [68] Stefan H. Bossmann. "S-Layer Proteins in Bioelectronic Applications". *Bioelectronics*. Ed. by Itamar Willner and Eugenii Katz. Wiley-VCH Verlag GmbH & Co. KGaA, 2005, pp. 395–426.
- [69] Roberto de la Rica and Hiroshi Matsui. "Applications of peptide and protein -based materials in bionanotechnology". *Chemical Society Reviews*, vol. 39, no. 9 (2010), pp. 3499–3509.
- [70] Tea Pavkov-Keller; Stefan Howorka, and Walter Keller. "The Structure of Bacterial S-Layer Proteins". *Progress in Molecular Biology and Translational Science*. Ed. by Stefan Howorka. Vol. 103. *Molecular Assembly in Natural and Engineered Systems*. Academic Press, 2011, pp. 73–130.
- [71] Simon R. Hall et al. "Site-Specific Organization of Gold Nanoparticles by Biomolecular Templating". *ChemPhysChem*, vol. 2, no. 3 (Mar. 16, 2001), pp. 184–186.
- [72] Erika Györvary et al. "Formation of nanoparticle arrays on S-layer protein lattices". *Journal of Nanoscience and Nanotechnology*, vol. 4, no. 1 (Feb. 2004), pp. 115–120.

Bibliography

- [73] Sonny S. Mark et al. “Bionanofabrication of Metallic and Semiconductor Nanoparticle Arrays Using S-Layer Protein Lattices with Different Lateral Spacings and Geometries”. *Langmuir*, vol. 22, no. 8 (Apr. 1, 2006), pp. 3763–3774.
- [74] Nicola Ilk et al. “Molecular Characterization of the S-Layer Gene, *sbpA*, of *Bacillus sphaericus* CCM 2177 and Production of a Functional S-Layer Fusion Protein with the Ability To Recrystallize in a Defined Orientation while Presenting the Fused Allergen”. *Applied and Environmental Microbiology*, vol. 68, no. 7 (July 1, 2002), pp. 3251–3260.
- [75] Parthasarathy Sampathkumar and M. Lane Gilchrist. “Synthesis and Characterization of Bioconjugates of S-Layer Proteins”. *Bioconjugate Chemistry*, vol. 15, no. 4 (July 1, 2004), pp. 685–693.
- [76] Jilin Tang et al. “Recognition Imaging and Highly Ordered Molecular Templating of Bacterial S-Layer Nanoarrays Containing Affinity-Tags”. *Nano Letters*, vol. 8, no. 12 (Dec. 10, 2008), pp. 4312–4319.
- [77] Xu-Ying Wang et al. “A S-Layer Protein of *Bacillus anthracis* as a Building Block for Functional Protein Arrays by In Vitro Self-Assembly”. *Small*, vol. 11, no. 43 (Nov. 1, 2015), pp. 5826–5832.
- [78] Lina Velásquez and Jenny Dussan. “Biosorption and bioaccumulation of heavy metals on dead and living biomass of *Bacillus sphaericus*”. *Journal of Hazardous Materials*, vol. 167, no. 1 (Aug. 15, 2009), pp. 713–716.
- [79] Anna A. Makarova et al. “Insight into Bio-metal Interface Formation in vacuo: Interplay of S-layer Protein with Copper and Iron”. *Scientific Reports*, vol. 5 (Mar. 4, 2015), p. 8710.
- [80] Chaohui Xue et al. “Protective action of S-layer proteins from *Lactobacillus paracasei* M7 against *Salmonella* infection and mediated inhibition of *Salmonella*-induced apoptosis”. *European Food Research and Technology*, vol. 240, no. 5 (Dec. 3, 2014), pp. 923–929.
- [81] K.w. Guarini; C.t. Black, and S.h.i. Yeung. “Optimization of Diblock Copolymer Thin Film Self Assembly”. *Advanced Materials*, vol. 14, no. 18 (Sept. 16, 2002), pp. 1290–1294.
- [82] I. W. Hamley. “Ordering in thin films of block copolymers: Fundamentals to potential applications”. *Progress in Polymer Science*, vol. 34, no. 11 (Nov. 2009), pp. 1161–1210.
- [83] Yiyong Mai and Adi Eisenberg. “Self-assembly of block copolymers”. *Chemical Society Reviews*, vol. 41, no. 18 (Aug. 20, 2012), pp. 5969–5985.
- [84] Xiaodan Gu et al. “An In Situ Grazing Incidence X-Ray Scattering Study of Block Copolymer Thin Films During Solvent Vapor Annealing”. *Advanced Materials*, vol. 26, no. 2 (Jan. 1, 2014), pp. 273–281.
- [85] Xiaodan Gu et al. “Controlling Domain Spacing and Grain Size in Cylindrical Block Copolymer Thin Films by Means of Thermal and Solvent Vapor Annealing”. *Macromolecules*, vol. 49, no. 9 (May 10, 2016), pp. 3373–3381.

- [86] Bernd Smarsly and Markus Antonietti. "Block Copolymers as Templates for the Generation of Mesosstructured Inorganic Materials". *Block Copolymers in Nanoscience*. Ed. by ssimo Lazzari Faculty of Chemistry; Guojun Liu, and Sébastien Lecommandoux. Wiley-VCH Verlag GmbH & Co. KGaA, 2006, pp. 291–307.
- [87] Stefan Howorka. "Creating regular arrays of nanoparticles with self-assembling protein building blocks". *Journal of Materials Chemistry*, vol. 17, no. 20 (May 16, 2007), pp. 2049–2053.
- [88] Jeong Gon Son et al. "Placement Control of Nanomaterial Arrays on the Surface- Reconstructed Block Copolymer Thin Films". *ACS Nano*, vol. 3, no. 12 (Dec. 22, 2009), pp. 3927–3934.
- [89] Jenny Malmström and Jadranka Travas-Sejdic. "Block copolymers for protein ordering". *Journal of Applied Polymer Science*, vol. 131, no. 14 (July 15, 2014), p. 40360.
- [90] Jong-in Hahm. "Fundamentals of Nanoscale Polymer–Protein Interactions and Potential Contributions to Solid-State Nanobioarrays". *Langmuir*, vol. 30, no. 33 (Aug. 26, 2014), pp. 9891–9904.
- [91] Younsoo Bae; Horacio Cabral, and Kazunori Kataoka. "Block Copolymer Micelles for Drug Delivery in Nanoscience". *Block Copolymers in Nanoscience*. Ed. by ssimo Lazzari Faculty of Chemistry; Guojun Liu, and Sébastien Lecommandoux. Wiley-VCH Verlag GmbH & Co. KGaA, 2006, pp. 73–89.
- [92] Olivier Diat and Gérard Gebel. "Block Ionomers for Fuel Cell Application". *Block Copolymers in Nanoscience*. Ed. by ssimo Lazzari Faculty of Chemistry; Guojun Liu, and Sébastien Lecommandoux. Wiley-VCH Verlag GmbH & Co. KGaA, 2006, pp. 337–366.
- [93] Jacob N. Israelachvili. *Intermolecular and Surface Forces 3rd Edition*. Boston: Academic Press, June 2011.
- [94] P. Eaton and P. West. *Atomic Force Microscopy*. Oxford University Press, May 1, 2010. 1 p.
- [95] Q. Zhong et al. "Fractured polymer/silica fiber surface studied by tapping mode atomic force microscopy". *Surface Science*, vol. 290, no. 1 (June 10, 1993), pp. L688–L692.
- [96] Martin Stark et al. "Inverting dynamic force microscopy: From signals to time-resolved interaction forces". *Proceedings of the National Academy of Sciences*, vol. 99, no. 13 (June 25, 2002), pp. 8473–8478.
- [97] Justin Legleiter et al. "Scanning probe acceleration microscopy (SPAM) in fluids: Mapping mechanical properties of surfaces at the nanoscale". *Proceedings of the National Academy of Sciences of the United States of America*, vol. 103, no. 13 (Mar. 28, 2006), pp. 4813–4818.
- [98] Michael E. McConney; Srikanth Singamaneni, and Vladimir V. Tsukruk. "Probing Soft Matter with the Atomic Force Microscopies: Imaging and Force Spectroscopy". *Polymer Reviews*, vol. 50, no. 3 (July 27, 2010), pp. 235–286.

Bibliography

- [99] Bede Pittenger; Erina Natalia, and Su Chanmin. "Quantitative mechanical property mapping at the nanoscale with PeakForce QNM". *Bruker*, vol. Application Note, no. 128 (Jan. 2010).
- [100] "PeakForce Tapping & QNM". *Bruker AFM Probes*, vol. <http://blog.brukerafmprobes.com/guide-to-spm-and-afm-modes/peakforce-tapping-onm> (June 1, 2011).
- [101] F. J. Giessibl and G. Binnig. "Investigation of the (001) cleavage plane of potassium bromide with an atomic force microscope at 4.2 K in ultra-high vacuum". *Ultramicroscopy*, vol. 42 (July 1, 1992), pp. 281–289.
- [102] P. K. Hansma et al. "Tapping mode atomic force microscopy in liquids". *Applied Physics Letters*, vol. 64, no. 13 (Mar. 28, 1994), pp. 1738–1740.
- [103] Detlef Lohse and Xuehua Zhang. "Surface nanobubbles and nanodroplets". *Reviews of Modern Physics*, vol. 87, no. 3 (Aug. 31, 2015), pp. 981–1035.
- [104] Claudio Canale et al. "Recognizing and Avoiding Artifacts in Atomic Force Microscopy Imaging". *Atomic Force Microscopy in Biomedical Research*. Ed. by Pier Carlo Braga and Davide Ricci. Methods in Molecular Biology 736. Humana Press, Jan. 1, 2011, pp. 31–43.
- [105] I. Horcas et al. "WSXM: A software for scanning probe microscopy and a tool for nanotechnology". *Review of Scientific Instruments*, vol. 78, no. 1 (Jan. 1, 2007), p. 013705.
- [106] Alejandro Gimeno et al. "'Flatten plus': a recent implementation in WSxM for biological research". *Bioinformatics*, vol. 31, no. 17 (Sept. 1, 2015), pp. 2918–2920.
- [107] B. A. Joyce. "Molecular beam epitaxy". *Reports on Progress in Physics*, vol. 48, no. 12 (1985), p. 1637.
- [108] John B. Fenn et al. "Electrospray ionization—principles and practice". *Mass Spectrometry Reviews*, vol. 9, no. 1 (Jan. 1, 1990), pp. 37–70.
- [109] Stephan Rauschenbach et al. "Electrospray Ion Beam Deposition: Soft-Landing and Fragmentation of Functional Molecules at Solid Surfaces". *ACS Nano*, vol. 3, no. 10 (Oct. 27, 2009), pp. 2901–2910.
- [110] Grant E. Johnson; Qichi Hu, and Julia Laskin. "Soft Landing of Complex Molecules on Surfaces". *Annual Review of Analytical Chemistry*, vol. 4, no. 1 (2011), pp. 83–104.
- [111] Zhitao Deng et al. "A Close Look at Proteins: Submolecular Resolution of Two- and Three-Dimensionally Folded Cytochrome c at Surfaces". *Nano Letters*, vol. 12, no. 5 (May 9, 2012), pp. 2452–2458.
- [112] Matthias S. Wilm and Matthias Mann. "Electrospray and Taylor-Cone theory, Dole's beam of macromolecules at last?" *International Journal of Mass Spectrometry and Ion Processes*, vol. 136, no. 2 (Sept. 22, 1994), pp. 167–180.
- [113] Lars Konermann et al. "Unraveling the Mechanism of Electrospray Ionization". *Analytical Chemistry*, vol. 85, no. 1 (Jan. 2, 2013), pp. 2–9.

- [114] Stephan Rauschenbach et al. "Electrospray Ion Beam Deposition of Clusters and Biomolecules". *Small*, vol. 2, no. 4 (Apr. 1, 2006), pp. 540–547.
- [115] Matthew Newville. *Fundamentals of XAFS*. Chicago: University of Chicago, 2004.
- [116] James E Penner-Hahn. "X-ray Absorption Spectroscopy". *Encyclopedia of Life Sciences*. Ed. by John Wiley & Sons, Ltd. Chichester, UK: John Wiley & Sons, Ltd, May 3, 2005.
- [117] James E. Penner-Hahn. "X-ray absorption spectroscopy in coordination chemistry". *Coordination Chemistry Reviews*, vol. 190-192 (Sept. 1999), pp. 1101–1123.
- [118] Frank M. F. de Groot et al. "*2p* x-ray absorption of d transition-metal compounds: An atomic multiplet description including the crystal field". *Physical Review B*, vol. 42, no. 9 (Sept. 15, 1990), pp. 5459–5468.
- [119] Frank M. F. de Groot. "Multiplet effects in X-ray spectroscopy". *Coordination Chemistry Reviews*. Synchrotron Radiation in Inorganic and Bioinorganic Chemistry, vol. 249, no. 1 (Jan. 2005), pp. 31–63.
- [120] P. S. Miedema; H. Ikeno, and F. M. F. de Groot. "First principles multiplet calculations of the calcium $L_{2,3}$ x-ray absorption spectra of CaO and CaF₂". *Journal of Physics: Condensed Matter*, vol. 23, no. 14 (2011), p. 145501.
- [121] G. W. Goodrich and W. C. Wiley. "Continuous Channel Electron Multiplier". *Review of Scientific Instruments*, vol. 33, no. 7 (July 1, 1962), pp. 761–762.
- [122] Debajeet K. Bora et al. "An ultra-high vacuum electrochemical flow cell for in situ/operando soft X-ray spectroscopy study." *The Review of scientific instruments*, vol. 85, no. 4 (Apr. 2014), pp. 043106–043106.
- [123] J.-H. Guo et al. "X-Ray Emission Spectroscopy of Hydrogen Bonding and Electronic Structure of Liquid Water". *Physical Review Letters*, vol. 89, no. 13 (Sept. 9, 2002), p. 137402.
- [124] J.-H. Guo et al. "Molecular Structure of Alcohol-Water Mixtures". *Physical Review Letters*, vol. 91, no. 15 (Oct. 7, 2003), p. 157401.
- [125] Peng Jiang et al. "In situ soft X-ray absorption spectroscopy investigation of electrochemical corrosion of copper in aqueous NaHCO₃ solution". *Electrochemistry Communications*, vol. 12, no. 6 (June 2010), pp. 820–822.
- [126] *X-Ray Attenuation Length*. URL: http://henke.lbl.gov/optical_constants/atten2.html (visited on 05/18/2017).
- [127] *Density of common materials*. URL: <http://henke.lbl.gov/cgi-bin/density.pl> (visited on 05/18/2017).
- [128] S. Tanuma; C. J. Powell, and D. R. Penn. "Calculations of electron inelastic mean free paths. III. Data for 15 inorganic compounds over the 50–2000 eV range". *Surface and Interface Analysis*, vol. 17, no. 13 (Dec. 1, 1991), pp. 927–939.

Bibliography

- [129] Niklas Ottosson et al. "Photoelectron spectroscopy of liquid water and aqueous solution: Electron effective attenuation lengths and emission-angle anisotropy". *Journal of Electron Spectroscopy and Related Phenomena*. Water and Hydrogen Bonds, vol. 177, no. 2 (Mar. 2010), pp. 60–70.
- [130] Claude F. Meares. "Peptide–Metal Interactions". *Encyclopedia of Inorganic Chemistry*. John Wiley & Sons, Ltd, 2006.
- [131] Crystal E. Valdez et al. "Mysteries of Metals in Metalloenzymes". *Accounts of Chemical Research*, vol. 47, no. 10 (Oct. 21, 2014), pp. 3110–3117.
- [132] Árpád Karsai et al. "Potassium-dependent oriented growth of amyloid β 25–35 fibrils on mica". *Nanotechnology*, vol. 18, no. 34 (2007), p. 345102.
- [133] Muyun Xie et al. "Peptide Self-Assembly on Mica under Ethanol-Containing Atmospheres: Effects of Ethanol on Epitaxial Growth of Peptide Nanofilaments". *The Journal of Physical Chemistry B*, vol. 116, no. 9 (Mar. 8, 2012), pp. 2927–2933.
- [134] Hai Li et al. "Organic Solvents Mediate Self-assembly of GAV-9 Peptide on Mica Surface". *Acta Biochimica et Biophysica Sinica*, vol. 39, no. 4 (Apr. 1, 2007), pp. 285–289.
- [135] Qiqige Du et al. "A comparative study on the self-assembly of an amyloid-like peptide at water–solid interfaces and in bulk solutions". *Microscopy Research and Technique*, vol. 78, no. 5 (May 1, 2015), pp. 375–381.
- [136] Evan T. Powers et al. "Ordered Langmuir–Blodgett Films of Amphiphilic β -Hairpin Peptides Imaged by Atomic Force Microscopy". *Angewandte Chemie International Edition*, vol. 41, no. 1 (Jan. 4, 2002), pp. 127–130.
- [137] Conor Whitehouse et al. "Adsorption and Self-Assembly of Peptides on Mica Substrates". *Angewandte Chemie International Edition*, vol. 44, no. 13 (Mar. 18, 2005), pp. 1965–1968.
- [138] Hanna Rapaport. "Ordered Peptide Assemblies at Interfaces". *Supramolecular Chemistry*, vol. 18, no. 5 (July 1, 2006), pp. 445–454.
- [139] Xingfei Zhou et al. "Hierarchical ordering of amyloid fibrils on the mica surface". *Nanoscale*, vol. 5, no. 11 (2013), pp. 4816–4822.
- [140] Ünige Murvai et al. "Structural and nanomechanical comparison of epitaxially and solution-grown amyloid β 25–35 fibrils". *Biochimica et Biophysica Acta (BBA) - Proteins and Proteomics*, vol. 1854, no. 5 (May 2015), pp. 327–332.
- [141] Linhao Sun et al. "Water stability of self-assembled peptide nanostructures for sequential formation of two-dimensional interstitial patterns on layered materials". Vol. 6, no. 99 (Oct. 10, 2016), pp. 96889–96897.
- [142] Jozef Adamcik et al. "Understanding amyloid aggregation by statistical analysis of atomic force microscopy images". *Nature Nanotechnology*, vol. 5, no. 6 (June 2010), pp. 423–428.
- [143] Stephan M. Dammer and Detlef Lohse. "Gas Enrichment at Liquid-Wall Interfaces". *Physical Review Letters*, vol. 96, no. 20 (May 24, 2006), p. 206101.

- [144] Daniel S. Wastl et al. "Observation of 4 nm Pitch Stripe Domains Formed by Exposing Graphene to Ambient Air". *ACS Nano*, vol. 7, no. 11 (Nov. 26, 2013), pp. 10032–10037.
- [145] Yi-Hsien Lu et al. "Interface-Induced Ordering of Gas Molecules Confined in a Small Space". *Scientific Reports*, vol. 4 (Nov. 26, 2014), p. 7189.
- [146] Yi-Hsien Lu; Chih-Wen Yang, and Ing-Shouh Hwang. "Atomic force microscopy study of nitrogen molecule self-assembly at the HOPG–water interface". *Applied Surface Science*, vol. 304 (June 2014), pp. 56–64.
- [147] Daniel S. Wastl; Alfred J. Weymouth, and Franz J. Giessibl. "Atomically Resolved Graphitic Surfaces in Air by Atomic Force Microscopy". *ACS Nano*, vol. 8, no. 5 (May 27, 2014), pp. 5233–5239.
- [148] Chung-Kai Fang et al. "Nucleation processes of nanobubbles at a solid/water interface". *Scientific Reports*, vol. 6 (Apr. 19, 2016), p. 24651.
- [149] Patrick Gallagher et al. "Switchable friction enabled by nanoscale self-assembly on graphene". *Nature Communications*, vol. 7 (Feb. 23, 2016), p. 10745.
- [150] Hsien-Chen Ko et al. "High-Resolution Characterization of Preferential Gas Adsorption at the Graphene–Water Interface". *Langmuir*, vol. 32, no. 43 (Nov. 1, 2016), pp. 11164–11171.
- [151] M. V. Maslova; L. G. Gerasimova, and W. Forsling. "Surface Properties of Cleaved Mica". *Colloid Journal*, vol. 66, no. 3 (May 1, 2004), pp. 322–328.
- [152] Ashley R. Cormier et al. "Molecular Structure of RADA16-I Designer Self-Assembling Peptide Nanofibers". *ACS Nano*, vol. 7, no. 9 (Sept. 24, 2013), pp. 7562–7572.
- [153] I Lasters et al. "Structural principles of parallel beta-barrels in proteins." *Proceedings of the National Academy of Sciences of the United States of America*, vol. 85, no. 10 (May 1988), pp. 3338–3342.
- [154] Rico Gutzler et al. "Mimicking Enzymatic Active Sites on Surfaces for Energy Conversion Chemistry". *Accounts of Chemical Research*, vol. 48, no. 7 (July 21, 2015), pp. 2132–2139.
- [155] A. Dean Sherry; Peter Caravan, and Robert E. Lenkinski. "Primer on gadolinium chemistry". *Journal of Magnetic Resonance Imaging*, vol. 30, no. 6 (Dec. 1, 2009), pp. 1240–1248.
- [156] Matthew F. Bush et al. "Collision Cross Sections of Proteins and Their Complexes: A Calibration Framework and Database for Gas-Phase Structural Biology". *Analytical Chemistry*, vol. 82, no. 22 (Nov. 15, 2010), pp. 9557–9565.
- [157] Feng Zhang et al. "Epitaxial Growth of Peptide Nanofilaments on Inorganic Surfaces: Effects of Interfacial Hydrophobicity/Hydrophilicity". *Angewandte Chemie International Edition*, vol. 45, no. 22 (May 26, 2006), pp. 3611–3613.
- [158] Claude F. Meares. "Peptide–Metal Interactions". *Encyclopedia of Inorganic Chemistry*. John Wiley & Sons, Ltd, 2006.

Bibliography

- [159] Uwe B Sleytr and Terry J Beveridge. “Bacterial S-layers”. *Trends in Microbiology*, vol. 7, no. 6 (June 1, 1999), pp. 253–260.
- [160] Robert P. Fagan and Neil F. Fairweather. “Biogenesis and functions of bacterial S-layers”. *Nature Reviews Microbiology*, vol. 12, no. 3 (Mar. 2014), pp. 211–222.
- [161] Dietmar Pum and Uwe B. Sleytr. “The application of bacterial S-layers in molecular nanotechnology”. *Trends in Biotechnology*, vol. 17, no. 1 (Jan. 1, 1999), pp. 8–12.
- [162] Sungwook Chung et al. “Self-catalyzed growth of S layers via an amorphous-to-crystalline transition limited by folding kinetics”. *Proceedings of the National Academy of Sciences*, vol. 107, no. 38 (Sept. 21, 2010), pp. 16536–16541.
- [163] Dietmar Pum; Jose Luis Toca-Herrera, and Uwe B. Sleytr. “S-Layer Protein Self-Assembly”. *International Journal of Molecular Sciences*, vol. 14, no. 2 (Jan. 25, 2013), pp. 2484–2501.
- [164] Dietmar Pum and Uwe B. Sleytr. “Reassembly of S-layer proteins”. *Nanotechnology*, vol. 25, no. 31 (2014), p. 312001.
- [165] Seong-Ho Shin and Sungwook Chung. “Direct observation of kinetic traps associated with structural transformations leading to multiple pathways of S-layer assembly”. *Proceedings of the National Academy of Sciences* (2012).
- [166] Wolfgang J. Parak; Friedrich C. Simmel, and Alexander W. Holleitner. “Top-Down Versus Bottom-Up”. *Nanotechnology*. 2010, pp. 41–71.
- [167] Xiaodan Gu et al. “High Aspect Ratio Sub-15 nm Silicon Trenches From Block Copolymer Templates”. *Advanced Materials*, vol. 24, no. 42 (Nov. 8, 2012), pp. 5688–5694.
- [168] Mehmet H. Ucisik et al. “S-layer fusion protein as a tool functionalizing emulsomes and CurcuEmulsomes for antibody binding and targeting”. *Colloids and Surfaces B: Biointerfaces*, vol. 128 (Apr. 1, 2015), pp. 132–139.
- [169] Dieter Moll et al. “S-layer-streptavidin fusion proteins as template for nanopatterned molecular arrays”. *Proceedings of the National Academy of Sciences*, vol. 99, no. 23 (Nov. 12, 2002), pp. 14646–14651.
- [170] Soojin Park et al. “Macroscopic 10-Terabit-per-Square-Inch Arrays from Block Copolymers with Lateral Order”. *Science*, vol. 323, no. 5917 (Feb. 20, 2009), pp. 1030–1033.
- [171] Susana Moreno-Flores et al. “From Native to Non-Native Two-Dimensional Protein Lattices through Underlying Hydrophilic/Hydrophobic Nanoprotrusions”. *Angewandte Chemie*, vol. 120, no. 25 (June 9, 2008), pp. 4785–4788.
- [172] Nitin Kumar et al. “Activity Study of Self-Assembled Proteins on Nanoscale Diblock Copolymer Templates”. *Langmuir*, vol. 23, no. 14 (July 2007), pp. 7416–7422.
- [173] Omkar Parajuli et al. “Evaluation of enzymatic activity on nanoscale polystyrene-block-polymethylmethacrylate diblock copolymer domains”. *The Journal of Physical Chemistry. B*, vol. 111, no. 50 (Dec. 20, 2007), pp. 14022–14027.

- [174] Sheng Song et al. "Ascertaining effects of nanoscale polymeric interfaces on competitive protein adsorption at the individual protein level". *Nanoscale*, vol. 8, no. 6 (Feb. 5, 2016), pp. 3496–3509.
- [175] David A. Cisneros et al. "Creating Ultrathin Nanoscopic Collagen Matrices For Biological And Biotechnological Applications". *Small*, vol. 3, no. 6 (June 4, 2007), pp. 956–963.
- [176] David J. S. Hulmes. "Building Collagen Molecules, Fibrils, and Suprafibrillar Structures". *Journal of Structural Biology*, vol. 137, no. 1 (Jan. 1, 2002), pp. 2–10.
- [177] Nima Saeidi et al. "Production of highly aligned collagen lamellae by combining shear force and thin film confinement". *Acta Biomaterialia*, vol. 7, no. 6 (June 2011), pp. 2437–2447.
- [178] Badri Narayanan et al. "Self-Assembly of Collagen on Flat Surfaces: The Interplay of Collagen–Collagen and Collagen–Substrate Interactions". *Langmuir*, vol. 30, no. 5 (Feb. 11, 2014), pp. 1343–1350.
- [179] Wee Wen Leow and Wonmuk Hwang. "Epitaxially Guided Assembly of Collagen Layers on Mica Surfaces". *Langmuir*, vol. 27, no. 17 (Sept. 6, 2011), pp. 10907–10913.
- [180] Hubert Bahl et al. "IV. Molecular biology of S-layers". *FEMS Microbiology Reviews*, vol. 20, no. 1 (June 1, 1997), pp. 47–98.
- [181] Margit Sára and Uwe B. Sleytr. "S-Layer Proteins". *Journal of Bacteriology*, vol. 182, no. 4 (Feb. 2000), pp. 859–868.
- [182] Joel B. Thompson; Susanne Schultze-Lam, and Terrence J. Beveridge. "Whiting events: biogenic origin due to the photosynthetic activity of cyanobacterial picoplankton". *Limnology and Oceanography*, vol. 42 (I 1997), pp. 133–141.
- [183] W. S. Broecker; A. Sanyal, and T. Takahashi. "The origin of Bahamian Whittings revisited". *Geophysical Research Letters*, vol. 27, no. 22 (Nov. 15, 2000), pp. 3759–3760.
- [184] Ivan Sondi and Mladen Juračić. "Whiting events and the formation of aragonite in Mediterranean Karstic Marine Lakes: new evidence on its biologically induced inorganic origin". *Sedimentology*, vol. 57, no. 1 (Jan. 2010), pp. 85–95.
- [185] Erik B. Larson and John E. Myroie. "A review of whiting formation in the Bahamas and new models". *Carbonates and Evaporites*, vol. 29, no. 4 (Dec. 1, 2014), pp. 337–347.
- [186] John W. Morse; Dwight K. Gledhill, and Frank J. Millero. "CaCO₃ precipitation kinetics in waters from the great Bahama bank: Implications for the relationship between bank hydrochemistry and whittings". *Geochimica et Cosmochimica Acta*, vol. 67, no. 15 (Aug. 1, 2003), pp. 2819–2826.
- [187] Hector Bustos-Serrano; John W. Morse, and Frank J. Millero. "The formation of whittings on the Little Bahama Bank". *Marine Chemistry*, vol. 113, no. 1 (Jan. 30, 2009), pp. 1–8.
- [188] J. B. Thompson and E. G. Ferris. "Cyanobacterial precipitation of gypsum, calcite, and magnesite from natural alkaline lake water". *Geology*, vol. 18, no. 10 (Oct. 1, 1990), pp. 995–998.

Bibliography

- [189] Joel B. Thompson. "Microbial Whitings". *Microbial Sediments*. Ed. by Dr Robert E. Riding and Dr Stanley M. Awramik. Springer Berlin Heidelberg, 2000, pp. 250–260.
- [190] Maria Dittrich and Martin Obst. "Are Picoplankton Responsible for Calcite Precipitation in Lakes?" *AMBIO: A Journal of the Human Environment*, vol. 33, no. 8 (Dec. 1, 2004), pp. 559–564.
- [191] M. Obst; B. Wehrli, and M. Dittrich. "CaCO₃ nucleation by cyanobacteria: laboratory evidence for a passive, surface-induced mechanism". *Geobiology*, vol. 7, no. 3 (June 1, 2009), pp. 324–347.
- [192] Walter E. Dean. "The carbon cycle and biogeochemical dynamics in lake sediments". *Journal of Paleolimnology*, vol. 21, no. 4 (May 1, 1999), pp. 375–393.
- [193] Ernest O. Lawrence and Stanley M. Livingston. "The production of high speed light ions without the use of high voltages". *Physical Review*, vol. 40 (1932), pp. 19–35.
- [194] K. Benzerara et al. "Scanning transmission X-ray microscopy study of microbial calcification". *Geobiology*, vol. 2, no. 4 (Oct. 1, 2004), pp. 249–259.
- [195] Carlos Escudero and Miquel Salmeron. "From solid–vacuum to solid–gas and solid–liquid interfaces: In situ studies of structure and dynamics under relevant conditions". *Surface Science*. *Surface Science under Environmental Conditions*, vol. 607 (Jan. 2013), pp. 2–9.
- [196] E. Beniash et al. "Amorphous calcium carbonate transforms into calcite during sea urchin larval spicule growth". *Proceedings of the Royal Society B: Biological Sciences*, vol. 264, no. 1380 (Mar. 22, 1997), pp. 461–465.
- [197] L. Addadi; S. Raz, and S. Weiner. "Taking Advantage of Disorder: Amorphous Calcium Carbonate and Its Roles in Biomineralization". *Advanced Materials*, vol. 15, no. 12 (June 17, 2003), pp. 959–970.
- [198] Yael Politi et al. "Sea Urchin Spine Calcite Forms via a Transient Amorphous Calcium Carbonate Phase". *Science*, vol. 306, no. 5699 (Nov. 12, 2004), pp. 1161–1164.
- [199] T. Yong-Jin Han and Joanna Aizenberg. "Calcium Carbonate Storage in Amorphous Form and Its Template-Induced Crystallization". *Chemistry of Materials*, vol. 20, no. 3 (Feb. 1, 2008), pp. 1064–1068.
- [200] Peter Fratzl et al. "A kinetic model of the transformation of a micropatterned amorphous precursor into a porous single crystal". *Acta Biomaterialia*, vol. 6, no. 3 (Mar. 2010), pp. 1001–1005.
- [201] Christopher J. Stephens et al. "Amorphous Calcium Carbonate is Stabilized in Confinement". *Advanced Functional Materials*, vol. 20, no. 13 (July 9, 2010), pp. 2108–2115.
- [202] Chantel C. Tester et al. "In vitro synthesis and stabilization of amorphous calcium carbonate (ACC) nanoparticles within liposomes". *CrystEngComm*, vol. 13, no. 12 (May 31, 2011), pp. 3975–3978.

- [203] Yutao U. T. Gong et al. "Phase transitions in biogenic amorphous calcium carbonate". *PNAS*, vol. 109, no. 16 (Apr. 17, 2012), pp. 6088–6093.
- [204] Assaf Gal et al. "Calcite Crystal Growth by a Solid-State Transformation of Stabilized Amorphous Calcium Carbonate Nanospheres in a Hydrogel". *Angewandte Chemie International Edition*, vol. 52, no. 18 (Apr. 26, 2013), pp. 4867–4870.
- [205] Michael H. Nielsen; Shaul Aloni, and James J. De Yoreo. "In situ TEM imaging of CaCO₃ nucleation reveals coexistence of direct and indirect pathways". *Science*, vol. 345, no. 6201 (Sept. 5, 2014), pp. 1158–1162.
- [206] Emilie M. Pouget et al. "The Development of Morphology and Structure in Hexagonal Vaterite". *Journal of the American Chemical Society*, vol. 132, no. 33 (Aug. 25, 2010), pp. 11560–11565.
- [207] Denis Gebauer et al. "Proto-Calcite and Proto-Vaterite in Amorphous Calcium Carbonates". *Angewandte Chemie International Edition*, vol. 49, no. 47 (Nov. 15, 2010), pp. 8889–8891.
- [208] Denis Gebauer; Antje Völkel, and Helmut Cölfen. "Stable Prenucleation Calcium Carbonate Clusters". *Science*, vol. 322, no. 5909 (Dec. 19, 2008), pp. 1819–1822.
- [209] Emilie M. Pouget et al. "The Initial Stages of Template-Controlled CaCO₃ Formation Revealed by Cryo-TEM". *Science*, vol. 323, no. 5920 (Mar. 13, 2009), pp. 1455–1458.
- [210] F. Marc Michel et al. "Structural Characteristics of Synthetic Amorphous Calcium Carbonate". *Chemistry of Materials*, vol. 20, no. 14 (July 1, 2008), pp. 4720–4728.
- [211] Laurie B. Gower and Damian J. Odom. "Deposition of calcium carbonate films by a polymer-induced liquid-precursor (PILP) process". *Journal of Crystal Growth*, vol. 210, no. 4 (Mar. 2000), pp. 719–734.
- [212] Stephan E. Wolf et al. "Early Homogenous Amorphous Precursor Stages of Calcium Carbonate and Subsequent Crystal Growth in Levitated Droplets". *Journal of the American Chemical Society*, vol. 130, no. 37 (Sept. 17, 2008), pp. 12342–12347.
- [213] Zhaoyong Zou et al. "On the Phase Diagram of Calcium Carbonate Solutions". *Advanced Materials Interfaces*, vol. 4, no. 1 (Jan. 1, 2017), p. 1600076.
- [214] Adam F. Wallace et al. "Microscopic Evidence for Liquid-Liquid Separation in Supersaturated CaCO₃ Solutions". *Science*, vol. 341, no. 6148 (Aug. 23, 2013), pp. 885–889.
- [215] Mark A. Bewernitz et al. "A metastable liquid precursor phase of calcium carbonate and its interactions with polyaspartate". *Faraday Discussions*, vol. 159, no. 0 (Mar. 18, 2013), pp. 291–312.
- [216] Denis Gebauer and Helmut Cölfen. "Prenucleation clusters and non-classical nucleation". *Nano Today*, vol. 6, no. 6 (Dec. 2011), pp. 564–584.
- [217] Paolo Raiteri and Julian D. Gale. "Water Is the Key to Nonclassical Nucleation of Amorphous Calcium Carbonate". *Journal of the American Chemical Society*, vol. 132, no. 49 (Dec. 15, 2010), pp. 17623–17634.

Bibliography

- [218] Raffaella Demichelis et al. “Stable prenucleation mineral clusters are liquid-like ionic polymers”. *Nature Communications*, vol. 2 (Dec. 20, 2011), p. 590.
- [219] Royce K. Lam et al. “Reversed interfacial fractionation of carbonate and bicarbonate evidenced by X-ray photoemission spectroscopy”. *The Journal of Chemical Physics*, vol. 146, no. 9 (Mar. 7, 2017), p. 094703.
- [220] Paul J. M. Smeets et al. “Calcium carbonate nucleation driven by ion binding in a biomimetic matrix revealed by in situ electron microscopy”. *Nature Materials*, vol. 14, no. 4 (Apr. 2015), pp. 394–399.
- [221] Amanda J. Page and Richard P. Sear. “Heterogeneous Nucleation in and out of Pores”. *Physical Review Letters*, vol. 97, no. 6 (Aug. 10, 2006), p. 065701.
- [222] Lester O. Hedges and Stephen Whitelam. “Patterning a surface so as to speed nucleation from solution”. *Soft Matter*, vol. 8, no. 33 (Aug. 1, 2012), pp. 8624–8635.
- [223] Pradyot Patnaik. *Handbook of Inorganic Chemicals*. 1st edition. New York: McGraw-Hill Professional, Nov. 20, 2002. 1086 pp.
- [224] Andy Ridgwell and Richard E. Zeebe. “The role of the global carbonate cycle in the regulation and evolution of the Earth system”. *Earth and Planetary Science Letters*, vol. 234, no. 3 (June 15, 2005), pp. 299–315.
- [225] Jon Petter Gustafsson. *Visual MINTeq*. Version 3.1. Stockholm, Dec. 13, 2016.
- [226] Maria Dittrich and Sabine Sibling. “Influence of H⁺ and Calcium Ions on Surface Functional Groups of *Synechococcus* PCC 7942 Cells”. *Langmuir*, vol. 22, no. 12 (June 1, 2006), pp. 5435–5442.
- [227] M. Obst; M. Dittrich, and H. Kuehn. “Calcium adsorption and changes of the surface microtopography of cyanobacteria studied by AFM, CFM, and TEM with respect to biogenic calcite nucleation”. *Geochemistry, Geophysics, Geosystems*, vol. 7, no. 6 (June 1, 2006), Q06011.
- [228] Susanne Schultze-Lam and Terry J Beveridge. “Nucleation of celestite and strontianite on a cyanobacterial S-layer”. *Applied and Environmental Microbiology*, vol. 60, no. 2 (1994), pp. 447–453.
- [229] G. J. Brunskill and S. D. Ludlam. “Fayetteville Green Lake, New York. I. Physical and Chemical Limnology”. *Limnology and Oceanography*, vol. 14, no. 6 (Nov. 1, 1969), pp. 817–829.
- [230] Taro Takahashi et al. “Chemical and Isotopic Balances for a Meromictic Lake”. *Limnology and Oceanography*, vol. 13, no. 2 (Apr. 1, 1968), pp. 272–292.
- [231] Ljerka Brečević and Arne Erik Nielsen. “Solubility of amorphous calcium carbonate”. *Journal of Crystal Growth*, vol. 98, no. 3 (Nov. 2, 1989), pp. 504–510.
- [232] S. J. Naftel et al. “Calcium L-edge XANES study of some calcium compounds”. *Journal of Synchrotron Radiation*, vol. 8, no. 2 (Mar. 1, 2001), pp. 255–257.

- [233] Yael Politi et al. “Transformation mechanism of amorphous calcium carbonate into calcite in the sea urchin larval spicule”. *Proceedings of the National Academy of Sciences*, vol. 105, no. 45 (Nov. 11, 2008), pp. 17362–17366.
- [234] Michael E. Fleet and Xiaoyang Liu. “Calcium L_{2,3}-edge XANES of carbonates, carbonate apatite, and oldhamite (CaS)”. *American Mineralogist*, vol. 94, no. 8 (Aug. 1, 2009), pp. 1235–1241.
- [235] Rebecca A. Metzler and Peter Rez. “Polarization Dependence of Aragonite Calcium L-Edge XANES Spectrum Indicates c and b Axes Orientation”. *The Journal of Physical Chemistry B*, vol. 118, no. 24 (June 19, 2014), pp. 6758–6766.
- [236] Albert C. Thompson et al. *X-ray Data Booklet*. Third. Berkeley, California: Center for X-Ray Optics and Advanced Light Source, Sept. 2009.
- [237] M. Obst et al. “Precipitation of amorphous CaCO₃ (aragonite-like) by cyanobacteria: A STXM study of the influence of EPS on the nucleation process”. *Geochimica et Cosmochimica Acta*, vol. 73, no. 14 (July 15, 2009), pp. 4180–4198.
- [238] Johannes V. Barth. “Molecular Architectonic on Metal Surfaces”. *Annual Review of Physical Chemistry*, vol. 58, no. 1 (2007), pp. 375–407.
- [239] James J. De Yoreo; Sungwook Chung, and Raymond W. Friddle. “In Situ Atomic Force Microscopy as a Tool for Investigating Interactions and Assembly Dynamics in Biomolecular and Biomineral Systems”. *Advanced Functional Materials*, vol. 23, no. 20 (May 28, 2013), pp. 2525–2538.
- [240] Thermo Spectronic. *Basic UV-Vis Theory, Concepts and Applications*.

Updated list of publications

An updated list of publications that have followed from the work presented in this thesis can be found here:

http://www.mpg-epfl.mpg.de/1007435/Max-Planck-EPFL_Nanolab

Curriculum Vitae

Name: Bart Willem Stel
Date of Birth: November 5, 1987
Nationality: Dutch

- 2014–2017 **Doctoral Studies (PhD)** – *Max-Planck-EPFL Lab for Molecular Nanoscience, École Polytechnique Fédérale de Lausanne, Switzerland.*
Thesis title: *In situ* Studies of Peptide and Protein Assemblies at the Solid-Liquid Interface: Hierarchical Self-Assembly, Dynamics and Functional Properties.
Thesis director: Dr. Magalí Lingenfelder
Thesis co-director: Prof. Klaus Kern
- 2013 **Master Thesis research** – *Lawrence Berkeley National Laboratory, United States & Max-Planck-EPFL Lab for Molecular Nanoscience, EPFL, Switzerland.*
Thesis title: CO₂ Sequestration Using Bacterial Surface Layers. (*Twente University, October 2013*)
Thesis director: Dr. Magalí Lingenfelder
- 2011–2013 **Master Applied Physics (MSc)** – *Physics of Complex Fluids group (PCF), Twente University, Netherlands.*
Thesis title: CO₂ Sequestration Using Bacterial Surface Layers.
Master Thesis research at the Max-Planck-EPFL Lab for Molecular Nanoscience with Dr. Magalí Lingenfelder.
- 2012 **Internship** – *Group of Prof. J. De Yoreo, Molecular Foundry, Lawrence Berkeley National Laboratory, United States.*
- 2006–2011 **Bachelor Applied Physics (BSc)** – *Twente University, Netherlands.*
Thesis title: Gecko's Adhesion to Walls.
Thesis director: Dr. Sissi de Beer
Including a Minor *Worldview in a Technological Society and International Exploration.*
- 2000–2006 **Secondary Education (High School)** – *Rembrandt College, Veenendaal, Netherlands.*